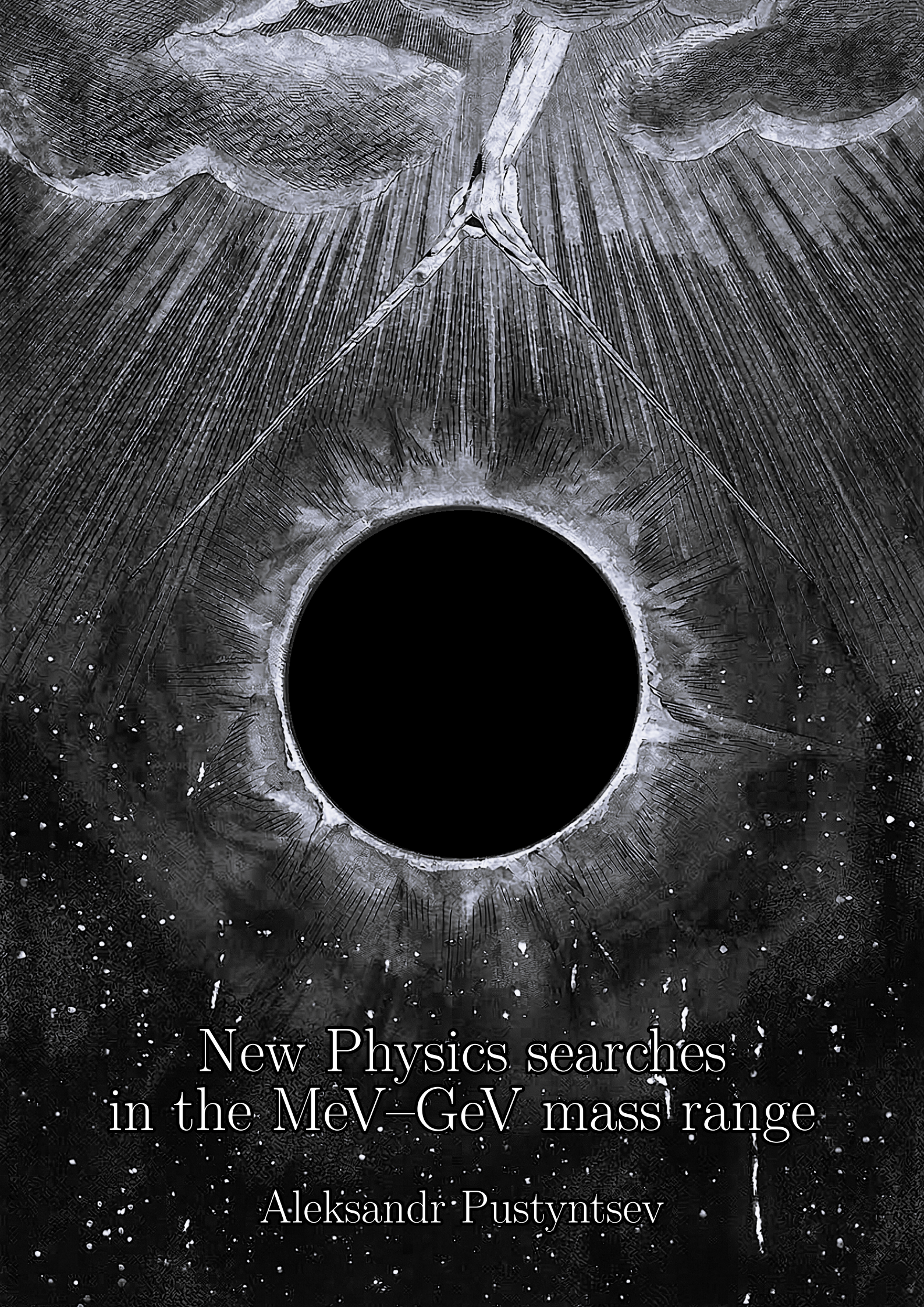

New Physics searches in the MeV–GeV mass range

Aleksandr Pustyntsev

New Physics searches in the MeV–GeV mass range

Dissertation
zur Erlangung des Grades
„ Doktor der Naturwissenschaften “

am Fachbereich Physik, Mathematik und Informatik
der Johannes Gutenberg-Universität Mainz

vorgelegt von

Aleksandr Pustyntsev

geboren in Norilsk, Russland

Mainz, 2026

Abstract

The search for light dark-sector particles in the MeV–GeV mass range has intensified over the past decade, driven by astrophysical evidence for dark matter, the strong CP problem, and persistent anomalies in particle physics—most notably the historical tension surrounding the muon anomalous magnetic moment, $(g-2)_\mu$. Together, these factors have stimulated a broad experimental program aimed at probing hidden-sector scenarios and exploring Beyond the Standard Model physics in a previously underexplored MeV–GeV region of parameter space.

A particularly well-motivated class of dark-sector candidates consists of axion-like particles, which generalize the canonical QCD axion by decoupling the strict mass-coupling relationship, allowing them to appear across a broader mass spectrum without necessarily addressing the strong CP problem. Arising naturally in many extensions of the Standard Model, these pseudoscalar states serve as prominent targets for low-energy precision probes.

In this thesis, constraints on the masses and couplings of ALPs and light scalar particles to photons and leptons are systematically derived. By utilizing data from current electron-positron collider experiments, such as BESIII and Belle II, and combining it with the most recent theoretical and experimental evaluations of lepton anomalous magnetic moments, the importance of a multi-coupling framework is demonstrated. A non-trivial interplay between leptonic and photonic interactions is revealed, showing that neglecting this dynamics can significantly obscure the true experimental bounds.

Furthermore, while existing high-energy collider experiments probe large portions of the sub-GeV parameter space, a persistent sensitivity gap in the mass range from a few to several hundred MeV is identified, primarily driven by the kinematic challenges of resolving highly collimated photon pairs. It is demonstrated that this gap can be effectively addressed by near-future, high-precision facilities. Specifically, the projected sensitivity of the MAGIX@MESA experiment, which operates below the hadroproduction threshold to provide a uniquely clean and well-controlled environment for direct BSM searches, is evaluated.

Complementary to this, a proposed Jefferson Lab program utilizing polarized positron scattering is explored. By exploiting novel polarization-dependent observables, such as the beam-normal single-spin asymmetry, it is shown how the helicity-conserving Standard Model background can be efficiently suppressed and how specific mediator spin structures can be disentangled. This framework is also extended to include vector and axial vector mediators, such as dark photons, thereby establishing a robust roadmap for discovering weakly coupled dark sector particles in the MeV–GeV mass range.

Zusammenfassung

Die Suche nach leichten Teilchen des dunklen Sektors im Massenbereich von MeV bis GeV wurde im vergangenen Jahrzehnt intensiviert, was durch astrophysikalische Hinweise auf Dunkle Materie, das starke CP-Problem und anhaltende Anomalien in der Teilchenphysik – allen voran die historische Diskrepanz rund um das anomale magnetische Moment des Myons, $(g-2)_\mu$ – vorangetrieben wurde. Zusammen wurde durch diese Faktoren ein breit angelegtes experimentelles Programm angeregt, welches darauf ausgerichtet ist, Hidden-Sector-Szenarien zu untersuchen und Physik jenseits des Standardmodells in einer zuvor wenig erforschten MeV–GeV-Region des Parameterraums zu erkunden.

Eine besonders gut motivierte Klasse von Kandidaten des dunklen Sektors wird von axionartigen Teilchen (ALPs) gebildet. Durch diese wird das kanonische QCD-Axion verallgemeinert, indem die strikte Beziehung zwischen Masse und Kopplung entkoppelt wird. Dadurch wird es ihnen ermöglicht, über ein breiteres Massenspektrum hinweg aufzutreten, ohne notwendigerweise das starke CP-Problem zu lösen. Da sie natürlicherweise in vielen Erweiterungen des Standardmodells entstehen, werden diese pseudoskalaren Zustände als prominente Ziele für niederenergetische Präzisionsuntersuchungen betrachtet.

In dieser Arbeit werden Einschränkungen für die Massen und Kopplungen von ALPs und leichten skalaren Teilchen an Photonen und Leptonen systematisch abgeleitet. Durch die Nutzung von Daten aktueller Elektron-Positron-Collider-Experimente wie BESIII und Belle II und deren Kombination mit den neuesten theoretischen und experimentellen Auswertungen der anomalen magnetischen Momente von Leptonen wird die Wichtigkeit eines Rahmenwerks multipler Kopplungen demonstriert. Ein nicht-triviales Zusammenspiel zwischen leptonischen und photonischen Wechselwirkungen wird aufgedeckt, wodurch gezeigt wird, dass die wahren experimentellen Grenzen erheblich verschleiert werden können, wenn diese Dynamik vernachlässigt wird.

Darüber hinaus wird – während weite Teile des Sub-GeV-Parameterraums durch existierende Hochenergie-Collider-Experimente untersucht werden – eine anhaltende Sensitivitätslücke im Massenbereich von wenigen bis mehreren hundert MeV identifiziert, welche primär durch die kinematischen Herausforderungen bei der Auflösung stark kollimierter Photonenpaare verursacht wird. Es wird demonstriert, dass diese Lücke durch hochpräzise Anlagen der nahen Zukunft effektiv geschlossen werden kann. Spezifisch wird die prognostizierte Sensitivität des MAGIX@MESA-Experiments evaluiert, welches unterhalb der Hadronenproduktionsschwelle betrieben wird, um eine einzigartig saubere und gut kontrollierte Umgebung für direkte BSM-Suchen bereitzustellen.

Ergänzend dazu wird ein am Jefferson Lab vorgeschlagenes Programm untersucht, bei dem polarisierte Positronenstreuung genutzt wird. Durch die Ausnutzung neuartiger polarisationsabhängiger Observablen, wie der strahlnormalen Einzelspin-Asymmetrie, wird gezeigt, wie der helizitätserhaltende Untergrund des Standardmodells effizient unterdrückt und wie spezifische Spin-Strukturen von Mediatoren entwirrt werden können. Dieses Konzept wird zudem dahingehend erweitert, dass Vektor- und Axialvektor-Mediatoren, wie etwa dunkle Photonen, einbezogen werden, wodurch ein robuster Fahrplan für die Entdeckung schwach gekoppelter Teilchen des dunklen Sektors im Massenbereich von MeV bis GeV etabliert wird.

List of publications

The results of this thesis are published in parts in the following articles:

Articles published in refereed journals

- A. Pustyntsev and M. Vanderhaeghen,
  Improved constraints for axion-like particles from 3-photon events at e^+e^- colliders,
  Eur. Phys. J. C **84** (2024).

- A. Pustyntsev and M. Vanderhaeghen,
  Constraints for scalars and pseudoscalars from $(g-2)_\ell$ and existing e^+e^- colliders,
  Phys. Rev. D **110**, 075027 (2024).

- A. Pustyntsev and M. Vanderhaeghen,
  Implications of recent $(g-2)_\mu$ measurements for MeV–GeV dark sector searches,
  Phys. Rev. D **112**, 095001 (2025).

Conference proceedings

- A. Pustyntsev and M. Vanderhaeghen,
  Study of axion-like particles constraints from 3-photon events at e^+e^- colliders,
  EPJ Web Conf. **303**, 05007 (2024).

Articles submitted for publication

- A. Pustyntsev, M. S. Ramasamy and M. Vanderhaeghen,
  New Physics Searches via Beam Normal Spin Asymmetry in Bhabha Scattering,
  under review at Phys. Rev. D., https://arxiv.org/abs/2511.22568v1.

Articles in preparation

- A. Pustyntsev and M. Vanderhaeghen,
  Sensitivity of MAGIX@MESA to BSM Effects via Bethe–Heitler Pair Production,
  in preparation, expected within first half of 2026.

The aforementioned works were supported by the Deutsche Forschungsgemeinschaft (DFG, German Research Foundation), in part through the Research Unit [Photon-photon interactions in the Standard Model and beyond, Projektnummer 458854507 - FOR 5327], and in part through the Cluster of Excellence [Precision Physics, Fundamental Interactions, and Structure of Matter] (PRISMA$^+$ EXC 2118/1) within the German Excellence Strategy (Project ID 39083149).

Contents

Chapter 1

Introduction

> If you can live without writing it,
> don't write at all.
>
> *Leo Tolstoy*

The Standard Model (SM) of particle physics describes the strong, weak, and electromagnetic interactions within the framework of quantum field theory. Its dynamics are governed by a non-abelian gauge symmetry with gauge group

$$SU(3)_C \otimes SU(2)_L \otimes U(1)_Y \,, \tag{1.1}$$

where C, L, and Y denote color, left-handed chirality, and weak hypercharge, respectively.

The matter fields are spin-1/2 fermions, which are organized into three generations and are chiral under the electroweak symmetry group. These are classified into quarks, which transform as triplets under $SU(3)_C$ and participate in the strong interaction, and leptons, which are color singlets. The interactions between these matter fields are mediated by spin-1 gauge bosons: eight massless gluons corresponding to the generators of $SU(3)_C$, and the $W^{\pm}$, Z^0, and photon fields arising from the electroweak sector.

Local gauge invariance strictly forbids explicit mass terms for both the fermions and the electroweak gauge bosons. To accommodate the massive physical states observed in nature, the SM employs the Brout-Englert-Higgs mechanism [1, 2]. A complex scalar $SU(2)_L$ doublet is introduced, acquiring a non-zero vacuum expectation value that spontaneously breaks the electroweak symmetry down to the electromagnetic subgroup, $U(1)_{\text{em}}$. This dynamically generates the masses of the $W^{\pm}$ and Z^0 bosons, while the fermions acquire mass via Yukawa interactions with the scalar field.

The experimental observation of the Higgs boson by the ATLAS and CMS collaborations in 2012, with a mass of $m_h \approx 125$ GeV, completed the predicted particle spectrum of the SM [3], which is depicted in Fig. 1.1. To date, the model has demonstrated remarkable success with explaining experimental measurements up to the TeV scale. However, despite its profound success in describing a broad range of phenomena, the SM is widely regarded as an effective theory valid up to a finite energy scale [4–7]. While precision measurements over several decades have confirmed its predictions with extraordinary accuracy, a number of empirical observations and theoretical considerations point to its incompleteness.

Among the most compelling open questions are the nature of dark matter [8–13], the absence of CP violation in the strong interaction [14–22], as well as the neutrino mass origin and the hierarchy of scales in fundamental interactions [23–26]. These and

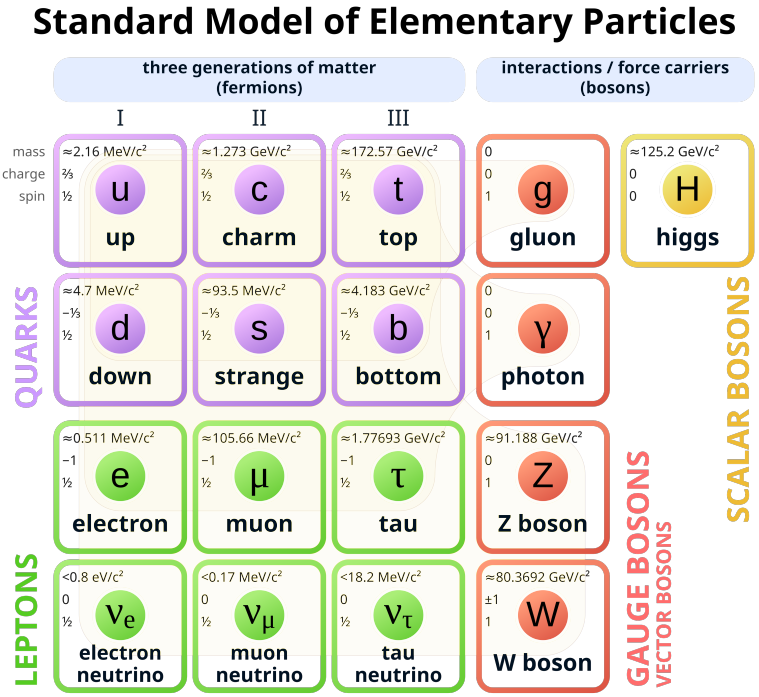

Figure 1.1: The Standard Model of particle physics.

other challenges have motivated the exploration of beyond the Standard Model (BSM) physics.

1.1 Observational evidence of BSM Physics

The most direct motivation for New Physics comes from cosmological and astrophysical observations that cannot be accommodated by the SM particle content.

Foremost among these is the existence of Dark Matter (DM). A wealth of gravitational evidence—ranging from galactic rotation curves and gravitational lensing to the power spectrum of the Cosmic Microwave Background (CMB)—indicates that roughly 26% of the universe's energy density consists of non-baryonic, cold dark matter. The SM offers no viable candidate for this matter; the neutrinos are too light and hot to account for the observed structure formation. Consequently, DM demands the introduction of new, stable (or exceptionally long-lived) particles, often hypothesized to reside in a "dark" or "hidden" sector that interacts with the SM via novel portal interactions.

Similarly, the observation of neutrino flavor oscillations provides robust evidence that neutrinos possess non-zero masses [27]. In the pristine SM, neutrinos are strictly massless because the theory lacks right-handed neutrino fields, thereby forbidding a Dirac mass term

$$\mathcal{L}_{\text{Dirac}} = -m_D \bar{\nu}_L \nu_R + \text{h.c.} \tag{1.2}$$

Alternatively, as neutrinos are electrically neutral, they could possess a Majorana mass term, which couples the left-handed field to its own charge-conjugate, $\nu_L^c = C\bar{\nu}_L^T$,

via

$$\mathcal{L}_{\text{Majorana}} = -\frac{1}{2} m_M \bar{\nu}_L^c \nu_L + \text{h.c.} \tag{1.3}$$

However, as ν_L is part of an $SU(2)_L$ doublet with hypercharge $Y = -1/2$, the bilinear $\bar{\nu}_L^c \nu_L$ transforms as a weak isospin triplet with $Y = -1$. Writing down this mass term would therefore explicitly violate the electroweak gauge symmetry. Furthermore, this term changes total lepton number by two units ($\Delta L = 2$), breaking the exact, anomaly-free $B - L$ (baryon minus lepton number) symmetry of the SM. Accommodating neutrino masses therefore necessitates extending the SM, either by introducing right-handed gauge singlets to generate Dirac masses, or by invoking high-scale lepton number violation—often dynamically realized via the seesaw mechanism—to generate Majorana masses.

Furthermore, the observable universe is composed almost entirely of matter, with an evident absence of primordial antimatter. To dynamically generate this baryon asymmetry (baryogenesis), the early universe must have satisfied the Sakharov conditions [28], which include the necessity of C and CP violation. While the SM incorporates CP violation via the irreducible phase in the Cabibbo-Kobayashi-Maskawa (CKM) matrix, the magnitude of this effect is orders of magnitude too small to generate the observed baryon-to-photon ratio. This deficit necessitates new possible sources of CP violation in the BSM landscape [29–32].

Beyond this, the structure of the SM exhibits unnatural fine-tuning, most prominently manifested in the strong CP problem. The non-abelian gauge structure of Quantum Chromodynamics (QCD) admits a topological vacuum term that explicitly violates P and CP symmetries

$$\mathcal{L}_\theta = \theta \frac{g^2}{32\pi^2} G^a_{\mu\nu} \tilde{G}^{a,\mu\nu}, \tag{1.4}$$

where g is the strong coupling constant, $G^a_{\mu\nu}$ is the gluon field strength tensor, and $\tilde{G}^{a,\mu\nu}$ is its dual. As will be discussed later, when the chiral transformation required to diagonalize the quark mass matrix M_q is accounted for, the physically observable parameter becomes $\bar{\theta} = \theta + \arg\det(M_q)$.

A non-zero $\bar{\theta}$ would induce a measurable permanent Electric Dipole Moment (EDM) for the neutron. However, as seen from Fig. 1.2, stringent experimental limits on this quantity require $\bar{\theta} \lesssim 10^{-10}$, while the SM provides no dynamical mechanism to explain the smallness of this parameter. Resolving this unnatural fine-tuning strongly motivates BSM physics frameworks, such as the Peccei-Quinn mechanism. This mechanism promotes $\bar{\theta}$ to a dynamical field and predicts the existence of a new pseudoscalar particle, the axion [14–17].

While originally motivated by the Peccei-Quinn solution to the strong CP problem, axions also constitute a particularly compelling class of dark sector states [33–35]. Further theoretical developments have inspired a broader class of pseudoscalar particles known as Axion-Like Particles (ALPs). In contrast to the QCD axion, ALPs are not constrained by a strict proportionality between their mass and coupling strength [36–40].

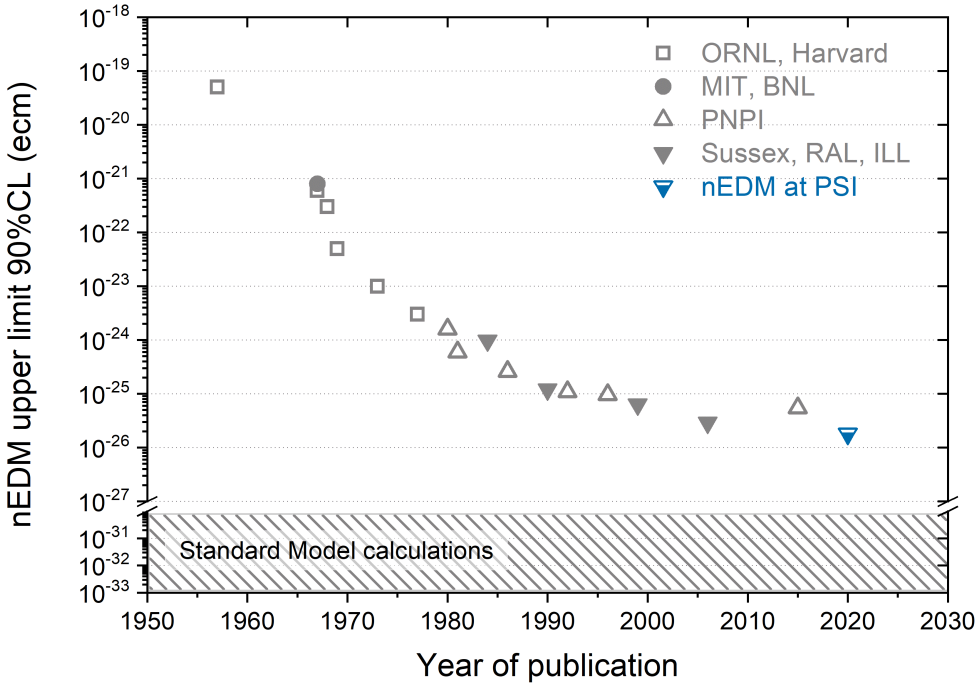

Figure 1.2: Experimental bounds on the neutron EDM over time [43, 44]. "Standard Model calculation" refers to the contribution arising solely from CP violation in the CKM matrix.

Such particles appear generically in various extensions of the SM, including string-inspired frameworks [41, 42]. Because they can naturally be light and exceptionally long-lived, ALPs represent highly motivated targets for intensity frontier experiments and form the primary focus of this work.

1.2 Experimental Probes

The theoretical and observational shortcomings of SM do not point to a single, unique energy scale or coupling strength for New Physics. Consequently, no single experimental design can comprehensively probe the vast BSM parameter space.

Historically, searches have been predominantly focused on the TeV energy scale, driven by naturalness arguments and the expectation that heavy new degrees of freedom would manifest at high energies [45–48]. However, the absence of unambiguous signals of New Physics in this regime has led to a growing interest in complementary approaches. In particular, light and weakly coupled new particles in the MeV-GeV mass range have emerged as well-motivated candidates that can evade existing constraints while remaining experimentally accessible [49–56].

To systematically address this diverse parameter space—from the TeV scale down to the sub-GeV regime—the modern experimental particle physics program is structured around three interconnected and complementary strategies: the Energy, Intensity, and Precision frontiers.

The Energy Frontier aims to further push the boundaries of achievable center-

of-mass energy, $\sqrt{s}$, in particle collisions. By relying on the mass-energy equivalence, high-energy colliders, such as the Large Hadron Collider (LHC), attempt the direct, on-shell production of heavy, previously inaccessible BSM resonances. This approach is historically the most direct path to discovery, having culminated in the observation of the top quark and the Higgs boson, and it continues to search for heavy phenomenological targets like supersymmetric partners or extended gauge bosons (e.g., Z').

The Intensity Frontier, conversely, trades maximum energy for increased collision statistics. It focuses on the low-mass regime ($m_{\text{BSM}} \lesssim \mathcal{O}(10)$ GeV), where new particles might be kinematically accessible but possess extremely suppressed couplings to the SM content. Experiments at this frontier, particularly fixed-target and beam dump facilities, utilize intense particle beams and high-Z targets to generate massive datasets.

The Precision Frontier takes an entirely different approach, probing for New Physics indirectly. Rather than producing BSM particles as real, asymptotic states, this frontier looks for their virtual effects occurring within quantum loops. By measuring fundamental observables—such as rare decay branching ratios, or the static electromagnetic properties of leptons—with exquisite accuracy, experiments can detect tiny deviations from the SM predictions.

These three frontiers do not operate in isolation; rather, they are highly complementary. An anomaly observed in a precision measurement, such as the tension between theory and experiment regarding the anomalous magnetic dipole moment of the muon, provides a targeted mass scale and coupling strength for direct searches at colliders or beam dumps.

1.2.1 Lepton dipole moment

The last aspect deserves special mention. Lepton dipole moments have long been established as powerful probes of quantum field theory (QFT) predictions [57–65]. While the Dirac equation predicts a gyromagnetic factor of $g_\ell = 2$ for point-like spin-1/2 fermions, quantum corrections induce deviations from this value. These effects are conventionally quantified in terms of the anomalous magnetic moment

$$a_\ell = \frac{g_\ell - 2}{2}, \tag{1.5}$$

which provides a precise and well-defined observable sensitive to radiative corrections.

The long-standing discrepancy between theoretical predictions and experimental measurements led to the establishment of the *Muon* $g-2$ *Theory Initiative* and the publication of the 2020 White Paper [66], which summarized the extensive efforts of the theoretical community. Comparing this consensus theory prediction with the experimental value measured by the Brookhaven E821 experiment [67] yields

$$a_\mu^{\text{exp.,2020}} = 116592089(63) \times 10^{-11}, \tag{1.6}$$
$$a_\mu^{\text{W.P.,2020}} = 116591810(43) \times 10^{-11}. \tag{1.7}$$

The difference between these two values established a discrepancy at the level of 3.7σ. This tension had long been considered one of the most significant hints of BSM physics

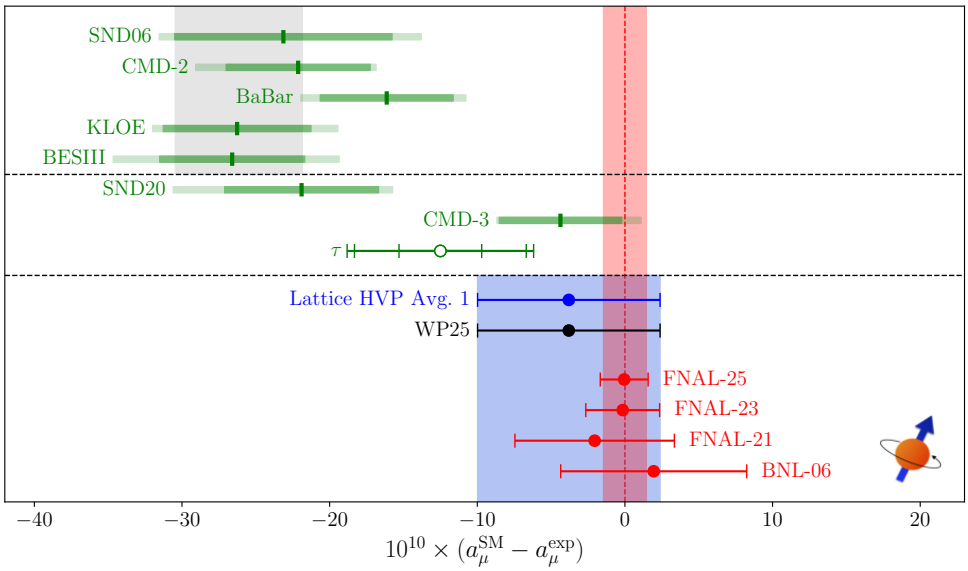

Figure 1.3: Summary of the current SM prediction for a_μ in comparison to experiment (red band and data points) [68].

[66]. Indeed, a simple dimensional estimate confirms the contribution of heavy New Physics to the anomalous magnetic moment generically scales as

$$\Delta a_\ell \sim \frac{m_\ell^2}{\Lambda^2}, \tag{1.8}$$

from which one sees that the muon, for instance, is approximately 40,000 times more sensitive to heavy physics than the electron. Although there are ways to depart from this statement [64], the quadratic dependence on m_ℓ is very generic and holds for a broad range of models.

The aforementioned deviation can be accommodated by a vector or scalar particle with a coupling to SM particles of order 10^{-4} to 10^{-3} and an MeV–GeV mass, being well within the reach of existing and near-future intensity frontier experiments. However, the ALP contribution to $(g-2)_\ell$ was historically disregarded as bearing no interest on its own, given that the provided correction is strictly *negative* while the reported discrepancy is *positive*. Nevertheless, this assumption holds only in the absence of an effective ALP-photon coupling. When these interactions are introduced, an additional diagrammatic contribution with a positive sign arises. The interplay of these two effects can therefore accommodate the observed anomaly with a GeV-scale ALP.

The situation evolved significantly over the subsequent five years, during which substantial progress in lattice QCD techniques was achieved. Therefore, the 2025 White Paper [68] reported an updated theoretical prediction, which can be directly compared against the most recent high-precision measurement from the Fermilab Muon $g-2$ experiment [70]

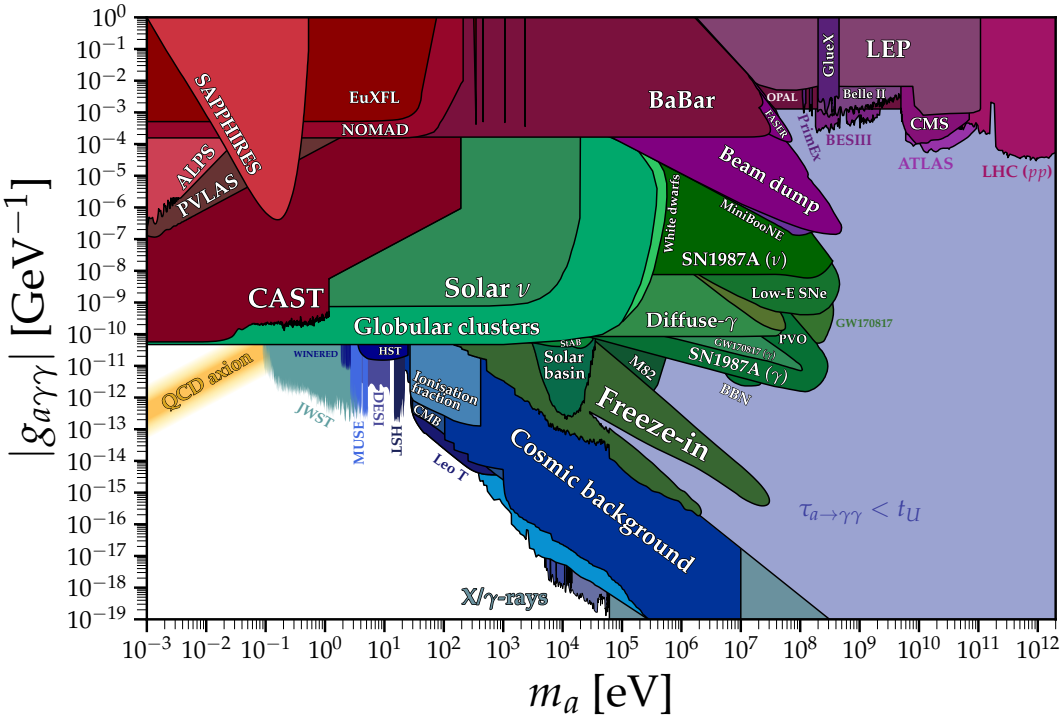

Figure 1.4: Experimental bounds on the coupling of the axion to two photons, with the yellow band representing the benchmark QCD axion models (single coupling scenario is assumed) [69].

$$a_\mu^{\text{exp.,2025}} = 116592071.5\,(14.5) \times 10^{-11}, \tag{1.9}$$

$$a_\mu^{\text{W.P.,2025}} = 116592033\,(62) \times 10^{-11}, \tag{1.10}$$

for which the discrepancy falls within the 1σ confidence interval, which is illustrated in Fig. 1.3.

Although this updated consensus removes the immediate need for a BSM explanation, it does not diminish the relevance of a_μ in the search for New Physics. Instead, it shifts the perspective: the remarkable agreement between theory and experiment transforms this observable from a phenomenological target into a rigorous constraint.

1.2.2 Low-energy precision experiments

The main focus of this thesis is dedicated to searches for BSM effects in the MeV–GeV mass range, a regime where existing constraints remain comparatively loose, as illustrated in Fig. 1.4. A visible gap can be seen between the low-mass region, which is heavily constrained by astrophysical data, and the high-mass region, where strong bounds have been established by the LHC. Another key aspect of this study is the emphasis on the interplay between the ALP-photon and ALP-lepton couplings, and the non-trivial dynamics they produce when considered simultaneously.

Existing bounds in this regime are derived from high-luminosity facilities such as BESIII and Belle II, alongside measurements from the LEP run at the Z pole. Search

channels include QED annihilation processes like $e^+e^- \to \gamma\gamma\gamma$, rare J/ψ meson decays at BESIII, and $Z \to \gamma\gamma\gamma$ decay searches from LEP.

Within this landscape, particular attention in this work is devoted to the Belle II experiment, located at the SuperKEKB asymmetric-energy B-factory. The accelerator operates primarily at the $\Upsilon(4S)$ resonance energy of $\sqrt{s} = 10.58\,\text{GeV}$ and is designed to deliver an instantaneous luminosity roughly 40 times larger than that of its predecessor, KEKB. The experiment continues to accumulate data, aiming to achieve an integrated luminosity of 50 ab^{-1} by the early 2030s and some of the most stringent constraints for BSM physics in the MeV–GeV region. Multi-photon final states, such as those from $e^+e^- \to \gamma a$, $a \to \gamma\gamma$ processes, are of particular interest in this kinematic regime.

Another compelling direction is the search for New Physics at low-energy precision facilities, such as the upcoming Mainz Energy-recovering Superconducting Accelerator (MESA). Operating below the pion production threshold, it combines high beam intensities with an exceptionally clean experimental environment, free of hadronic backgrounds.

Complementary to this program, a low-energy precision experiment at Jefferson Lab (JLab) is expected to begin operation on a similar timescale. This effort will employ polarized positron scattering on an atomic target, enabling access to polarization-sensitive observables—such as the beam-normal single-spin asymmetry—measured with unprecedented precision. This not only constitutes a novel approach to light BSM searches, but also provides a stringent precision test of the SM, since the beam-normal single-spin asymmetry in Bhabha scattering has never been measured before.

1.3 Outline

This thesis investigates the phenomenology of ALPs and related hidden sector mediators, focusing on the MeV–GeV mass window. By systematically analyzing high-intensity electron-positron colliders experiments, low-energy fixed-target facilities, and precision measurements of lepton dipole moments, updated and robust bounds on the BSM parameter space are derived. Particular emphasis is placed on the simultaneous treatment of multiple interaction channels to capture the non-trivial dynamics between photonic and leptonic couplings.

The work is organized as follows:

- **Chapter 2** provides an overview of the axion and ALP formalism, detailing their connection to open questions such as the neutron EDM, and reviews their relevant interactions. Rather than analyzing a specific UV-complete theory, our primary objective is to conduct a phenomenological study focused on a generic pseudoscalar particle that respects shift invariance and couples to SM leptons and gauge bosons.

  Furthermore, an analysis of shift-symmetric pseudoscalars at electron–positron colliders, including BESIII, Belle II, and LEP, is performed. A detailed numerical phase-space integration of final-state particles is performed—incorporating detector geometry, kinematic cuts, and energy thresholds. A primary conclusion of this analysis is that more contributions to the production cross section do not guarantee a higher signal yield as one must take into account not only how the mediator is

produced, but also how it *decays*. These branching ratio effects can suppress event yields, thereby relaxing previously established bounds in the lower-mass regime.

- **Chapter 3** shifts focus to the precision frontier, utilizing the anomalous magnetic moments of the electron and muon, $(g-2)_e$ and $(g-2)_\mu$, as constraint tools. By applying recent theoretical and experimental results, the viable parameter space for BSM mediators is systematically revised. The analysis incorporates 1-loop diagrammatic contributions for ALPs and subsequently extends the methodology to generic vector and axial vector scenarios, providing rigorous bounds on these interactions.

- **Chapter 4** addresses the kinematic limitations of high-energy colliders in the sub-GeV regime—specifically the finite angular resolution for highly collimated decay products—by exploring the potential of the upcoming MESA facility. Operating below the hadronic production threshold to avoid hadronic uncertainties, this experiment offers a combination of high-resolution magnetic spectrometers covering a broad range of angles, a setup allowing a dedicated optimization for BSM searches, and high beam intensity.

  This results in a uniquely sensitive probe of New Physics effects. In this chapter, search strategies based on Bethe-Heitler pair production are applied, and their potential as a versatile probe for mediators of different quantum numbers is demonstrated.

- Finally, **Chapter 5** investigates a novel approach to BSM searches utilizing polarized positron scattering at a proposed Jefferson Lab experiment. The focus is placed on polarization-sensitive observables, specifically the beam-normal single-spin asymmetry. By identifying a kinematic regime where the helicity-conserving QED background vanishes, leveraging the helicity-flipping nature of scalar couplings, and employing interference with the tree-level QED amplitude to enhance the signal-to-background ratio, competitive sensitivity projections, with a potential extension to double-spin asymmetries are derived.

Chapter 2

ALPs searches at e^+e^- colliders

> The hardest thing of all is to find a black cat in a dark room, especially if there is no cat.
>
> *Unattributed author*

This chapter reviews the theoretical motivation and experimental prospects for axions and ALPs as well-motivated SM extensions. We begin with a brief overview of the strong CP problem in quantum chromodynamics and its connection to the neutron electric dipole moment (nEDM), highlighting how the absence of observed CP violation in the strong sector motivates the introduction of the QCD axion. We then proceed with the broader class of ALP scenarios, which arise naturally in a wide range of ultraviolet-complete theories and provide a theoretically rich framework for exploring BSM physics.

The effective interactions of ALPs with SM fields—particularly photons and leptons—are subsequently discussed at the level of low-energy effective field theory, with emphasis on the generic features relevant for collider phenomenology. These couplings govern both the production mechanisms and decay signatures of ALPs at electron–positron collider facilities. The dominant backgrounds are identified, and the role of experimental cuts and detector-specific kinematic selections are examined. Special attention is paid to the impact of branching-ratio effects and loop-induced corrections, which can substantially modify expected signal rates and therefore influence the interpretation of experimental constraints.

The chapter concludes with a discussion of the current status and projected reach of existing and forthcoming electron–positron collider experiments, outlining their complementarity with other laboratory, astrophysical, and cosmological probes in constraining the ALP parameter space.

The results presented in this chapter are published in the works [71] and [72]. They have been reported at the MENU 2023 conference as a poster talk, at the EINN 2023 conference as a pre-conference talk and at the main poster session of the conference.

2.1 Axion and the strong CP problem

Let us consider some $SU(N)$ Yang–Mills theory coupled to a single fermion field f with strength g. The Lagrangian can be written as [22]

$$\mathcal{L}_{\text{Y.-M.}} = \bar{f}\left(i\not{D} - m_f e^{i\theta_f\gamma^5}\right) f - \frac{1}{4}G^a_{\mu\nu}G^{a,\mu\nu} + \theta\frac{g^2}{32\pi^2}G^a_{\mu\nu}\tilde{G}^{a,\mu\nu}, \tag{2.1}$$

where D_μ denotes the gauge-covariant derivative, and the dual field strength is taken according to the standard definition

$$\tilde{G}^{a,\mu\nu} = \frac{1}{2}\varepsilon^{\mu\nu\alpha\beta}G^a_{\alpha\beta}, \tag{2.2}$$

with $\varepsilon^{\mu\nu\alpha\beta}$ being the totally antisymmetric Levi-Civita symbol.

This Lagrangian contains two potential sources of CP violation: the phase θ_f in the fermion mass, and the *topological term*, proportional to θ. Two important properties of the latter are:

- As a consequence of the axial anomaly (arising from the transformation of the path integral measure and thus being a purely quantum effect) the divergence of the axial current satisfies

$$\partial_\mu\left(\bar{f}\gamma^\mu\gamma^5 f\right) = 2im_f\bar{f}\gamma^5 f - \underbrace{\frac{g^2}{16\pi^2}G^a_{\mu\nu}\tilde{G}^{a,\mu\nu}}_{\text{anomaly contribution}}. \tag{2.3}$$

  Thus, if the theory contains a massless fermion, the θ-term can then be removed by an axial rotation of the fermion field

$$f' = e^{i\beta\gamma^5}f, \tag{2.4}$$

  with $\beta = \theta_f/2$. This observation also illustrates that θ is a periodic parameter, with values identified modulo 2π, i.e., $\theta \in [0, 2\pi)$. On the other hand, it implies that neither θ nor θ_f are meaningful on their own; instead, their sum forms an observable

$$\bar{\theta} = \theta + \theta_f. \tag{2.5}$$

  For a theory containing multiple massive fermions, this definition generalizes to

$$\bar{\theta} = \theta + \arg\det\left(M_f\right), \tag{2.6}$$

  with M_f being the fermion mass matrix.

- The topological term can be expressed as a total derivative

$$G^a_{\mu\nu}\tilde{G}^{a\,\mu\nu} = \partial_\mu K^\mu, \tag{2.7}$$

  in terms of the Chern–Simons current

$$K^\mu = \varepsilon^{\mu\alpha\beta\gamma}\left(A^a_\alpha G^a_{\beta\gamma} - \frac{g}{3}f^{abc}A^a_\alpha A^b_\beta A^c_\gamma\right), \tag{2.8}$$

  where f^{abc} are the structure constants of the gauge group. Nevertheless, the fact that the topological term can be brought to the form (2.8) does not imply that it makes no contributions to physical observables—this statement is only true in *perturbation theory*, but fails in the *non-perturbative regime*.

The topological term, in fact, is responsible for the plethora of physical phenomena, most notably Yang–Mills instantons. Crucially, it also induces a nEDM estimated as

$$d_n \sim 10^{-16}\bar{\theta}\ \mathrm{e}\cdot\mathrm{cm}, \tag{2.9}$$

which, as shown in Fig. 1.2, is many orders of magnitude larger than experimental bounds unless $\bar{\theta} \lesssim 10^{-10}$. This extreme smallness of $\bar{\theta}$ constitutes the strong CP problem.

2.1.1 Neutron electric dipole moment

The existence of nEDM is forbidden by both parity P and time-reversal T symmetries, as can be seen directly from the transformation properties of the relevant 3-vectors [73]. Clearly, if the neutron possessed a nonzero permanent EDM, it would define a fixed spatial direction. For a particle in its ground state, however, Lorentz invariance allows no preferred direction other than that defined by the spin. Consequently, in order to preserve this symmetry, the EDM vector must be proportional to the spin vector

$$\mathbf{d} \propto \mathbf{s}, \tag{2.10}$$

which has immediate implications for discrete symmetries. Indeed, under a parity transformation, the spin vector $\mathbf{s}$, being an angular momentum, remains unchanged. In contrast, EDM, classically defined as

$$\mathbf{d} = \sum_i q_i \mathbf{r}_i, \tag{2.11}$$

where q_i and $\mathbf{r}_i$ denote the charge and position vector of the i-th constituent, is a polar vector and therefore changes sign under parity. Hence, parity symmetry is incompatible with a nonzero proportionality between $\mathbf{d}$ and $\mathbf{s}$, driving us to the conclusion that

$$\mathbf{d} \equiv 0. \tag{2.12}$$

A similar argument follows from time-reversal symmetry. Under such a transformation, the spin vector $\mathbf{s}$, being an angular momentum, is odd and changes sign, while the electric dipole moment $\mathbf{d}$ is even. As a result, the existence of a permanent electric dipole moment is again forbidden.

2.1.2 Peccei-Quinn solution

Likely the most compelling solution to the aforementioned problem was proposed by Peccei and Quinn, with further developments by Wilczek and Weinberg [14–17]. It was inspired by the resolution of the $U(1)$ problem in QCD and is based on postulating the existence of a new global chiral symmetry, $U(1)_{\mathrm{PQ}}$, spontaneously broken at some scale f_a. The associated pseudo–Nambu–Goldstone boson, known as the axion, couples to the gluon field through the effective Lagrangian

$$\mathcal{L}_{\mathrm{axion}} = \frac{\alpha_s}{8\pi} \frac{a}{f_a} G^a_{\mu\nu} \tilde{G}^{a\,\mu\nu}, \tag{2.13}$$

where the coupling constant is defined in the standard way, $\alpha_s = g^2/(4\pi)$.

As a consequence, the effective $\bar{\theta}$ parameter of QCD becomes a dynamical quantity

$$\bar{\theta}_{\mathrm{eff}} = \bar{\theta} + \frac{a}{f_a}, \tag{2.14}$$

which is then driven to zero, provided that the vacuum mean value of the axion field satisfies $\langle a \rangle = -f_a \bar{\theta}$.

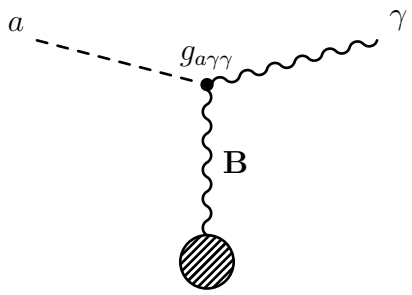

Figure 2.1: Axion conversion into a photon in a magnetic field **B**.

The exact realization of the Peccei–Quinn symmetry breaking is, however, model-dependent and can happen via various mechanisms. Two benchmark implementations commonly discussed in the literature are the Kim–Shifman–Vainshtein–Zakharov (KSVZ) [18] and Dine–Fischler–Srednicki–Zhitnitsky (DFSZ) [19] axion models, both of which introduce new heavy BSM states.

In KSVZ-type models, the Standard Model fields are neutral under the $U(1)_{\mathrm{PQ}}$ symmetry. The axion couples to gluons through loops of new heavy vector-like quarks that carry PQ charge but are electrically neutral under the Standard Model gauge group. As a result, the axion has no tree-level couplings to Standard Model fermions.

In contrast, DFSZ-type models assign $U(1)_{\mathrm{PQ}}$ charges directly to the Standard Model quarks and leptons. Consistency of the symmetry requires the introduction of an additional Higgs doublet, and the axion emerges from the phases of the Higgs fields and a Standard Model singlet. In this case, the axion possesses tree-level couplings to Standard Model fermions, with strengths suppressed by the PQ scale f_a.

Despite the differences in their UV completions, both KSVZ and DFSZ axion models share a key phenomenological feature: the axion mass is inversely proportional to the Peccei–Quinn scale f_a

$$m_a \sim \frac{\Lambda_{\mathrm{QCD}}^2}{f_a}, \tag{2.15}$$

where Λ_{QCD} is the QCD confinement scale. Consequently, the strength of axion interactions with photons, nucleons, and electrons is also suppressed by f_a, leading to a linear relation between the axion mass and its couplings. A parameter space, defined by this, motivated a wide range of laboratory experiments and astrophysical searches, as can be seen in Fig. 1.4. Together they span more than 15 orders of magnitude in mass, probed by techniques ranging from astrophysical surveys to high-energy LHC collider studies.

Low-energy constraints typically rely on axion-photon conversion in macroscopic magnetic fields, a process analogous to the inverse Primakoff effect, as shown in Fig. 2.1. In this low-mass regime, the absence of other kinematically accessible Standard Model decay channels ensures that these limits suffer from relatively little model dependence. Conversely, high-energy collider bounds are subject to significant model dependence. In these environments, both the production and decay mechanisms must be explicitly accounted for, and the interplay between multiple simultaneous couplings becomes highly relevant, often yielding non-trivial kinematic dynamics.

Axions are appealing for multiple reasons. In addition to providing a solution to the

long-standing strong CP problem, they may constitute a component of dark matter [33–40] and could help explain other phenomena such as the TeV transparency of the Universe [74, 75] and anomalous stellar cooling [76, 77]. Moreover, string theory naturally predicts a plethora of pseudoscalar particles [41, 42], one of which could be *the* QCD axion.

Early proposals for a weak-scale QCD axion were experimentally excluded long ago, shifting attention to light and ultralight axions with masses of $m_a \lesssim 10^{-3}\,\text{eV}$. Nevertheless, non-benchmark QCD axions could still be viable in the MeV–GeV mass range and evade current experimental constraints.

Another research direction is the study of the phenomenology of axion-like particles—a natural generalization of the QCD axion, but not constrained by the linear mass–coupling relation. **Some** ALPs may still address the strong CP problem, while many others arise in theoretical contexts unrelated to QCD, such as string theory or other extensions of the Standard Model. Such a generic ALP within the MeV–GeV mass range will be the main subject of this work.

2.2 Low-energy interactions between ALPs and gauge bosons

The two-photon coupling is a ubiquitous feature of ALP models, allowing for a wide range of experimental search strategies, ranging from to astrophysical observations to beam dump, fixed-target, and collider experiments, as illustrated in Fig. 1.4.

In order to understand it, we begin with the generic gauge-invariant Lagrangian describing ALP interactions with electroweak gauge bosons [78], analogous to the ALP-gluon coupling

$$\mathcal{L}_{a-\text{E.W.}} = -\frac{g_{aBB}}{4} a B^{\mu\nu} \tilde{B}_{\mu\nu} - \frac{g_{aWW}}{4} a \mathbf{W}^{\mu\nu} \tilde{\mathbf{W}}_{\mu\nu}, \tag{2.16}$$

where $B^{\mu\nu}$ and $\mathbf{W}^{\mu\nu}$ refer to the $U(1)$ and $SU(2)$ field tensors, respectively. The corresponding dual pseudotensors are defined in the standard way, while g_{aBB} and g_{aWW} are the coupling constants of GeV^{-1} dimension.

After the Higgs mechanism is introduced, the effective interaction of ALPs and photons is given by

$$\mathcal{L}_{a\gamma\gamma} = -\frac{g_{a\gamma\gamma}}{4} a F^{\mu\nu} \tilde{F}_{\mu\nu} - \frac{g_{a\gamma Z}}{2} a F^{\mu\nu} \tilde{Z}_{\mu\nu}, \tag{2.17}$$

where the new coupling constants were defined

$$g_{a\gamma\gamma} = g_{aBB} \cos^2\theta_w + g_{aWW} \sin^2\theta_w, \tag{2.18}$$

$$g_{a\gamma Z} = \frac{g_{aWW} - g_{aBB}}{2} \sin(2\theta_w), \tag{2.19}$$

with θ_w being the weak mixing angle. The ratio of g_{aBB} and g_{aWW} is of key importance for ALPs studies at e^+e^- colliders. In particular, $a\gamma Z$ interaction potentially leads to the anomalous decay $Z \to \gamma\gamma\gamma$, which was a subject of LEP studies [79, 80]. Such a process would be suppressed if the condition $g_{aWW} \approx g_{aBB}$ is fulfilled.

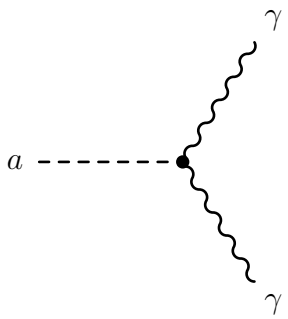

Figure 2.2: ALP decay to two photons in the lowest order.

Searches for flavor-changing processes, however, impose stringent constraints on the coupling g_{aWW} [81, 82], while the limits on g_{aBB} are more relaxed. It is therefore reasonable to assume that the coupling between ALPs and **W** is, at best, subdominant, i.e. $g_{aBB} \gg g_{aWW}$. In this case one can express

$$g_{a\gamma\gamma} \approx -\cot\theta_w g_{a\gamma Z} \approx -1.9\, g_{a\gamma Z}. \tag{2.20}$$

Of course, the Lagrangian (2.16) also leads to a nonzero aZZ and aWW interactions. However, they are irrelevant in the domain of interest corresponding to e^+e^- colliders with center-of-momentum energy below 10 GeV, since the direct production of Z and W bosons is not possible.

The $a\gamma\gamma$ decay, illustrated in Fig. 2.2, plays a central role in ALP searches, as it determines the ALP lifetime τ_a. The corresponding matrix element is given by

$$\mathcal{M}_{a\to\gamma\gamma}(k_1,k_2) = -ig_{a\gamma\gamma}\varepsilon^{\kappa\beta\mu\nu}k_{1,\kappa}k_{2,\beta}\epsilon^*_\mu(k_1,\lambda_1)\,\epsilon^*_\nu(k_2,\lambda_2)\,, \tag{2.21}$$

where $\epsilon_\mu(k_1,\lambda_1)$ and $\epsilon_\mu(k_2,\lambda_2)$ are the polarization vectors of the photons with 4-momenta k_1, k_2 and helicities λ_1, λ_2, respectively. Summing over the final-state photon helicities, we obtain

$$\sum_f |\mathcal{M}_{a\to\gamma\gamma}(k_1,k_2)|^2 = 2g^2_{a\gamma\gamma}(k_1k_2)^2\,. \tag{2.22}$$

The corresponding decay width is then obtained as

$$\Gamma_{a\gamma\gamma} \equiv \tau_a^{-1} = \frac{g^2_{a\gamma\gamma}m_a^3}{64\pi}. \tag{2.23}$$

Given the existing experimental constraints on $g_{a\gamma\gamma}$, it is reasonable to assume that the decay width $\Gamma_{a\to\gamma\gamma}$ is extremely small, leading to potentially large decay lengths, in particular for ALPs produced with sizable energies and thus large Lorentz boosts. Nevertheless, for a range of parameters relevant to the present study, the fraction of ALPs decaying within a detector of characteristic size L_D remains close to unity.

Indeed, this fraction is given by

$$p_a = 1 - \exp\left(-\frac{L_D}{\gamma_a\tau_a}\right), \tag{2.24}$$

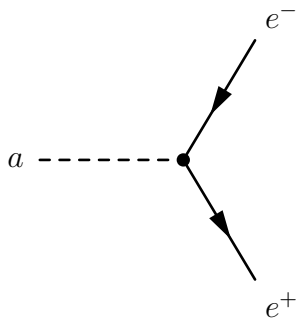

Figure 2.3: ALP decay to the lepton pair in the lowest order.

where $\gamma_a = E_a/m_a$ denotes the Lorentz factor of the ALP, E_a being the ALP energy. For typical detector dimensions of a few meters, $p_a \simeq 1$ whenever the decay length is comparable to the detector size.

As an illustrative benchmark, taking $m_a = 1\,\mathrm{GeV}$ and $g_{a\gamma\gamma} = 10^{-3}\,\mathrm{GeV}^{-1}$ yields a proper lifetime $\tau_a \simeq 2 \times 10^8\,\mathrm{GeV}^{-1}$. Using the conversion $1\,\mathrm{m} \simeq 5.07 \times 10^{15}\,\mathrm{GeV}^{-1}$, one finds $L_D/(\gamma_a\tau_a) \gg 1$ for meter-scale detectors, implying that the probability for an ALP to escape the detector without decaying is exponentially suppressed.

2.3 Interaction with leptons

MeV–GeV mass range ALPs are often assumed to be isolated from the QCD sector, with the respective coupling to be subdominant at best, as such interactions typically induce tightly constrained flavour-changing processes [83, 84]. By contrast, couplings to charged leptons are significantly less constrained and therefore must be taken into consideration.

Owing to the origin of axions and ALPs as pseudo-Goldstone bosons, it is implied that only derivative couplings (respecting the shift symmetry) with leptons are allowed. The lowest order operator of such an effective interaction has the form

$$\mathcal{L}_{a\ell\ell} = -\frac{g_{a\ell\ell}}{2m_\ell}\partial_\mu a\,\bar{\ell}\gamma^5\gamma^\mu\ell, \tag{2.25}$$

where ℓ stands for the lepton field, m_ℓ denotes its mass and $g_{a\ell\ell}$ is the dimensionless coupling constant. At the level of tree diagram calculations $\mathcal{L}_{a\ell\ell}$ can be equivalently reduced to a pseudoscalar Yukawa interaction

$$\mathcal{L}_{a\ell\ell} = -ig_{a\ell\ell}a\,\bar{\ell}\gamma^5\ell. \tag{2.26}$$

It is clear that lepton universality requires a large enhancement of the ALP coupling to the muon, as compared to the electron, namely

$$g_{a\mu\mu} \approx \frac{m_\mu}{m_e}g_{aee}, \tag{2.27}$$

and even more enhanced tau-lepton coupling.

We are interested in the $a \to \ell^+\ell^-$ decay shown on Fig. 2.3, which is given by the matrix element

$$\mathcal{M}_{a\to e^+e^-} = g_{aee}\bar{u}\left(p_-, s_-\right)\gamma^5 v\left(p_+, s_+\right), \tag{2.28}$$

where $u\left(p_-, s_-\right)$ and $v\left(p_+, s_+\right)$ are the bispinors describing electron and positron with momenta $p_\pm$ and helicities $s_\pm$, respectively. After summing over the final helicities, the decay width for this process reads

$$\Gamma_{a\ell\ell} = \frac{g_{a\ell\ell}^2}{4\pi}\sqrt{\frac{m_a^2}{4} - m_\ell^2}\,\Theta\left[m_a - 2m_\ell\right], \tag{2.29}$$

where the Heaviside step function $\Theta\left(x\right)$ enforces the kinematic threshold.

In the absence of additional interactions, the total decay width of the ALP is assumed to consist of the di-photon and di-lepton channels

$$\Gamma_a = \Gamma_{a\gamma\gamma} + \sum_{\ell=e,\mu,\tau}\Gamma_{a\ell\ell}, \tag{2.30}$$

since the decay $a \to \gamma Z$ is kinematically forbidden in the energy range of interest.

2.4 Cross section and observables

Electron–positron colliders, such as BESIII and Belle II, probe an important mass range that bridges the gap between the ultralight to MeV regime constrained by astrophysical observations and the higher MeV–GeV masses explored in comprehensive LHC studies [69]. At these facilities, the main ALP production mechanism is ALP-strahlung, namely the process

$$e^+e^- \to \gamma^* \to \gamma a, \tag{2.31}$$

followed by the decay $a \to \gamma\gamma$, as illustrated in Fig. 2.4. This channel depends solely on the ALP–photon coupling and has been extensively studied both theoretically and experimentally. The corresponding (resonant) amplitude can be written as

$$\mathcal{M}_{\text{res}} = i\frac{\mathcal{H}_{\text{res}}\left(k_1\right)}{K_{23}^2 - m_a^2 + im_a\Gamma_a} \times \mathcal{M}_{a\to\gamma\gamma}\left(k_2, k_3\right) + \text{crossed terms} \tag{2.32}$$

where $\mathcal{H}_{\text{res}}$ represents the amplitude for the subprocess $e^+e^- \to a\gamma_i$,

$$\mathcal{H}_{\text{res}}\left(k_i\right) = -ieg_{a\gamma\gamma}\,\varepsilon_{\alpha\beta\mu\gamma}q^\alpha k_i^\beta\epsilon^\gamma\left(k_i, \lambda_i\right) \times \frac{\bar{v}\left(p_+, s_+\right)\gamma^\mu u\left(p_-, s_-\right)}{s}, \tag{2.33}$$

where e denotes the electron charge, $q = p_+ + p_-$ is the four-momentum of the virtual photon, and $s = q^2 = 4E^2$ is the Mandelstam variable, with E being the initial electron (positron) energy in the center-of-momentum frame. We further define the ALP four-momentum as $K_{23} = k_2 + k_3$ and neglect the electron mass m_e, since the condition

$$\frac{m_e^2}{s} \ll 1 \tag{2.34}$$

is fulfilled.

The resonant ALP-strahlung, however, is not the only possibility. Once the ALP–lepton coupling is taken into account, the two additional processes shown in Fig. 2.5 also

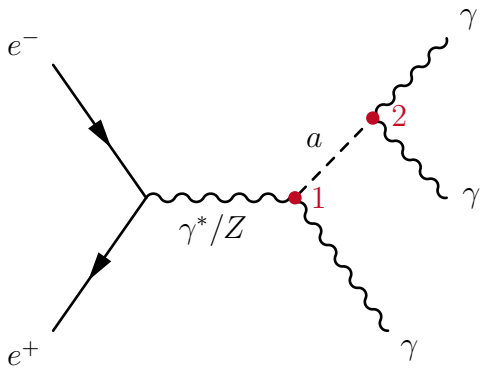

Figure 2.4: Resonant ALP production at e^+e^- colliders via the intermediate photon/Z-boson. Graphs which are obtained by crossing are not shown, but are evaluated too.

contribute. These channels were not considered in earlier works based on the argument that additional production mechanisms can only enhance the total signal cross section, thus providing stronger and less conservative constraints.

This reasoning appears to be incomplete. A consistent treatment must account not only for the ALP production mechanisms, but also how it decays. Due to branching ratio effects, the total cross section for processes involving an intermediate ALP may in fact become smaller for a nonzero value of $g_{a\ell\ell}$ than in the case $g_{a\ell\ell} = 0$. This effect becomes especially relevant in light of the comparatively weak experimental bounds on ALP–lepton couplings [71, 72, 85, 86].

The amplitudes of interest can be expressed as

$$\mathcal{M}_{\text{non.-res.}} = i\frac{\mathcal{H}_1(k_1) + \mathcal{H}_2(k_1)}{K_{23}^2 - m_a^2 + im_a\Gamma_a} \times \mathcal{M}_{a\to\gamma\gamma}(k_2, k_3) + \text{crossed terms}, \tag{2.35}$$

where $\mathcal{H}_i(k_i)$ denote amplitudes for the corresponding $2 \to 2$ process

$$\mathcal{H}_1(k_i) = eg_{aee}\,\epsilon_\eta^*(k_i, \lambda_i) \times \bar{v}(p_+, s_+)\,\gamma^\eta \frac{\hat{l}_i}{l_i^2}\gamma^5 u(p_-, s_-)\,, \tag{2.36}$$

$$\mathcal{H}_2(k_i) = eg_{aee}\,\epsilon_\lambda^*(k_i, \lambda_i) \times \bar{v}(p_+, s_+)\,\gamma^5 \frac{\hat{f}_i}{f_i^2}\gamma^\lambda u(p_-, s_-)\,, \tag{2.37}$$

with the internal electron momenta

$$l_i = k_i - p_+, \quad f_i = p_- - k_i. \tag{2.38}$$

It is worth noticing that there is no interference between resonant and non-resonant amplitudes $\mathcal{M}_{\text{res.}}$ and $\mathcal{M}_{\text{non.-res.}}$.

The next step involves kinematic considerations. In particular, it is generally assumed that ALPs are long-lived particles, such that their decay width Γ_a is small, typically much smaller than the experimental resolution of the invariant mass of the two-photon system into which the ALP decays. As a consequence, the phase-space integration

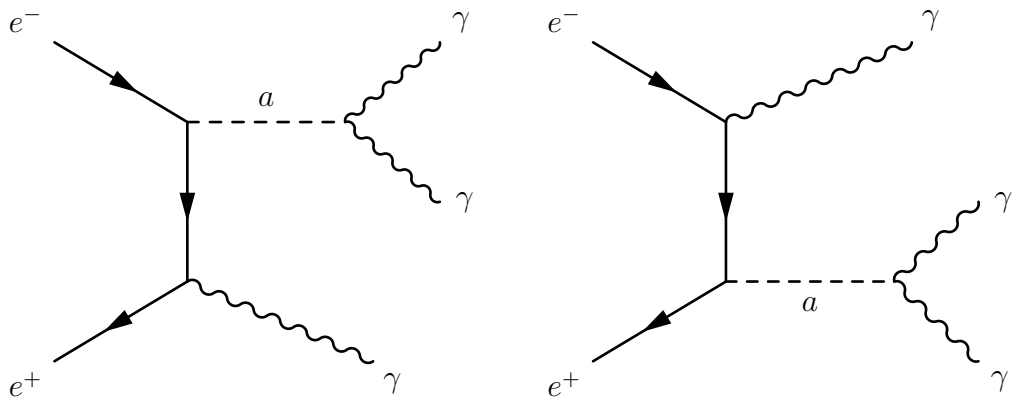

Figure 2.5: Non-resonant ALP production at e^+e^- colliders via the initial state radiation. Graphs which are obtained by crossing are not shown, but are evaluated too.

receives its dominant contribution only from a narrow region where the invariant mass of the photon pair produced by the ALP is close to m_a^2.

In this kinematic regime, only the terms diagonal in the ALP momenta, i.e. those proportional to

$$\left|\frac{1}{K_{ij}^2 - m_a^2 + i m_a \Gamma_a}\right|^2 \qquad \text{with} \qquad i \neq j, \tag{2.39}$$

survive and make contribution to the total cross section. In other words, after the integration over the phase space the total cross section can be represented as a cross section obtained from only Feynman diagrams shown in Figs. 2.4 and 2.5 multiplied by a factor of three to account for the 3 channels. Performing the average over initial helicity states the sum over final, we obtain

$$\bar{\sum_i}\sum_f \left|\mathcal{H}_{\text{res.}}\left(k_1\right)\right|^2 = \frac{2e^2 g_{a\gamma\gamma}^2}{s^2}\left[\left(k_1 p_+\right)^2 + \left(k_1 p_-\right)^2\right]\left(p_- p_+\right), \tag{2.40}$$

$$\bar{\sum_i}\sum_f \left|\mathcal{H}_1\left(k_1\right) + \mathcal{H}_2\left(k_1\right)\right|^2 = e^2 g_{aee}^2\left(\frac{p_- k_1}{p_+ k_1} + \frac{p_+ k_1}{p_- k_1} + 2\frac{\left(p_+ K_{23}\right)\left(p_- K_{23}\right)}{\left(p_- k_1\right)\left(p_+ k_1\right)}\right). \tag{2.41}$$

It is also noteworthy that the two diagrams exhibit completely different behaviour as functions of the ALP mass. The resonant contribution vanishes as m_a^2 approaches s: at threshold the final–state photon becomes soft, and the anomaly–induced vertex forces the amplitude to zero. In contrast, the non–resonant contribution receives a collinear enhancement from the electron propagators and therefore grows as long as $m_a^2 \lesssim s$.

This becomes especially clear if one introduces Mandelstam variables for the $2 \to 2$ subprocess $e^+e^- \to \gamma a$ as

$$s = \left(p_+ + p_-\right)^2 = \left(k_1 + K_{23}\right)^2, \tag{2.42a}$$

$$t = \left(p_+ - k_1\right)^2 = \left(p_- - K_{23}\right)^2, \tag{2.42b}$$

$$u = \left(p_- - k_1\right)^2 = \left(p_+ - K_{23}\right)^2. \tag{2.42c}$$

In terms of these variables, the squared helicity amplitudes written above can be cast into a compact form

$$\bar{\sum_i}\sum_f \left|\mathcal{H}_{\text{res.}}\left(k_1\right)\right|^2 = e^2 g_{a\gamma\gamma}^2 \left(\frac{t^2+u^2}{4s}\right), \tag{2.43}$$

$$\bar{\sum_i}\sum_f \left|\mathcal{H}_1\left(k_1\right)+\mathcal{H}_2\left(k_1\right)\right|^2 = e^2 g_{aee}^2 \left(\frac{s^2+m_a^4}{tu}\right). \tag{2.44}$$

Next, in the adopted $2 \to 2$ kinematics, the Mandelstam variables t and u can be expressed in terms of the scattering angle θ in the center-of-momentum frame as

$$t = -\frac{s-m_a^2}{2}\left(1-\cos\theta\right), \tag{2.45}$$

$$u = -\frac{s-m_a^2}{2}\left(1+\cos\theta\right). \tag{2.46}$$

So that the squared amplitudes are reduced to

$$\bar{\sum_i}\sum_f \left|\mathcal{H}_{\text{res.}}\left(k_1\right)\right|^2 = e^2 g_{a\gamma\gamma}^2 \left(s-m_a^2\right)^2 \left(\frac{1+\cos^2\theta}{8s}\right), \tag{2.47}$$

$$\bar{\sum_i}\sum_f \left|\mathcal{H}_1\left(k_1\right)+\mathcal{H}_2\left(k_1\right)\right|^2 = \frac{4e^2 g_{aee}^2}{\left(s-m_a^2\right)^2}\left(\frac{s^2+m_a^4}{\sin^2\theta}\right), \tag{2.48}$$

justifying the statement above regarding their scaling properties.

2.4.1 ALP contributions to Z boson decays

The Large Electron–Positron (LEP) Collider has collected a large data set at the Z pole, i.e. at

$$\sqrt{s} \simeq M_Z \simeq 91.2 \text{ GeV}. \tag{2.49}$$

In this kinematic regime, an additional ALP production channel becomes accessible, namely the production of on-shell Z bosons followed by their decay into an ALP and a single photon. The corresponding Feynman diagram is analogous to the one shown in Fig. 2.4, with the virtual photon propagator replaced by a Z-boson propagator. Due to the resonant nature of this process, it dominates all other contributions.

The matrix element can be obtained from Eq. (2.32) by replacing the propagator and coupling as

$$\frac{1}{s} \to \frac{1}{s-M_Z^2+iM_Z\Gamma_Z}, \tag{2.50}$$

$$g_{a\gamma\gamma} \to g_{a\gamma Z}. \tag{2.51}$$

Such a process was the subject of LEP studies, which put stringent limits on its rate, resulting in one of the most restrictive bounds on ALP–photon couplings so far [79, 80].

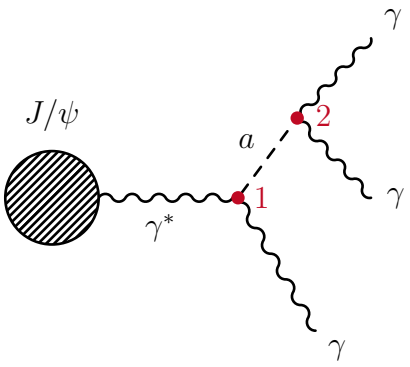

Figure 2.6: ALP production at via the J/ψ meson radiative decay.

2.4.2 ALP contributions to J/ψ decays

Another possible search strategy is via vector-meson decays, as illustrated in Fig. 2.6. This approach has been extensively studied at BESIII utilizing decays of the J/ψ meson [87, 88]. The branching fraction of the radiative decay $J/\psi \to a\gamma$ can be related to the leptonic decay $J/\psi \to e^+e^-$ as

$$\frac{\mathcal{B}\left(J/\psi \to a\gamma\right)}{\mathcal{B}\left(J/\psi \to e^+e^-\right)} = \frac{m_{J/\psi}^2}{32\pi\alpha}\, g_{a\gamma\gamma}^2 \left(1 - \frac{m_a^2}{m_{J/\psi}^2}\right)^2, \tag{2.52}$$

where α denotes the fine-structure constant and $m_{J/\psi}$ is the mass of the J/ψ meson.

This approach is advantageous for several reasons. First, it easily scalable, as the BESIII data set continues to grow, from approximately 2.7×10^9 J/ψ decays in 2022 to about 10^{10} decays in 2024. Second, ALP–lepton couplings enter only through branching-ratio effects, thereby introducing smaller theoretical uncertainties.

Before concluding this part, it is important to note that the diagrams shown in Figs. 2.4 and 2.6 involve the ALP–photon coupling twice, but in distinct ways. Specifically, one vertex corresponds to a Primakoff-like process (with one photon being virtual), while the other describes the ALP decay. Since these couplings must be treated as *effective*, they can differ due to loop corrections and, in principle, are not identical [71, 89]. The associated effects are outlined in Appendix 2A.

2.4.3 Phase space integration

The cross section of $e^+e^- \to \gamma\gamma\gamma$ process is given by the expression

$$\sigma = \frac{1}{3!}\int d_{LIPS}\,(2\pi)^4\,\delta^{[4]}\left(p_- + p_+ - k_1 - k_2 - k_3\right) \times \frac{1}{2s}\bar{\sum_i}\sum_f \left|\mathcal{M}_{e^+e^-\to\gamma\gamma\gamma}\right|^2, \tag{2.53}$$

where d_{LIPS} stands for the Lorentz-invariant phase space of the three final photons

$$d_{LIPS} = \frac{d^3k_1}{2\omega_1\,(2\pi)^3}\frac{d^3k_2}{2\omega_2\,(2\pi)^3}\frac{d^3k_3}{2\omega_3\,(2\pi)^3}, \tag{2.54}$$

and $1/3!$ accounts for the permutation properties of 3 bosons in the final state.

After the integration with the delta function, the phase space can be expressed as

$$\begin{aligned} & d_{LIPS}\,(2\pi)^4\,\delta^{[4]}\left(p_- + p_+ - k_1 - k_2 - k_3\right) \\ & = \frac{1}{2^8\pi^5}\frac{\omega_1\omega_2}{2E + \omega_1\left(\cos\theta_{12} - 1\right)} d\omega_1 d\Omega_1 d\Omega_2, \end{aligned} \tag{2.55}$$

with θ_{12} denoting the angle between $\mathbf{k}_1$ and $\mathbf{k}_2$ momenta. The remaining phase space is parameterized as

$$d\Omega_1 d\Omega_2 = 2\pi d\phi\, d\cos\theta_{1-} d\cos\theta_{2-}, \tag{2.56}$$

where θ_{i-} is the angle between $\mathbf{p}_-$ and $\mathbf{k}_i$, leading to

$$\cos\theta_{12} = \sin\theta_{1-}\sin\theta_{2-}\cos\phi + \cos\theta_{1-}\cos\theta_{2-}. \tag{2.57}$$

Furthermore, in the center-of-momentum frame it holds

$$\begin{cases} \omega_1 + \omega_2 + \omega_3 = 2E, \\ \mathbf{k}_1 + \mathbf{k}_2 + \mathbf{k}_3 = 0, \end{cases} \tag{2.58}$$

allowing us to express ω_2 as

$$\omega_2 = \frac{2E\left(E - \omega_1\right)}{2E + \omega_1\left(\cos\theta_{12} - 1\right)}. \tag{2.59}$$

For the ALP-associated process, the photon opposite to the ALP in center-of-momentum frame is denoted by k_1. In this case, the integration over $d\omega_1$ can be removed if the definition of the delta function

$$\begin{aligned} & \frac{1}{\left(K_{23}^2 - m_a^2\right)^2 + \left(m_a\Gamma_a\right)^2} \to \frac{\pi}{m_a\Gamma_a}\delta\left(K_{23}^2 - m_a^2\right) \\ & = \frac{\pi}{m_a\Gamma_a}\frac{1}{4E}\,\delta\left(\omega_1 - \frac{4E^2 - m_a^2}{4E}\right), \end{aligned} \tag{2.60}$$

is applied.

From this we also observe that one photon is always emitted with a fixed energy

$$\omega = \frac{4E^2 - m_a^2}{4E}. \tag{2.61}$$

After the integration over the full phase space, the cross section of the $2 \to 3$ process with the intermediate ALP can be written in the compact form

$$\sigma_{e^+e^-\to\gamma\gamma\gamma} = \sigma_{e^+e^-\to a\gamma} \times \frac{\Gamma_{a\gamma\gamma}}{\Gamma_a}. \tag{2.62}$$

For the particular case of $g_{a\gamma\gamma} = 10^{-4}\,\mathrm{GeV}^{-1}$ and $g_{aee} = 10^{-4}$, one obtains

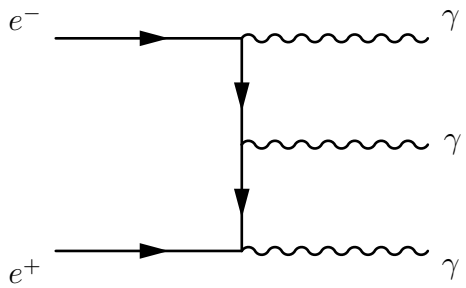

Figure 2.7: QED background to the ALP production at e^+e^- colliders. Graphs which are obtained by crossing are not shown, but are evaluated too (6 in total).

$$\frac{\Gamma_{a\gamma\gamma}}{\Gamma_a} \approx 0.01, \quad \text{for} \quad m_a = 0.3\,\text{GeV}, \tag{2.63}$$

$$\frac{\Gamma_{a\gamma\gamma}}{\Gamma_a} \approx 0.53, \quad \text{for} \quad m_a = 3\,\text{GeV}, \tag{2.64}$$

which clearly illustrates that a better signal over background ratio is not guaranteed by simply including more production channels.

Lastly, if $g_{aee} = 0$, the ALP decays directly to photons and this formula can be simplified further (notably, it is independent of s if $m_a^2 \ll s$) as

$$\sigma_{e^+e^-\to a\gamma} = \frac{\alpha g_{a\gamma\gamma}^2}{24}\left(1 - \frac{m_a^2}{s}\right)^3, \tag{2.65}$$

where $\alpha \equiv e^2/4\pi$. It is noteworthy that in the limit $m_a^2/s \to 0$ this cross section becomes independent of m_a.

For a realistic detector, one has to integrate the cross section formula over the phase space, restricted by the experimental setup, as discussed below.

2.4.4 Background analysis

The final ingredient for a search for the potential signal is to understand the SM background for ALP production. In this case, it is dominated by the QED process $e^+e^- \to \gamma\gamma\gamma$, shown in Fig. 2.7. At leading order, which is sufficient for the purposes of this analysis, the cross section is determined by the square of the matrix element and can be expressed in compact form as [90, 91]

$$\bar{\sum_i}\sum_f |\mathcal{M}_{\text{QED}}|^2 = s\,(4\pi\alpha)^3\,\frac{\sum_{i=1}^3 (p_+k_i)\,(p_-k_i)\left[(p_+k_i)^2 + (p_-k_i)^2\right]}{\prod_{i=1}^3 (p_+k_i)\,(p_-k_i)}, \tag{2.66}$$

where the sum runs over final spin states and the average is taken over the initial spins.

The QED contribution has been cross-checked against earlier results [92] as well as against the BabaYaga event generator. Fig. 2.8 shows the corresponding QED photon energy distributions at Belle II kinematics, as described in Sec 2.5. A distinct peak in the photon energy spectrum would indicate ALP production. Further contributions, such as those from π_0, η, and η' mesons, are relevant only near their respective masses.

Other background processes, e.g. radiative Bhabha scattering $e^+e^- \to e^+e^-\gamma$ and other processes are negligible [78].

We also note that, in some cases, the two photons cannot be resolved in the electromagnetic calorimeter and are therefore detected as a single photon with combined energy. In particular, this occurs in the low-mass ALP regime, where $m_a^2/s \ll 1$, as the decay products are highly collimated. The large two-photon background from QED annihilation, $e^+e^- \to \gamma\gamma$, in turn poses significant challenges for event reconstruction and subsequent analysis. As a result, the sensitivity of BESIII and Belle II is limited by thresholds of a few hundred MeV. Nevertheless, such kinematics were studied at LEP, where a threshold of $m_a = 3\,\text{GeV}$ was defined to separate the $\gamma\gamma$ and $\gamma\gamma\gamma$ regimes.

The expected sensitivity can be estimated using

$$\frac{\sigma_{ALP}}{\sigma_{QED}} = \frac{N}{\sqrt{L\sigma_{QED}}}, \tag{2.67}$$

where L denotes the integrated luminosity and N is the number of standard deviations that determines whether or not a fluctuation is considered as a signal. We conventionally set $N = 2$, which refers to 95% confidence level.

2.5 Sensitivity to ALPs of existing e^+e^- facilities

The coming years promise significant progress in the area of collider-based BSM searches, driven primarily by the Belle II experiment [93]. The test run performed in 2018 resulted in a total of $445\,\text{pb}^{-1}$ collected data, which was used in searches for ALPs, demonstrating the experiment's effectiveness [94]. Belle II now aims to accumulate an ambitious $50\,\text{ab}^{-1}$ of integrated luminosity by 2030, opening new opportunities to probe a wide range of New Physics scenarios. This high-luminosity reach is particularly important for "bump hunt" searches, which look for narrow resonances either in the energy spectra of emitted particles or in their invariant-mass distributions.

Indeed, as seen in Eq. (2.67), the sensitivity to BSM couplings scales as $L^{-1/4}$. This means that improving the reach by an order of magnitude requires increasing the integrated luminosity by four orders of magnitude, or finding a highly efficient way to suppress backgrounds. Such scaling makes these searches inherently challenging and places Belle II at the center of current and future efforts in this direction.

As for the experimental setup, Belle II is an asymmetric collider, with electron and positron beam energies of 7 GeV and 4 GeV, respectively. This asymmetry requires a boost with velocity $\beta \simeq 0.27$ to the center-of-momentum frame, in which the particles have energies of $E = 5.29\,\text{GeV}$. The angular coverage of the electromagnetic calorimeter in the laboratory frame is $12.4° < \theta < 155.1°$.

The angular region $37.3° < \theta < 123.7°$ provides the best energy resolution, avoiding areas close to detector gaps, and offers the lowest beam-induced background levels. Following Ref. [78], we impose a photon energy threshold of 0.25 GeV in the center-of-momentum frame. Our analysis requires all three photons to fall within this acceptance, and, unless stated otherwise, these selection criteria are applied everywhere below.

It is noteworthy that in the absence of phase space restrictions, the background cross section $d\sigma_{\text{QED}}/dm^2_{\gamma\gamma}$ exhibits a characteristic U-shape, diverging at the kinematic bound-

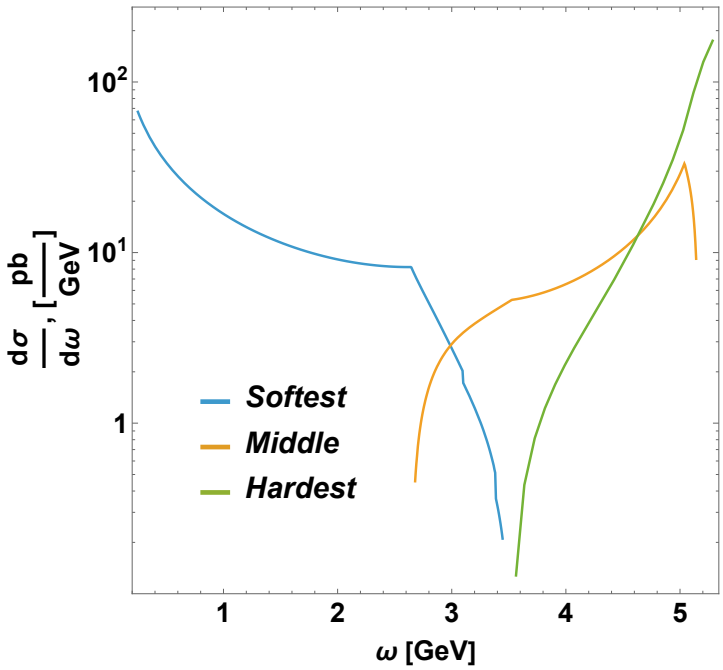

Figure 2.8: QED background energy spectrum for the softest, middle, and hardest photons in the $e^+e^- \to \gamma\gamma\gamma$ process at Belle II kinematics. Sharp spikes are due to the detector threshold effects.

aries. This behavior is driven entirely by the soft divergence common to radiative QED processes.

Indeed, in the center-of-momentum frame, the invariant mass is related to the recoil energy as

$$m_{12}^2 = \omega_1\omega_2\,(1 - \cos\theta_{12}) = s - 2\sqrt{s}\omega_3, \tag{2.68}$$

so that in the limit $m_{12}^2 \to s$, one necessarily finds $\omega_3 \to 0$. The cross-section then diverges due to the bremsstrahlung pole associated with the emission of a soft γ_3. In reality, however, this divergence is truncated by the finite (and, in fact, relatively large) energy selection threshold.

In the opposite limit, $m_{12}^2 \to 0$, either one of the photons (ω_1 or ω_2) is soft, or the pair is produced collinearly. While the soft contribution would cause a divergence, it is similarly removed by the energy cuts. Lastly, the collinear configuration does not lead to a divergence, as there is no collinear singularity for photon splitting in QED.

The ALP parameter space constrained by e^+e^- colliders in the absence of lepton couplings (i.e. subject of [79, 80, 87, 88, 94] studies) is shown in Fig. 2.9, together with the CMS and ATLAS bounds [95, 96]. Although Eq. (2.47) suggests a flat sensitivity in the limit $m_a^2/s \to 0$, background suppression enables a more effective scan of the low-mass region.

Fig. 2.10 illustrates the corresponding constraints when both photon and electron couplings are taken into account, a scenario that arises, for example, in certain non-benchmark QCD-inspired models. Despite the presence of additional production channels induced by the electron coupling, the resulting bounds are weakened due to the

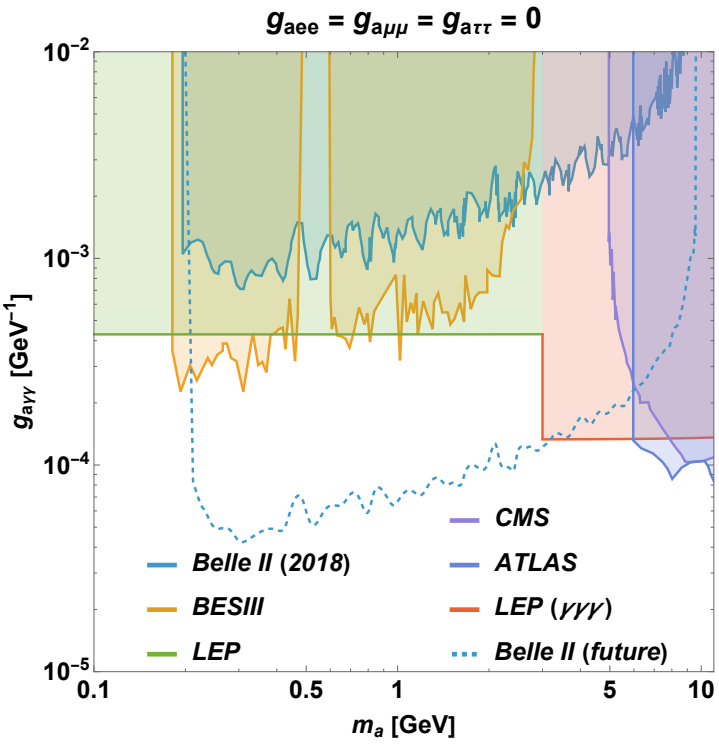

Figure 2.9: ALP constraints in the single photon coupling scenario (colored regions are excluded). Existing bounds are adapted from [79, 80, 87, 88, 94–96].

reduced branching ratio into photons [71, 86]. This effect is particularly visible in the low-mass region, which previously showed enhanced sensitivity but is now significantly relaxed. In the high–mass region, deviations also appear due to the completely opposite m_a^2–dependences of the two contributions discussed above. Remarkably, such an interplay of two couplings becomes more relevant with higher statistics and does not seriously affect Belle II 2018 results.

Finally, Fig. 2.11 shows the exclusion limits obtained when muon and tau couplings are also considered [72], under the assumption of lepton universality discussed in Sec. 2.3. It is evident that their inclusion leads to even more pronounced effects.

We would also like to emphasize the projection curves are quite conservative. The setup and selection procedures are likely to be further optimized compared to the 2018 test run, so we expect the final curve to be even more improved. In particular, upgrading the spatial resolution of photons would allow to access the currently unexplored region $m_a < 0.2\,\text{GeV}$

On the other hand, more data probing the ALP-lepton couplings are required to comprehensively explore the MeV–GeV parameter space. In this work, we focus on $\gamma\gamma\gamma$ final states, but detailed studies of leptonic final states at BESIII or Belle II could improve existing constraints, in the latter case even with the relatively limited data from its test run.

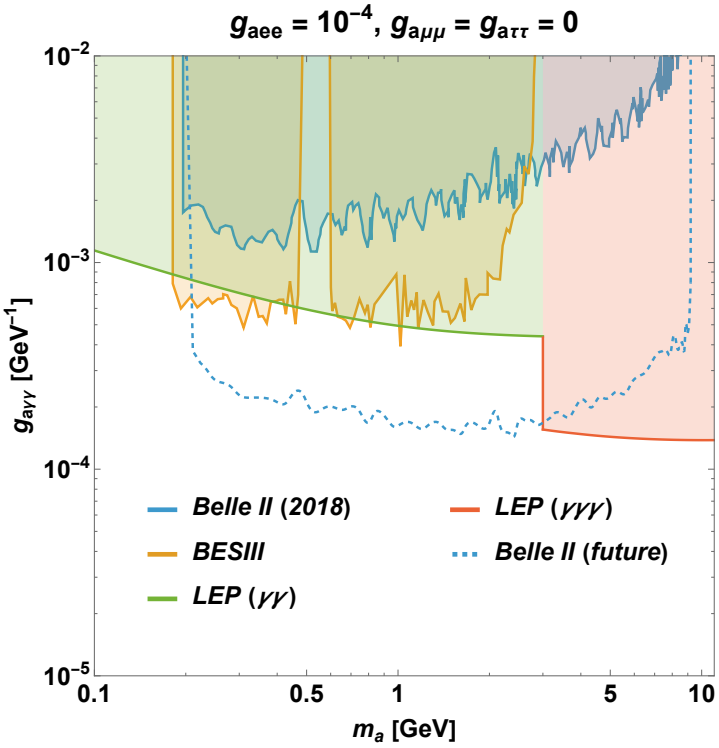

Figure 2.10: ALP constraints with both photon and electron couplings taken into account (colored regions are excluded).

2.6 Constraints for a scalar mediator

Scalars in the few hundred MeV to GeV mass range represent another scenario frequently discussed in the context of New Physics [52, 60, 61, 97–99]. Despite the current measurements of Higgs boson properties fitting well within the Standard Model, the structure of the Higgs sector could potentially be more complicated, possibly including an additional scalar doublet [100–102]. Furthermore, particles of this nature typically have couplings to fermions that are proportional to m_f. Possible dark scalars are also widely discussed in different contexts and can be favored for many reasons [60, 103–106], but in general, their limits are less extensively studied compared to those for pseudoscalars.

The Lagrangian of scalar-lepton and scalar-photon interactions has some notable modifications, compared to the case of pseudoscalars. It is effectively given by

$$\mathcal{L}_{\text{scalar}} = -g_{s\ell\ell} s\, \bar{l} l - \frac{g_{s\gamma\gamma}}{4} s F^{\mu\nu} F_{\mu\nu} - \frac{g_{s\gamma Z}}{2} s F^{\mu\nu} Z_{\mu\nu}. \tag{2.69}$$

The relation (2.20) between $\gamma\gamma$ and γZ couplings still holds in the scalar case. We also not that as e^+e^- collider experiments do not measure polarization observables, they have no direct sensitivity to the parity of the mediator.

Implementing these adjustments, we can apply the same search strategy as that used for ALPs in the previous section. The differences between scalar and pseudoscalar scenarios arise then from two sources: the partial decay widths into photons and charged leptons, as well as the corresponding angular distributions.

For a scalar mediator s, the relevant partial widths are given by

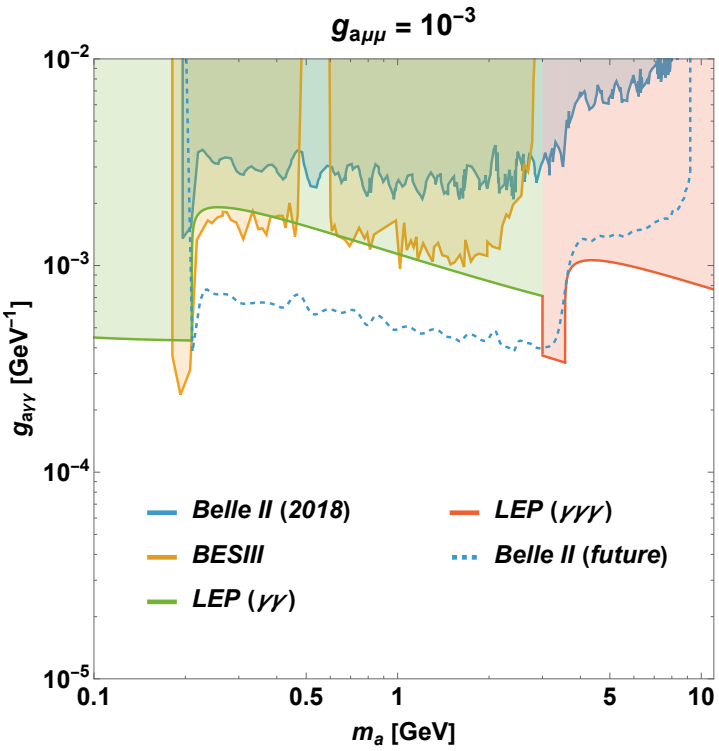

Figure 2.11: ALP constraints with photon and lepton couplings taken into account (colored regions are excluded). Lepton universality is assumed, so that g_{aee}, $g_{a\mu\mu}$ and $g_{a\tau\tau}$ are proportional to each other, see (2.27).

$$\Gamma_{s\gamma\gamma} = \frac{g_{s\gamma\gamma}^2 m_s^3}{64\pi}, \tag{2.70}$$

$$\Gamma_{s\ell\ell} = \frac{g_{s\ell\ell}^2}{\pi m_s^2}\left(\frac{m_s^2}{4} - m_\ell^2\right)^{3/2} \Theta\left[m_s - 2m_\ell\right], \tag{2.71}$$

From these expressions it is clear that the difference between the total decay widths of the scalar and pseudoscalar mediators is suppressed by $\mathcal{O}\left(m_\ell^2/m_a^2\right)$. Similarly, the difference in the angular distributions is also suppressed in the kinematic regime of interest. As a result, both lead to nearly identical experimental signatures in the searches considered here. Therefore, our results for the pseudoscalar case, shown in Figs. 2.9–2.11, were found to be applicable to the scalar case as well [72].

2.7 Results and discussion

In this chapter we thoroughly examined ALPs and scalars coupled to leptons and photons in a minimal way. Constraints from $e^+e^- \to \gamma\gamma\gamma$ annihilation from both existing and upcoming experiments were derived. These included the LEP run at the Z-pole, whose results remain highly competitive, as well as Belle II data from the 2018 run and the ongoing BESIII study of J/ψ decays.

Our analysis has emphasized the significance of simultaneous consideration of couplings of ALPs and scalars to both leptons and photons, revealing the intricate interplay between these interactions and their implications for experimental constraints. We demonstrated that the commonly adopted single-coupling assumption—often considered "conservative"—may not always hold true, as both the production and decay mechanisms of the mediators must be accounted for. Given the relatively weak constraints on lepton couplings in this mass regime, previously reported sensitivity curves could be significantly relaxed, particularly in the low-mass region.

Therefore, a detailed investigation of processes such as $e^+e^- \to$ leptons at Belle II and BESIII would be highly valuable. To date, neither experiment has reported such an analysis. A dedicated study of these channels would not only complement existing $\gamma\gamma\gamma$ final-state analyses and remove this ambiguity, but also establish a more direct connection to other phenomena, such as the $(g-2)_\mu$ tensions, which is the focus of the following chapter.

Although the growing Belle II dataset is expected to improve the sensitivity to ALP and scalar parameter spaces by up to an order of magnitude, a substantial region will remain unexplored. Furthermore, finite detector resolution in existing analyses leaves a noticeable gap in coverage from the MeV scale up to approximately 200 MeV. Nevertheless, this region can be probed using complementary low-energy facilities, such as the MAGIX@MESA experiment and the JLab polarized positron beam program, as detailed in Chapters 4 and 5.

Finally, it is worth noting that the anticipated improvements at high-energy colliders rely on accumulating orders of magnitude more data, 10.000 times in case of Belle II. This highlights the intrinsic inefficiency of a purely luminosity-driven approach, as the sensitivity to BSM couplings scales only as $\text{Luminosity}^{-1/4}$. An alternative search strategy, utilizing polarization-sensitive observables at low-energy precision experiments, is presented in Chapter 5.

Appendix 2A: Loop-induced effects

The correction $\delta g_{a\gamma\gamma}$ to the tree-level ALP–photon coupling $g^0_{a\gamma\gamma}$ induced by the electron loop must be considered in two distinct scenarios: a Primakoff-like process with one photon real and the other virtual, or a decay process where both photons are real. In contrast, the ALP–electron coupling is unambiguous, as it appears only once in each of the relevant diagrams.

This effect can be significant, since the correction induced by the electron triangle shown in Fig. 2.12 is enhanced by the small electron mass [71, 89]. Indeed, a simple dimensional analysis leads to

$$\delta g_{a\gamma\gamma} = \frac{\alpha g^0_{aee}}{\pi m_e}\left[1 + F\left(m_a^2, q^2\right)\right], \tag{2.72}$$

where g^0_{aee} denotes the tree-level ALP–electron coupling, and q is the virtual photon momentum. The first term is a direct consequence of the axial anomaly (2.3), and calculating the function $F\left(m_a^2, q^2\right)$ using standard QFT techniques does not pose any difficulties [107]. In fact, after applying some trivial simplifications to the Dirac structures in the numerator it can be expressed in terms of the well-known scalar triangle function C_0 [108], which yields

$$F\left(m_a^2, q^2\right) = \left(\frac{4m_e^2}{m_a^2}\right)\left(\frac{m_a^2}{m_a^2 - q^2}\right)\left[f^2\left(\frac{4m_e^2}{q^2}\right) - f^2\left(\frac{4m_e^2}{m_a^2}\right)\right], \tag{2.73}$$

whereas $f\left(x\right)$ is defined by

$$f\left(x\right) = \Theta\left(x-1\right)\arcsin\left(\frac{1}{\sqrt{x}}\right) + \frac{1}{2}\Theta\left(1-x\right)\left[\pi + i\ln\left(\frac{1+\sqrt{1-x}}{1-\sqrt{1-x}}\right)\right]. \tag{2.74}$$

In case of the two-photon decay $q^2 = 0$, so the result takes the form

$$F\left(m_a^2, 0\right) = -\left(\frac{4m_e^2}{m_a^2}\right) f^2\left(\frac{4m_e^2}{m_a^2}\right). \tag{2.75}$$

Both $F\left(m_a^2, q^2\right)$ and $F\left(m_a^2, 0\right)$ are suppressed by the factor of $4m_e^2/m_a^2$. However, due to its structure, $F\left(m_a^2, q^2\right)$ appears to be suppressed twice

$$\begin{aligned} &m_a^2 \frac{f^2\left(\frac{4m_e^2}{q^2}\right) - f^2\left(\frac{4m_e^2}{m_a^2}\right)}{m_a^2 - q^2} \\ &\approx \left(\frac{4m_e^2}{q^2}\right)\left.\frac{df^2(x)}{dx}\right|_{x=\frac{4m_e^2}{m_a^2}} + \mathcal{O}\left(\frac{4m_e^2}{m_a^2}\left(\frac{q^2 - m_a^2}{q^2}\right)\right). \end{aligned} \tag{2.76}$$

Fig. 2.13 illustrates the behaviour of $F\left(m_a^2, q^2\right)$ and $F\left(m_a^2, 0\right)$ within the relevant domain, specifically Belle II kinematics where $\sqrt{s} = 10.58\,\text{GeV}$. We see that both functions approach zero as m_a increases and bring the correction roughly of

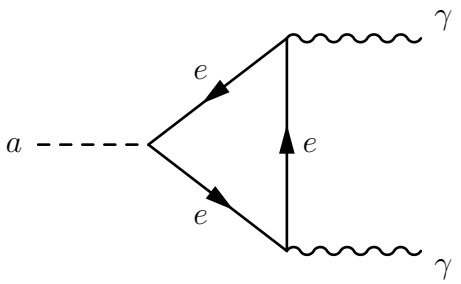

Figure 2.12: Electron loop–induced correction to the ALP-photon coupling.

$$\delta g_{a\gamma\gamma}^{\text{decay}} = \frac{\alpha g_{aee}^0}{\pi m_e}\left[1 + O\left(10^{-3}\right)\right], \tag{2.77}$$

$$\delta g_{a\gamma\gamma}^{\text{Prima}} = \frac{\alpha g_{aee}^0}{\pi m_e}\left[1 + O\left(10^{-6}\right)\right], \tag{2.78}$$

clearly illustrating that for the Belle II analysis the difference of two effective ALP-photon couplings is negligible.

The correction itself is enhanced by the factor $1/m_e$ and can be estimated as

$$\delta g_{a\gamma\gamma} \approx \frac{4.6 g_{aee}^0}{\text{GeV}} \lesssim \frac{4.6 \times 10^{-4}}{\text{GeV}}, \tag{2.79}$$

which, however, does not exclude any parameter space by itself since the experiment is only sensitive to the effective coupling $g_{a\gamma\gamma}^{\text{eff}} = g_{a\gamma\gamma}^0 + \delta g_{a\gamma\gamma}$, unless one adopts an assumption of photophobic ALP with $g_{a\gamma\gamma}^0 = 0$, which can be the case in some specific models, but not in general.

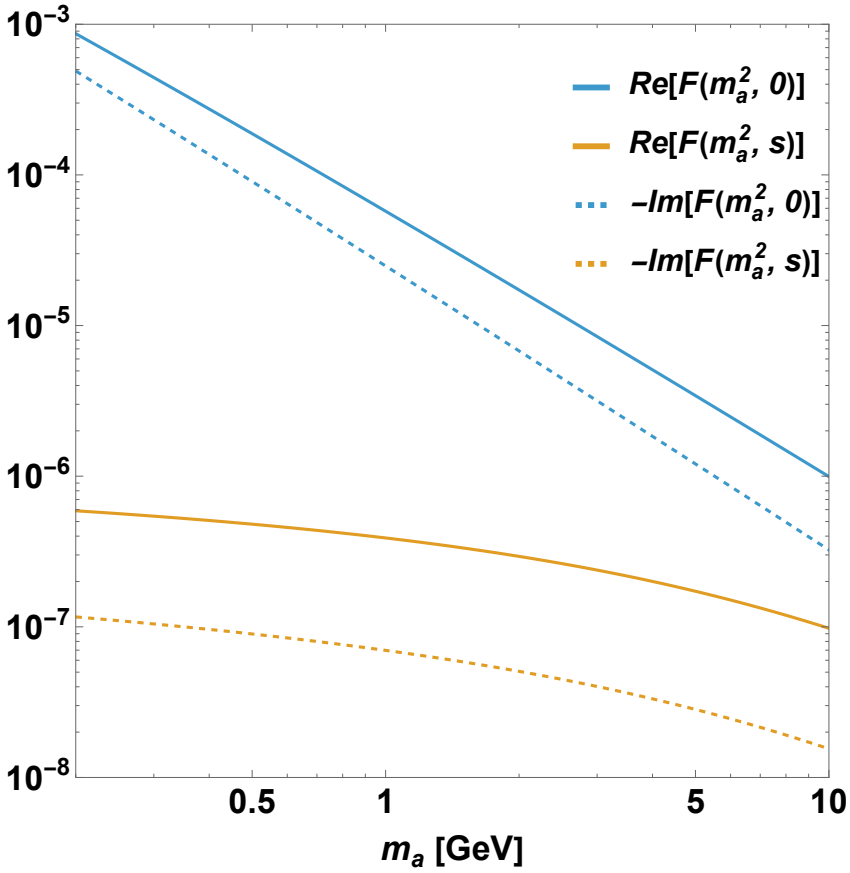

Figure 2.13: Real and imaginary components of $F\left(m_a^2, 0\right)$ and $F\left(m_a^2, q^2\right)$, which distinguish $g_{a\gamma\gamma}^{\text{decay}}$ and $g_{a\gamma\gamma}^{\text{Primakoff}}$, as functions of m_a. The value $s = 112\,\text{GeV}^2$ is set, corresponding to the kinematics of the Belle II experiment.

Chapter 3

BSM probes via lepton dipole moments

> A theory is something nobody believes, except the person who made it. An experiment is something everybody believes, except the person who made it.
>
> *Albert Einstein*

It is well established that the leading order SM contribution to the anomalous magnetic moment of the electron arises from the 1-loop QED vertex correction [109], shown in Fig. 3.1, and is given by

$$a_e = \frac{\alpha}{2\pi}. \tag{3.1}$$

This result represented one of the earliest and most significant successes of quantum field theory (QFT), establishing the predictive power of quantum electrodynamics. To date, the QED corrections to the electron anomalous magnetic moment has been computed up to the fourth order in α [110], while for the muon, it is known up to the fifth order [68]. Achieving this unprecedented level of precision required the calculation of more than 10,000 Feynman diagrams in total.

As the SM contribution is established with such extraordinary accuracy, these dipole moments serve as remarkably sensitive tools for probing New Physics. In this chapter, we focus on the constraints derived from the anomalous magnetic moments of charged leptons, with a particular emphasis on their implications for ALPs and related hidden sector scenarios. We derive bounds on the relevant effective couplings and masses, analyze the parametric dependence of these constraints, and conclude by highlighting the complementarity between bounds obtained from lepton dipole moments and those arising from direct searches at high-intensity collider experiments.

The material of this chapter has been published in the works [72] and [111], presented at the FOR5327 research group workshop (2025), as well as at the "Axions in Stockholm 2025" conference and at the EINN 2025 conference as a part of the parallel session.

3.1 Scaling properties of the anomalous magnetic moments

It is commonly known [112] that, once the loop corrections are taken into account, the lepton current is modified according to

$$\bar{u}\left(p'\right)\gamma^{\mu}u\left(p\right) \rightarrow \bar{u}\left(p'\right)\Gamma^{\mu}\left(p',p\right)u\left(p\right), \tag{3.2}$$

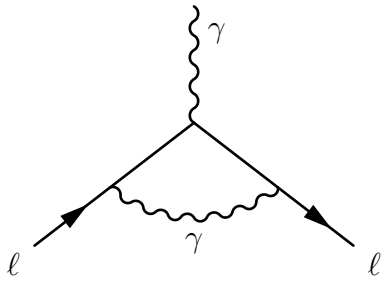

Figure 3.1: Lowest–order QED contribution to the lepton anomalous magnetic moment.

where Γ^μ denotes the full one-particle-irreducible vertex function. For a theory invariant under C, P, and T transformations, the most general Lorentz-covariant decomposition of this function can be written as

$$\Gamma^\mu\left(p', p\right) = F_1\left(q^2\right)\gamma^\mu + \frac{i\sigma^{\mu\nu}q_\mu}{2m_\ell}F_2\left(q^2\right), \tag{3.3}$$

where F_1 and F_2 are the Dirac and Pauli form factors, respectively, and $q = p' - p$ denotes the momentum transfer.

The normalization of the electromagnetic charge implies

$$F_1(0) = 1, \tag{3.4}$$

while the Pauli form factor at zero momentum transfer determines the anomalous magnetic moment

$$a_\ell = F_2(0). \tag{3.5}$$

The parameterization (3.3) has an important implication for the scaling behaviour of the anomalous magnetic moment. Indeed, at energies well below the mass scale of heavy new states, the contribution to this observable can be effectively described by the dimension-five dipole operator

$$\mathcal{L}_{\text{dipole}} = \frac{c}{\Lambda}\bar{\ell}\sigma^{\mu\nu}F_{\mu\nu}\ell, \tag{3.6}$$

where Λ denotes the characteristic scale of the heavy physics and c is a dimensionless coupling constant. The Dirac structure of this operator can be expanded as

$$\bar{\ell}\sigma^{\mu\nu}\ell = \bar{\ell}_R\sigma^{\mu\nu}\ell_L + \bar{\ell}_L\sigma^{\mu\nu}\ell_R, \tag{3.7}$$

so that the operator necessarily flips chirality. Meanwhile, in the SM and in most UV completions, the only renormalizable interaction mixing left- and right-chiral fields is the Dirac mass term $m_\ell\bar{\ell}_L\ell_R + \text{h.c.}$ Consequently, any amplitude generating the dipole operator must contain a chirality flip proportional to m_ℓ.

In addition to that, in order to extract the contribution to the anomalous magnetic moment, the dipole operator must be matched onto the decomposition of the electromagnetic vertex

$$\frac{i}{2m_\ell}F_2(0)\,\sigma^{\mu\nu}q_\nu, \tag{3.8}$$

which introduces an additional factor of m_ℓ. Consequently, the contribution of heavy New Physics to the anomalous magnetic moment generically scales as

$$\Delta a_\ell \sim \frac{[\text{coupling}]^2}{16\pi^2}\frac{m_\ell^2}{\Lambda^2}\mathcal{O}(1) + \text{corrections}, \tag{3.9}$$

from which we see that the muon, for instance, is approximately 40,000 times more sensitive to heavy physics than the electron. Although there are ways to depart from this statement [64], the quadratic dependence on m_ℓ is very generic and holds for a broad range of models.

3.2 Anomalous magnetic moment of the muon

In recent years, the anomalous magnetic moment of the muon has remained one of the most extensively discussed topics in particle physics. As a remarkably precise observable, it serves as one of the most stringent and robust tests of the Standard Model.

The theoretical prediction, a_μ^{SM}, is traditionally decomposed into three distinct parts: the quantum electrodynamics (QED), electroweak (EW), and hadronic contributions. While the QED and EW sectors have been calculated to exquisite precision—evaluated up to five and two loops, respectively—the hadronic sector strictly dominates the overall theoretical uncertainty. Specifically, as the Hadronic Vacuum Polarization (HVP) and Hadronic Light-by-Light (HLbL) scattering processes involve non-perturbative QCD dynamics at low energies. Consequently, determining their exact values historically required complex data-driven dispersive approaches or massive lattice QCD simulations.

As introduced in Section 1.2.1, the long-standing discrepancy regarding these hadronic contributions and the overall theoretical consensus culminated in the 2020 White Paper [66] published by the *Muon* $g-2$ *Theory Initiative*, providing a comprehensive review of the aforementioned corrections. Comparing this theory prediction with the measurements from the Brookhaven E821 experiment [67], one observes a deviation at the level of 3.7σ

$$\Delta a_\mu^{2020} = a_\mu^{\text{exp.,\,2020}} - a_\mu^{\text{W.P.,\,2020}} = 279(76)\times 10^{-11}. \tag{3.10}$$

This tension has stimulated significant further efforts, both toward improving SM calculations—most notably through lattice-based approaches—and toward exploring physics BSM as a possible explanation of the observed deviation. The latter direction attracted particular attention, as the anomaly could be conveniently explained by the contribution of a vector mediator in the MeV–GeV mass range, commonly known as a dark photon, with a coupling to muon of order $\mathcal{O}(10^{-3})$ [58]. Such scenarios are experimentally accessible to existing beam dump and collider facilities and were subject of numerous studies [113–121]. Other plausible explanations widely discussed in the literature include Dark Higgs–like models and ALPs [60, 61, 85, 122–124], which naturally lead to the scaling of coupling (2.27) and thus are capable of addressing the $(g-2)_\mu$ discrepancy without violating the $(g-2)_e$ value, which is in agreement with the experiment [110, 125].

Over the subsequent five years, substantial progress in lattice QCD evaluations of the hadronic vacuum polarization led to a rigorous reassessment of SM prediction. Incorpo-

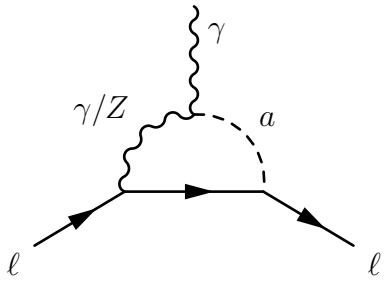

Figure 3.2: Barr–Zee–type contribution to the lepton dipole moment. The crossed diagram is not shown, but taken into account too.

rating these advances, the 2025 White Paper [68] reported an updated consensus value. The updated discrepancy evaluates to

$$\Delta a_\mu^{2025} = 38.5\,(63.7) \times 10^{-11}, \tag{3.11}$$

now falling within the 1σ confidence interval.

Although this updated value no longer points to a compelling indication of New Physics, at the same time it provides one of the most powerful constraints on possible BSM scenarios. In particular, the muon anomalous magnetic moment now serves as a stringent probe for revisiting and restricting the parameter space of light scalars, pseudoscalars, vector, and axial vector mediators in the MeV–GeV mass range, in which existing constraints remain comparatively underexplored [111]. The implications of these constraints, and their impact on the parameter space of such models, constitute the main subject of the following sections.

3.3 ALP contributions to the lepton magnetic moment

The first and most evident contribution of ALPs to $(g-2)_\ell$ arises from the one-loop Yukawa-type vertex correction, which can be obtained from Fig. 3.1 by replacing the internal photon propagator with the corresponding ALP propagator. This correction involves only the ALP–lepton coupling $g_{a\ell\ell}$, and the corresponding vertex function is given by

$$\Gamma^\mu_{\text{Yuk.},a}\,(p,p') = -i^3\,\frac{g_{a\ell\ell}^2}{4m_\ell^2}\int \frac{\gamma^5 \not{k}\cdot S_\ell\,(p'+k)\cdot\gamma^\mu\cdot S_\ell\,(p+k)\cdot\gamma^5\not{k}}{k^2-m_a^2+i\epsilon}\,\frac{d^4k}{(2\pi)^4}, \tag{3.12}$$

where a shorthand

$$S_\ell\,(p) = \frac{\not{p}+m_\ell}{p^2-m_\ell^2+i\epsilon}, \tag{3.13}$$

was used for a lepton propagator.

The evaluation of this integral follows the textbook calculation of the QED vertex correction and can be performed with the usual QFT techniques [107, 112]. The most straightforward of those is to apply the Feynman parametrization

$$\frac{1}{D_1 D_2 D_3} = 2\int_0^1 dz_1 \int_0^{z_1} \frac{dz_2}{\left[D_1 + (D_2 - D_1)\, z_1 + (D_3 - D_2)\, z_2\right]^{-3}}. \tag{3.14}$$

For the purposes of this work, it is useful to keep the three propagators in the general form

$$D_1 = k^2 - m_1^2 + i\epsilon, \tag{3.15}$$
$$D_2 = (k + K_1)^2 - m_2^2 + i\epsilon, \tag{3.16}$$
$$D_3 = (k + K_2)^2 - m_3^2 + i\epsilon, \tag{3.17}$$

where m_i are the internal masses and K_1, K_2 denote the external momenta flowing into the loop.

After one introduces the shifted loop momentum

$$k' = k + (z_1 - z_2)\, K_1 + z_2 K_2, \tag{3.18}$$

the denominator of the triangle integral takes the standard form

$$k'^2 - \Delta\left(K_1^2, K_2^2, (K_1 + K_2)^2, m_1^2, m_2^2, m_3^2\right), \tag{3.19}$$

where the effective mass parameter is given by

$$\begin{aligned}\Delta\left(K_1^2, K_2^2, (K_1 + K_2)^2, m_1^2, m_2^2, m_3^2\right) &= m_1^2 - \left(K_1^2 - m_2^2 + m_1^2\right) z_1 \\ &- \left(K_2^2 - K_1^2 - m_3^2 + m_2^2\right) z_2 + K_1^2 (z_1 - z_2)^2 + K_2^2 z_2^2 - 2\,(K_1 K_2)\, z_2\, (z_1 - z_2).\end{aligned} \tag{3.20}$$

The mixed last term is understood as

$$2\,(K_1 K_2) = (K_1 + K_2)^2 - K_1^2 - K_2^2, \tag{3.21}$$

so that the scalar triangle function indeed depends only on the three internal masses, the virtualities of the two external legs, and their invariant mass [108].

Clearly, in the case of the ALP-induced vertex correction one has to simply replace

$$K_1 = p', \qquad K_2 = p, \tag{3.22}$$
$$m_1 = m_a, \qquad m_2 = m_3 = m_\ell. \tag{3.23}$$

After performing trivial algebraic manipulations with the numerator and projecting the result onto the parameterization (3.3), we obtain [60]

$$\Delta a_\ell^{\mathrm{Yuk},\, a} = -\frac{g_{a\ell\ell}^2}{8\pi^2}\frac{1}{r_a}\int_0^1 \frac{(1-z)^3}{(1-z)^2\, r_a^{-1} + z} dz, \tag{3.24}$$

where the dimensionless ratio

$$r_i = \frac{m_i^2}{m_\ell^2}, \tag{3.25}$$

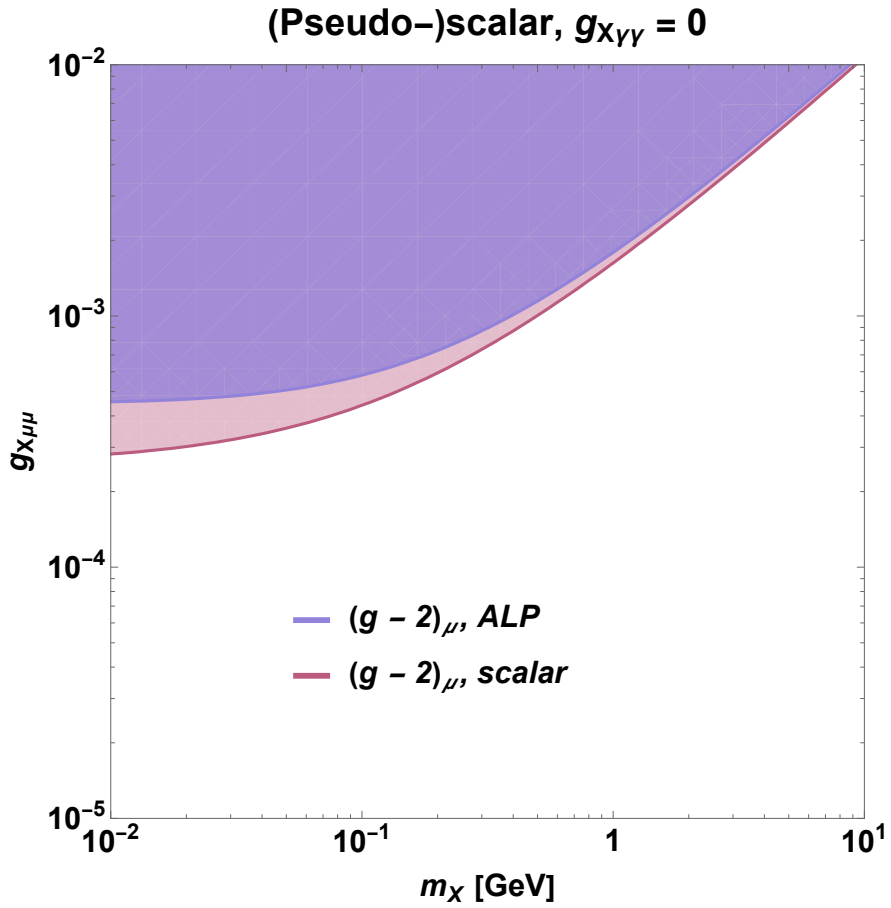

Figure 3.3: ALP-muon and scalar-muon coupling constraints under the assumption of a single-coupling contribution. X denotes either ALP or scalar.

has been introduced, so that we see the expected $\propto m_\ell^2$ behavior, and z denotes the remaining Feynman parameter. Nevertheless, it is obvious that this naive scaling can be violated even in such a simple model. For instance, in the light mediator limit, where the condition $r_a \to 0$ is met, this contribution tends to a constant

$$\Delta a_\ell^{\text{Yuk},\,a} \approx -\frac{1}{2}\frac{g_{a\ell\ell}^2}{8\pi^2}. \tag{3.26}$$

We also note that in this particular case the simplified Yukawa-like coupling in Eq. (2.26) yields the same result as the derivative coupling in Eq. (3.51). The full analytical expression amounts to

$$\begin{aligned}\Delta a_\ell^{\text{Yuk},\,a} &= \frac{g_{a\ell\ell}^2}{8\pi^2} \\ &\times \left[-\frac{1}{2} - r_a - \frac{r_a\,(1-r_a)}{2}\ln r_a + \frac{r_a\,(3-r_a)}{\sqrt{1-4r_a^{-1}}}\ln\left(\frac{\sqrt{r_a}+\sqrt{r_a-4}}{2}\right)\right].\end{aligned} \tag{3.27}$$

But in fact, the most noteworthy property of this result can be identified directly from Eq. (3.24), without the need to study the more involved analytic expression in

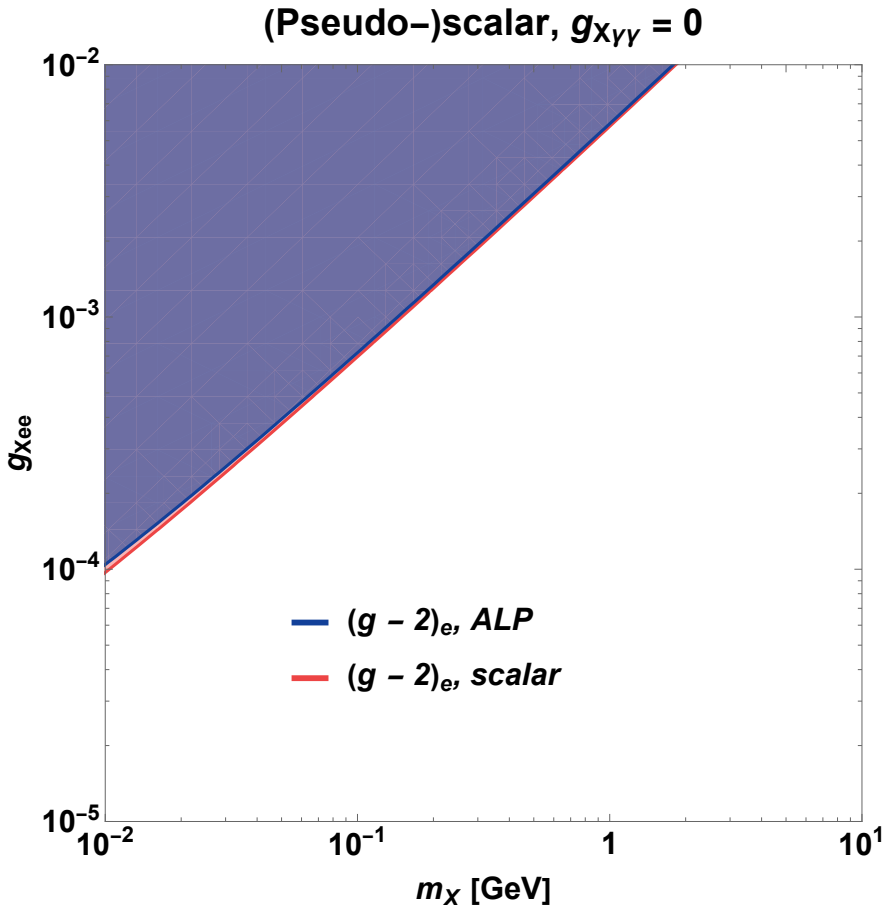

Figure 3.4: ALP-electron and scalar-electron coupling constraints under the assumption of a single-coupling contribution. X denotes either ALP or scalar.

Eq. (3.27). Namely, the Yukawa–type contribution induced by an ALP to the lepton anomalous magnetic moment is *negative*, whereas the experimentally observed anomaly in Eq. (3.10) is *positive*. Therefore, this contribution has typically been considered as bearing no significance on its own, unless there are other effects that could compensate for it.

The situation changes once the photon coupling is taken into account simultaneously with the lepton coupling. In this case, Barr–Zee–type diagrams, shown in Fig. 3.2, arise and become relevant. For the diagram with an internal photon leg, the corresponding vertex function reads

$$\begin{aligned}\Gamma^{\mu}_{\text{B.-Z.},\,a}\left(p,p'\right) &= -i^4 \frac{g_{a\ell\ell} g_{a\gamma\gamma}}{2m_\ell} \\ &\times \int \frac{\gamma^5 \not{k} \cdot S_\ell\left(p'+k\right) \cdot \gamma^\rho \cdot D_{F,\rho\sigma}\left(k+q\right) \cdot \epsilon^{\alpha\beta\sigma\mu} k_\alpha q_\beta}{k^2 - m_a^2 + i\epsilon} \frac{d^4k}{\left(2\pi\right)^4} + \text{crossed.}\end{aligned} \tag{3.28}$$

For compactness, we introduced the shorthand notation for the photon propagator

$$D_F^{\mu\nu}\left(k\right) = \frac{g^{\mu\nu}}{k^2 + i\epsilon}. \tag{3.29}$$

The evaluation of this contribution is technically more involved compared to the Yukawa diagram (3.12) for two distinct reasons, one purely algebraic and one phenomenological:

- γ^5 in combination with the Levi–Civita tensor produces a number of Dirac structures in the numerator to be handled.
- The diagram is logarithmically divergent. Since we do not assume a specific UV-complete completion of the ALP effective theory, this divergence is regulated by introducing a cutoff Λ, which characterizes the range of validity of the effective Lagrangian (2.16).

As our primary goal is to derive constraints on ALP interactions rather than to compute the magnetic moment correction in some specific ultraviolet completion, it is sufficient to retain this cutoff dependence explicitly. In the absence of new weak-scale states observed at LHC energies, the cutoff is expected to lie at least at the $\mathcal{O}\,(\mathrm{TeV})$ scale. A benchmark value of $\Lambda = 1\,\mathrm{TeV}$ is commonly adopted in the literature for studying ALP constraints [55, 61, 85, 122, 124, 126] and we adopt this value throughout our analysis.

Explicitly, the Barr–Zee correction with an internal photon leg is given by

$$\begin{aligned}\Delta a_\gamma^{\text{B.-Z.},\,a} &= \frac{m_\ell g_{a\ell\ell} g_{a\gamma\gamma}}{8\pi^2} \ln\Lambda^2 - \frac{m_\ell g_{a\ell\ell} g_{a\gamma\gamma}}{8\pi^2} \\ &\times \int_0^1 dz_1 \int_0^{z_1} \left[(1+3z_2)\ln\Delta_\gamma + \frac{m_\ell^2 z_2^3}{\Delta_\gamma}\right] dz_2,\end{aligned} \tag{3.30}$$

$$\Delta_\gamma = m_\ell^2 z_2^2 + m_a^2\,(1-z_1)\,. \tag{3.31}$$

The integration over the Feynman parameters is quite cumbersome in this case, but can nevertheless be done analytically. The result is

$$\begin{aligned}\Delta a_\gamma^{\text{B.-Z.},\,a} = \frac{m_\ell g_{a\ell\ell} g_{a\gamma\gamma}}{8\pi^2} \Bigg[&\ln\left(\frac{\Lambda^2}{m_\ell^2}\right) + \frac{13}{6} \\ &- \frac{r_a^2 \ln r_a}{6} + \frac{r_a}{3} + \frac{r_a+2}{3}\sqrt{r_a\,(r_a-4)}\,\ln\left(\frac{\sqrt{r_a}+\sqrt{r_a-4}}{2}\right)\Bigg]\,.\end{aligned} \tag{3.32}$$

This contribution, although proportional to the lepton mass m_ℓ, does not become negligible in the case of the electron, as the ratio r_a becomes large enough to compensate for the suppression of the prefactor.

If the internal line corresponds instead to a Z-boson instead, one has to replace

$$\Delta_\gamma \to \Delta_Z = m_\ell^2 y^2 + m_a^2\,(1-x) + m_Z^2\,(x-y)\,, \tag{3.33}$$

$$g_{a\gamma\gamma} \to -\frac{4\sin^2\theta_w - 1}{4\sin\theta_w\cos\theta_w} g_{a\gamma Z}, \tag{3.34}$$

in Eqs. (3.30). The resulting analytic expression is

$$\Delta a_Z^{\text{B.-Z.},a} = -\frac{4\sin^2\theta_w - 1}{4\sin\theta_w\cos\theta_w}\frac{m_\ell g_{a\ell\ell} g_{a\gamma Z}}{8\pi^2}\left[\ln\left(\frac{\Lambda^2}{M_Z^2}\right) + \frac{13}{6}\right.$$
$$+ \frac{r_a}{3}\frac{r_a+2}{r_a-r_Z}\mathcal{F}(m_a) - \frac{r_Z}{3}\frac{r_Z+2}{r_a-r_Z}\mathcal{F}(M_Z) + \frac{r_a+r_Z}{3} \tag{3.35}$$
$$\left. - \frac{6r_a + r_Z^3 - 6r_Z}{6(r_a-r_Z)}\ln\left(\frac{r_a}{r_Z}\right) - \frac{r_a^2 + r_a r_Z + r_Z^2 - 6}{6}\ln r_a\right],$$

where it was also denoted

$$\mathcal{F}(M) = \frac{\sqrt{M^2(M^2-4m_\ell^2)}}{m_\ell^2}\ln\left(\frac{\sqrt{M^2-4m_\ell^2}+M}{2m_\ell}\right). \tag{3.36}$$

It is noteworthy that the two Lagrangians (2.26) and (3.51) yield expressions that differ only by the replacement

$$\frac{13}{6} \to 2, \tag{3.37}$$

in both cases.

Clearly, the contribution of the Z-boson is suppressed by the prefactor

$$-\frac{4\sin^2\theta_w - 1}{4\sin\theta_w\cos\theta_w} \approx 0.07 \tag{3.38}$$

Then it is evident that, given also the relation (2.20) between the two couplings, the Z-boson contribution constitutes only a minor correction—typically at the level of a few percent—relative to that of the photon. Moreover, for the choice $\Lambda = 1\,\text{TeV}$, the logarithmically divergent term dominates the total ALP–photon loop contribution to $(g-2)_\mu$, accounting for roughly 90% of the effect for $m_a = 1\,\text{GeV}$.

Larger values of Λ further enhance the logarithmic term, yielding a larger correction and, consequently, stronger constraints on the ALP–photon coupling. This makes $\Lambda = 1\,\text{TeV}$ a well-motivated choice for obtaining a conservative exclusion limit, and we adopt this value throughout our analysis.

Finally, we note that the Barr–Zee diagram depends on the relative sign of the two couplings, and a positive contribution to a_ℓ requires $g_{a\ell\ell}\, g_{a\gamma\gamma} > 0$. In this case, the Δa_μ^{2020} anomaly could have been explained by an ALP with $g_{a\gamma\gamma}\, g_{a\mu\mu} \approx 10^{-7}$ and m_a in the few hundred MeV to GeV range. When deriving constraints, we will always assume the *cancellation scenario*, where the Yukawa and Barr–Zee diagrams partially cancel each other out. In this case, the provided limits will be conservative.

3.3.1 Scalar contribution to the lepton magnetic moment

Before analyzing the results obtained in the previous section, it is also imperative to investigate the scalar scenario (2.69). The calculation is analogous to the pseudoscalar case and is in fact simpler, as neither γ^5 nor the Levi–Civita tensor appears. The Yukawa contribution is

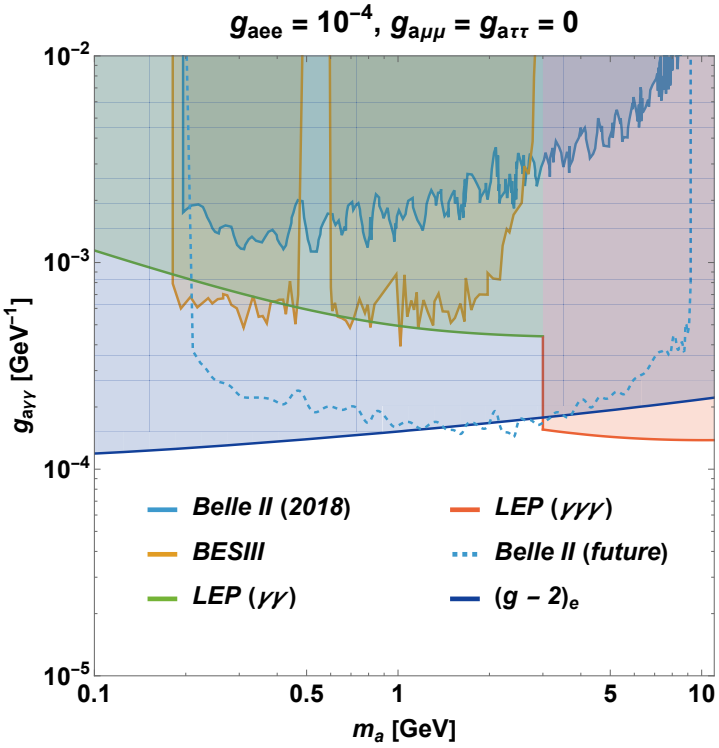

Figure 3.5: ALP constraints from e^+e^- collider experiments and $(g-2)_e$ measurements with both photon and electron couplings taken into account.

$$\Gamma^{\mu}_{\text{Yuk.},\,s}\left(p,p'\right) = -i^3 g^2_{s\ell\ell}\int \frac{S_\ell\left(p'+k\right)\cdot\gamma^\mu\cdot S_\ell\left(p+k\right)}{k^2-m_a^2+i\epsilon}\frac{d^4k}{\left(2\pi\right)^4}, \tag{3.39}$$

while the Barr–Zee diagram takes the form

$$\begin{aligned}&\Gamma^{\mu}_{\text{B.-Z.},\,s}\left(p,p'\right) = -i^5 g_{s\ell\ell}g_{s\gamma\gamma}\\ &\times\int \frac{S_\ell\left(p'+k\right)\cdot\gamma^\rho\cdot D_{F,\rho\sigma}\left(k+q\right)\cdot\left[\left[q^2+(kq)\right]g^{\sigma\mu}-(q+k)^\mu q^\sigma\right]}{k^2-m_a^2+i\epsilon}\frac{d^4k}{\left(2\pi\right)^4}\\ &+\text{crossed.}\end{aligned} \tag{3.40}$$

After Feynman parameters are introduced, these expressions give rise to the correction

$$\Delta a_\ell^{\text{Yuk},\,s} = \frac{g^2_{s\ell\ell}}{8\pi^2}\frac{1}{r_s}\int_0^1 \frac{\left(1-z\right)^2\left(1+z\right)}{\left(1-z\right)^2 r_s^{-1}+z}\,dz, \tag{3.41}$$

$$\Delta a_\gamma^{\text{B.-Z.},\,s} = \frac{m_\ell g_{s\ell\ell}g_{s\gamma\gamma}}{8\pi^2}\ln\Lambda^2 - \frac{m_\ell g_{s\ell\ell}g_{s\gamma\gamma}}{4\pi^2}\int_0^1 dz_1\int_0^{z_1}\ln\Delta_\gamma\,dz_2. \tag{3.42}$$

One important modification is that the Yukawa-like term $\Delta a_\ell^{\text{Yuk},\,s}$ is now positive, so that it is capable of resolving the Δa_μ^{2020} discrepancy on it's own. There is, in principle, also the possibility of a scenario in which the scalar and pseudoscalar contributions cancel each other at the one-loop level.

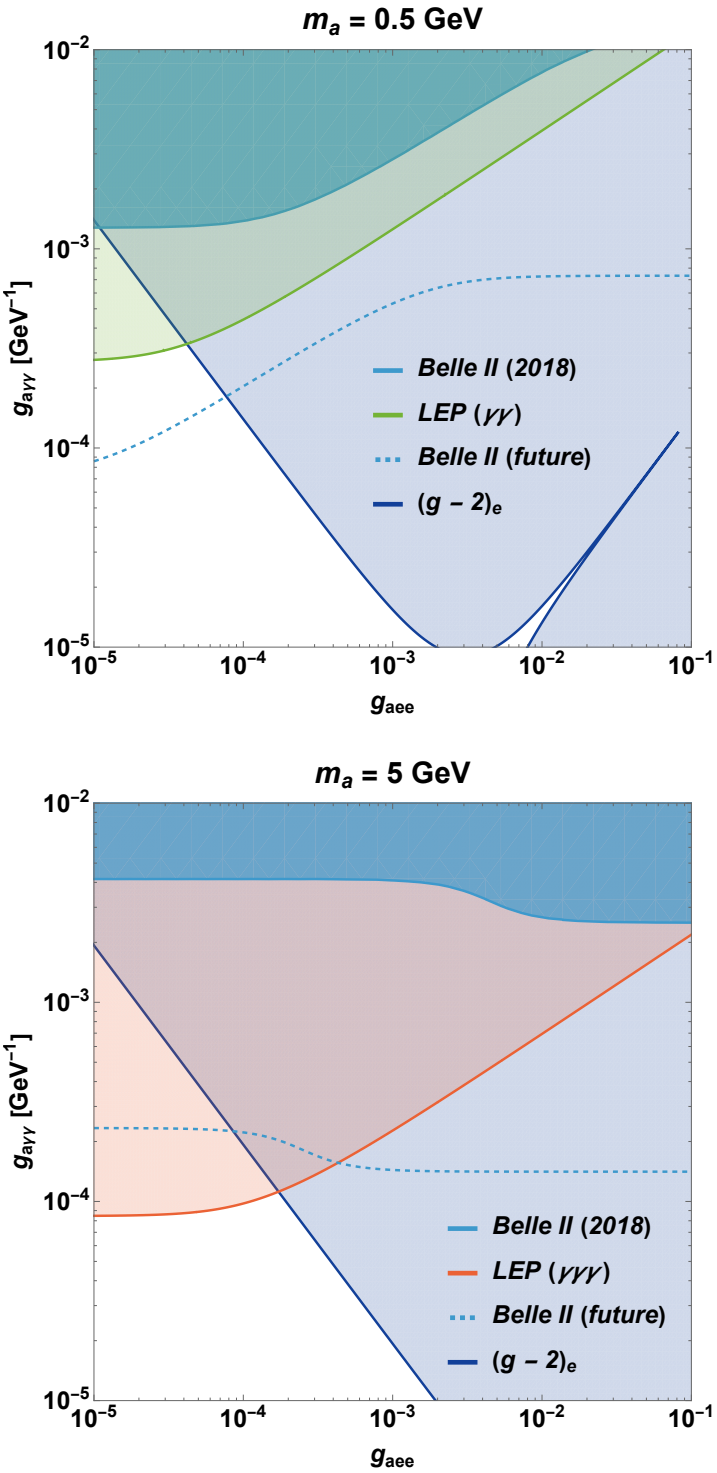

Figure 3.6: Exclusion limits on the $(g_{aee}, g_{a\gamma\gamma})$ parameter space for masses $m_a = 0.5$ and 5 GeV under the assumption $g_{a\mu\mu} = g_{a\tau\tau} = 0$.

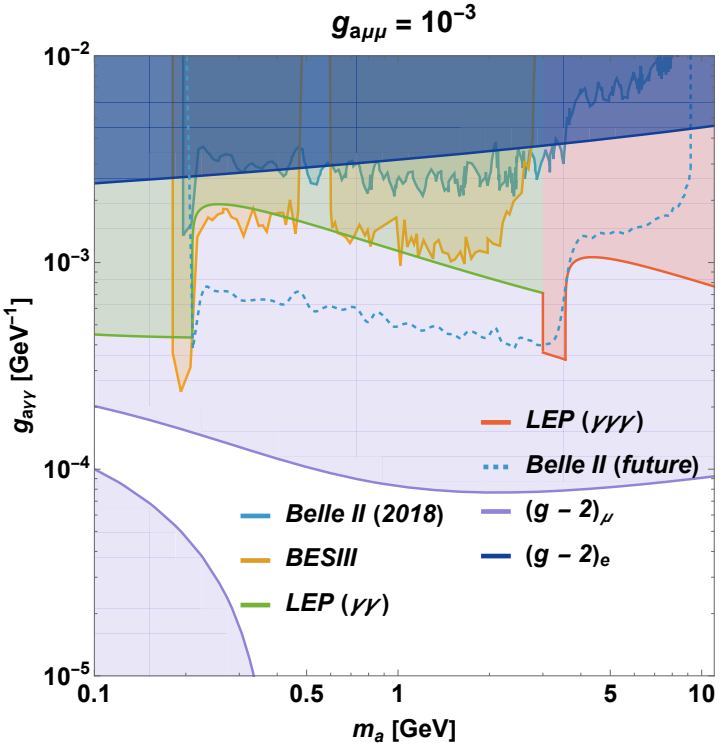

Figure 3.7: ALP constraints from e^+e^- collider experiments and $(g-2)_\ell$ measurements with photon and lepton couplings taken into account. Lepton universality is assumed, so that g_{aee}, $g_{a\mu\mu}$ and $g_{a\tau\tau}$ are proportional to each other, see (2.27).

The above integrals can be evaluated analytically in a straightforward way. For the Yukawa graph one finds

$$\begin{aligned}\Delta a_\ell^{\text{Yuk},\,s} &= \frac{g_{s\ell\ell}^2}{8\pi^2} \\ &\times \left[\frac{3}{2} - r_s - \frac{r_s\,(3-r_s)}{2}\ln r_s - \frac{(1-r_s)\,(4-r_s)}{\sqrt{1-4r_s^{-1}}}\ln\left(\frac{\sqrt{r_s}+\sqrt{r_s-4}}{2}\right)\right],\end{aligned} \tag{3.43}$$

so that in the light mediator limit we obtain

$$\Delta a_\ell^{\text{Yuk},\,s} \approx \frac{3}{2}\frac{g_{s\ell\ell}^2}{8\pi^2}, \tag{3.44}$$

and we see once again that naive scaling arguments can be misleading, even in minimal, assumption-free setups. It is also noteworthy that the magnitude of this contribution is three times larger than in the pseudoscalar case.

In turn, the Barr–Zee contribution evaluates to

$$\Delta a_\gamma^{\text{B.-Z.},\,s} = \frac{m_\ell g_{s\ell\ell} g_{s\gamma\gamma}}{8\pi^2}\left[\ln\left(\frac{\Lambda^2}{m_\ell^2}\right) - \frac{r_s-9}{3} - \frac{6r_s - r_s^2}{6}\ln r_s - \frac{r_s\,(r_s-4)^2}{6}\frac{1}{\sqrt{r_s}}\frac{1}{\sqrt{r_s-4}}\ln\left(\frac{\sqrt{r_s}+\sqrt{r_s-4}}{\sqrt{r_s}-\sqrt{r_s-4}}\right)\right]. \tag{3.45}$$

Finally, the Barr–Zee contribution with an internal Z boson is obtained from $\Delta a_\ell^{\text{Yuk.},\,s}$ via the replacement rule given in Eq. (3.33), analogously to the ALP case. The resulting expression can be conveniently parameterized as

$$\Delta a_Z^{\text{B.-Z.},\,s} = -\frac{4\sin^2\theta_w - 1}{4\sin\theta_w\cos\theta_w}\frac{m_\ell g_{s\ell\ell} g_{s\gamma Z}}{8\pi^2}\left(\ln\left(\frac{\Lambda^2}{m_\ell^2}\right) - 2\frac{\mathcal{K}(M_Z) - \mathcal{K}(m_a)}{M_Z^2 - m_a^2}\right), \tag{3.46}$$

where an auxiliary function was defined

$$\mathcal{K}(M) = \frac{M^4}{6m_\ell^2} - \frac{3M^2}{2} - \frac{5m_\ell^2}{9} + \frac{M^4}{2m_\ell^2}\left(1 - \frac{M^2}{6m_\ell^2}\right)\ln\left(\frac{M^2}{m_\ell^2}\right) + \frac{M^4\,(M^2-4m_\ell^2)^2}{12m_\ell^6}\frac{m_\ell^2}{M\sqrt{M^2-4m_\ell^2}}\ln\left(\frac{M+\sqrt{M^2-4m_\ell^2}}{M-\sqrt{M^2-4m_\ell^2}}\right). \tag{3.47}$$

Once the scalar–photon coupling is included, two qualitatively different scenarios emerge. If $g_{s\mu\mu}$ and $g_{s\gamma\gamma}$ have opposite signs, partial cancellation between the Yukawa and Barr–Zee contributions occurs; if they share the same sign, the two contributions add up. Both scenarios can accommodate the observed muon anomalous magnetic moment Δa_μ^{2020}, in contrast to the pseudoscalar case, where only one sign choice is viable. For sufficiently small values of $g_{s\gamma\gamma}$, the distinction between the two scenarios disappears, as the Yukawa contribution dominates.

3.4 Combined constrains for ALPs from $(g-2)_\ell$ and e^+e^- colliders

Figs. 3.3 and 3.4 illustrate the resulting constraints for scalar and pseudoscalar mediators in the absence of a photon coupling. The constraints on the electron coupling are derived using the values

$$a_{e,\,\text{th.}} = 115965218.1643\,(764)\times 10^{-11}, \tag{3.48}$$

$$a_{e,\,\text{exp.}} = 115965218.062\,(12)\times 10^{-11}, \tag{3.49}$$

where an agreement between theory and experiment is observed. Unless specified, 2σ confidence level is assumed for all bounds.

In the low-mass limit, the exclusion curves approach a constant value, reflecting the fact that the contribution to Δa_ℓ becomes nearly constant, see Eqs. (3.26) and (3.44).

The bounds for the scalar case are also slightly stronger, owing to the aforementioned enhancement of the scalar contribution relative to the pseudoscalar by a factor of three.

It is worth noting that constraints from the electron anomalous magnetic moment are among the few available probes of the electron–ALP coupling in the MeV to sub–GeV mass range. Reconstructing events with such low invariant masses at collider experiments is challenging, as the resulting leptons typically do not carry sufficient transverse momentum to end up in the calorimeters and trigger the event. This situation may soon improve with the upcoming MESA@MAGIX and JLab polarized positron programs, which are designed to explore this region of parameter space. These developments will be discussed in Chapter 3 and 4 of this work.

Next, Fig. 3.5 shows the projection onto the $(m_a, g_{a\gamma\gamma})$ plane for a fixed value of the ALP–electron coupling, $g_{aee} = 10^{-4}$, same as in Fig. 2.10. Fig. 3.6, in turn, illustrates the projection onto the $(g_{aee}, g_{a\gamma\gamma})$ plane for two representative ALP masses, $m_a = 0.5\,\text{GeV}$ and $m_a = 5\,\text{GeV}$. The visible thin line in the first case represents the situation where the Yukawa and Barr–Zee contributions cancel each other out.

Figs. 3.9 and 3.8 show the corresponding exclusion limits when muon and tau couplings are also included, assuming lepton universality, see Eq. (2.27). The resulting bounds are not only comparable to, but in fact significantly more stringent than, those obtained from previous collider experiments, even when near-future projections are taken into account.

We also emphasize that, apart from the effective Lagrangians in Eqs. (3.51) and (2.16)—which constitute the only dimension-five operators permitted for ALPs on general theoretical considerations—and the well-motivated choice $\Lambda = 1\,\text{TeV}$ discussed above, the exclusion limits derived from $(g-2)_\ell$ do not rely on any additional model-specific assumptions.

Nevertheless, it is important to keep in mind the non-trivial interplay between the two couplings. As illustrated in Fig. 3.9, the bounds can shift significantly if the muon coupling is further constrained to sufficiently small values, underscoring both the complementarity of the two approaches and the relevance of upcoming Belle II results for BSM searches in this sector. This further motivates detailed investigations of processes such as $e^+e^- \to \ell^+\ell^-$ at the Belle II and BESIII experiments, which could provide direct probes of $g_{a\ell\ell}$ couplings that have not been reported so far.

Before concluding, we note that the interactions considered in this work do not generate electric dipole moments, i.e. they do not induce CP-odd effects. Such contributions could arise, for example, from parity-violating couplings of the ALPs to gauge fields, such as

$$-\frac{\tilde{g}_{a\gamma\gamma}}{2} a F^{\mu\nu} F_{\mu\nu}, \tag{3.50}$$

or from interactions involving mixed-parity states coupled to leptons,

$$\mathcal{L}_{a\ell\ell} = -\tilde{g}_{a\ell\ell} a\, \bar{\ell} \left(1 + \gamma^5\right) \ell. \tag{3.51}$$

Both operators violate CP and can induce EDMs for charged leptons at loop level. However, these effects are subject to extremely stringent experimental bounds, owing to the tight constraints on lepton EDMs. As a result, the corresponding couplings $\tilde{g}_{a\gamma\gamma}$ and

$\tilde{g}_{a\ell\ell}$ are far more strongly constrained than the CP-even couplings $g_{a\gamma\gamma}$ and $g_{a\ell\ell}$ studied in this work [57, 65, 127]. We therefore neglect these CP-violating interactions in the present analysis.

Lastly, the bounds obtained in the scalar scenario are of comparable strength and are therefore not shown. Our conclusions for the pseudoscalar case apply almost equally to the scalar case.

3.5 Dark photon bounds

The results of $(g-2)_\ell$ measurements are not restricted to ALP scenarios and can be applied to a broad class of BSM models. In this section, we extend the formalism developed above to revisit the parameter space of dark photon models [106]. In the minimal setup, the relevant Lagrangian reads

$$\mathcal{L}_{\text{D.P.}} = -\frac{1}{4}F^{\mu\nu}F_{\mu\nu} - \frac{1}{4}F'^{\mu\nu}F'_{\mu\nu} - \frac{\epsilon}{2}F^{\mu\nu}F'_{\mu\nu} + \frac{m'^2_A}{2}A'_\mu A'^\mu + eJ^\mu A_\mu + e'J'^\mu A'_\mu, \tag{3.52}$$

where $F_{\mu\nu}$ denotes the SM $U(1)$ field strength, $F'_{\mu\nu}$ that of the dark photon A'_μ, and ϵ parametrizes kinetic mixing between the two. The fields A_μ and A'_μ couple to the SM and dark sector currents J^μ and J'^μ, respectively.

The apparent freedom in the choice of charge or hypercharge couplings, in fact, amounts to the rescaling of ϵ, with both leading to the same physics. In the following, we assume ϵ to be the kinetic mixing with the photon.

The kinetic mixing term can be eliminated by the field redefinition

$$A_\mu \to A_\mu - \epsilon A'_\mu, \tag{3.53}$$
$$A'_\mu \to A'_\mu, \tag{3.54}$$

which then induces the interaction terms

$$eJ^\mu A_\mu + \left(e'J'^\mu - \epsilon eJ^\mu\right)A'_\mu. \tag{3.55}$$

The next step crucially depends on whether the dark photon mass m'_A vanishes. If A'_μ remains massless, the Lagrangian preserves a residual freedom under orthogonal rotations in the $\left(A_\mu, A'_\mu\right)$ field space. One may then perform an additional transformation

$$\begin{pmatrix} A_\mu \\ A'_\mu \end{pmatrix} = \begin{pmatrix} \cos\theta & \sin\theta \\ -\sin\theta & \cos\theta \end{pmatrix}\begin{pmatrix} \tilde{A}_\mu \\ \tilde{A}'_\mu \end{pmatrix}, \tag{3.56}$$

which brings the interaction Lagrangian to the form

$$eJ^\mu\left(\cos\theta\tilde{A}_\mu + \sin\theta\tilde{A}'_\mu\right) - \epsilon eJ^\mu\left(-\sin\theta\tilde{A}_\mu + \cos\theta\tilde{A}'_\mu\right). \tag{3.57}$$

And we see that by choosing $\tan\theta = \epsilon$, we can decouple $\tilde{A}'_\mu$ completely from SM matter.

In contrast, if the dark photon is massive, its interaction with SM leptons cannot be simply rotated away. The magnitude of this coupling is controlled by the kinetic mixing

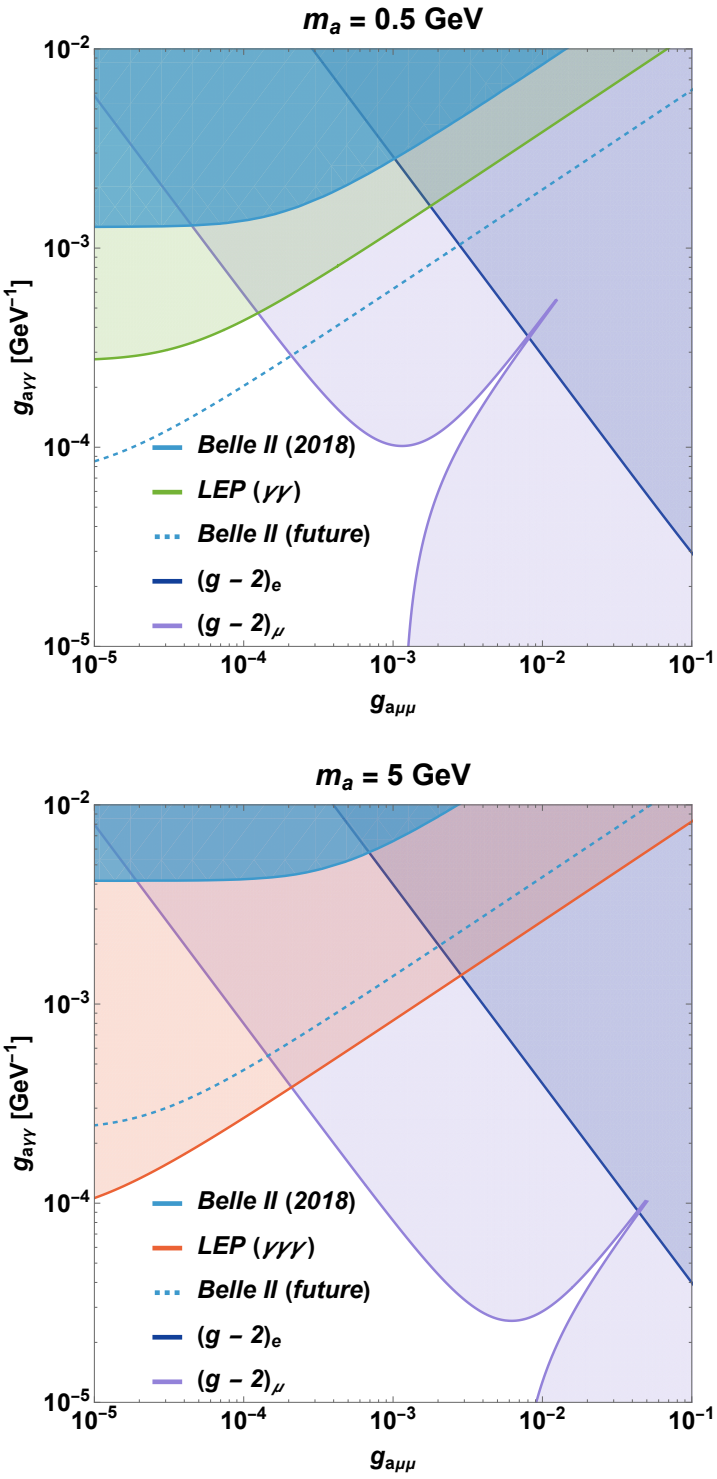

Figure 3.8: Exclusion limits on the $(g_{a\mu\mu}, g_{a\gamma\gamma})$ parameter space for masses $m_a = 0.5$ and 5 GeV. Lepton universality is assumed to relate ALP-muon and ALP-electron coupling.

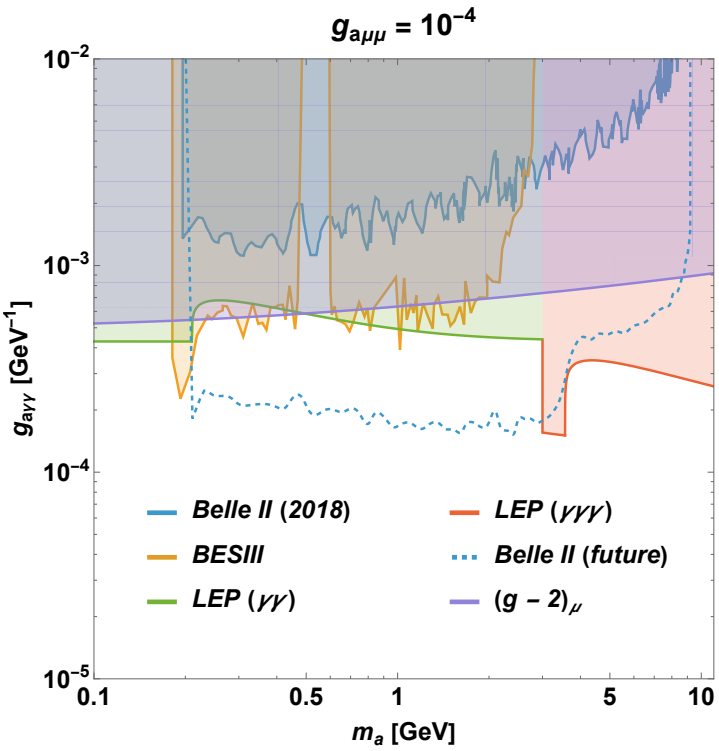

Figure 3.9: ALP constraints from e^+e^- collider experiments and $(g-2)_\ell$ measurements with photon and lepton couplings taken into account. Lepton universality is assumed, so that g_{aee}, $g_{a\mu\mu}$ and $g_{a\tau\tau}$ are proportional to each other, see (2.27). The $(g-2)_e$ was found to be noncompetitive for the chosen value of $g_{a\mu\mu}$.

parameter ϵ of an arbitrary magnitude, depending on the UV completion of the theory. Nevertheless, it is clear that ϵ cannot be of $\mathcal{O}(1)$, as the dark photon with such a large coupling would have most likely be already discovered in existing experiments. It is more natural to expect kinetic mixing to be generated at the one- or two-loop level, leading to a suppression of order $(16\pi^2)^{-1}$ or $(16\pi^2)^{-2}$. The relevant parameter space then lies in the range between $\epsilon \sim 10^{-5}$ and 10^{-3}, which is accessible to current beam dump and collider experiments.

Dark photons contribute to the anomalous magnetic moment of leptons via the vertex correction diagram shown in Fig. 3.1, whose evaluation is analogous to the standard QED calculation,

$$\Delta a_{\text{D.P.}} = \frac{\alpha\epsilon^2 m_\ell^2}{\pi}\int_0^1 \frac{z^2(1-z)}{m_\ell^2 z^2 + m_A'^2(1-z)}dz. \tag{3.58}$$

We see that the dependence m_ℓ^2 is in place again, and the correction is positive [128]. The analytic expression can be written as

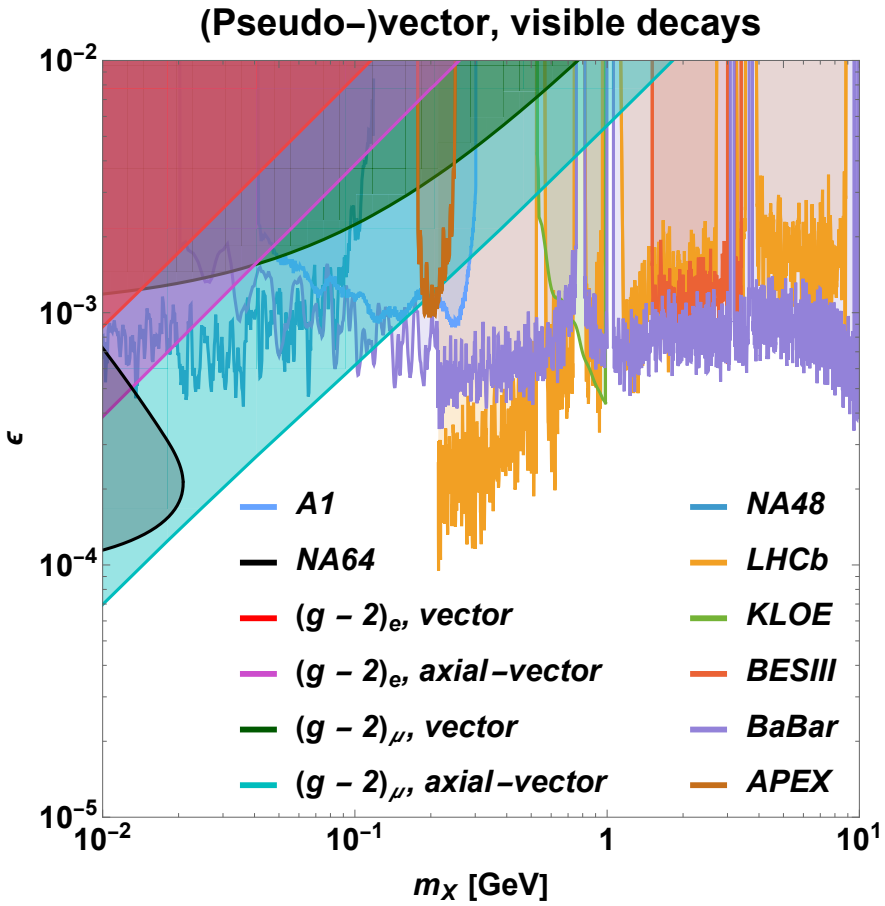

Figure 3.10: Constraints on the allowed BSM parameter space from $(g-2)_e$ and from existing experiments looking for visible A' decays for the vector/axial vector scenarios [113–116, 118–121].

$$\Delta a_{\text{D.P.}} = \frac{\alpha\epsilon^2}{\pi}\left[\frac{1-2r_A}{2}\right. \\ \left. + \frac{r_A\,(r_A-2)}{2}\ln r_A - \frac{\sqrt{r_A}\,(r_A^2-4r_A+2)}{\sqrt{r_A-4}}\ln\left(\frac{\sqrt{r_A}+\sqrt{r_A-4}}{2}\right)\right], \tag{3.59}$$

where $r_A = m_A'^2/m_\ell^2$, in analogy with the ALP case, cf. Eq. (3.25). In the limit where the dark photon mass becomes negligible compared to that of the lepton, this reproduces the QED result

$$\Delta a_{\text{D.P.}} \approx \frac{\alpha\epsilon^2}{2\pi}. \tag{3.60}$$

Finally, it is imperative to apply the same formalism to an axial vector mediator with interaction Lagrangian

$$\mathcal{L}_{\text{axial vector}} = -e\epsilon\bar{\ell}\gamma^5 \not{A}'\ell, \tag{3.61}$$

which contributes to the anomalous magnetic moment as

$$\Delta a_{\text{axial vector}} = -\frac{\alpha\epsilon^2 m_\ell^2}{\pi}\int_0^1 \frac{z\,(1-z)\,(4-z)+2\frac{m_\ell^2}{m_A'^2}z^3}{m_\ell^2 z^2 + m_A'^2\,(1-z)}dz. \tag{3.62}$$

The key difference between vector and axial vector mediators is the appearance of additional terms in the numerator proportional to $m_\ell^2/m_A'^2$, which originate from the longitudinal $k^\mu k^\nu/m_A'^2$ component of the massive spin-1 propagator [128]. While this term vanishes for a conserved vector current, it survives in the axial case and leads to an enhancement of the contribution to Δa_ℓ for light axial vectors. The resulting correction is purely negative.

The corresponding analytic expression can again be obtained in closed form

$$\begin{aligned}\Delta a_{\text{axial vector}} = -\frac{\alpha\epsilon^2}{\pi}\Bigg[&\frac{1}{r_A}+\frac{2r_A-5}{2}\\ &-\frac{r_A^2-4r_A+2}{2}\ln r_A+(r_A-2)\sqrt{r_A\,(r_A-4)}\ln\left(\frac{\sqrt{r_A}+\sqrt{r_A-4}}{2}\right)\Bigg].\end{aligned} \tag{3.63}$$

Unlike other mediators, the contribution of the axial vector does not tend to a constant value in the low-mass limit; instead, it grows

$$\Delta a_{\text{axial vector}} \approx -\frac{\alpha\epsilon^2}{\pi}\frac{1}{r_A}. \tag{3.64}$$

Figs. 3.10 and 3.11 show the resulting constraints for vector and axial vector mediators, assuming visible and invisible decay channels, respectively, with the latter being a common scenario when the mediator couples to dark sector particles, i.e. J'_μ currents. We find that competitive limits are obtained in this way, particularly in the axial vector case due to the longitudinal enhancement discussed above. These are complementary to collider and beam dump searches, but most importantly, these bounds are largely independent of specific assumptions about the decay properties of the mediator.

3.6 Results and discussion

Over the past decade, the muon magnetic anomaly has been one of the most intensively studied topics in particle physics. Significant advancements in both experimental measurements and theoretical calculations were made, which ultimately allowed the tensions to be resolved within the Standard Model.

At the same time, these developments have provided one of the most stringent tools for constraining BSM physics, which we used to revise the parameter space of potential scalars, pseudoscalars, vectors and axial vectors in the MeV-GeV mass range—the region, which remains comparatively underconstrained and therefore represents a particularly relevant target for complementary probes.

No specific ultraviolet-complete model was assumed in deriving the bounds on scalar and pseudoscalar interactions. Instead, an EFT approach was adopted with a conservative ultraviolet cutoff of $\Lambda = 1\,\text{TeV}$. Depending on the value of $g_{a\mu\mu}$, the resulting limits can be up to an order of magnitude more restrictive than those previously reported, clearly illustrating the strength of this analysis.

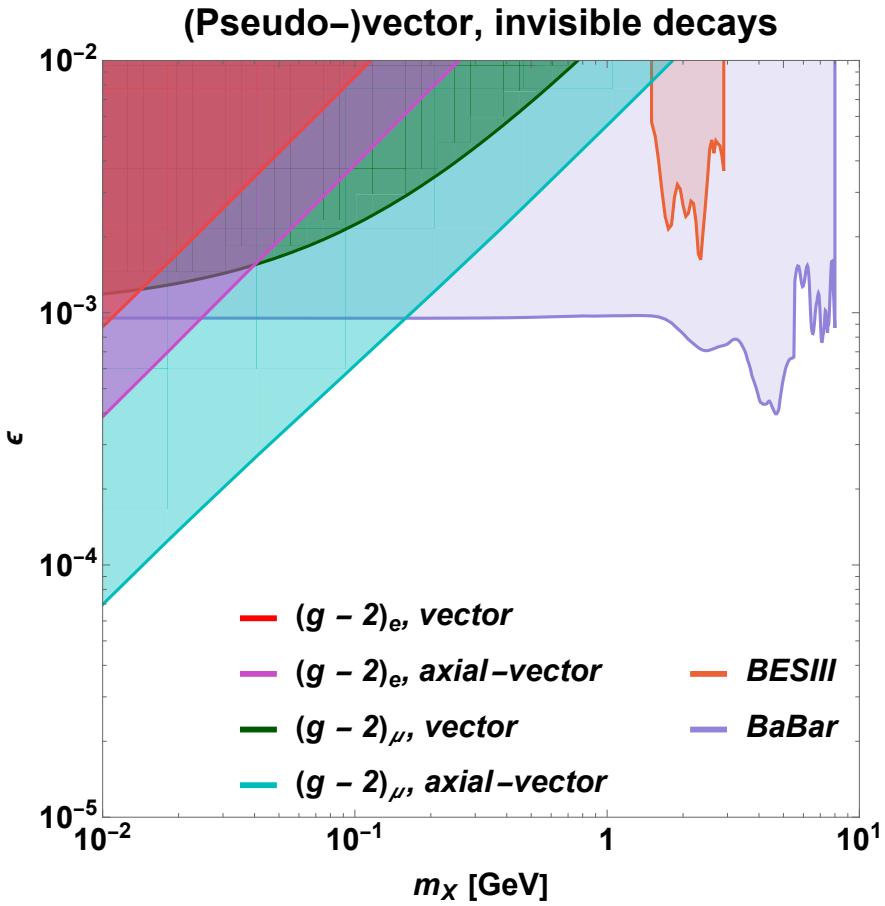

Figure 3.11: Constraints on the allowed BSM parameter space from $(g-2)_e$ and from existing experiments looking for invisible A' decays for the vector/axial vector scenarios [129, 130].

The analysis further demonstrates the complementarity between lepton magnetic moment measurements and collider searches, as they probe different regions of parameter space with distinct sensitivity patterns. With the continued data accumulation at Belle II and BESIII, substantial improvements in the corresponding constraints can be anticipated. We also note that the current uncertainty in $(g-2)_\mu$ is dominated by theory errors. Further efforts in advancing lattice and data-driven calculations are expected to yield additional sensitivity gains and narrow down the viable parameter space even more.

Finally, for vector and axial vector cases, although the constraints obtained are less stringent, especially in the case of invisibly decaying mediators, they nevertheless offer competitive exclusion limits that remain independent of other search strategies and do not imply specific assumptions about the A' decays.

Chapter 4

BSM searches at MAGIX@MESA experiment

Brevity is the soul of wit.

William Shakespeare

The previous two chapters were dedicated to the search for New Physics at e^+e^- collider facilities, complemented by constraints from lepton anomalous magnetic moments. While these approaches have proven powerful, they are not exhaustive. In particular, the parameter space in the few MeV to sub-GeV mass range remains largely underexplored.

The main reason for this gap lies in detector thresholds and the challenges of event reconstruction in the kinematic regime where $m_X^2/s \ll 1$. Under these conditions, the decay products of a light mediator are emitted with large momenta in forward direction. Consequently, a decay into a photon pair—typical for ALPs—is often reconstructed in the calorimeter as a single, merged photon cluster. This merged signal is heavily polluted by the overwhelming QED background from processes such as $e^+e^- \to \gamma\gamma$.

These challenges have motivated the development of complementary low-energy, high-precision experiments, such as the MESA facility [131, 132] and, in particular, its MAGIX experiment [133] (MESA Gas Internal target eXperiment). Operating at electron beam energies up to $E_{\text{beam}} = 105\,\text{MeV}$, below the pion production threshold, and at very high luminosities, MAGIX provides a kinematic regime largely free from backgrounds associated with secondary hadronic processes. This configuration yields an exceptionally clean environment, making it particularly well suited for precision measurements and searches for weakly coupled BSM particles.

In the following sections, we will discuss the setup of this experiment in detail. Furthermore, we will demonstrate that the MAGIX experiment can serve as a highly versatile setup for testing BSM mediators of different quantum numbers, particularly through the Bethe-Heitler pair production.

This section is based on work in preparation for publication, preliminary entitled as "Sensitivity of MESA to BSM effects via Bethe-Heitler pair production", expected to be released within the first half of 2026.

4.1 MESA facility and MAGIX experiment

The MESA facility at Johannes Gutenberg University Mainz is designed to support a broad precision physics program at the intensity frontier. Its flagship P2 experiment aims to measure the weak mixing angle, $\sin^2\theta_W$, at very low momentum transfer via parity-violating electron–proton scattering, providing a stringent test of the SM via electroweak radiative corrections. In addition to that, the DarkMESA experiment plans

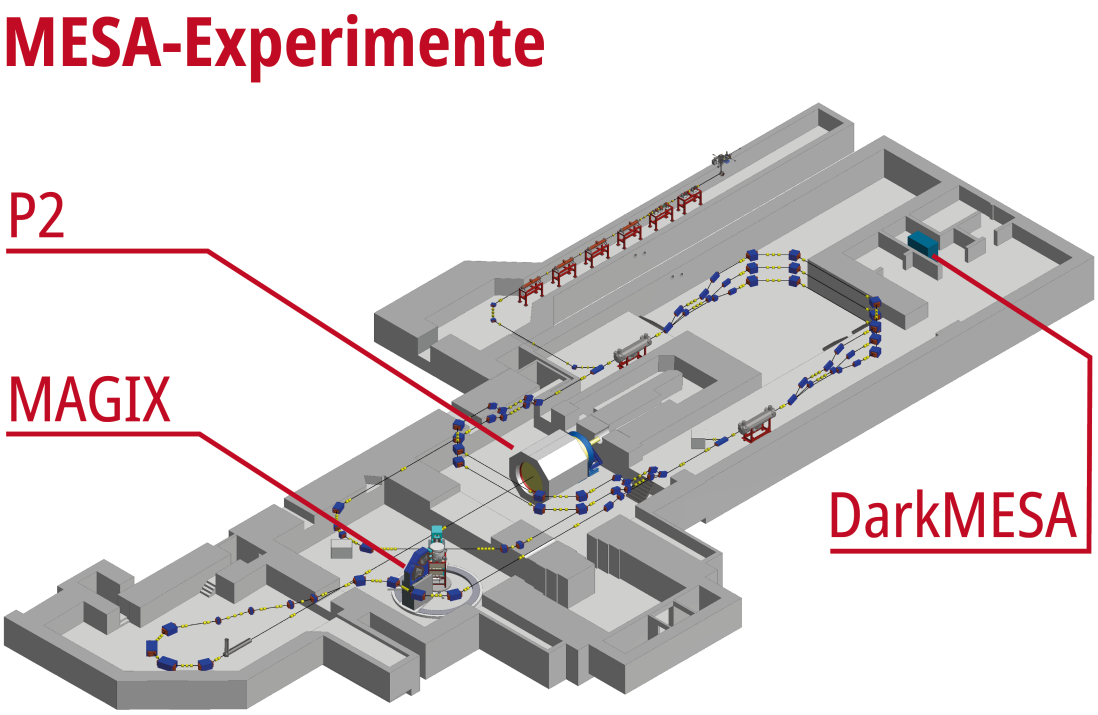

Figure 4.1: Overview of the MESA facility.

to utilize the presence of a beam dump in the P2 experiment as a target and intends to detect any dark matter created in the dump.

Complementing these is the MAGIX setup, which uses high-resolution magnetic spectrometers and internal gas targets to study electron scattering. Alongside precise determinations of proton electromagnetic form factors, it serves as a highly sensitive probe for weakly coupled light particles in the dark sector, such as dark photons and ALPs. The schematics of the whole setup is shown in Figs. 4.1 and 4.2.

MAGIX will ultimately operate at the energy-recovering mode with a windowless gas-jet target to achieve the highest luminosities and minimize window-induced background. However, initial operations will utilize a conventional solid fixed target in extracted beam mode. For the BSM search program, a ^{181}Ta target is planned; its large atomic number $Z = 73$ enhances the production cross section for processes scaling with Z^2, maximizing the expected signal yield. In the first phase, the beam energy is foreseen to be 55 MeV and will later be increased to 105 MeV.

The spectrometers of the MAGIX experiment setup are mounted on rotatable platforms and can be positioned independently around the common interaction point located at the center of the scattering chamber. The spectrometer STAR is installed on the right-hand side of the beam pipe, which direction is understood as 0°, while PORT is located symmetrically on the left-hand side.

The central acceptance of STAR is designed to cover scattering angles from −45° to 165°. PORT provides angular coverage from −15° to −165°. Since both spectrometers are mounted on platforms, the geometry imposes the minimal achievable angular sepa-

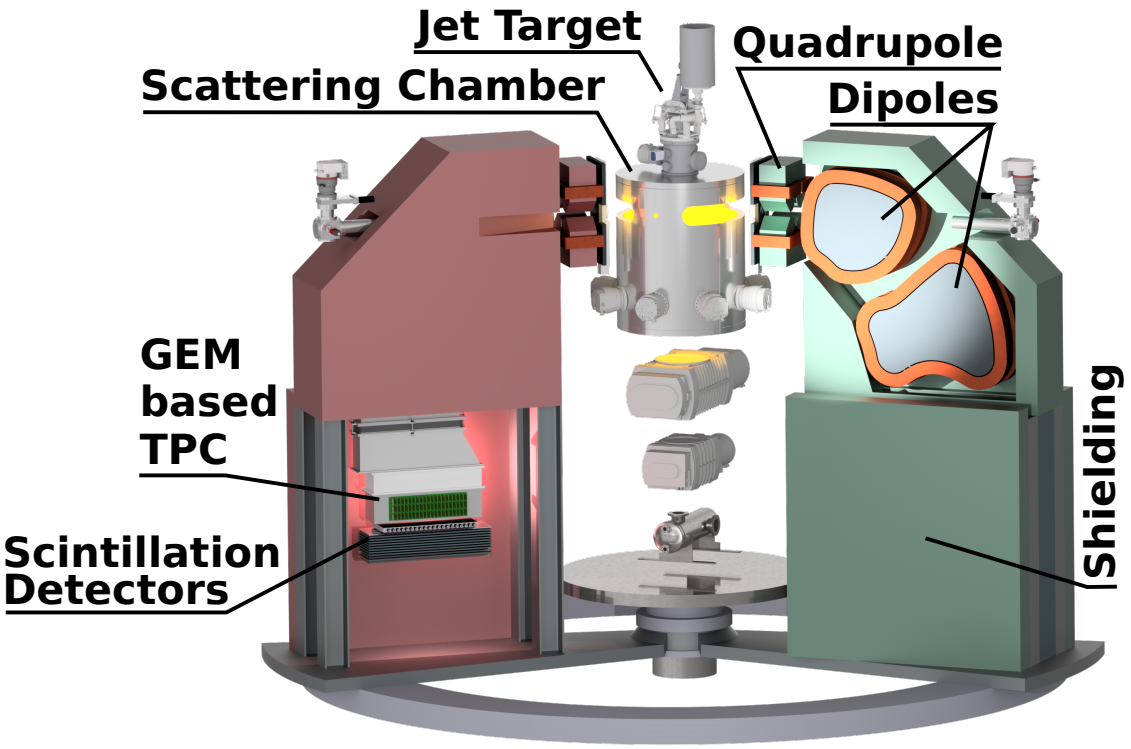

Figure 4.2: Overview of the MAGIX apparatus.

ration between STAR and PORT to be 47°. Their half-opening angles in both the polar and azimuthal directions are planned to be 2.75° degrees.

4.2 Bethe–Heitler process as a probe of New Physics

BSM searches based on the Bethe–Heitler process in fixed-target experiments have previously been discussed in the context of dark photon searches at the Mainz Microtron [114]. The maximum beam energy of 855, MeV allowed sensitivity to dark photon masses in the range $50\,\text{MeV} \lesssim m'_A \lesssim 300\,\text{MeV}$ and to kinetic mixing parameters down to $\varepsilon \sim 10^{-3}$, resulting at the time in one of the most stringent constraints on the kinetic mixing of a light vector mediator.

The relevant background contributions to such searches consist of timelike and spacelike Bethe–Heitler amplitudes, which are illustrated in Fig. 4.3. There, k (k') denotes the incoming (scattered) beam electron and $l_\pm$ the produced lepton pair. Off-target radiation is suppressed due to the large nuclear mass.

A key property of this process is that, in the presence of two indistinguishable fermions in the final state, the total amplitude must be antisymmetrized under their exchange. The full matrix element therefore takes the form

$$\mathcal{M}^{\text{total}} = \mathcal{M}\left(k', l_-\right) - \mathcal{M}\left(l_-, k'\right), \tag{4.1}$$

reflecting Fermi–Dirac statistics. This antisymmetrization is not required in processes such as muon-pair production, where the final-state particles are distinguishable.

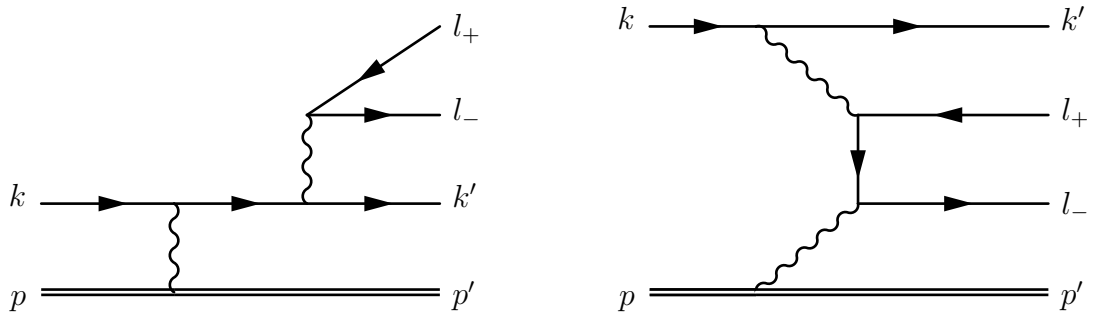

Figure 4.3: QED contribution to the Bethe-Heitler pair production, timelike (left) and spacelike (right). Graphs which are obtained by crossing are not shown, but are evaluated too.

The BSM contribution arises when one of the photons in the corresponding diagram is replaced by the mediator particle. Given the narrow decay width of such a mediator and the assumption of absent coupling to nucleons, the only relevant contribution originates from timelike production.

In the following, we discuss this framework in the context of the MAGIX experiment at MESA. The signal over background ratio is estimated, and the projected sensitivity reach is derived for scalar, pseudoscalar, vector, and axial vector mediators, demonstrating the versatility of this search strategy.

4.2.1 QED background

We consider the QED process of electron–positron pair production in the external electromagnetic field of a heavy nucleus. In the domain of interest, it can be treated as infinitely heavy and therefore stationary. Under this assumption, the target acts as a static source of the external field and absorbs only spatial momentum, while no energy is transferred.

The four-momentum conservation can thus be written as

$$k + \Delta = k' + l_+ + l_-. \tag{4.2}$$

Since no energy transfer occurs to the target, the condition $\Delta_0 = 0$ is imposed. Consequently, the momentum transfer is purely spatial.

In the external-field approximation, the nuclear electromagnetic field is described by the static Coulomb potential in momentum space

$$A_\mu^N = \left(-\frac{ZeF\left(Q_t^2\right)}{\Delta^2}, 0, 0, 0 \right), \tag{4.3}$$

where $F\left(Q_t^2\right)$ is the nuclear form factor accounting for the finite spatial charge distribution, and we denoted $Q_t^2 \equiv -\Delta^2$. We also adopt the standard parameterization

$$F\left(Q_t^2\right) = \frac{3}{\left(Q_t R_N\right)^3} \left[\sin\left(Q_t R_N\right) - \left(Q_t R_N\right)\cos\left(Q_t R_N\right)\right] e^{-s^2 Q_t^2/2}, \tag{4.4}$$

which corresponds to a hard-sphere charge distribution of radius $R_N = 1.21 A^{1/3}\,\mathrm{fm}$, supplemented by a Gaussian surface smearing characterized by $s = 0.9\,\mathrm{fm}$.

For later convenience, we also introduce the auxiliary momentum variables

$$q = k - k', \tag{4.5}$$
$$q' = l_+ + l_-. \tag{4.6}$$

The timelike amplitude (including both direct and crossed diagrams) can then be written in factorized form as

$$\mathcal{M}_{\mathrm{TL}} = e^4 \frac{A_\mu^N I_{\mathrm{TL}}^{\mu\alpha} j_\alpha^{\mathrm{pair}}}{\Delta^2} \frac{1}{q'^2}, \tag{4.7}$$

where the leptonic tensor and the pair current are defined as

$$I_{\mathrm{TL}}^{\mu\alpha} = \bar{u}(k') \left(\gamma^\mu \frac{\not{k} - \not{q}' + m_e}{(k-q')^2 - m_e^2} \gamma^\alpha + \gamma^\alpha \frac{\not{k}' + \not{q}' + m_e}{(k'+q')^2 - m_e^2} \gamma^\mu \right) u(k), \tag{4.8}$$
$$j_\alpha^{\mathrm{pair}} = \bar{u}(l_-) \gamma_\alpha v(l_+). \tag{4.9}$$

Meanwhile, the spacelike amplitude has a structure

$$\mathcal{M}_{\mathrm{SL}} = e^4 \frac{A_\mu^N I_{\mathrm{SL}}^{\mu\alpha} j_\alpha^{\mathrm{beam}}}{\Delta^2} \frac{1}{q^2}. \tag{4.10}$$

Analogously to the timelike case, we parameterize via the tensor I_{SL} and the beam current j^{beam}. Explicitly

$$I_{\mathrm{SL}}^{\mu\alpha} = \bar{u}(l_-) \left(\gamma^\mu \frac{\not{q} - \not{l}_+ + m_\ell}{(q-l_+)^2 - m_\ell^2} \gamma^\alpha + \gamma^\alpha \frac{\not{l}_- - \not{q} + m_\ell}{(l_- - q)^2 - m_\ell^2} \gamma^\mu \right) v(l_+), \tag{4.11}$$
$$j_\alpha^{\mathrm{beam}} = \bar{u}(k') \gamma_\alpha u(k). \tag{4.12}$$

Since we consider electron–positron pair production, $\ell = e$, these amplitudes must be antisymmetrized, as indicated in Eq. (4.1), to satisfy the Pauli exclusion principle.

Further details on the integration over the final-state phase space, the kinematical setup, and the signal optimization are provided in Appendix 4A, while we now turn to the BSM mediator contributions to this process.

4.2.2 BSM contributions to the cross section

Next, we examine the BSM contributions, considering generic scalar, pseudoscalar, vector, and axial vector mediators. The corresponding interaction Lagrangian terms are given by

$$\mathcal{L}_S = -g\, s\, \bar{\ell}\ell, \tag{4.13a}$$
$$\mathcal{L}_P = -g\, a\, \bar{\ell}\gamma^5\ell, \tag{4.13b}$$
$$\mathcal{L}_V = -e\, \epsilon\, \bar{\ell} \not{V} \ell, \tag{4.13c}$$
$$\mathcal{L}_A = -e\, \epsilon\, \bar{\ell}\gamma^5 \not{A} \ell, \tag{4.13d}$$

where s (a) is a scalar (pseudoscalar) field coupled to SM leptons with strength g, and V^μ (A^μ) denote the vector (axial vector) mediator fields respectively, with ϵ originating from the kinetic mixing.

Given the extremely small decay width, it is reasonable to apply the narrow width approximation, analogous to the approach used for the $e^+e^- \to \gamma\gamma\gamma$ process, see Eq. (2.60). In such a case, however, only the timelike diagram contributes, as it alone yields the delta function responsible for a distinct resonance bump in the electron-positron pair spectrum. The effect of final-state antisymmetrization is also washed out then for the same reason, as well as the interference with QED process.

As for the matrix element, it is sufficient to replace

$$\begin{aligned} \text{scalar:} &\quad \gamma_\alpha \to 1, && \text{(4.14a)}\\ \text{pseudoscalar:} &\quad \gamma_\alpha \to \gamma^5, && \text{(4.14b)}\\ \text{vector:} &\quad \text{vertex does not change}, && \text{(4.14c)}\\ \text{pseudovector:} &\quad \gamma_\alpha \to \gamma_\alpha\gamma^5. && \text{(4.14d)} \end{aligned}$$

The coupling e^2 is replaced by g^2 for the scalar and pseudoscalar, and by $e^2\epsilon^2$ for the vector and axial vector. The photon propagator must also be replaced with the respective BSM particle propagator, incorporating the correct numerator, mass and decay width. For the latter we assume 100% branching ratio into electron-positron pairs.

The scalar and pseudoscalar decay widths are provided in Eqs. (2.70) and (2.29), respectively. For the vector and axial vector mediators, these are given by

$$\Gamma_X = \frac{|\mathcal{M}_{\text{decay}}|^2}{8\pi m_X^2}\sqrt{\frac{m_X^2}{4} - m_\ell^2}, \tag{4.15}$$

where the squared matrix elements are evaluated as

$$|\mathcal{M}_{\text{decay}}|^2 = e^2\epsilon^2 \times \begin{cases} \frac{4}{3}\left(m_X^2 + 2m_\ell^2\right), & \text{vector},\\ \frac{4}{3}\left(m_X^2 - 4m_\ell^2\right), & \text{pseudovector}. \end{cases} \tag{4.16}$$

Finally, we address the assumptions regarding the BSM mediator decay modes. In the kinematic region of interest, the only accessible final states are e^+e^- and $\gamma\gamma$ pairs. While the Landau-Yang theorem forbids massive spin-1 particles from decaying into two photons, this channel remains open for scalars and pseudoscalars. However, the corresponding decay width scales as m_X^3, in contrast to the leptonic channel, which scales linearly with m_X, as seen from Eqs. (2.23), (2.29) and (2.70). In the relatively low-mass range studied here, the diphoton mode is therefore strongly suppressed. Under the assumption of exclusively visible decays, neglecting this contribution is well justified.

If invisible decay channels are present—e.g., into dark matter states—the signal yield is reduced. Nevertheless, the proposed framework remains fully applicable in such scenarios; however, because a larger total width Γ_X suppresses the visible signal, the resulting constraints must be reinterpreted as bounds on the effective coupling scaled by the branching ratio, rather than on the electron coupling alone, provided that Γ_X remains below the experimental invariant mass resolution.

Setup	PORT	STAR
I	$-45°$	$15°$
II	$-30°$	$30°$

Table 4.1: Benchmark setups for the MAGIX@MESA experiment.

4.3 Sensitivity projections for BSM scenarios

To perform the phase space integration for both the QED background and the BSM signals, we utilized a C++ code employing the VEGAS algorithm. The integration was performed over e^+e^- invariant mass bins of 0.5 MeV width, followed by a systematic bin-by-bin scan for the BSM signal.

As noted previously in the context of the $e^+e^- \to \gamma\gamma\gamma$ analysis, the biggest problem of the beam dump search strategy is its *inefficiency*. Indeed, as seen from Eq. (2.67), the reach for the BSM coupling scales as $L^{-1/4}$. Consequently, without a tailored optimization strategy, achieving a twofold improvement in coupling sensitivity requires a sixteen-fold increase in the collected dataset.

For the vector and axial vector contributions, the timelike QED diagram depicted in Fig. 4.3 constitutes an irreducible background, as it exhibits an identical angular distribution to the signal. It is therefore advantageous to maximize the overall event rate. Although this approach increases both the signal and background yields, the sensitivity reach scales with $\sqrt{\sigma_{\text{QED}}}$; thus, the overall statistical significance of the signal ultimately improves.

To achieve this goal, the STAR spectrometer is positioned at an angle of $15°$ relative to the beam axis, while the PORT spectrometer is located at $-45°$ (where the negative sign indicates an azimuthal angle of $\phi = 180°$ in spherical coordinates). By detecting the electron in PORT and the positron in STAR, this asymmetric configuration avoids the beam-induced pollution, while still benefiting from the forward enhancement of the cross section. This choice will be referred to as Setup I.

An alternative is to place the spectrometers symmetrically at $30°$ and $-30°$. This configuration, denoted as Setup II, yields constraints of comparable strength and is slightly more sensitive to higher-mass mediators. A summary of the corresponding parameters is provided in Table 4.1 for both setups.

Instantaneous luminosity of MESA is expected to be up to $10^{35}\,\text{cm}^{-2}\text{s}^{-1}$, so that 1 day of operation results in $\approx 8.64 \times 10^3\,\text{pb}^{-1}$ of integrated luminosity L. Unless specified, two weeks of continuous operation are assumed for all bounds.

Figs. 4.4 and 4.5 illustrate the projected sensitivity reach for scalar/pseudoscalar and vector/axial vector mediators, respectively, at beam energies of 55 and 105 MeV, together with existing bounds from $(g-2)_e$ measurements [111, 125] and visible decay constraints on dark photons from A1@MAMI [114], BaBar [115], NA48/2 studies of the π^0 decays [116], and the NA64 analyses [134].

The NA64 bound was also translated to the scalar case. Additionally, we incorporate projections for the Mu3e experiment based on the $\mu^+ \to e^+\bar{\nu}_\mu\nu_e X$ decay, assuming 2.5×10^{15} and 5.5×10^{16} produced μ^+, respectively (labeled as I and II), adapted from [135]. We further reproduced limits from the SINDRUM experiment [136], which

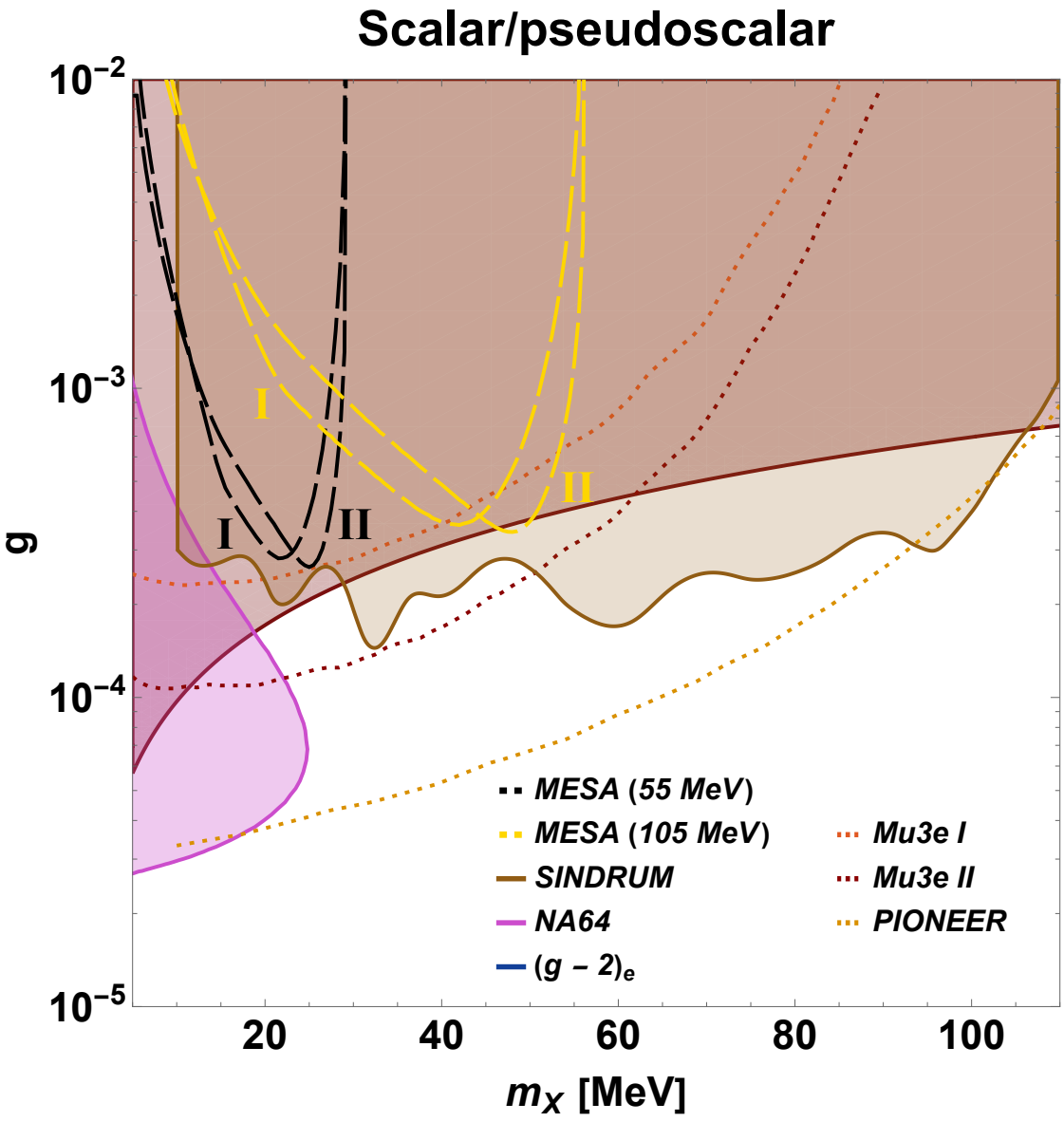

Figure 4.4: Constraints on the allowed BSM parameter space from $(g-2)_e$ for the scalar and pseudoscalar scenario, together with the projected sensitivity of a future MAGIX@MESA experiment for the two benchmark configurations, I and II, see Table 4.1. Results are shown for beam energies of 55 MeV and 105 MeV, with the projected sensitivities indicated by dashed lines. A single $(g-2)_e$ bound for scalar and pseudoscalar is shown, as the difference between them is negligible (see Fig. 3.4). Other near-future experiments are shown as dotted lines.

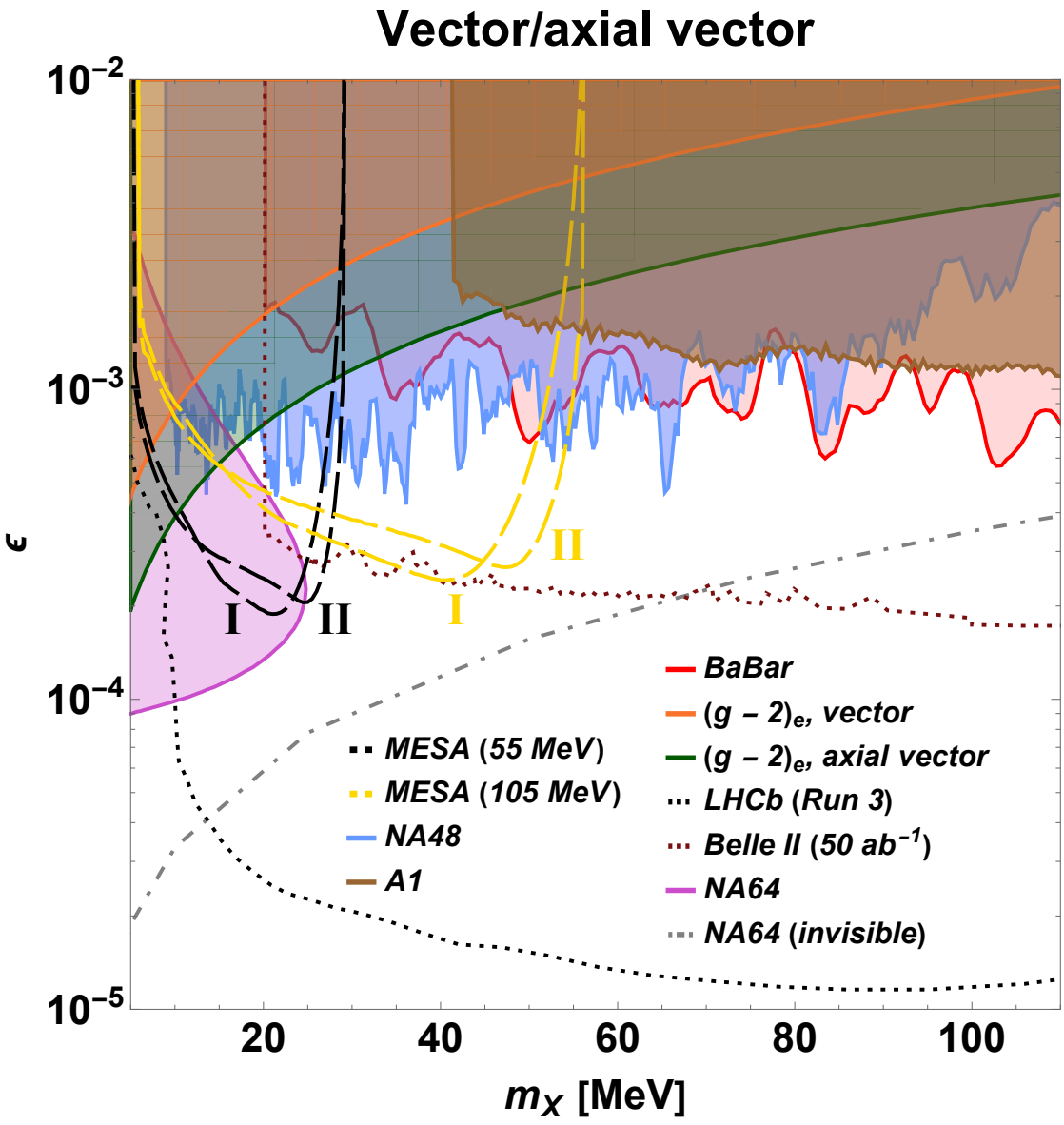

Figure 4.5: Constraints on the allowed BSM parameter space from $(g-2)_e$ and from existing experiments looking for visible e^+e^- decay, for the vector and axial vector scenarios, together with the projected sensitivity of MAGIX@MESA experiment for the two benchmark configurations, I and II, see Table 4.1. Results are shown for beam energies of 55 MeV and 105 MeV, with the projected sensitivities indicated by dashed lines. Other near-future experiments are shown as dotted lines. The gray dot-dashed curve indicating limits from NA64 searches for invisibly decaying mediators is also shown for comparison.

searched for the $\pi^+ \to e^+\nu X$ process, alongside the projected sensitivity of PIONEER, which aims to improve the branching ratio limit on this decay to $\mathcal{O}(10^{-11})$. In both aforementioned processes, the scalar X is emitted from the final-state positron and subsequently decays as $X \to e^+e^-$.

In all cases, parity effects were found to be negligible, as they contribute only at order $\mathcal{O}(m_e^2/s)$. The energy selection threshold $R_{\min}$ was set as 5 MeV (although this quantity has yet to be measured once the beam is available).

We note that while the $(g-2)_e$ constraints in the scalar and pseudoscalar scenarios may seem stronger than those projected for MAGIX@MESA, they are subject to potential Barr–Zee correction, as explained in Sec. 3.3. These contributions can be significantly enhanced by the mediator-to-electron mass ratio, as follows from Eqs. (3.30) and (3.45) (even though the explicit prefactor of m_e suggests suppression, the polynomial structure can compensate for this factor and yield numerically large effects). In contrast, MAGIX@MESA provides a direct probe of the electron coupling, while branching ratio effects induced by photon couplings are negligible, as discussed above. We also emphasize that it represents one of the few experiments in this domain that is sensitive to electron–axion and electron–scalar couplings without relying on lepton universality or other similar assumptions.

We also emphasize that while recent missing-energy searches at NA64 [137] have placed severe constraints on the parameter space of vector mediators decaying invisibly into dark sector states, these bounds are inherently model-dependent. The NA64 invisible limit in Fig. 5.6 (gray dot-dashed line) assumes a dark coupling $\alpha_D = 0.1$ and dark fermion masses $m_\chi = m'_A/3$. These constraints do not apply to the minimal scenario considered in this work, where the mediator decays with a 100% branching ratio into visible e^+e^- pairs; however, they show the complementarity of the two search strategies.

4.4 Results and discussion

The presented constraints were derived employing the bin width of 0.5 MeV, the energy selection of $S_{\text{sum}} = 0.9$, and the effective data-taking period of two weeks. In addition, the configuration was optimized for dark photon searches; a dedicated optimization for scalar mediator production would be expected to yield additional sensitivity gains.

Even within this conservative setup, sensitivity to BSM couplings as small as $\mathcal{O}(10^{-4})$ is demonstrated. Further improvements could be achieved through an extended search program with increased integrated luminosity and advancing the energy and invariant mass resolution of the detected e^+e^- pairs.

Finally, the results presented here correspond to the conventional heavy-target configuration of MAGIX@MESA, while its full physics potential will be realized only after the implementation of the energy-recovery mode with gas-jet target. A detailed sensitivity study of this upgraded configuration would be highly valuable, but is left for future work.

Appendix 4A: Phase space integration

In this Appendix, we provide the technical details on the phase space integration, as well as the setup and optimization of the MAGIX@MESA experiment.

We begin by introducing an appropriate parameterization of the cross section. In the limit of an infinitely heavy nucleus, the differential cross section reduces to the expression [112]

$$\begin{aligned} d\sigma &= 2\pi\delta\left(E_i - E_f\right)\frac{|\mathcal{M}|^2}{2\,|\mathbf{k}|}\frac{d^3k'}{(2\pi)^3\,2E'}\frac{d^3l_+}{(2\pi)^3\,2E_+}\frac{d^3l_-}{(2\pi)^3\,2E_-} \\ &= \frac{1}{16}\frac{|\mathcal{M}|^2}{(2\pi)^8}\frac{|\mathbf{k}'|\,|\mathbf{l}_+|\,|\mathbf{l}_-|}{|\mathbf{k}|}dE_+dE_-d\Omega'd\Omega_+d\Omega_-, \end{aligned} \tag{4.17}$$

where the delta function was used to eliminate the integration over $E' = E - E_+ - E_-$ and an identity

$$|\mathbf{p}|\,d\,|\mathbf{p}| = EdE, \tag{4.18}$$

was used multiple times.

After the basic transformations are performed, it is very reasonable to parameterize the solid angles of final leptons as

$$d\Omega_+d\Omega_- = d\Omega_+d\Omega_{\ell\ell}, \tag{4.19}$$

where $\Omega_{\ell\ell}$ denotes the relative angle between l_+ and l_-.

The next step is to trade the polar angle θ_+ for the invariant mass of the lepton pair, $s_{\ell\ell}$. Using the standard relation between the relative angle and the pair invariant mass, we transform the angular measure as

$$d\Omega_+ = d\cos\theta_+d\phi_+ = \frac{ds_{\ell\ell}}{2|\mathbf{l}_+||\mathbf{l}_-|}d\phi_{\ell\ell}, \tag{4.20}$$

Substituting this into the phase space measure, we obtain

$$d\sigma = \frac{1}{32}\frac{|\mathcal{M}|^2}{(2\pi)^8}\frac{|\mathbf{k}'|}{|\mathbf{k}|}dE_+dE_-d\Omega'd\Omega_-d\phi_{\ell\ell}ds_{\ell\ell}. \tag{4.21}$$

Finally, two additional symmetry factors must be included. First, averaging over the helicity states of the initial electron introduces a factor of 1/2. Second, because the two final-state leptons are identical and the amplitude is antisymmetrized with respect to their exchange, an additional combinatorial factor of 1/2 is required. Together, these factors modify the overall normalization of the cross section to 1/128.

4.4.1 Lab frame parameterization

We adopt a standard right-handed laboratory coordinate frame. The incident beam is aligned with the z-axis, the y-axis points vertically toward the ceiling, and the x-axis

lies horizontally parallel to the floor (see Fig. 4.2). Consequently, the STAR and PORT spectrometers are positioned in the horizontal xz-plane.

The 3-momenta of the initial beam, the emitted electron, and the recoil electron are parameterized using standard spherical coordinates

$$\mathbf{k} = \begin{pmatrix} 0 \\ 0 \\ \sqrt{E_k^2 - m_e^2} \end{pmatrix}, \quad \mathbf{l}_- = |\mathbf{l}_-| \begin{pmatrix} \sin\theta_- \cos\phi_- \\ \sin\theta_- \sin\phi_- \\ \cos\theta_- \end{pmatrix}, \quad \mathbf{k}' = |\mathbf{k}'| \begin{pmatrix} \sin\theta' \cos\phi' \\ \sin\theta' \sin\phi' \\ \cos\theta' \end{pmatrix}. \tag{4.22}$$

Since the integration variables are transformed to the pair invariant mass $s_{\ell\ell}$, the positron's 3-momentum $\mathbf{l}_+$ is most naturally parameterized relative to the emitted electron. To achieve this, we construct a local orthonormal basis $(\mathbf{u}_x, \mathbf{u}_y, \mathbf{u}_z)$ directly aligned with $\mathbf{l}_-$.

First, we define the local longitudinal axis to point along the electron's direction

$$\mathbf{u}_z = \frac{\mathbf{l}_-}{|\mathbf{l}_-|}. \tag{4.23}$$

Next, we define the local y-axis to be perpendicular to the plane spanned by the electron and the incident beam (the global laboratory $\hat{\mathbf{z}}$ direction)

$$\mathbf{u}_y = \frac{\mathbf{k} \times \mathbf{u}_z}{|\mathbf{k} \times \mathbf{u}_z|}. \tag{4.24}$$

We complete the right-handed triad by defining the local x-axis

$$\mathbf{u}_x = \mathbf{u}_y \times \mathbf{u}_z. \tag{4.25}$$

With this local basis established, the positron 3-vector is constructed by rotating it away from the electron axis by the pair opening angle $\theta_{\ell\ell}$ and the pair azimuthal angle $\phi_{\ell\ell}$

$$\mathbf{l}_+ = |\mathbf{l}_+| \left(\sin\theta_{\ell\ell}\cos\phi_{\ell\ell}\,\mathbf{u}_x + \sin\theta_{\ell\ell}\sin\phi_{\ell\ell}\,\mathbf{u}_y + \cos\theta_{\ell\ell}\,\mathbf{u}_z\right). \tag{4.26}$$

So that the angle $\theta_{\ell\ell}$ can be expressed as

$$\theta_{\ell\ell} = \frac{2m_{\ell\ell}^2 + 2E_+E_- - s_{\ell\ell}}{2\,|\mathbf{l}_+|\,|\mathbf{l}_-|}. \tag{4.27}$$

The remaining step is to understand the integration limits. Obviously, the maximum energy the pair can achieve is

$$E_{\max} = (E - E')_{\max} = \begin{cases} E - m_e, & \text{beam electron lost,} \\ E - R_{\min}, & \text{beam electron resolved,} \end{cases} \tag{4.28}$$

which depends on the experimental reconstruction scenario—i.e., whether the recoil beam electron is reconstructed or not—with $R_{\min}$ being the minimum energy threshold imposed by the detector.

The phase space integration is therefore performed within limits

$$\int_{m_e}^{E_{\max}} dE_+ \int_{m_e}^{E_{\max}-E_+} dE_- \int_{-1}^{1} d\cos\theta' \int_0^{2\pi} d\phi' \int_{-1}^{1} d\cos\theta_- \int_0^{2\pi} d\phi_- \\ \times \int_0^{2\pi} d\phi_{\ell\ell} \int_{4m_e^2}^{E_{\max}^2} \frac{d\sigma}{dE_+ dE_- d\Omega' d\Omega_- d\phi_{\ell\ell} ds_{\ell\ell}} \times \Theta\left[\text{kinematical cuts}\right] ds_{\ell\ell}, \tag{4.29}$$

where the Heaviside function Θ enforces the kinematical cuts corresponding to the experimental setup. In particular, the polar and azimuthal angles of the produced positron

$$\theta_+ = \arccos\left(\frac{l_{+,z}}{|\mathbf{l}_+|}\right), \tag{4.30}$$

$$\phi_+ = \arctan\left(\frac{l_{+,y}}{l_{+,x}}\right), \tag{4.31}$$

are required to lie within the spectrometer acceptance. Such an implementation via the Heaviside function, although seemingly trivial, allows one to optimize the Monte Carlo integration procedure, which would otherwise require cumbersome transformations to calculate the lab frame integration limits directly.

If advantageous in terms of signal over background optimization, an additional restriction to a finite energy window

$$E_\pm \in \left[R_{\min}, R_{\max}\right], \tag{4.32}$$

$$E_+ + E_- > S_{\text{sum}} \times E_{\text{beam}}, \quad S_{\text{sum}} \in (0,1)\,. \tag{4.33}$$

may also be imposed.

Since most background counts originate from near-forward kinematics, where the initial electron scatters along the beam axis, escaping detection, it is considered lost, while the produced pair is assumed to be resolved within the spectrometers.

Chapter 5

BSM probes via polarization-sensitive observables

Measure what is measurable, and
make measurable what is not so.
Galileo Galilei

Polarized beams play a central role in the experimental programs of next generation lepton accelerators [138–140]. So far the measurements of polarization observables in the electron scattering off the nucleon appeared to be extremely enriching: they have revealed the unexpected magnitude and behavior of the proton's electric form factor at high momentum transfer rates [141, 142], opened the investigation of the 3-dimensional partonic structure of nucleons and nuclei via the generalized parton distributions [143–148] and allowed to achieve the smallest polarized beam asymmetries ever measured (a few $\times 10^{-7}$) [149].

Polarized positron beams, in particular the JLab polarized positron program, will extend these capabilities even further (see [139, 140] and links therein). In particular, relatively large interference effects are predicted for the $e^+ + N \to e^+ + N + \gamma$ process, opening the way to constrain Generalized Parton Distributions with potentially unprecedented precision. Polarized positrons are also invaluable for studying two-photon exchange contributions and related problems, as the interference with the dominant one-photon amplitude can reach the percent level in certain kinematics. On top of that, polarized lepton beams will provide the ability to test New Physics effects via a precise measurement of the electroweak coupling parameters, the investigation of charged lepton flavor violation, and the search for new particles linked to dark matter.

The present chapter focuses on this latter direction. The uniqueness of the JLab positron project results from a high intensity positron beam with high degree of polarization. Upon interacting with electrons in a fixed target, this allows access to polarization-sensitive observables of the Bhabha scattering $e^+e^- \to e^+e^-$, in particular the beam normal spin asymmetry, which is proportional to an absorptive (imaginary) part of the scattering amplitude. The 11 GeV beam at JLab will allow access to the Bhabha process up to center-of-momentum energies $\sqrt{s} \simeq 106$ MeV. Being below any hadron production threshold this process is theoretically very clean as it cannot get contributions from any hadronic absorptive part. Moreover, the leading QED contribution to this asymmetry vanishes at a fixed scattering angle, yielding a kinematic point with strongly reduced SM background for BSM searches. Since QED interactions at energies much larger than the electron mass are helicity-conserving, particularly strong bounds can be derived for dark sector mediators which induce a lepton helicity flip, such as scalars. Furthermore, our findings show that the projected dark photon search range

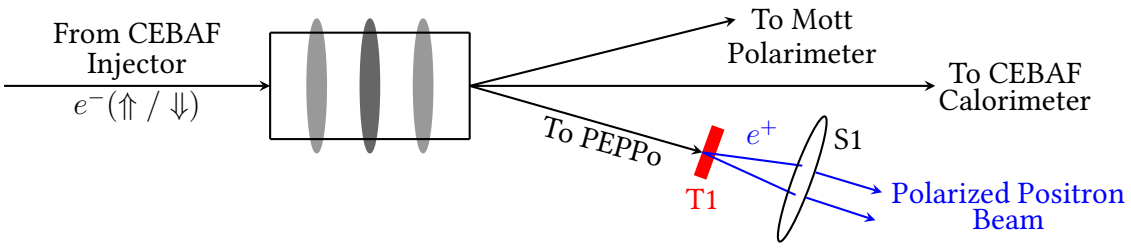

Figure 5.1: Schematic of the PEPPo line and apparatus illustrating the principle of operation of the experiment.

can also be extended significantly beyond the existing limits, demonstrating the complementarity and broad potential of e^+e^- polarization observables in light messenger particle searches.

This section is based on the results of the work [150], which was presented (with preliminary results) at the EINN 2025 conference as part of the parallel session and at the LEEPP workshop at JLab.

5.1 Polarized positrons at Jefferson Lab

JLab has initiated a program to produce and utilize high-quality polarized positron beams, with the goal of enabling precision studies of electromagnetic and weak interactions, as well as searches for BSM physics. Unlike conventional electron beams, producing polarized positrons requires a dedicated generation scheme that preserves both spin orientation and sufficient intensity for experimental applications.

The polarized positron beam at JLab is produced via a two-step process. First, a high-intensity polarized electron beam from the Continuous Electron Beam Accelerator Facility (CEBAF) is directed onto a thin high-Z target, typically tungsten, generating bremsstrahlung photons. The polarization of the initial electron beam is transferred to the emitted photons through circular polarization. In the second step, these circularly polarized photons undergo pair production in a secondary target, producing electron–positron pairs. The spin polarization is thus transferred from the initial electron to the outgoing positron giving rise to the program name Polarized Electrons for Polarized Positrons (PEPPo). The whole setup is schematically shown in Fig. 5.1.

Optimizing the polarization and intensity of the positron beam requires careful consideration of target thickness, beam energy, and collimation, as well as mitigation of depolarizing effects during transport through the accelerator. Advanced simulations and test experiments at JLab have demonstrated that positron polarizations up to 75% are achievable, with intensities sufficient for high-precision measurements. By selecting appropriate photon and positron kinematics, a beam with significant longitudinal polarization can be extracted and accelerated up to 11 GeV for experimental use.

Beyond beam production, the JLab polarized positron program offers several key scientific advantages. It enables high-precision measurements of parity-violating asymmetries in elastic and inelastic scattering and provides complementary sensitivity to hadronic structure and electroweak couplings relative to polarized electron beams. On-

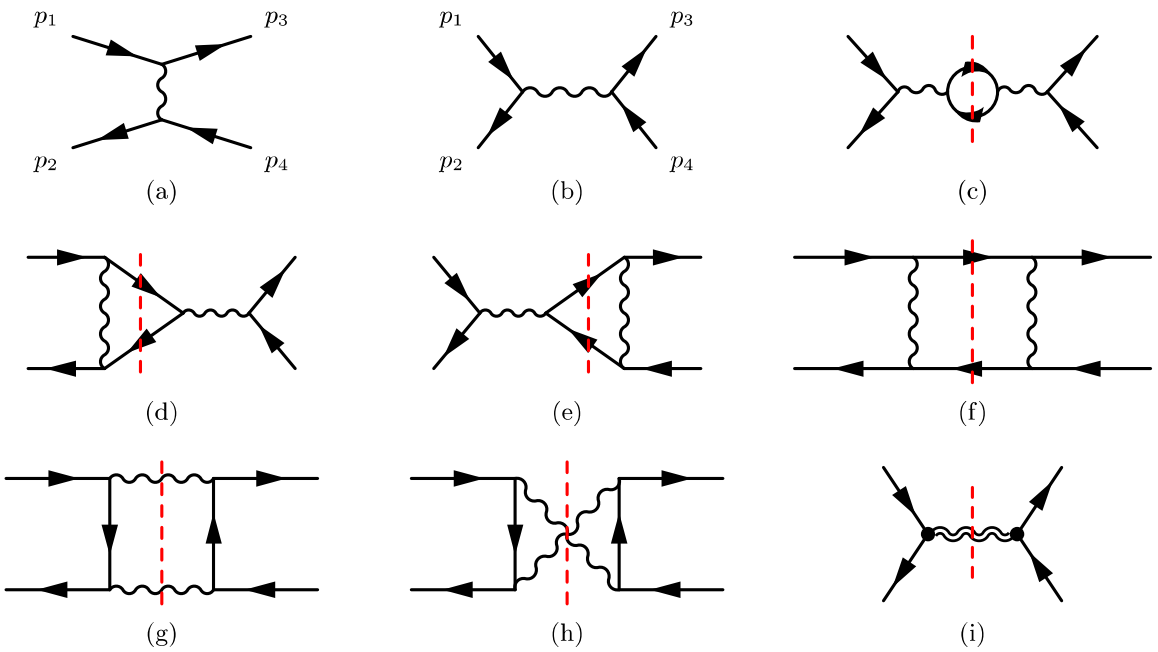

Figure 5.2: Feynman diagrams contributing to B_n at 1-loop order (a-h), and the BSM contribution (i). The red vertical line shows the physical-region cuts.

going development focuses on maximizing polarization and intensity while minimizing emittance and energy spread, ensuring seamless integration with existing accelerator infrastructure and experimental halls.

5.2 Single-spin asymmetry in Bhabha scattering

In this work, we consider the Bhabha scattering

$$e^-\left(p_1, s_1\right) + e^+\left(p_2, s_2\right) \to e^-\left(p_3, s_3\right) + e^+\left(p_4, s_4\right), \tag{5.1}$$

where p_1 and p_2 (p_3 and p_4) denote the initial (final) electron and positron four-momenta, and the s_i stand for the corresponding helicities.

The most general description of this process involves sixteen independent helicity amplitudes. However, imposing parity (P), time reversal (T), and charge conjugation (C) invariance reduces the number of independent amplitudes to five, which is illustrated in Table 5.1.

These five helicity amplitudes can be mapped onto five independent Dirac bilinears [151]. The proof, however, is nontrivial and requires a certain amount of algebra; it is therefore presented in Appendix 5A, where the necessary steps are shown in detail.

The choice of the five bilinears is, in addition, not unique. For the purpose of studying contributions from C-, P-, and T-conserving dark-sector mediators, it is convenient to parameterize the scattering amplitude, $\mathcal{M} = i\mathcal{T}$ in terms of the following covariant structures

$$\begin{aligned}\mathcal{T} = {} & S\,\bar{u}_3 u_1\,\bar{v}_2 v_4 + P\,\bar{u}_3\gamma^5 u_1\,\bar{v}_2\gamma^5 v_4 + V\,\bar{u}_3\gamma^\mu u_1\,\bar{v}_2\gamma_\mu v_4 \\ & + A\,\bar{u}_3\gamma^\mu\gamma^5 u_1\,\bar{v}_2\gamma_\mu\gamma^5 v_4 + T\,\bar{u}_3\sigma^{\mu\nu} u_1\,\bar{v}_2\sigma_{\mu\nu} v_4,\end{aligned} \tag{5.2}$$

Parity (P)	Time reversal (T)	Charge conjugation (C)
$\mathcal{M}_{\uparrow\uparrow\uparrow\uparrow} = \mathcal{M}_{\downarrow\downarrow\downarrow\downarrow}$		
$\mathcal{M}_{\downarrow\uparrow\uparrow\uparrow} = \mathcal{M}_{\uparrow\downarrow\downarrow\downarrow}$		$\mathcal{M}_{\downarrow\uparrow\uparrow\uparrow} = \mathcal{M}_{\uparrow\downarrow\uparrow\uparrow}$
$\mathcal{M}_{\uparrow\downarrow\uparrow\uparrow} = \mathcal{M}_{\downarrow\uparrow\downarrow\downarrow}$		
$\mathcal{M}_{\downarrow\downarrow\uparrow\uparrow} = \mathcal{M}_{\uparrow\uparrow\downarrow\downarrow}$		
$\mathcal{M}_{\uparrow\uparrow\downarrow\uparrow} = \mathcal{M}_{\downarrow\downarrow\uparrow\downarrow}$	$\mathcal{M}_{\uparrow\uparrow\downarrow\uparrow} = \mathcal{M}_{\downarrow\uparrow\uparrow\uparrow}$	
$\mathcal{M}_{\downarrow\uparrow\downarrow\uparrow} = \mathcal{M}_{\uparrow\downarrow\uparrow\downarrow}$		
$\mathcal{M}_{\uparrow\downarrow\downarrow\uparrow} = \mathcal{M}_{\downarrow\uparrow\uparrow\downarrow}$		
$\mathcal{M}_{\downarrow\downarrow\downarrow\uparrow} = \mathcal{M}_{\uparrow\uparrow\uparrow\downarrow}$	$\mathcal{M}_{\uparrow\uparrow\uparrow\downarrow} = \mathcal{M}_{\uparrow\downarrow\uparrow\uparrow}$	

Table 5.1: Relations among helicity amplitudes imposed by parity (P), time reversal (T), and charge conjugation (C) invariance for Bhabha scattering.

where the tensor structure is defined as

$$\sigma^{\mu\nu} = \frac{i}{2}\left(\gamma^\mu\gamma^\nu - \gamma^\nu\gamma^\mu\right). \tag{5.3}$$

Additional details concerning the Dirac algebra underlying this construction are provided in Appendix 5B.

In Eq. (5.2), the invariant amplitudes S, P, V, A, and T correspond to scalar, pseudoscalar, vector, axial vector, and tensor interactions, respectively. These amplitudes are functions of the Mandelstam variables, defined in the standard way as

$$s = (p_1 + p_2)^2, \quad t = (p_1 - p_3)^2, \quad u = (p_1 - p_4)^2. \tag{5.4}$$

The parameterization in Eq. (5.2) is arguably the most natural choice—particularly in the context of BSM searches. It is expressed in terms of the t-channel structures $\bar{u}_3\Gamma_i u_1\, \bar{v}_2\Gamma_i v_4$, while contributions originating from s-channel bilinears of the form $\bar{v}_2\Gamma_i u_1\, \bar{u}_3\Gamma_i v_4$ can be mapped onto the same basis via Fierz rearrangements

$$\bar{v}_2\Gamma_i u_1\, \bar{u}_3\Gamma_i v_4 = \sum_j C_{ij}\, \bar{u}_3\Gamma_j u_1\, \bar{v}_2\Gamma_j v_4, \tag{5.5}$$

where the respective coefficients are given in Table 5.2.

This choice of t-channel basis is appealing for two reasons. First, as shown in Appendix 5A, this representation allows for the most straightforward proof of completeness of the basis in Eq. (5.2). Second, in the kinematic regime relevant for the JLab measurement, the amplitude is dominated by t-channel exchange over a broad range of scattering angles.

We also emphasize that such a parameterization relies on C-symmetry and is therefore not applicable to processes such as lepton–proton scattering, see Table 5.1. A decomposition of the scattering amplitude in terms of Lorentz covariants is still possible; however, it generally requires a larger set of independent structures (six in the case of lepton–proton scattering) and cannot be expressed solely in terms of Dirac bilinears S, P, V, A and T.

$\times$	S	P	V	A	T
S	$1/4$	$1/4$	$1/4$	$-1/4$	$1/8$
P	$1/4$	$1/4$	$-1/4$	$1/4$	$1/8$
V	1	-1	$-1/2$	$-1/2$	0
A	-1	1	$-1/2$	$-1/2$	0
T	3	3	0	0	$-1/2$

Table 5.2: Fierz rearrangement coefficients C_{ij} for products of Dirac bilinears in the (S, P, V, A, T) basis.

Finally, we note that this decomposition implies that integration over the loop moment has already been performed. In fact, many "unwanted" terms vanish as a result of integration over the angular variables, but not at the level of the integrand itself.

We now consider the beam-normal single-spin asymmetry, which is given by the difference of the beam-polarized differential cross sections, $d\sigma_\uparrow$ and $d\sigma_\downarrow$, in the center-of-momentum frame as functions of the scattering angle θ

$$B_n = \frac{\frac{d\sigma_\uparrow}{d\cos\theta} - \frac{d\sigma_\downarrow}{d\cos\theta}}{\frac{d\sigma_\uparrow}{d\cos\theta} + \frac{d\sigma_\downarrow}{d\cos\theta}}. \tag{5.6}$$

At leading order, the denominator can be identified with the unpolarized tree-level cross section σ_0. For a polarized positron beam, the usual spin sum is replaced according to [112]

$$v\bar{v} = \frac{1}{2}\left(\not{p} - m_e\right)\left(1 - \gamma^5 \not{\mathcal{S}}\right), \tag{5.7}$$

where $\mathcal{S}^\mu$ denotes the particle polarization four-vector. It is quite evident that in parity-conserving theories, a single-spin asymmetry can only arise from the transverse component of this polarization. Indeed, the only true scalar that can be formed from the polarization $\mathcal{S}$, the initial (final) particle momentum p (p') is

$$B_n \propto \mathcal{S} \cdot (p \times p'), \tag{5.8}$$

which nullifies any spin component lying in the $p \times p'$ plane.

Next, the asymmetry can be computed directly from the polarized cross sections $\sigma_\uparrow$ and $\sigma_\downarrow$. In practice, however, the calculation is considerably simplified by employing the standard expression for the differential cross section

$$\frac{d\sigma}{d\cos\theta} = \frac{|\mathcal{M}|^2}{32\pi s}, \tag{5.9}$$

leading to

$$\begin{aligned} B_n = &-\frac{1}{128\pi s \sigma_0} \sum_i \sum_j c_i c_j^* \operatorname{Tr}\Big\{\left(\not{p}_3 + m_e\right)\Gamma_i\left(\not{p}_1 + m_e\right)\Gamma_j\Big\} \\ &\times \operatorname{Tr}\Big\{\gamma^5 \not{\mathcal{S}}\left(\not{p}_2 - m_e\right)\Gamma_i\left(\not{p}_4 - m_e\right)\Gamma_j\Big\}. \end{aligned} \tag{5.10}$$

This expression can now be combined with the decomposition (5.2), so that Γ_i stands for the Dirac bilinears and c_i are the corresponding numerical coefficients associated with the structures (S, P, V, A, T).

5.2.1 Basis construction

While the resulting traces can be evaluated in a straightforward way, it is convenient to first introduce a set of auxiliary four-vectors

$$P_- = \frac{p_1 + p_3}{2}, \qquad P_+ = \frac{p_2 + p_4}{2}, \tag{5.11a}$$

$$q = p_1 - p_3 = p_4 - p_2, \tag{5.11b}$$

$$n = P_- \times q \times P_+, \tag{5.11c}$$

where the triple product is expressed via the Levi–Civita tensor as

$$n_\mu = \varepsilon_{\mu\alpha\beta\gamma} P_-^\alpha q^\beta P_+^\gamma. \tag{5.12}$$

From these definitions it follows immediately that

$$(P_\pm q) = (P_\pm n) = (qn) = 0. \tag{5.13}$$

We can also introduce an auxiliary four-vector

$$P'_- = P_- - \frac{(P_- P_+)}{P_+^2} P_+, \tag{5.14}$$

so that the four-vectors P_+, P'_-, q, and n are mutually orthogonal (although not orthonormal).

It is evident that $P_\pm$ are timelike, which means there exists a rest frame for each of them. In such a reference frame, n_μ (as follows from the definition of the Levi-Civita tensor) possesses only a spatial component, meaning that it is spacelike.

Since the scalar product of P'_- and P_+ is zero, it follows that P'_- must also be spacelike. Finally, by definition, q is determined to be spacelike.

The set $\left(P_+, q, P'_-, n\right)$ may therefore be used as a basis to decompose the metric tensor

$$g^{\mu\nu} = \sum_{i=1}^{4} \frac{e_i^\mu e_i^\nu}{(e_i e_i)} = \frac{P_+^\mu P_+^\nu}{P_+^2} + \frac{q^\mu q^\nu}{q^2} + \frac{P'^\mu_- P'^\nu_-}{P'^2_-} + \frac{n^\mu n^\nu}{n^2}. \tag{5.15}$$

Alternatively, one may employ the set $(P_+ + P_-, P_+ - P_-, q, n)$.

It is imperative now to express the relevant scalar products in terms of the Mandelstam variables

$$q^2 = t, \tag{5.16a}$$
$$(P_- P_+) = \frac{s-u}{4}, \tag{5.16b}$$
$$P_\pm^2 = -\frac{t}{4} + m_e^2 = \frac{s+u}{4}, \tag{5.16c}$$
$$P_-'^2 = \frac{4m_e^2 - t}{4} - \frac{(s-u)^2}{4\left(4m_e^2 - t\right)} = \frac{su}{s+u}, \tag{5.16d}$$
$$n^2 = \frac{t}{16}\left[(s-u)^2 - \left(t - 4m_e^2\right)^2\right] = -\frac{stu}{4}. \tag{5.16e}$$

On top of that, we note that these quantities satisfy the identity

$$n^2 = -P_+^2\, q^2\, P_-'^2. \tag{5.17}$$

Next, using the momentum conservation

$$p_1 + p_2 = p_3 + p_4, \tag{5.18}$$

we can express the external momenta in terms of the basis vectors as

$$p_1 = P_- + \frac{q}{2}, \qquad p_2 = P_+ - \frac{q}{2}, \tag{5.19a}$$
$$p_3 = P_- - \frac{q}{2}, \qquad p_4 = P_+ + \frac{q}{2}. \tag{5.19b}$$

Finally, we recall the Dirac equation for on-shell spinors

$$\left(\not{p} - m_e\right) u\left(p\right) = 0, \qquad \bar{u}\left(p\right)\left(\not{p} - m_e\right) = 0, \tag{5.20a}$$
$$\left(\not{p} + m_e\right) v\left(p\right) = 0, \qquad \bar{v}\left(p\right)\left(\not{p} + m_e\right) = 0, \tag{5.20b}$$

which will be used multiple times in subsequent calculations.

5.2.2 Beam-normal asymmetry B_n

We now return to (5.10). Using the Dirac equation and the notation introduced in the previous section, we bring the full result as

$$\begin{aligned}&\mathrm{Tr}\Big\{\left(\not{p}_3 + m_e\right)\Gamma_i\left(\not{p}_1 + m_e\right)\Gamma_j\Big\} \times \mathrm{Tr}\Big\{\gamma^5 \not{\mathcal{S}}\left(\not{p}_2 - m_e\right)\Gamma_i\left(\not{p}_4 - m_e\right)\Gamma_j\Big\} \\ &= -32 i m_e\left(\mathcal{S} n\right) N_{ij},\end{aligned} \tag{5.21}$$

where the numerical coefficients N_{ij} are listed in Table 5.3. Most of these combinations vanish due to the properties of the γ^5 matrix. The calculations for the remaining cases, straightforward but rather lengthy, are collected in Appendix 5C.

N_{ij}	$\mathbb{1}$	γ^5	γ^μ	$\gamma^\mu\gamma^5$	$\sigma^{\mu\nu}$
$\mathbb{1}$	0	0	1	0	2
γ^5	0	0	0	0	0
γ^μ	-1	0	0	1	0
$\gamma^\mu\gamma^5$	0	0	-1	0	-2
$\sigma^{\mu\nu}$	-2	0	0	2	0

Table 5.3: Trace coefficients N_{ij} for combinations of Dirac bilinears, where i labels the row and j labels the column.

Since these coefficients are antisymmetric, $N_{ij} = -N_{ji}$, and the each contribution carries an explicit factor of i, the result can be expressed in terms of the imaginary parts of the coupling combinations

$$B_n = \frac{m_e\,(\mathcal{S}n)}{2\pi s\sigma_0}\,\mathrm{Im}\,\{S\,V^* + 2S\,T^* - AV^* - 2A\,T^*\}. \tag{5.22}$$

We can simplify it even further by introducing a normalized four-vector

$$\hat{n}^\mu = \frac{n^\mu}{\sqrt{(-n^2)}}, \tag{5.23}$$

so that the final result becomes

$$\boxed{B_n = \frac{m_e\sqrt{stu}}{4\pi s\sigma_0}\,(\mathcal{S}\hat{n})\,\mathrm{Im}\,\{(S-A)\,(V^* + 2T^*)\}.} \tag{5.24}$$

It only involves the decomposition coefficients S, V, A, T of the Bhabha scattering amplitude.

We also observe that in the center-of-momentum frame the four-vector $\hat{n}^\mu$ can be expressed as $\hat{n}^\mu = (0, \hat{\mathbf{n}})$, with $\hat{\mathbf{n}}$ being the unit three-vector normal to the scattering plane. One thus sees that the factor $(\mathcal{S}\hat{n})$ in Eq. (5.24) leads to a nonzero single spin asymmetry for a polarization normal to the scattering plane. In the following the asymmetry is shown using the sign convention

$$\mathcal{S}\hat{n} = +1. \tag{5.25}$$

Next, we note that the beam-normal spin asymmetry (5.24) requires the imaginary part of the amplitude to be nonzero. Furthermore, it has to be emphasized that an amplitude containing a pseudoscalar exchange—the P term in Eq. (5.2)—does not contribute to B_n.

In the following sections we will therefore discuss subsequently the QED contribution to B_n as well as the s-channel resonance excitation of a BSM dark sector messenger particle of different quantum numbers.

5.3 Imaginary parts of 1-loop QED correction to Bhabha scattering

The tree-level QED diagrams to the Bhabha process are shown in Figs. 5.2a and 5.2b. One easily obtains

$$\mathcal{M}_s = \frac{ie^2}{s}\,\bar{v}_2\gamma_\mu u_1\,\bar{u}_3\gamma^\mu v_4, \tag{5.26}$$

$$\mathcal{M}_t = -\frac{ie^2}{t}\,\bar{u}_3\gamma_\mu u_1\,\bar{v}_2\gamma^\mu v_4, \tag{5.27}$$

where an additional sign is required due to the Pauli principle. Projected on the basis of Eq. (5.2), they yield

$$V = -e^2\left(\frac{1}{t}+\frac{1}{2s}\right), \tag{5.28}$$

$$S = -P = -2A = \frac{e^2}{s}, \qquad T = 0. \tag{5.29}$$

As these amplitudes produce an imaginary part, B_n is zero at tree-level in QED. The leading nonvanishing contribution therefore arises from the interference between tree-level and 1-loop diagrams, which can be represented in the form

$$\begin{aligned}&\mathrm{Im}\left[(S-A)\,(V^*+2T^*)\right]\\ &= (V+2T)\,\mathrm{Im}\left[S-A\right] - (S-A)\,\mathrm{Im}\left[V+2T\right]\\ &\approx (V+2T)_{1\gamma}\,\mathrm{Im}\left[S-A\right]_{1-\mathrm{loop}} - (S-A)_{1\gamma}\,\mathrm{Im}\left[V+2T\right]_{1-\mathrm{loop}},\end{aligned} \tag{5.30}$$

where the subscript 1γ denotes the tree-level (one-photon exchange) contribution.

The most direct way to extract the expansion coefficients that enter B_n is to perform a dispersive calculation of the 1-loop corrections to Bhabha scattering. The relevant contributions are

- s-channel vacuum polarization with intermediate e^+e^- loop, Fig. 5.2c,
- s-channel vertex corrections on both the initial- and final-state lepton lines combined with the t-channel two-photon box diagrams, for which only the direct graph yields a nonzero imaginary part, Figs. 5.2d-f,
- s-channel direct and crossed two-photon box diagrams, Figs. 5.2g and 5.2h.

All other 1-loop diagrams have vanishing discontinuities and therefore do not contribute to B_n. The box diagrams are, of course, the most challenging ones. An additional complication arises from the projection onto the chosen Dirac basis of Eq. (5.2): the amplitude is not given *a priori* in this parameterization, and lengthy Dirac-algebra manipulations are required to cast the result into the desired form. Moreover, taking the limit $m_e^2/s \to 0$ from the start leads to incorrect results, since this procedure eliminates

terms contributing to the S, P, and T structures; the massless limit can only be taken after the projection has been carried out.

Furthermore, a number of cancellations happens among the individual contributions, as will be shown below. The vertex correction diagrams and t-channel box diagrams of Figs. 5.2d-f require an infrared regulator, which is removed when calculating their contribution to B_n, rendering it an infrared-safe observable. Furthermore, any logarithmic dependence on the electron mass cancels out in the final result.

5.3.1 Vacuum polarization

The 1-loop QED vacuum polarization diagram, shown in Fig. 5.2c, is, of course, the most trivial of the corrections we have to consider. It is well known [112] and can be written as

$$\mathcal{T}_{\text{V.P.}} = e^2 \frac{\Pi(s)}{s} \bar{v}_2 \gamma^\mu u_1 \, \bar{u}_3 \gamma_\mu v_4, \tag{5.31}$$

$$\text{Im}\left[\Pi(s)\right] = -\frac{\alpha}{6} \beta \left(3 - \beta^2\right) \Theta\left(s - 4m_e^2\right), \tag{5.32}$$

where $\beta = \sqrt{1 - 4m_e^2/s}$ is the lepton velocity in the center-of-momentum frame. Employing the Fierz identities, we obtain

$$(\text{Im}\, S)_{\text{V.P.}} = -\frac{e^2}{s}\frac{\alpha}{6}\beta\left(3 - \beta^2\right), \tag{5.33a}$$

$$(\text{Im}\, P)_{\text{V.P.}} = -\left(\text{Im}\, S\right)_{\text{V.P.}} = 2\left(\text{Im}\, V\right)_{\text{V.P.}} = 2\left(\text{Im}\, A\right)_{\text{V.P.}}, \tag{5.33b}$$

$$(\text{Im}\, T)_{\text{V.P.}} = 0. \tag{5.33c}$$

In the ultrarelativistic limit, $m_e^2 \ll s$, one simply replaces

$$\beta\left(3 - \beta^2\right) = 2 + \mathcal{O}\left(\frac{m_e^2}{s}\right), \tag{5.34}$$

in these expressions. The corresponding contribution to the beam-normal spin asymmetry takes the form

$$B_n^{\text{V.P.}} = -\frac{\alpha m_e}{\sqrt{s}} \frac{x^3\sqrt{1-x^2}}{\left(1 - x^2 + x^4\right)^2} + \mathcal{O}\left(\frac{m_e^2}{s}\right), \tag{5.35}$$

where the variable

$$x = \sin\left(\frac{\theta}{2}\right), \tag{5.36}$$

has been introduced, so that

$$t = -s\beta^2 x^2, \tag{5.37}$$

$$u = -s\beta^2\left(1 - x^2\right). \tag{5.38}$$

Finally, we observe that $B_n^{\text{V.P.}}$ is strictly negative, which is illustrated in Fig. 5.3 for a JLab center-of-momentum energy of $\sqrt{s} = 106\,\text{MeV}$.

5.3.2 Vertex correction

The vertex corrections shown in Figs. 5.2d and 5.2e cannot be individually projected separately onto the basis (5.2), as only *their sum* satisfies the required C-, P-, and T-symmetry constraints. The combined contribution is

$$\begin{aligned}\mathcal{T}_{\text{Vertex}} = \frac{e^2}{s}\Bigg[&\bar{v}_2\gamma^\mu u_1\,\bar{u}_3\left(F_1(s)\,\gamma_\mu + iF_2(s)\,\sigma_{\mu\nu}\frac{(p_3+p_4)^\nu}{2m_e}\right)v_4\\ &+\bar{v}_2\left(F_1(s)\,\gamma_\mu - iF_2(s)\,\sigma_{\mu\nu}\frac{(p_1+p_2)^\nu}{2m_e}\right)u_1\,\bar{u}_3\gamma^\mu v_4\Bigg],\end{aligned} \tag{5.39}$$

where the Dirac and Pauli form factors F_1 and F_2 have been introduced. Their imaginary parts are given by [112]

$$\begin{aligned}\operatorname{Im}\left[F_1(s)\right] &= \frac{\alpha}{4\sqrt{s\left(s-4m_e^2\right)}}\left[-3s+8m_e^2+2\left(s-2m_e^2\right)\ln\left(\frac{s-4m_e^2}{m_\gamma^2}\right)\right]\\ &\approx -\frac{\alpha}{2}\left[\frac{3}{2}+\ln\left(\frac{m_\gamma^2}{s}\right)\right]+\mathcal{O}\left(\frac{m_e^2}{s}\right),\end{aligned} \tag{5.40}$$

$$\operatorname{Im}\left[F_2(s)\right] = \frac{\alpha m_e^2}{\sqrt{s\left(s-4m_e^2\right)}} \approx \frac{\alpha m_e^2}{s}+\mathcal{O}\left(\frac{m_e^2}{s}\right), \tag{5.41}$$

where a fictitious photon mass m_γ has been enforced to regulate the infrared behaviour of F_1.

To cast the amplitude into the desired basis, we employ the Gordon identity

$$\bar{u}(p')\,\gamma^\mu u(p) = \bar{u}(p')\left[\frac{(p'+p)^\mu}{2m_\ell}+\frac{i\sigma^{\mu\nu}(p'-p)_\nu}{2m_\ell}\right]u(p), \tag{5.42}$$

together with the Dirac equation (5.20). In the case where u is replaced by v, the corresponding momentum simply changes sign. After some straightforward algebra, the vertex contribution reduces to

$$\begin{aligned}\mathcal{T}_{\text{Vertex}} = \frac{e^2}{s}\Bigg\{&2\left[F_1(s)+F_2(s)\right]\,\bar{v}_2\gamma^\mu u_1\,\bar{u}_3\gamma_\mu v_4 - 2F_2(s)\,\bar{v}_2 u_1\,\bar{u}_3 v_4\\ &+\frac{F_2(s)}{m_e}\left(\bar{v}_2\not{q}u_1\,\bar{u}_3 v_4 - \bar{v}_2 u_1\,\bar{u}_3\not{q}v_4\right)\Bigg\}.\end{aligned} \tag{5.43}$$

The first two terms are already expressed in the desired form, while the third term has to be projected yet. For this purpose we apply algebraically trivial identities

$$\bar{v}_2\left(\not{p}_4-\not{p}_3\right)u_1 = -2m_e\,\bar{v}_2 u_1 + 2\,\bar{v}_2\not{q}u_1, \tag{5.44a}$$

$$\bar{u}_3\left(\not{p}_2-\not{p}_1\right)v_4 = -2m_e\,\bar{u}_3 v_4 - 2\,\bar{u}_3\not{q}v_4, \tag{5.44b}$$

which can obtained by applying the Dirac equation (5.20).

We can now employ the results derived in Appendix 5B, in particular Eq. (5.116), which completes the projection onto the S, P, V, A, T basis. Collecting the relevant terms, we obtain

$$\begin{aligned}\mathrm{Im}\left[\mathcal{T}_{\mathrm{Vertex}}\right] = \frac{\alpha e^2}{s}\Bigg\{ & \frac{t-u}{4s}\,\bar{v}_2 u_1\,\bar{u}_3 v_4 + \frac{t-u}{4s}\,\bar{v}_2\gamma^5 u_1\,\bar{u}_3\gamma^5 v_4 \\ & + \left[\frac{m_e^2}{s} - \frac{3}{2} - \ln\left(\frac{m_\gamma^2}{s}\right)\right]\bar{v}_2\gamma^\mu u_1\,\bar{u}_3\gamma_\mu v_4 + \frac{1}{8}\,\bar{v}_2\sigma^{\mu\nu}u_1\,\bar{u}_3\sigma_{\mu\nu}v_4\Bigg\}.\end{aligned} \tag{5.45}$$

Finally, the Fierz identities allow us to recast this onto the t-channel basis as

$$\begin{aligned}\mathrm{Im}\left[\mathcal{T}_{\mathrm{Vertex}}\right] = \frac{\alpha e^2}{s}\Bigg\{ & \left[-1 + \frac{t}{4s} - \ln\left(\frac{m_\gamma^2}{s}\right)\right]\bar{u}_3 u_1\,\bar{v}_2 v_4 \\ & + \left[2 + \frac{t}{4s} + \ln\left(\frac{m_\gamma^2}{s}\right)\right]\bar{u}_3\gamma^5 u_1\,\bar{u}_3\gamma^5 v_4 \\ & + \frac{1}{2}\left[\frac{3}{2} + \ln\left(\frac{m_\gamma^2}{s}\right)\right]\bar{u}_3\gamma^\mu u_1\,\bar{v}_2\gamma_\mu v_4 \\ & + \frac{1}{2}\left[\frac{3}{2} + \ln\left(\frac{m_\gamma^2}{s}\right)\right]\bar{u}_3\gamma^\mu\gamma^5 u_1\,\bar{v}_2\gamma_\mu\gamma^5 v_4 + \frac{t}{8s}\,\bar{u}_3\sigma^{\mu\nu}u_1\,\bar{v}_2\sigma_{\mu\nu}v_4\Bigg\}.\end{aligned} \tag{5.46}$$

However, this expression by itself is not meaningfull as it contains an infrared divergence. To establish a connection with physical observables, we need to combine it with the t-channel diagram shown in Fig. 5.2f, which contains an infrared divergence too, and we will see that these two are to cancel each other out.

5.3.3 t-channel box correction

The box diagram shown in Fig. 5.2f can be expressed as

$$\begin{aligned}\mathcal{M}_{t-\mathrm{box}} = - & \underbrace{i^2\,(-i)^2}_{\text{Propagators}}\overbrace{(-ie)^4}^{\text{Vertices}}\int \bar{u}\,(p_3)\,\frac{\gamma^\mu\,(\not{k}+m_e)\,\gamma^\nu}{k^2-m_e^2+i\varepsilon}u\,(p_1) \\ & \times\,\bar{v}\,(p_2)\,\frac{\gamma^\alpha\left(-\not{p}_1-\not{p}_2+\not{k}+m_e\right)\gamma^\beta}{(p_1+p_2-k)^2-m_e^2+i\varepsilon}v\,(p_4) \\ & \times\,\frac{g_{\mu\beta}}{(p_3-k)^2-m_\gamma^2+i\varepsilon}\,\frac{g_{\nu\alpha}}{(p_1-k)^2-m_\gamma^2+i\varepsilon}\,\frac{d^4k}{(2\pi)^4},\end{aligned} \tag{5.47}$$

and an extra sign in front of everything is due to the Pauli principle. The photon mass is introduced to regulate the IR-behaviour.

The diagram itself is entirely standard and can be, in principle, evaluated in a straightforward manner. However, the common Feynman parameter technique turns out to be highly inefficient in this case. Indeed, after shifting the loop momentum k, a large number of additional Dirac structures are generated in the numerator, since $\not{k}$ appears in both spinor chains. All these structures must then be reduced and projected onto the basis of Eq. (5.2)—a process that is quite cumbersome and obscure, as many nontrivial cancellations occur in the process. Moreover, performing the resulting triple integral over the Feynman parameters z_1, z_2 and z_3 is technically demanding and requires careful control of the analytic structure of the denominator.

For these reasons, we instead adopt a dispersive approach to evaluate this graph. This method directly isolates the imaginary part, which is the only component relevant for the computation of the spin asymmetry in the present context. For this purpose we replace

$$\frac{1}{p^2 - m_e^2 + i\varepsilon} = (-2\pi i)\,\delta\left(p^2 - m_e^2\right)\theta\left(\pm p^0\right), \tag{5.48}$$

the "+" sign is chosen for an outcoming line, and a "−" sign is required for an incoming line.

The direct diagram allows for a single cut through the electron lines. The subsequent steps become particularly trivial in the center-of-momentum frame, where the conditions

$$P_-^0 + P_+^0 = \sqrt{s}, \tag{5.49}$$
$$\mathbf{P}_- + \mathbf{P}_+ = 0, \tag{5.50}$$

hold. The product of delta functions then enforces the constraints

$$\begin{aligned}&\delta\left(k^2 - m_e^2\right)\delta\left[(P_- + P_+ - k)^2 - m_e^2\right]\theta\left(k^0\right)\theta\left(P_-^0 + P_+^0 - k^0\right)\\ &= \frac{1}{\beta\sqrt{s}}\delta\left(|\mathbf{k}| - \frac{\beta\sqrt{s}}{2}\right)\frac{1}{2\sqrt{s}}\delta\left(k^0 - \frac{\sqrt{s}}{2}\right),\end{aligned} \tag{5.51}$$

i.e. the first delta function eliminates the integration over $|\mathbf{k}|$, while the second fixes k^0. We also note that together they imply

$$[k\,(P_- + P_+)] = \frac{s}{2}. \tag{5.52}$$

Before going further, we note that we consider only the direct graph, as the crossed diagram produces no imaginary part. Indeed, the internal particles cannot simultaneously go on-shell in this kinematics, as the unitarity cut would require satisfying the product of functions

$$\delta\left(k^2 - m_e^2\right)\delta\left[(p_1 - p_4 - k)^2 - m_e^2\right]\theta\left(k^0\right)\theta\left(p_1^0 - p_4^0 - k^0\right). \tag{5.53}$$

However, we know that in the center-of-momentum frame the energy transfer is zero, i.e.

$$p_1^0 - p_4^0 = 0. \tag{5.54}$$

Meanwhile, the first theta function enforces the four-vector k to be timelike with $k^0 > 0$. Therefore, the second theta function never contributes in the physical region, and the cut constraints cannot be satisfied.

Next, we recall that the volume element takes the form

$$d^4k = dk^0 d\Omega_{\mathbf{k}} \left|\mathbf{k}\right|^2 d\left|\mathbf{k}\right|, \tag{5.55}$$

and therefore the imaginary part of the loop integral becomes

$$\begin{aligned}
&\operatorname{Im}\mathcal{T}_{t-\text{box}} \\
&= -\frac{e^2\alpha\beta}{16\pi}\int \frac{\bar{u}_3\gamma^\mu\left(\not{k}+m_e\right)\gamma^\nu u_1\,\bar{v}_2\gamma_\nu\left(-\not{p}_1-\not{p}_2+\not{k}+m_e\right)\gamma_\mu v_4}{\left((p_3-k)^2-m_\gamma^2\right)\left((p_1-k)^2-m_\gamma^2\right)} d\Omega_{\mathbf{k}}.
\end{aligned} \tag{5.56}$$

The integral contains terms quadratic in k, as well as linear and k-independent. The corresponding angular integrals can be performed sequentially; however, taken individually they cannot be projected onto the desired basis. In particular, many "unwanted" terms vanish upon integration over the azimuthal angle $\phi_{\mathbf{k}}$, and the remaining ones cancel each other out after combining the linear and quadratic contributions.

The complete calculation is rather cumbersome and involves several intermediate steps. It is therefore presented in Appendix 5D and, partially, Appendix 5E, where the projection procedure is also described in detail. In the ultrarelativistic limit, the result takes the compact form

$$\begin{aligned}
\operatorname{Im}\mathcal{T}_{t-\text{box}} = -\frac{e^2\alpha}{4}\Bigg\{ &\frac{s-u}{su^2}\left[u - s\ln\left(-\frac{t}{s}\right)\right]\bar{u}_3 u_1\,\bar{v}_2 v_4 \\
&+\frac{s-u}{su^2}\left[u - s\ln\left(-\frac{t}{s}\right)\right]\bar{u}_3\gamma^5 u_1\,\bar{v}_2\gamma^5 v_4 \\
&+\frac{1}{u^2}\left[u - \frac{s^2+3u^2}{t}\ln\left(-\frac{m_\gamma^2}{t}\right) - (s-u)\ln\left(\frac{m_\gamma^2}{s}\right)\right]\bar{u}_3\gamma^\mu u_1\,\bar{v}_2\gamma_\mu v_4 \\
&+\frac{1}{u^2}\left[u + (s-u)\ln\left(-\frac{s}{t}\right)\right]\bar{u}_3\gamma^\mu\gamma^5 u_1\,\bar{v}_2\gamma_\mu\gamma^5 v_4 \\
&+\frac{t}{2su^2}\left[u - s\ln\left(-\frac{t}{s}\right)\right]\bar{u}_3\sigma^{\mu\nu}u_1\,\bar{v}_2\sigma_{\mu\nu}v_4\Bigg\} + \mathcal{O}\left(\frac{m_e^2}{s}\right).
\end{aligned} \tag{5.57}$$

Remarkably, by assuming $m_e = 0$ from the outset one reproduces the coefficients for the V and A structures correctly, but the S, P, and T contributions would be lost.

We now combine this expression with the vertex correction given in Eq. (5.46). The logarithmic dependence on the artificial photon mass cancels in the sum, and the complete result takes the form

$$B_n^{t-\text{box+Vertex}} = -\frac{\alpha m_e}{\sqrt{s}} \frac{x^3 \left[2\left(x^6 - 3x^4 - x^2 + 3\right) - 3\left(x^2 - 2\right)\ln\left(x^2\right)\right]}{2\sqrt{1-x^2}\left(1 - x^2 + x^4\right)^2} + \mathcal{O}\left(\frac{m_e^2}{s}\right). \tag{5.58}$$

Finally, we note that this contribution has a zero crossing at $\approx 80°$, which can be seen from Fig. 5.3. The zero-crossing point position is independent of $\sqrt{s}$, as it only comes in a prefactor to the whole expression.

5.3.4 s-channel box correction

We now turn to the last remaining contribution, namely the s-channel box diagrams shown in 5.2g and 5.2h. In contrast to the t-channel case, both the direct and crossed topologies give rise to a non-vanishing imaginary part. Summing these two contributions, we write

$$\begin{aligned}\mathcal{M}_{s-\text{box}} = e^4 \int & \bar{v}_2 \gamma_\nu \left(\not{p}_1 - \not{k} + m_e\right) \gamma_\mu u_1 \\ & \times \bar{u}_3 \left[\frac{\gamma^\mu \left(\not{p}_3 - \not{k} + m_e\right) \gamma^\nu}{\left(p_3 - k\right)^2 - m_e^2 + i\varepsilon} + \frac{\gamma^\nu \left(\not{k} - \not{p}_4 + m_e\right) \gamma^\mu}{\left(k - p_4\right)^2 - m_e^2 + i\varepsilon}\right] v_4 \\ & \times \frac{1}{\left(p_1 - k\right)^2 - m_e^2 + i\varepsilon} \frac{1}{k^2 + i\varepsilon} \frac{1}{\left(p_1 + p_2 - k\right)^2 + i\varepsilon} \frac{d^4k}{(2\pi)^4}.\end{aligned} \tag{5.59}$$

Just as in the case of the t-box, we proceed with the dispersive calculation to extract the imaginary part, which is now simplified, as there is no need to handle the photon mass - both topologies are infrared-safe. Performing a single cut through the two photon lines, we obtain

$$\begin{aligned}&\delta\left(k^2\right) \delta\left[\left(P_- + P_+ - k\right)^2\right] \theta\left(k^0\right) \theta\left(P_-^0 + P_+^0 - k^0\right) \\ &= \frac{1}{\sqrt{s}} \delta\left(|\mathbf{k}| - \frac{\sqrt{s}}{2}\right) \frac{1}{2\sqrt{s}} \delta\left(k^0 - \frac{\sqrt{s}}{2}\right),\end{aligned} \tag{5.60}$$

which constrains the loop momentum to satisfy

$$\left[k\left(P_- + P_+\right)\right] = \frac{s}{2}. \tag{5.61}$$

As a result, the imaginary part reduces to an angular integral of the form

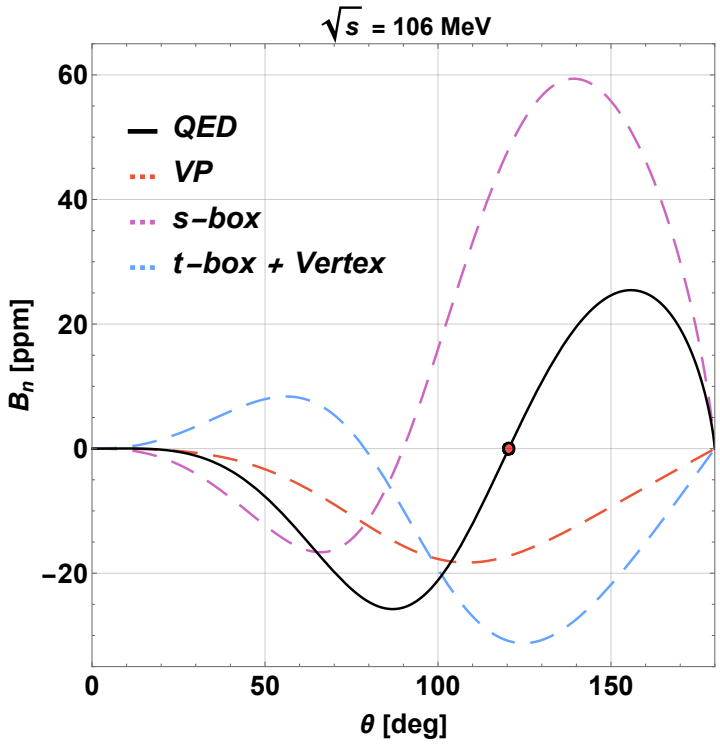

Figure 5.3: QED contributions to beam-normal spin asymmetry B_n. The QED zero-crossing point is marked with a red dot. "VP" stands for vacuum polarization.

$$
\begin{aligned}
\mathrm{Im}\,\mathcal{T}_{s-\mathrm{box}} &= \frac{e^2\alpha}{16\pi}\int \frac{1}{(p_1-k)^2-m_e^2} \\
&\times\Bigg[\frac{1}{(p_3-k)^2-m_e^2}\Big[\bar v_2\gamma^\nu \not k\gamma^\mu u_1\,\bar u_3\gamma_\mu \not k\gamma_\nu v_4 - 2\,\bar v_2\gamma^\nu \not k \not p_3 u_1\,\bar u_3\gamma_\nu v_4 \\
&- 2\,\bar v_2\gamma^\nu u_1\,\bar u_3 \not p_1 \not k\gamma_\nu v_4 + 4\,(p_1p_3)\;\bar v_2\gamma^\nu u_1\,\bar u_3\gamma_\nu v_4\Big] \\
&- \frac{1}{(k-p_4)^2-m_e^2}\Big[\bar v_2\gamma^\nu \not k\gamma^\mu u_1\,\bar u_3\gamma_\nu \not k\gamma_\mu v_4 - 2\,\bar v_2\gamma^\nu \not k \not p_4 u_1\,\bar u_3\gamma_\nu v_4 \\
&- 2\,\bar v_2\gamma^\nu u_1\,\bar u_3\gamma_\nu \not k \not p_1 v_4 + 4\,(p_1p_4)\;\bar v_2\gamma^\nu u_1\,\bar u_3\gamma_\nu v_4\Big]\Bigg]\,d\Omega_{\mathbf{k}},
\end{aligned}
\tag{5.62}
$$

where the Dirac equation (5.20) has been applied to the spinor chains to prepare the expression for the subsequent calculation.

Although the resulting expression is, obviously, quite lengthy, the structure is transparent: it decomposes into terms quadratic, linear, and independent in the loop momentum k. Each of these can be treated in direct analogy with the corresponding structures encountered in the t-box calculation (we also note that the k-independent term is already given in the desired basis). In the Appendix 5F, we carry out this program explicitly and show that the result can be cast in the form

$$
\begin{aligned}
&\operatorname{Im}\mathcal{T}_{s-\text{box}} = \frac{e^2\alpha}{4s} \\
&\times \Bigg\{ \left[-4 - \frac{s}{t} - \frac{s}{u} + \frac{t^2-u^2}{u^2} \ln\left(-\frac{t}{s}\right) - \frac{t^2-u^2}{t^2} \ln\left(-\frac{u}{s}\right) \right] \bar{v}_2 u_1 \, \bar{u}_3 v_4 \\
&+ \left[-4 - \frac{s}{t} - \frac{s}{u} + \frac{t^2-u^2}{u^2} \ln\left(-\frac{t}{s}\right) - \frac{t^2-u^2}{t^2} \ln\left(-\frac{u}{s}\right) \right] \bar{v}_2 \gamma^5 u_1 \, \bar{u}_3 \gamma^5 v_4 \\
&+ \left[\frac{s}{t} - \frac{s}{u} + \frac{3u^2+t^2}{u^2} \ln\left(-\frac{t}{s}\right) - \frac{3t^2+u^2}{t^2} \ln\left(-\frac{u}{s}\right) \right] \bar{v}_2 \gamma^\mu u_1 \, \bar{u}_3 \gamma_\mu v_4 \\
&+ \left[-\frac{s}{t} - \frac{s}{u} + \frac{t^2-u^2}{u^2} \ln\left(-\frac{t}{s}\right) - \frac{t^2-u^2}{t^2} \ln\left(-\frac{u}{s}\right) \right] \bar{v}_2 \gamma^\mu \gamma^5 u_1 \, \bar{u}_3 \gamma_\mu \gamma^5 v_4 \\
&+ \frac{s}{2} \left[\frac{1}{u} - \frac{1}{t} + \frac{t+u}{u^2} \ln\left(-\frac{t}{s}\right) - \frac{t+u}{t^2} \ln\left(-\frac{u}{s}\right) \right] \bar{v}_2 \sigma^{\mu\nu} u_1 \, \bar{u}_3 \sigma_{\mu\nu} v_4 \Bigg\} \\
&+ \mathcal{O}\left(\frac{m_e^2}{s}\right).
\end{aligned}
\tag{5.63}
$$

Although the direct and crossed box diagrams separately contain terms proportional to $\ln(m_e^2/s)$, in the final result they cancel each other out. As in the previous case, by setting $m_e = 0$ from the start one would reproduce the coefficients V and A correctly, but the S, P, and T terms would be missed.

The final step consists in projecting the result onto the t-channel structures utilizing the Fierz identities given in Table 5.2. Carrying out this transformation yields

$$
B_n^{s-\text{box}} = -\frac{\alpha m_e}{\sqrt{s}} \frac{x\,(2x^2-1)\left[3x^2 \ln(x^2) + (x^2-1)\left(2x^2 - 3\ln(1-x^2)\right)\right]}{2\sqrt{1-x^2}\,(1-x^2+x^4)^2}. \tag{5.64}
$$

We note that this contribution exhibits a zero crossing precisely at 90°. The corresponding plot is shown in Fig. 5.3, alongside the other QED contributions.

5.3.5 Full QED result

We calculated the relevant 1-loop QED diagrams and projected them onto the Dirac basis in Eq. (5.2). Our result for B_n obtained from Eq. (5.24) verifies the expression given in the literature [152]. Although the derivation was technically demanding, in the ultra-relativistic limit the it can be expressed in compact form

$$
\begin{aligned}
B_n^{\text{QED, 1-loop}} &= \frac{\alpha m_e}{\sqrt{s}} \frac{x}{2\sqrt{1-x^2}\,(1-x^2+x^4)^2} \\
&\times \Big[2x^2\left(1-x^2\right)\left(-5+x^4\right) - 3x^2\left(1+x^2\right)\ln\left(x^2\right) \\
&+ 3\left(1-x^2\right)\left(1-2x^2\right)\ln\left(1-x^2\right) + \mathcal{O}\left(\frac{m_e^2}{s}\right) \Big].
\end{aligned}
\tag{5.65}
$$

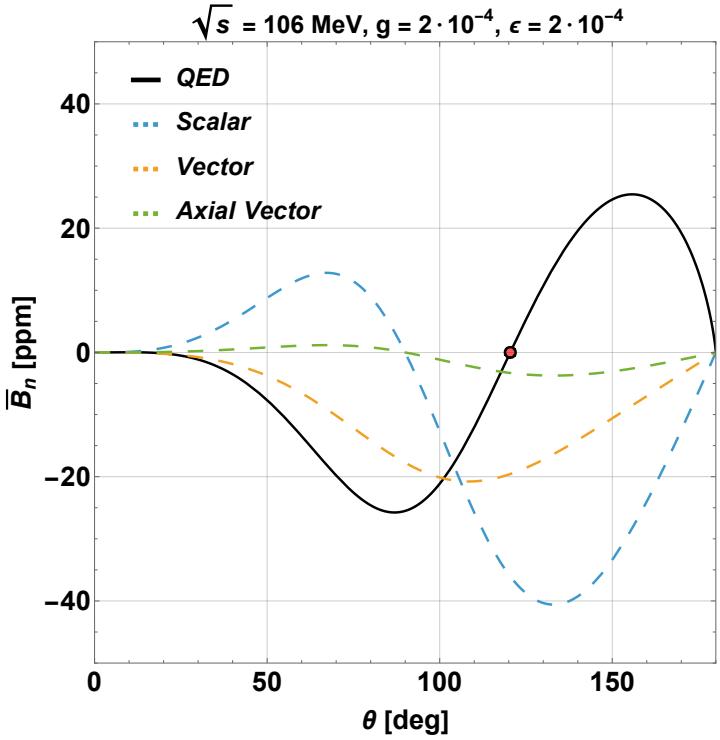

Figure 5.4: Comparison of the angular dependence of the QED and BSM contributions to the Bhabha beam normal spin asymmetry $\bar{B}_n$ for indicated values of BSM coupling strengths, for an 11 GeV e^+ beam at JLab. The numerator and denominator in $\bar{B}_n$ are integrated over a bin in s of size $2m_e\delta E_+$, with $\delta E_+ = 0.5$ MeV. The QED zero-crossing point is marked with a red dot.

The QED full result for B_n, shown on Fig. 5.3 together with the individual contributions, exhibits a zero crossing at $\theta \approx 120.4°$ due to cancellations between different discontinuities. In the ultra-relativistic regime, where the only kinematic dependence appears in the overall prefactor, the position of this zero is independent of $\sqrt{s}$, thus providing a kinematic point that is effectively background free.

While two-loop effects or finite-mass corrections could in principle shift this zero, these contributions are expected to lie well below the anticipated experimental precision for B_n, estimated at ~ 1 ppm [153]. Furthermore, a real experiment will measure over a finite angular bin $\Delta\theta$, expected to be 10° or smaller. Integrating the smoothly varying SM distribution over a symmetric bin centered on the zero-crossing cancels the SM background to first order. Other potential backgrounds from positron-nucleus elastic scattering $e^+N \to e^+N$ can be effectively eliminated by utilizing the distinct kinematics of the Bhabha process, specifically by requiring a coincidence detection of the final state e^+e^- pair.

Other potential backgrounds from positron-nucleus elastic scattering $e^+N \to e^+N$ can be effectively eliminated by utilizing the distinct kinematics of the Bhabha process, specifically by requiring a coincidence detection of the final state e^+e^- pair.

5.4 BSM contributions to single spin asymmetry

We next discuss the sensitivity of B_n to BSM messengers. As the exchange of a pseudoscalar particle provides no contribution to B_n, seen from Eq. (5.24), three BSM mediators with minimal couplings to SM leptons are considered below: a scalar, a vector, and an axial vector. Their interaction terms are provided in Eqs. (4.13).

The considered BSM contribution to B_n arises from the interference between the tree-level QED amplitude and the s-channel tree-level BSM amplitude, shown in Fig. 5.2i. It might therefore appear that the pseudoscalar operator could still yield a non-vanishing contribution, since the BSM interaction enters in the s-channel, whereas the amplitude decomposition in (5.2) is formulated in the t-channel. In that case, one would naturally suspect that the Fierz transformations summarized in Table 5.2 generate residual terms that survive the projection. However, a direct calculation shows that this is not the case: although S, V, A and T terms indeed arise, they mutually cancel each other, as can be seen explicitly from the corresponding coefficients

$$S_S = P_S = V_S = -A_S = 2T_S = -\frac{1}{4}\frac{g^2}{s - m_S^2 + im_S\Gamma_S}, \tag{5.66a}$$

$$S_V = -P_V = -2V_V = -2A_V = \frac{e^2\epsilon^2}{s - m_V^2 + im_V\Gamma_V}, \qquad T_V = 0, \tag{5.66b}$$

$$S_A = -P_A = 2V_A = 2A_A = \frac{e^2\epsilon^2}{s - m_A^2 + im_A\Gamma_A}, \qquad T_A = 0, \tag{5.66c}$$

where the subscripts S, V, and A denote scalar, vector, and axial vector BSM particles, respectively, and should not be confused with the notation used for the decomposition coefficients.

The imaginary part of the amplitudes is resulting from the propagator

$$\frac{1}{s - m_X^2 + im_X\Gamma_X}, \tag{5.67}$$

where m_X and Γ_X denote the mediator mass and total decay width. In the minimal model considered here, the latter consists of a single contribution from the mediator's coupling to electrons, see Eqs. (2.70) and (4.16) for the respective expressions. In the narrow width approximation we simplify it further by employing the replacement

$$\frac{im_X\Gamma_X}{(s - m_X^2)^2 + m_X^2\Gamma_X^2} \to i\pi\delta\left(s - m_X^2\right). \tag{5.68}$$

To determine the sensitivity reach of the dark messenger coupling as function of its mass m_X, the count rates in numerator and denominator in B_n must be integrated over a bin in the e^+e^- invariant mass around a given central value s_0. For a smoothly varying function, such as the QED cross section, this amounts to the factor

$$\int_{s_0-\frac{\delta s}{2}}^{s_0+\frac{\delta s}{2}} f(s)\,\mathrm{d}s = 2m_e\,\delta E_+\,f(s_0), \tag{5.69}$$

with δE_+ the bin width in the positron (*lab*) beam energy. To remain conservative, we adopt a bin width of $\delta E_+ = 0.5\,\text{MeV}$. For the QED contribution, this factor cancels out between numerator and denominator, but it becomes relevant for the BSM-induced result. Denoting the asymmetry in which numerator and denominator are integrated over a bin in s of size $2m_e\,\delta E_+$ as $\bar{B}_n$, we find that the interference between tree-level QED and BSM processes results in

$$\bar{B}_n^{\text{BSM, tree}} = \frac{\sqrt{s}}{\delta E_+}\frac{x\sqrt{1-x^2}}{8}\frac{N_i}{\left(1-x^2+x^4\right)^2}, \tag{5.70}$$

where the numerator function N_i for scalar (N_S), vector (N_V), and axial vector (N_A) exchange is given by

$$N_S = \frac{g^2}{\alpha}\,x^2\left(1-2x^2\right), \tag{5.71a}$$
$$N_V = -4\pi\epsilon^2\,3x^2, \tag{5.71b}$$
$$N_A = 4\pi\epsilon^2\,x^2\left(1-2x^2\right). \tag{5.71c}$$

Note that in the ultra-relativistic regime the scalar and axial vector follow the same angular dependence up to the coupling constant. The vector contribution, in turn, exhibits the same angular dependence as the QED vacuum polarization (5.35).

In contrast to the full QED result, which decreases with energy as $1/\sqrt{s}$, the BSM-induced spin asymmetry grows proportionally to $\sqrt{s}$, improving the signal-to-background ratio at higher beam energies. Furthermore, one notices from Eqs. (5.71a) that the observable B_n depends quadratically on the BSM couplings, as it results from the product of a large tree-level QED amplitude and the absorptive part of a BSM amplitude. This is in contrast to BSM searches in unpolarized observables, for which the BSM signal goes with the fourth power of the small coupling constant. One thus sees that the tree-level QED process serves as an amplifier of a possible BSM signal.

The result for the angular dependence of B_n is shown in Fig. 5.4 for an 11 GeV positron beam at JLab. The coupling strengths $g = 2\times10^{-4}$ and $\epsilon = 2\times10^{-4}$ are chosen for illustration. Even for such small values, one sees that the BSM effects in the vicinity of the QED zero crossing can be sizable compared to the expected ppm-level experimental precision, enabling enhanced sensitivity or, in the absence of a signal, competitive limits to be set.

We made an assessment of the parameter space that can be probed at JLab, where the scan over the range of m_X can be performed with the initial state radiation technique. Requiring the BSM contribution to produce a 2σ signal above the projected experimental uncertainty of 1 ppm yields the limits shown in Figs. 5.5 and 5.6, where the existing bounds and near-future projection are also added (same as in Chapter 4).

5.5 Results and discussion

The Bhabha beam normal spin asymmetry, which can be accessed using a polarized positron beam at JLab, provides a uniquely sensitive probe of BSM mediators. The

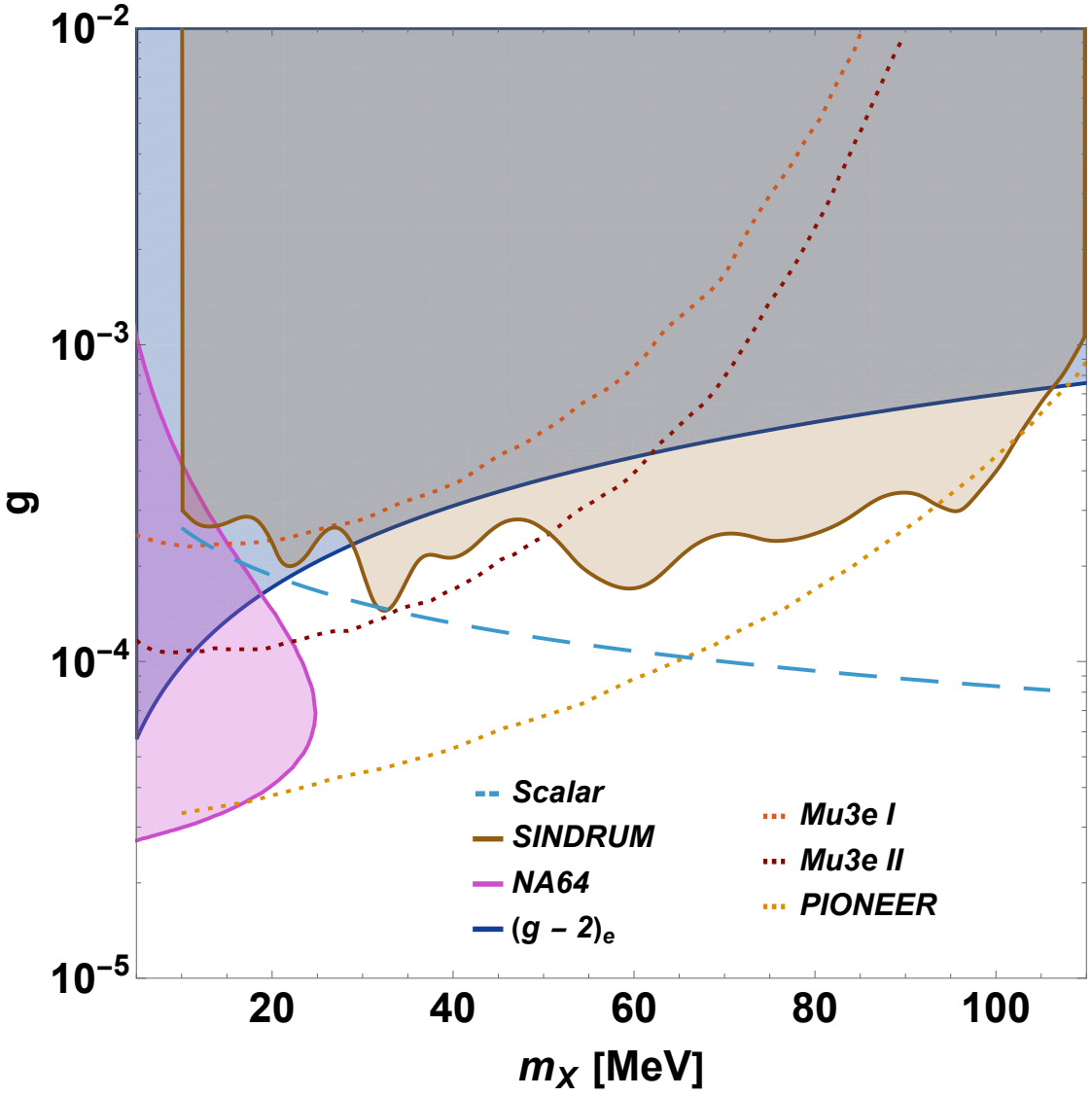

Figure 5.5: Constraints on the allowed BSM parameter space from $(g-2)_e$ and from existing experiments looking for visible e^+e^- decay, for the scalar scenario, together with the projected sensitivity (corresponding with a 1 ppm precision on B_n) of a future JLab polarized-positron experiment shown as dashed line. Other near-future experiments are shown as dotted lines.

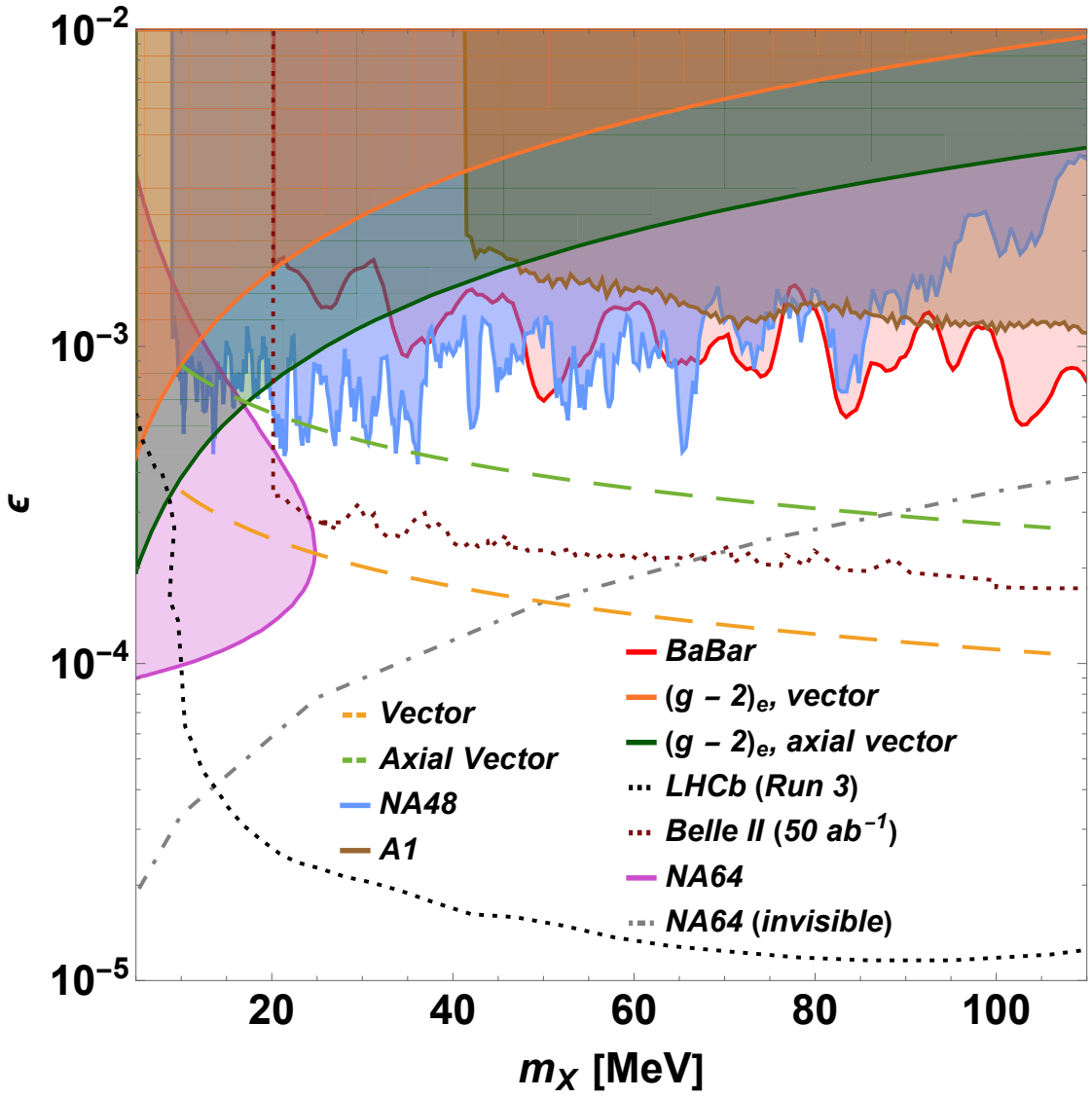

Figure 5.6: Constraints on the allowed BSM parameter space from $(g-2)_e$ and from existing experiments looking for visible e^+e^- decay, for the vector and axial vector scenarios, together with the projected sensitivity (corresponding with a 1 ppm precision on B_n) of a future JLab polarized-positron experiment shown as dashed lines. Other near-future experiments are shown as dotted lines. The gray dot-dashed curve indicating limits from NA64 searches for invisibly decaying mediators is also shown for comparison.

uniqueness is threefold: firstly the JLab energy region, which corresponds with a maximum c.m. energy of 106 MeV of the Bhabha process prevents any hadronic discontinuity to contribute. Secondly, the leading QED result has a zero in the angular distribution due to cancellations between different discontinuities, allowing for a kinematic point which is nearly background free. Thirdly, the enhanced sensitivity of the observable B_n to a BSM contribution results from the quadratic dependence on the coupling, in contrast to BSM searches in unpolarized processes, for which the BSM signal goes with the fourth power of the small coupling constant.

We have shown that up to an order of magnitude extension in reach can be obtained, in particular for the scalar and vector scenarios. Our estimates were done in a conservative way, and additional improvements in energy resolution or experimental precision could strengthen the final results. While the analysis presented in this work focused on the most natural scenarios involving scalar, vector, and axial vector mediators, the method can be straightforwardly extended to a broader class of models, including tensor-coupled interactions [154].

The analysis must ideally be extended to double-spin asymmetries. Among these, the transverse-transverse asymmetries, A_{TT} and A'_{TT}, present a highly promising, albeit exceptionally challenging, frontier for future JLab studies [153].

The standard transverse asymmetry, A_{TT}, is driven by helicity-conserving amplitudes and features an azimuthal oscillation proportional to $\cos(2\phi)$. Lacking helicity suppression, it constitutes a massive SM background, typically four orders of magnitude larger than the BSM signals of interest. While this large amplitude makes it an excellent "candle" for beam polarimetry, it completely swamps the BSM signal in a naive measurement.

In contrast, the A'_{TT} asymmetry isolates a doubly helicity-suppressed component of the cross section. This suppression diminishes the SM contribution, yielding a flat, monopole signal. This geometric behavior makes A'_{TT} an optimally sensitive, nearly background-free window for probing spin-0 mediators.

The primary experimental challenge in isolating A'_{TT} lies in the magnitude of the A_{TT} background. While spatial averaging across an azimuthally symmetric detector array should theoretically cancel the $\cos(2\phi)$ oscillation, this approach is critically vulnerable to hardware imperfections.

To overcome this systematic barrier, a technically elegant solution was proposed to shift the phase by 90° for the half duration of the experiment. Averaging the data across these polarization states cancels both the physical A_{TT} background and the false asymmetries induced by detector non-linearities, allowing the A'_{TT} signal to be safely extracted.

Lastly, this framework is not limited to the fixed-target JLab setup. For instance, the planned polarization upgrade for Belle II offers an opportunity to apply these BSM search techniques at an e^+e^- collider [155]. While this extension has the potential to significantly improve existing bounds, operating at higher energies requires a precise understanding of hadronic contributions, in particular, the hadronic vacuum polarization (HVP). This could, in addition, provide valuable connections to other persisting topics, such as the ongoing tensions between data-driven and lattice QCD determinations of these corrections.

Appendix 5A: Matrix element decomposition

The fact that C-, P- and T- symmetries leave only five independent helicity amplitudes out of total sixteen can be understood from the relations listed in Table 5.1. The nontrivial exercise, however, is to relate these to Dirac structures rather than helicity amplitudes.

For this purpose, we begin with the scattering channel. In the most general case, an amplitude can be parameterized in terms of either electron or positron line as a combination of Dirac bilinears

$$\begin{aligned}\mathcal{T} &= E_S\,\bar{u}_3 u_1 + E_P\,\bar{u}_3\gamma^5 u_1 + E_V\,\bar{u}_3 \not{a} u_1 + E_A\,\bar{u}_3 \not{a}\gamma^5 u_1 + E_T\,c^{\mu\nu}\,\bar{u}_3\sigma_{\mu\nu}u_1 \\ &= P_S\,\bar{v}_2 v_4 + P_P\,\bar{v}_2\gamma^5 v_4 + P_V\,\bar{v}_2 \not{a}' v_4 + P_A\,\bar{v}_2 \not{a}'\gamma^5 v_4 + P_T\,c'^{\mu\nu}\,\bar{v}_2\sigma_{\mu\nu}v_4.\end{aligned} \tag{5.72}$$

Here, a^μ and a'^μ represent arbitrary four-vectors, while $c^{\mu\nu}$ and $c'^{\mu\nu}$ are arbitrary tensors.

Any four-vector in this space can be represented as a linear combination of the basis vectors $P_\pm$, q, and n. Moreover, terms involving P_- or q, when sandwiched between the spinors $\bar{u}_3$ and u_1, vanish or reduce to scalar coefficients via the Dirac equation (5.20), as they consist of p_1 and p_3.

Furthermore, from the definition of the vector n_μ, it follows that the contraction $\not{n}$ can be related to a product of three Dirac matrices via the identity

$$\not{P}_-\not{q}\not{P}_+ = -\,(P_-P_+)\,\not{q} - i\not{n}\gamma^5. \tag{5.73}$$

Keeping this in mind, let's now transform

$$\begin{aligned}&\bar{u}_3\not{P}_-\not{q}\not{P}_+\gamma^5 u_1 = \frac{1}{2}\,\bar{u}_3\left[4m_e\,(p_1P_+) - 2m_e\not{P}_+\not{p}_1 - 2\,(p_1p_3)\,\not{P}_+\right]\gamma^5 u_1 \\ &= \frac{1}{2}\,\bar{u}_3\left[4m_e\,(P_-P_+) + q^2\not{P}_+\right]u_1 = 2m_e\,(P_-P_+)\;\bar{u}_3\gamma^5 u_1 + \frac{q^2}{2}\,\bar{u}_3\not{P}_+\gamma^5 u_1.\end{aligned} \tag{5.74}$$

An analogous calculation for the positron spinors yields

$$\begin{aligned}&\bar{v}_2\not{P}_-\not{q}\not{P}_+\gamma^5 v_4 = \frac{1}{2}\,\bar{v}_2\left[-4m_e\,(P_-p_2) + 2m_e\not{p}_2\not{P}_- + 2\,(p_4p_2)\,\not{P}_-\right]\gamma^5 v_4 \\ &= \frac{1}{2}\,\bar{v}_2\left[-4m_e\,(P_-P_+) - q^2\not{P}_-\right]v_4 = -2m_e\,(P_-P_+)\;\bar{v}_2\gamma^5 v_4 - \frac{q^2}{2}\,\bar{v}_2\not{P}_-\gamma^5 v_4.\end{aligned} \tag{5.75}$$

From these expressions we deduce the identities

$$\bar{u}_3\not{n}u_1 = i\,\bar{u}_3\not{P}_-\not{q}\not{P}_+\gamma^5 u_1 - 2im_e\,(P_-P_+)\;\bar{u}_3\gamma^5 u_1 = \frac{iq^2}{2}\,\bar{u}_3\not{P}_+\gamma^5 u_1, \tag{5.76a}$$

$$\bar{v}_2\not{n}v_4 = i\,\bar{v}_2\not{P}_-\not{q}\not{P}_+\gamma^5 v_4 + 2im_e\,(P_-P_+)\;\bar{v}_2\gamma^5 v_4 = -\frac{iq^2}{2}\,\bar{v}_2\not{P}_-\gamma^5 v_4, \tag{5.76b}$$

which can be used to get rid of $\not{n}$ is the final formulas.

Similar steps can be taken in the case where γ^5 is involved

$$\begin{aligned}\bar{u}_3 \not{P}_- \not{q} \not{P}_+ u_1 &= \frac{1}{2}\,\bar{u}_3 \left(\not{p}_3 \not{p}_1 - \not{p}_1 \not{p}_3\right) \not{P}_+ u_1 \\ &= \frac{1}{2}\,\bar{u}_3 \left[4m_e\,(P_- P_+) - 4P_-^2 \not{P}_+\right] u_1 = 2m_e\,(P_- P_+)\;\bar{u}_3 u_1 - 2P_-^2\,\bar{u}_3 \not{P}_+ u_1.\end{aligned} \tag{5.77}$$

For the positron spinor chain we obtain

$$\begin{aligned}\bar{v}_2 \not{P}_- \not{q} \not{P}_+ v_4 &= \frac{1}{2}\,\bar{v}_2 \not{P}_- \left(\not{p}_4 \not{p}_2 - \not{p}_2 \not{p}_4\right) v_4 = \\ &= \frac{1}{2}\,\bar{v}_2 \left[4m_e\,(P_- P_+) + 4P_+^2 \not{P}_-\right] v_4 = 2m_e\,(P_- P_+)\;\bar{v}_2 v_4 + 2P_+^2\,\bar{v}_2 \not{P}_- v_4.\end{aligned} \tag{5.78}$$

Consequently, the $\not{n}$ can be removed from the studied expressions

$$\bar{u}_3 \not{n} \gamma^5 u_1 = -\frac{i}{2}\left[(s+u)\;\bar{u}_3 \not{P}_+ u_1 - m_e\,(s-u)\;\bar{u}_3 u_1\right], \tag{5.79a}$$

$$\bar{v}_2 \not{n} \gamma^5 v_4 = \frac{i}{2}\left[(s+u)\;\bar{v}_2 \not{P}_- v_4 + m_e\,(s-u)\;\bar{v}_2 v_4\right]. \tag{5.79b}$$

The outcome is that the vector and pseudovector terms for the electron and positron lines can be fully expressed via the structures $E_3\,\bar{u}_3 \not{P}_+ u_1 + E_4\,\bar{u}_3 \not{P}_+ u_1$ or $P_4\,\bar{v}_2 \not{P}_- v_4 + P_4\,\bar{v}_2 \not{P}_- \gamma^5 v_4$ for electron- and positron-line representation, respectively, as all other structures are reducible.

Finally, we address the tensor structure $\sigma_{\mu\nu}$. The key observation is that an arbitrary tensor $c^{\mu\nu}$ can be expanded in the basis of the four linearly independent vectors $\{v_i\} = \{P_+, P'_-, q, n\}$ as

$$c^{\mu\nu} = \sum_{i,j} A_{ij} v_i^\mu v_j^\nu = A_{11} P_+^\mu P_+^\nu + A_{12} P_+^\mu P_-^{\prime\nu} + A_{13} P_+^\mu q^\nu + A_{14} P_+^\mu n^\nu + \ldots, \tag{5.80}$$

where A_{ij} are scalar coefficients

$$A_{ij} = c_{\mu\nu} v_i^\mu v_j^\nu. \tag{5.81}$$

When contracted with the antisymmetric matrix $\sigma_{\mu\nu}$, all diagonal terms, $i = j$, vanish identically. Additionally, in the case of the electron line representation, P_- and q vanish again due to the Dirac equation, while $\not{n}$ can be reduced to the equation (5.73) and, subsequently, to the equations (5.76) and (5.95). Thus, we roll back to the terms already discussed, and the tensor is completely reduced to them.

Applying the same line of reasoning to the positron-line representation, we conclude that the most general parameterization for each line reads

$$\begin{aligned}\mathcal{T} &= E_1\,\bar{u}_3 u_1 + E_2\,\bar{u}_3 \gamma^5 u_1 + E_3\,\bar{u}_3 \not{P}_+ u_1 + E_4\,\bar{u}_3 \not{P}_+ \gamma^5 u_1 \\ &= P_1\,\bar{v}_2 v_4 + P_2\,\bar{v}_2 \gamma^5 v_4 + P_3\,\bar{v}_2 \not{P}_- v_4 + P_A\,\bar{v}_2 \not{P}_- \gamma^5 v_4,\end{aligned} \tag{5.82}$$

but given that both representations contain no Lorentz indices contracted with some external tensors, we conclude that the most general parameterization of the matrix element is in fact the direct product of the two

$$\begin{aligned}\mathcal{T} = &\left[E_1\,\bar{u}_3 u_1 + E_2\,\bar{u}_3\gamma^5 u_1 + E_3\,\bar{u}_3 \not{P}_+ u_1 + E_4\,\bar{u}_3 \not{P}_+\gamma^5 u_1\right] \\ &\times \left[P_1\,\bar{v}_2 v_4 + P_2\,\bar{v}_2\gamma^5 v_4 + P_3\,\bar{v}_2 \not{P}_- v_4 + P_A\,\bar{v}_2 \not{P}_-\gamma^5 v_4\right],\end{aligned} \tag{5.83}$$

as we managed to "disentangle" the electron and positron lines from each other.

This leaves us with $4 \times 4 = 16$ possible terms, but symmetry constraints reduce this number. Indeed, P-symmetry prohibits mixing terms containing γ^5 with those that don't, reducing their number by a factor of two.

Next, T-symmetry prohibits cross terms of the form

$$\bar{u}_3\gamma^5 u_1\,\bar{v}_2 \not{P}_-\gamma^5 v_4, \qquad \bar{u}_3 \not{P}_+\gamma^5 u_1\,\bar{v}_2\gamma^5 v_4, \tag{5.84}$$

as being T-odd, leaving us with just six independent amplitudes

$$\begin{aligned}\mathcal{T} = &\, c_1\,\bar{u}_3 u_1\,\bar{v}_2 v_4 + c_2\,\bar{u}_3\gamma^5 u_1\,\bar{v}_2\gamma^5 v_4 + c_3\,\bar{u}_3 \not{P}_+ u_1\,\bar{v}_2 \not{P}_- v_4 \\ &+ c_4\,\bar{u}_3 \not{P}_+\gamma^5 u_1\,\bar{v}_2 \not{P}_-\gamma^5 v_4 + c_5\,\bar{u}_3 u_1\,\bar{v}_2 \not{P}_- v_4 + c_6\,\bar{u}_3 u_1\,\bar{v}_2 \not{P}_+ v_4,\end{aligned} \tag{5.85}$$

which can be used as a basis for processes such as the electron-proton scattering.

If, in addition, charge symmetry is imposed, the coefficients c_5 and c_6 are no longer independent, since the amplitude must remain invariant under the interchange $P_- \leftrightarrow P_+$. For identical-particle scattering this implies $c_5 = c_6$, whereas for particle–antiparticle scattering one finds $c_5 = -c_6$.

Therefore, the remaining goal is to relate the structures

$$\bar{u}_3 \not{P}_+ u_1\,\bar{v}_2 \not{P}_- v_4, \tag{5.86a}$$
$$\bar{u}_3 \not{P}_+\gamma^5 u_1\,\bar{v}_2 \not{P}_-\gamma^5 v_4, \tag{5.86b}$$
$$\bar{u}_3 \not{P}_+ u_1\,\bar{v}_2 v_4 - \bar{u}_3 u_1\,\bar{v}_2 \not{P}_- v_4. \tag{5.86c}$$

to the S, P, V, A, T decomposition applied in (5.2), which is performed in Appendix 5B.

Appendix 5B: Dirac algebra

In this section we review the Dirac-algebra identities used in deriving the results presented in the main part of this chapter. It also serves as a continuation of Appendix 5A, as we demonstrate the way to express Eqs. (5.86) in the S, P, V, A, T basis.

The identities required for this reduction are neither trivial nor commonly known in the literature; for this reason, we present their derivation in detail. Our ultimate goal is to express the Bhabha scattering amplitude in terms of the basis introduced in Eq. (5.2).

Scattering channel chains

We begin by analyzing the scattering channel relations. The starting point is to apply a trick

$$\gamma^\mu = \gamma_\nu\, g^{\mu\nu} = \not{P}_+ \frac{P_+^\mu}{P_+^2} + \not{q}\frac{q^\mu}{q^2} + \not{P}'_- \frac{P_-'^\mu}{P_-'^2} + \not{n}\frac{n^\mu}{n^2}, \tag{5.87}$$

where we have used the metric decomposition (5.15). Now we combine these results with the identity in Eq. (5.87) to rewrite the vector currents as

$$\begin{aligned}
&\bar{u}_3\gamma^\mu u_1 \\
&= \bar{u}_3 \not{P}_+ u_1 \left(\frac{P_+^\mu}{P_+^2} - \frac{(P_-P_+)}{P_+^2}\frac{P_-'^\mu}{P_-'^2} \right) + \frac{iq^2}{2}\,\bar{u}_3 \not{P}_+ \gamma^5 u_1 \frac{n^\mu}{n^2} + m_e\,\bar{u}_3 u_1 \frac{P_-'^\mu}{P_-'^2},
\end{aligned} \tag{5.88}$$

$$\begin{aligned}
&\bar{v}_2\gamma^\mu v_4 \\
&= \bar{v}_2 \not{P}_- v_4 \frac{P_-'^\mu}{P_-'^2} - \frac{iq^2}{2}\,\bar{v}_2 \not{P}_- \gamma^5 v_4 \frac{n^\mu}{n^2} + m_e\,\bar{v}_2 v_4 \left(\frac{(P_-P_+)}{P_+^2}\frac{P_-'^\mu}{P_-'^2} - \frac{P_+^\mu}{P_+^2} \right).
\end{aligned} \tag{5.89}$$

Their contraction therefore becomes

$$\begin{aligned}
\bar{u}_3\gamma^\mu u_1\,\bar{v}_2\gamma_\mu v_4 = &-\frac{(P_-P_+)}{P_+^2 P_-'^2}\,\bar{u}_3 \not{P}_+ u_1\,\bar{v}_2 \not{P}_- v_4 + \frac{t^2}{4n^2}\,\bar{u}_3 \not{P}_+ \gamma^5 u_1\,\bar{v}_2 \not{P}_- \gamma^5 v_4 \\
&+ m_e \left[\frac{1}{P_-'^2}\,\bar{u}_3 u_1\,\bar{v}_2 \not{P}_- v_4 - \left(\frac{1}{P_+^2} + \frac{(P_-P_+)^2}{P_+^4 P_-'^2} \right) \bar{u}_3 \not{P}_+ u_1\,\bar{v}_2 v_4 \right] \\
&+ m_e^2 \frac{(P_-P_+)}{P_+^2 P_-'^2}\,\bar{u}_3 u_1\,\bar{v}_2 v_4.
\end{aligned} \tag{5.90}$$

So that one can easily rewrite this expression in terms of the Mandelstam variables and express the first "unwanted" term as

$$\begin{aligned}
\bar{u}_3 \not{P}_+ u_1\,\bar{v}_2 \not{P}_- v_4 = &-\frac{su}{s-u}\,\bar{u}_3\gamma^\mu u_1\,\bar{v}_2\gamma_\mu v_4 - \frac{t}{s-u}\,\bar{u}_3 \not{P}_+ \gamma^5 u_1\,\bar{v}_2 \not{P}_- \gamma^5 v_4 \\
&+ m_e \frac{s+u}{s-u} \left[\bar{u}_3 u_1\,\bar{v}_2 \not{P}_- v_4 - \bar{u}_3 \not{P}_+ u_1\,\bar{v}_2 v_4 \right] + m_e^2\,\bar{u}_3 u_1\,\bar{v}_2 v_4.
\end{aligned} \tag{5.91}$$

Acting similarly for the second one, we obtain

$$\begin{aligned}\bar{u}_3 \not{P}_+ \gamma^5 u_1\, \bar{v}_2 \not{P}_- \gamma^5 v_4 = &-\frac{s-u}{t}\, \bar{u}_3 \not{P}_+ u_1\, \bar{v}_2 \not{P}_- v_4 - \frac{su}{t}\, \bar{u}_3 \gamma^\mu u_1\, \bar{v}_2 \gamma^\mu v_4 \\ &+ m_e \frac{s+u}{t} \left[\bar{u}_3 u_1\, \bar{v}_2 \not{P}_- v_4 - \bar{u}_3 \not{P}_+ u_1\, \bar{v}_2 v_4\right] \\ &+ m_e^2 \frac{s-u}{t}\, \bar{u}_3 u_1\, \bar{v}_2 v_4.\end{aligned} \tag{5.92}$$

We observe that both terms can be eliminated provided that the mixed contribution in square brackets can be removed. This, however, is not easy to achieve. Before making the next step in this direction, we have to find the expression for the product of axial currents, similar to (5.90).

The corresponding steps are, in principle, analogous to those illustrated above. First we observe that the triple product $\not{P}_- \not{q} \not{P}_+$ placed between electron spinors can be transformed via

$$\begin{aligned}&\bar{u}_3 \not{P}_- \not{q} \not{P}_+ u_1 = \frac{1}{2}\, \bar{u}_3 \left(\not{p}_3 \not{p}_1 - \not{p}_1 \not{p}_3\right) \not{P}_+ u_1 \\ &= \frac{1}{2}\, \bar{u}_3 \left[4m_e\, (P_- P_+) - 4P_-^2 \not{P}_+\right] u_1 = 2m_e\, (P_- P_+)\, \bar{u}_3 u_1 - 2P_-^2\, \bar{u}_3 \not{P}_+ u_1.\end{aligned} \tag{5.93}$$

For the positron spinor chain we obtain

$$\begin{aligned}&\bar{v}_2 \not{P}_- \not{q} \not{P}_+ v_4 = \frac{1}{2}\, \bar{v}_2 \not{P}_- \left(\not{p}_4 \not{p}_2 - \not{p}_2 \not{p}_4\right) v_4 = \\ &= \frac{1}{2}\, \bar{v}_2 \left[4m_e\, (P_- P_+) + 4P_+^2 \not{P}_-\right] v_4 = 2m_e\, (P_- P_+)\, \bar{v}_2 v_4 + 2P_+^2\, \bar{v}_2 \not{P}_- v_4.\end{aligned} \tag{5.94}$$

Consequently, the $\not{n}$ can be removed from the studied expressions

$$\bar{u}_3 \not{n} \gamma^5 u_1 = -\frac{i}{2} \left[(s+u)\, \bar{u}_3 \not{P}_+ u_1 - m_e\, (s-u)\, \bar{u}_3 u_1\right], \tag{5.95}$$

$$\bar{v}_2 \not{n} \gamma^5 v_4 = \frac{i}{2} \left[(s+u)\, \bar{v}_2 \not{P}_- v_4 + m_e\, (s-u)\, \bar{v}_2 v_4\right]. \tag{5.96}$$

The electron axial current can then be decomposed as

$$\begin{aligned}\bar{u}_3 \gamma^\mu \gamma^5 u_1 = \bar{u}_3 \not{P}_+ \gamma^5 u_1 \left(\frac{P_+^\mu}{P_+^2} - \frac{(P_- P_+)}{P_+^2} \frac{P_-'^\mu}{P_-'^2}\right) - i \frac{s+u}{2}\, \bar{u}_3 \not{P}_+ u_1\, \frac{n^\mu}{n^2} \\ + i m_e \frac{s-u}{2}\, \bar{u}_3 u_1\, \frac{n^\mu}{n^2} - 2m_e\, \bar{u}_3 \gamma^5 u_1\, \frac{q^\mu}{q^2}.\end{aligned} \tag{5.97}$$

Similarly, for the positron axial current we obtain

$$\begin{aligned}\bar{v}_2 \gamma^\mu \gamma^5 v_4 = \bar{v}_2 \not{P}_- \gamma^5 v_4\, \frac{P_-'^\mu}{P_-'^2} + i\, \frac{s+u}{2}\, \bar{v}_2 \not{P}_- v_4\, \frac{n^\mu}{n^2} \\ + i m_e \frac{s-u}{2}\, \bar{v}_2 v_4\, \frac{n^\mu}{n^2} + 2m_e\, \bar{v}_2 \gamma^5 v_4\, \frac{q^\mu}{q^2}.\end{aligned} \tag{5.98}$$

Contracting the two currents yields

$$\begin{aligned}\bar{u}_3\gamma^\mu\gamma^5 u_1\,\bar{v}_2\gamma_\mu\gamma^5 v_4 = &-\frac{4m_e^2}{t}\,\bar{u}_3\gamma^5 u_1\,\bar{v}_2\gamma^5 v_4\\ &-\frac{1}{P_+^2P_-'^2}\frac{s-u}{4}\,\bar{u}_3\not{P}_+\gamma^5 u_1\,\bar{v}_2\not{P}_-\gamma^5 v_4\\ &+\frac{s+u}{4n^2}\,\bar{u}_3\not{P}_+ u_1\,\Big[(s+u)\,\bar{v}_2\not{P}_- v_4 + m_e\,(s-u)\,\bar{v}_2 v_4\Big]\\ &-m_e\frac{s-u}{4n^2}\,\bar{u}_3 u_1\,\Big[(s+u)\,\bar{v}_2\not{P}_- v_4 + m_e\,(s-u)\,\bar{v}_2 v_4\Big].\end{aligned} \tag{5.99}$$

Combining this result with (5.91) allows us to express the "unwanted" structure $\bar{u}_3\not{P}_+u_1\,\bar{v}_2\not{P}_-v_4$ in terms of the desired basis (5.2)

$$\begin{aligned}&\bar{u}_3\not{P}_+u_1\,\bar{v}_2\not{P}_-v_4\\ &= -m_e^2\,\bar{u}_3\gamma^5 u_1\,\bar{v}_2\gamma^5 v_4 + \frac{s-u}{4}\,\bar{u}_3\gamma^\mu u_1\,\bar{v}_2\gamma_\mu v_4 - \frac{t}{4}\,\bar{u}_3\gamma^\mu\gamma^5 u_1\,\bar{v}_2\gamma_\mu\gamma^5 v_4.\end{aligned} \tag{5.100}$$

Proceeding analogously with (5.92), one finds

$$\begin{aligned}\bar{u}_3\not{P}_+\gamma^5 u_1\,\bar{v}_2\not{P}_-\gamma^5 v_4 = &-\frac{(s+u)^2}{4t}\,\bar{u}_3\gamma^\mu u_1\,\bar{v}_2\gamma_\mu v_4 + \frac{s-u}{4}\,\bar{u}_3\gamma^\mu\gamma^5 u_1\,\bar{v}_2\gamma_\mu\gamma^5 v_4\\ &+m_e^2\frac{s-u}{t}\Big[\bar{u}_3 u_1\,\bar{v}_2 v_4 + \bar{u}_3\gamma^5 u_1\,\bar{v}_2\gamma^5 v_4\Big]\\ &-m_e\frac{s+u}{t}\Big[\bar{u}_3\not{P}_+ u_1\,\bar{v}_2 v_4 - \bar{u}_3 u_1\,\bar{v}_2\not{P}_- v_4\Big].\end{aligned} \tag{5.101}$$

Therefore, we still have to find a way to remove the mixed contribution standing in the square brackets. To do this, however, one more nontrivial trick is required. Let's consider the Dirac structure of the form

$$\begin{aligned}&\bar{u}_3\Big[\gamma^\mu\not{P}_-\gamma^\nu - \gamma^\nu\not{P}_-\gamma^\mu\Big]\,u_1\,\bar{v}_2\Big[\gamma_\mu\not{P}_+\gamma_\nu - \gamma_\nu\not{P}_+\gamma_\mu\Big]\,v_4\\ &= 2m_e\Big[-4m_e\,\bar{u}_3\gamma^\nu u_1\,\bar{v}_2\gamma_\nu v_4 + 4\,\bar{u}_3 u_1\,\bar{v}_2\not{P}_- v_4\Big]\\ &-2m_e\Big[4m_e\,\bar{u}_3\gamma^\nu u_1\,\bar{v}_2\gamma_\nu v_4 + 4\,\bar{u}_3\not{P}_+ u_1\,\bar{v}_2 v_4\Big]\\ &+4m_e^2\,\bar{u}_3\sigma^{\mu\nu}u_1\,\bar{v}_2\sigma_{\mu\nu}v_4 + 2t\,\bar{u}_3\gamma^\mu u_1\,\bar{v}_2\gamma_\mu v_4,\end{aligned} \tag{5.102}$$

where only the Dirac equation (5.20) was used.

At the same time, we note that the product of three Dirac matrices introduced above satisfies the identity

$$\gamma^\mu\not{P}\gamma^\nu - \gamma^\nu\not{P}\gamma^\mu = -2i\gamma_\alpha\gamma^5\varepsilon^{\mu\nu\alpha\beta}P_\beta. \tag{5.103}$$

Utilizing this relation, we rewrite the identity (5.102) as

$$\begin{aligned}&\bar{u}_3\left[\gamma^\mu \not{P}_-\gamma^\nu - \gamma^\nu \not{P}_-\gamma^\mu\right] u_1\,\bar{v}_2\left[\gamma_\mu \not{P}_+\gamma_\nu - \gamma_\nu \not{P}_+\gamma_\mu\right] v_4\\&= 2\,(s-u)\;\bar{u}_3\gamma^\mu\gamma^5 u_1\,\bar{v}_2\gamma_\mu\gamma^5 v_4 - 8\,\bar{u}_3\not{P}_+\gamma^5 u_1\,\bar{v}_2\not{P}_-\gamma^5 v_4,\end{aligned} \tag{5.104}$$

which provides an additional relation between the combination $\bar{u}_3\not{P}_+\gamma^5 u_1\,\bar{v}_2\not{P}_-\gamma^5 v_4$ and the mixed term.

$$\begin{aligned}4m_e^2\,\bar{u}_3\sigma^{\mu\nu}u_1\,\bar{v}_2\sigma_{\mu\nu}v_4 &= -2\left(t-8m_e^2\right)\bar{u}_3\gamma^\mu u_1\,\bar{v}_2\gamma_\mu v_4\\&\quad + 2\,(s-u)\;\bar{u}_3\gamma^\mu\gamma^5 u_1\,\bar{v}_2\gamma_\mu\gamma^5 v_4 - 8\,\bar{u}_3\not{P}_+\gamma^5 u_1\,\bar{v}_2\not{P}_-\gamma^5 v_4\\&\quad + 8m_e\left[\bar{u}_3\not{P}_+ u_1\,\bar{v}_2 v_4 - \bar{u}_3 u_1\,\bar{v}_2\not{P}_- v_4\right].\end{aligned} \tag{5.105}$$

Substituting Eq. (5.101) and solving for the remaining mixed bilinear, we obtain

$$\begin{aligned}&m_e\left[\bar{u}_3\not{P}_+ u_1\,\bar{v}_2 v_4 - \bar{u}_3 u_1\,\bar{v}_2\not{P}_- v_4\right]\\&= \frac{s-u}{4}\left[\bar{u}_3 u_1\,\bar{v}_2 v_4 + \bar{u}_3\gamma^5 u_1\,\bar{v}_2\gamma^5 v_4\right] - m_e^2\,\bar{u}_3\gamma^\mu u_1\,\bar{v}_2\gamma_\mu v_4\\&+ \frac{t}{8}\,\bar{u}_3\sigma^{\mu\nu}u_1\,\bar{v}_2\sigma_{\mu\nu}v_4.\end{aligned} \tag{5.106}$$

Applied back to (5.101), this yields

$$\begin{aligned}&4\,\bar{u}_3\not{P}_+\gamma^5 u_1\,\bar{v}_2\not{P}_-\gamma^5 v_4\\&= (s-u)\left[\bar{u}_3 u_1\,\bar{v}_2 v_4 + \bar{u}_3\gamma^5 u_1\,\bar{v}_2\gamma^5 v_4 + \bar{u}_3\gamma^\mu\gamma^5 u_1\,\bar{v}_2\gamma_\mu\gamma^5 v_4\right]\\&+ (s+u)\left[\bar{u}_3\gamma^\mu u_1\,\bar{v}_2\gamma_\mu v_4 - \frac{\bar{u}_3\sigma^{\mu\nu}u_1\,\bar{v}_2\sigma_{\mu\nu}v_4}{2}\right].\end{aligned} \tag{5.107}$$

We would like now to emphasize a crucial aspect of the entire procedure, which is evident from Eq. (5.106), namely the appearance of an overall factor of m_e. In the evaluation of the diagrams considered above, this specific spinor structure always occurs multiplied by this prefactor. If the electron mass were set to zero from the start, these contributions to the S, P, V, A, and T structures would be lost, leading to an incorrect result. It is therefore essential to retain a finite electron mass throughout the projection onto the Dirac basis and only afterwards neglect terms suppressed by m_e^2/s.

It is also obvious that the obtained formulas allow us to complete the proof of the completeness of the basis (5.2).

Before we conclude, let's note that a representation of these formulas in terms of $\not{n}$ can be obtained by using equations (5.76) and (5.95) to remove $\not{P}_\pm$. In particular, for an axial-like chain (5.107) they give

$$\begin{aligned}\frac{16}{t^2}\,\bar{u}_3\not{n}u_1\,\bar{v}_2\not{n}v_4 &= (s-u)\left[\bar{u}_3 u_1\,\bar{v}_2 v_4 + \bar{u}_3\gamma^5 u_1\,\bar{v}_2\gamma^5 v_4 + \bar{u}_3\gamma^\mu\gamma^5 u_1\,\bar{v}_2\gamma_\mu\gamma^5 v_4\right]\\&\quad + (s+u)\left[\bar{u}_3\gamma^\mu u_1\,\bar{v}_2\gamma_\mu v_4 - \frac{\bar{u}_3\sigma^{\mu\nu}u_1\,\bar{v}_2\sigma_{\mu\nu}v_4}{2}\right].\end{aligned} \tag{5.108}$$

While for the mixed term in (5.106) we obtain

$$\begin{aligned}
&2i\left[\bar{u}_3\not{k}\gamma^5 u_1\,\bar{v}_2 v_4+\bar{u}_3 u_1\,\bar{v}_2\not{k}\gamma^5 v_4\right]\\
&=-\frac{\left(4m_e^2+t\right)(s-u)}{4m_e}\,\bar{v}_2 u_1\,\bar{u}_3 v_4-\frac{\left(t-4m_e^2\right)(s-u)}{4m_e}\,\bar{u}_3\gamma^5 u_1\,\bar{v}_2\gamma^5 v_4\\
&+m_e\left(t-4m_e^2\right)\,\bar{v}_2\gamma^\mu u_1\,\bar{u}_3\gamma_\mu v_4-\frac{t\left(t-4m_e^2\right)}{8m_e}\,\bar{v}_2\sigma^{\mu\nu}u_1\,\bar{u}_3\sigma_{\mu\nu}v_4,
\end{aligned}\tag{5.109}$$

whereas for the vector-like chain (5.100) one writes

$$\begin{aligned}
\frac{16}{t}\,\bar{u}_3\not{k}\gamma^5 u_1\,\bar{v}_2\not{k}\gamma^5 v_4=&-(s-u)^2\,\bar{u}_3 u_1\,\bar{v}_2 v_4\\
&+\frac{(s+u)\left((s-u)^2-4m_e^2(s+u)\right)}{t}\,\bar{u}_3\gamma^5 u_1\,\bar{v}_2\gamma^5 v_4\\
&-\left(s^2-u^2\right)\left[\bar{u}_3\gamma^\mu u_1\,\bar{v}_2\gamma_\mu v_4-\frac{\bar{u}_3\sigma^{\mu\nu}u_1\,\bar{v}_2\sigma_{\mu\nu}v_4}{2}\right]\\
&-(s+u)^2\,\bar{u}_3\gamma^\mu\gamma^5 u_1\,\bar{v}_2\gamma_\mu\gamma^5 v_4.
\end{aligned}\tag{5.110}$$

Annihilation channel chains

The identities in the annihilation channel follow the same pattern as those in the scattering channel and can be derived by applying the same sequence of steps. Therefore, it is quite obvious that the difference amounts to the replacement

$$p_2\leftrightarrow -p_3.\tag{5.111}$$

Therefore, to save some space and ink, we present only the final result. The axial chain gives

$$\begin{aligned}
\frac{16}{s^2}\,\bar{v}_2\not{k}u_1\,\bar{u}_3\not{k}v_4=&(t-u)\left[\bar{v}_2 u_1\,\bar{u}_3 v_4+\bar{v}_2\gamma^5 u_1\,\bar{u}_3\gamma^5 v_4+\bar{v}_2\gamma^\mu\gamma^5 u_1\,\bar{u}_3\gamma_\mu\gamma^5 v_4\right]\\
&+(t+u)\left[\bar{v}_2\gamma_\mu u_1\,\bar{u}_3\gamma^\mu v_4-\frac{\bar{v}_2\sigma^{\mu\nu}u_1\,\bar{u}_3\sigma_{\mu\nu}v_4}{2}\right].
\end{aligned}\tag{5.112}$$

While the mixed chain becomes

$$\begin{aligned}
&2i\left[\bar{v}_2\not{k}\gamma^5 u_1\,\bar{u}_3 v_4+\bar{v}_2 u_1\,\bar{u}_3\not{k}\gamma^5 v_4\right]\\
&=-\frac{\left(4m_e^2+s\right)(t-u)}{4m_e}\,\bar{v}_2 u_1\,\bar{u}_3 v_4-\frac{\left(s-4m_e^2\right)(t-u)}{4m_e}\,\bar{v}_2\gamma^5 u_1\,\bar{u}_3\gamma^5 v_4\\
&+m_e\left(s-4m_e^2\right)\,\bar{v}_2\gamma^\mu u_1\,\bar{u}_3\gamma_\mu v_4-\frac{s\left(s-4m_e^2\right)}{8m_e}\,\bar{v}_2\sigma^{\mu\nu}u_1\,\bar{u}_3\sigma_{\mu\nu}v_4.
\end{aligned}\tag{5.113}$$

And, lastly, the vector identity transforms to

$$\begin{aligned}\frac{16}{s}\,\bar{v}_2\not{n}\gamma^5 u_1\,\bar{u}_3\not{n}\gamma^5 v_4 = &-(t-u)^2\;\bar{v}_2 u_1\,\bar{u}_3 v_4\\ &+\frac{(t+u)\left((t-u)^2-4m_e^2\,(t+u)\right)}{s}\,\bar{v}_2\gamma^5 u_1\,\bar{u}_3\gamma^5 v_4\\ &-\left(t^2-u^2\right)\left[\bar{v}_2\gamma^\mu u_1\,\bar{u}_3\gamma_\mu v_4-\frac{\bar{v}_2\sigma^{\mu\nu}u_1\,\bar{u}_3\sigma_{\mu\nu}v_4}{2}\right]\\ &-(t+u)^2\;\bar{v}_2\gamma^\mu\gamma^5 u_1\,\bar{u}_3\gamma_\mu\gamma^5 v_4.\end{aligned}\tag{5.114}$$

As in the scattering case, alternative representations can be obtained by eliminating the $\not{n}$ structures using the Dirac equation (5.20). For the axial chain this leads to

$$\begin{aligned}&\bar{v}_2\left(\not{p}_4-\not{p}_3\right)u_1\,\bar{u}_3\left(\not{p}_1-\not{p}_2\right)v_4\\ &=-4m_e^2\,\bar{v}_2\gamma^5 u_1\,\bar{u}_3\gamma^5 v_4+(t-u)\;\bar{v}_2\gamma^\mu u_1\,\bar{u}_3\gamma_\mu v_4-s\,\bar{v}_2\gamma^\mu\gamma^5 u_1\,\bar{u}_3\gamma^\mu\gamma^5 v_4.\end{aligned}\tag{5.115}$$

Similarly, for the mixed chain one obtains

$$\begin{aligned}&m_e\left[\bar{v}_2\left(\not{p}_4-\not{p}_3\right)u_1\,\bar{u}_3 v_4-\bar{v}_2 u_1\,\bar{u}_3\left(\not{p}_1-\not{p}_2\right)v_4\right]\\ &=\frac{t-u}{2}\left[\bar{v}_2 u_1\,\bar{u}_3 v_4+\bar{v}_2\gamma^5 u_1\,\bar{u}_3\gamma^5 v_4\right]\\ &-2m_e^2\,\bar{v}_2\gamma^\mu u_1\,\bar{u}_3\gamma_\mu v_4+\frac{s}{4}\,\bar{v}_2\sigma^{\mu\nu}u_1\,\bar{u}_3\sigma_{\mu\nu}v_4.\end{aligned}\tag{5.116}$$

Finally, the corresponding vector expression reads

$$\begin{aligned}&\bar{v}_2\left(\not{p}_4-\not{p}_3\right)\gamma^5 u_1\,\bar{u}_3\left(\not{p}_1-\not{p}_2\right)\gamma^5 v_4\\ &=(t-u)\left[\bar{v}_2 u_1\,\bar{u}_3 v_4+\bar{v}_2\gamma^5 u_1\,\bar{u}_3\gamma^5 v_4+\bar{v}_2\gamma^\mu\gamma^5 u_1\,\bar{u}_3\gamma_\mu\gamma^5 v_4\right]\\ &+(t+u)\left[\bar{v}_2\gamma^\mu u_1\,\bar{u}_3\gamma_\mu v_4-\frac{\bar{v}_2\sigma^{\mu\nu}u_1\,\bar{u}_3\sigma_{\mu\nu}v_4}{2}\right].\end{aligned}\tag{5.117}$$

Mathematica-based projection algorithm

The section above demonstrates how Dirac structures can be projected onto the basis (5.2) by exploiting properties of gamma matrices, the Dirac equation, and a set of purely algebraic manipulations. Given the complexity and obscurity of these steps, one naturally asks whether an alternative, self-contained procedure for performing the projection exists, particularly with possible extensions to more complicated reactions—such as lepton-nucleon scattering, where the C-parity argument does not hold, or in parity-broken theories.

Such an alternative approach can indeed be formulated, although it is conceptually distinct from the algebraic manipulations presented above and can be seen as somewhat less transparent. Nevertheless, it serves as a valuable cross-check of the result and can be fully automated.

This method is based on the observation that the set of Dirac structures (S, P, V, A, T) forms a basis of the relevant space. Consequently, any arbitrary Dirac structure x—such as a complex scattering amplitude containing multiple contracted gamma matrices—can be exactly expanded as

$$x = \sum_i c_i y_i, \tag{5.118}$$

where the c_i are numerical decomposition coefficients to be determined, and the basis, in principle, can contain any number of elements. A standard way to extract the coefficients is to introduce a scalar product and consider

$$\langle x, y_j \rangle = \sum_i c_i \langle y_i, y_j \rangle. \tag{5.119}$$

While the scalar product $\langle y_i, y_j \rangle$ is often assumed to be proportional to the Kronecker delta, this orthogonality is not required in general. In the non-orthogonal case, the quantities

$$M_{ij} = \langle y_i, y_j \rangle, \tag{5.120}$$

are known to form a Gram matrix. One thus obtains a linear system of equations that can be solved by matrix inversion

$$c_i = \sum_j \left(M^{-1}\right)_{ij} \langle x, y_j \rangle, \tag{5.121}$$

provided the determinant of the Gram matrix is non-zero.

The only obstacle is, therefore, to understand how the scalar product is organized and how to form the desired non-degenerate system of equations. A straightforward and physically motivated choice is to multiply both sides of the decomposition by a given basis structure, take the sqaure of the absolute value, and sum over all helicity states. This procedure eliminates the external spinors and leaves expressions that depend only on Mandelstam invariants.

As an explicit example, let's consider the scalar chain

$$\begin{aligned}\sum_{s_i} \left| \bar{u}_3 u_1 \, \bar{v}_2 v_4 \times \mathcal{T} \right|^2 = \sum_{s_i} \Big| \bar{u}_3 u_1 \, \bar{v}_2 v_4 \times \Big(& S \, \bar{u}_3 u_1 \, \bar{v}_2 v_4 + P \, \bar{u}_3 \gamma^5 u_1 \, \bar{v}_2 \gamma^5 v_4 \\ & + V \, \bar{u}_3 \gamma_\mu u_1 \, \bar{v}_2 \gamma^\mu v_4 + A \, \bar{u}_3 \gamma_\mu \gamma^5 u_1 \, \bar{v}_2 \gamma^\mu \gamma^5 v_4 + T \, \bar{u}_3 \sigma_{\mu\nu} u_1 \, \bar{v}_2 \sigma^{\mu\nu} v_4 \Big) \Big|^2 .\end{aligned} \tag{5.122}$$

Repeating this procedure for each of the five basis structures yields a complete system of equations for the coefficients S, P, V, A and T. Although the resulting trace calculations are algebraically tedious, they can be efficiently automated using MATHEMATICA together with the FEYNCALC package.

To illustrate this procedure, we consider the structure (5.110), denoted here by $\mathcal{T}_{\text{Ex.}}$. We begin by analyzing the right-hand side of the decomposition

$$\sum_{s_i} \left|\text{Scalar} \times \text{Basis}\right|^2 = 4S_{\text{Ex.}}\,(s+u)^2 + 8\,(u-s)\left(2m_e^2\,V_{\text{Ex.}} + t\,T_{\text{Ex.}}\right), \tag{5.123a}$$

$$\sum_{s_i} \left|\text{Pseudoscalar} \times \text{Basis}\right|^2 = 4t\left(t\,P_{\text{Ex.}} - 4m_e^2\,A_{\text{Ex.}} + 2\,(u-s)\;T_{\text{Ex.}}\right), \tag{5.123b}$$

$$\begin{aligned}\sum_{s_i} \left|\text{Vector} \times \text{Basis}\right|^2 &= 8\,(u-s)\left(2m_e^2\,S_{\text{Ex.}} - t\,A_{\text{Ex.}}\right)\\ &+ 8\left(8m_e^4 - 8m_e^2 s + 2s^2 + 2st + t^2\right)\;V_{\text{Ex.}} + 96m_e^2 t\,T_{\text{Ex.}},\end{aligned} \tag{5.123c}$$

$$\begin{aligned}&\sum_{s_i} \left|\text{Pseudovector} \times \text{Basis}\right|^2\\ &= 8\left[(s-u)\left(t\,V_{\text{Ex.}} + 12m_e^2\,T_{\text{Ex.}}\right) - 2m_e^2 t\,P_{\text{Ex.}} + \left(8m_e^4 + s^2 + u^2\right)\;A_{\text{Ex.}}\right],\end{aligned} \tag{5.123d}$$

$$\begin{aligned}\sum_{s_i} \left|\text{Tensor} \times \text{Basis}\right|^2 &= 8\,(u-s)\left[t\,(S_{\text{Ex.}} + P_{\text{Ex.}}) - 12m_e^2\,A_{\text{Ex.}}\right]\\ &+ 96m_e^2 t\,V_{\text{Ex.}} + 32\left[24m_e^4 - 4m_e^2\,(s+u) + (s-u)^2\right]\;T_{\text{Ex.}},\end{aligned} \tag{5.123e}$$

where the sum over all spins was applied. At the same time, the left-hand side evaluates to

$$\sum_{s_i} \left|\text{Scalar} \times \mathcal{T}_{\text{Ex.}}\right|^2 = 0, \tag{5.124a}$$

$$\sum_{s_i} \left|\text{Pseudoscalar} \times \mathcal{T}_{\text{Ex.}}\right|^2 = 0, \tag{5.124b}$$

$$\sum_{s_i} \left|\text{Vector} \times \mathcal{T}_{\text{Ex.}}\right|^2 = -16stu\,(s-u)\,, \tag{5.124c}$$

$$\sum_{s_i} \left|\text{Pseudovector} \times \mathcal{T}_{\text{Ex.}}\right|^2 = -16su\,(s+u)^2\,, \tag{5.124d}$$

$$\sum_{s_i} \left|\text{Tensor} \times \mathcal{T}_{\text{Ex.}}\right|^2 = -128m_e^2 su\,(s-u)\,, \tag{5.124e}$$

upon performing the same spin sums. Equating both sides and solving the resulting system of linear equations, we obtain

$$S_{\text{Ex.}} = -\,(s-u)^2\,, \tag{5.125a}$$

$$P_{\text{Ex.}} = \frac{(s+u)\left((s-u)^2 - 4m_e^2\,(s+u)\right)}{t}, \tag{5.125b}$$

$$V_{\text{Ex.}} = -\left(s^2 - u^2\right), \tag{5.125c}$$

$$A_{\text{Ex.}} = -\,(s+u)^2\,, \tag{5.125d}$$

$$T_{\text{Ex.}} = \frac{s^2 - u^2}{2}, \tag{5.125e}$$

in exact agreement with the previously derived result (5.110). A straightforward consistency check is provided by verifying that the condition

$$\sum_{s_i} \Big| \mathcal{T}_{\text{Ex.}} - \big(S_{\text{Ex.}}\, \bar{u}_3 u_1\, \bar{v}_2 v_4 + P_{\text{Ex.}}\, \bar{u}_3 \gamma^5 u_1\, \bar{v}_2 \gamma^5 v_4 + V_{\text{Ex.}}\, \bar{u}_3 \gamma_\mu u_1\, \bar{v}_2 \gamma^\mu v_4 \\ + A_{\text{Ex.}}\, \bar{u}_3 \gamma_\mu \gamma^5 u_1\, \bar{v}_2 \gamma^\mu \gamma^5 v_4 + T_{\text{Ex.}}\, \bar{u}_3 \sigma_{\mu\nu} u_1\, \bar{v}_2 \sigma^{\mu\nu} v_4 \big) \Big|^2 = 0, \tag{5.126}$$

holds.

Before concluding, it is worth emphasizing that a generic Dirac structure is not guaranteed to admit a decomposition in the chosen basis, even when written in terms of the external electron and positron spinors u_1, $\bar{v}_2$, $\bar{u}_3$, and v_4. The existence of such a decomposition in the present case follows from the discrete P-, T-, and C-invariance of the QED Bhabha scattering, which eliminates a large class of otherwise possible Dirac structures.

For example, a term of the form

$$\bar{v}_2 \gamma^5 u_1\, \bar{u}_3 \not{n} v_4 - \bar{v}_2 \not{n} u_1\, \bar{u}_3 \gamma^5 v_4, \tag{5.127}$$

cannot be expanded in this basis, despite the fact that it arises in the calculation of the s-channel box diagram. Nevertheless, contributions of this type either vanish upon angular integration or cancel among themselves in the final, physically observable expression.

Appendix 5C: Trace evaluation

We now return to Eq. (5.10) to derive the trace identities, which led to the result in Eq. (5.21). These calculations are algebraically trivial, but the respective steps are quite lengthy.

The first case to consider is $\Gamma_i = \mathbb{1}$, i.e. the scalar bilinear. Due to the presence of γ^5 in the second trace, only vector- and tensor-like Γ_j lead to nonvanishing contributions. The vector one gives

$$\begin{aligned}
&\mathrm{Tr}\Big\{\left(\not{p}_3 + m_e\right)\left(\not{p}_1 + m_e\right)\gamma^\mu\Big\} \times \mathrm{Tr}\Big\{\gamma^5 \not{\mathcal{S}}\left(\not{p}_2 - m_e\right)\left(\not{p}_4 - m_e\right)\gamma_\mu\Big\} \\
&= 4m_e\left(p_1^\mu + p_3^\mu\right) \times 4i\varepsilon_{\mu\alpha\beta\sigma} p_2^\alpha p_4^\beta \mathcal{S}^\sigma = 8m_e P_-^\mu \times 4i\varepsilon_{\mu\alpha\beta\sigma} P_+^\alpha q^\beta \mathcal{S}^\sigma \\
&= 32 i m_e \left(\mathcal{S}n\right).
\end{aligned} \tag{5.128}$$

While the tensor amounts to

$$\begin{aligned}
&\mathrm{Tr}\Big\{\left(\not{p}_3 + m_e\right)\left(\not{p}_1 + m_e\right)\sigma^{\mu\nu}\Big\} \times \mathrm{Tr}\Big\{\gamma^5 \not{\mathcal{S}}\left(\not{p}_2 - m_e\right)\left(\not{p}_4 - m_e\right)\sigma_{\mu\nu}\Big\} \\
&= 4i\left(p_1^\mu p_3^\nu - p_1^\nu p_3^\mu\right) \times 4m_e \varepsilon_{\mu\nu\alpha\beta}\left(p_2^\alpha + p_4^\alpha\right)\mathcal{S}^\beta = 8i p_1^\mu p_3^\nu \times 8m_e \varepsilon_{\mu\nu\alpha\beta} P_+^\alpha \mathcal{S}^\beta \\
&= -8i P_-^\mu q^\nu \times 8m_e \varepsilon_{\mu\nu\alpha\beta} P_+^\alpha \mathcal{S}^\beta = 64 i m_e \left(\mathcal{S}n\right),
\end{aligned} \tag{5.129}$$

verifying the result given in Table 5.3. We therefore proceed with the pseudoscalar choice, $\Gamma_i = \gamma^5$.

In contrast to the scalar case—where the second trace in Eq. (5.10) vanished for most combinations due to the presence of γ^5 originating from the spinor sum ansatz (5.7)—here it is the first trace that enforces the vanishing of nearly all contributions. The only nontrivial case that has enough gamma matrices to survive is the combination with $\Gamma_j = \sigma^{\mu\nu}$

$$\begin{aligned}
&\mathrm{Tr}\Big\{\left(\not{p}_3 + m_e\right)\gamma^5\left(\not{p}_1 + m_e\right)\sigma^{\mu\nu}\Big\} \times \mathrm{Tr}\Big\{\not{\mathcal{S}}\left(\not{p}_2 + m_e\right)\left(\not{p}_4 - m_e\right)\sigma_{\mu\nu}\Big\} \\
&= 4\varepsilon_{\mu\nu\alpha\beta} p_1^\alpha p_3^\beta \times 4i m_e \left(\mathcal{S}^\nu q^\mu - \mathcal{S}^\mu q^\nu\right) = 0.
\end{aligned} \tag{5.130}$$

But we see that it now vanishes due to the antisymmetry of the Levi–Civita tensor together with the definition $q = p_1 - p_3$. Consequently, the pseudoscalar structure drops out entirely from B_n and does not contribute.

We next consider the case $\Gamma_i = \gamma^\mu$. The choices $\Gamma_j = \mathbb{1}$ and $\Gamma_j = \gamma^5$ reduce to structures already analyzed above, and the corresponding result is antisymmetric under the interchange $i \leftrightarrow j$. We therefore first examine $\Gamma_j = \gamma^\mu$

$$\begin{aligned}
&\mathrm{Tr}\Big\{\left(\not{p}_3 + m_e\right)\gamma^\mu\left(\not{p}_1 + m_e\right)\gamma^\nu\Big\} \times \mathrm{Tr}\Big\{\gamma^5 \not{\mathcal{S}}\left(\not{p}_2 - m_e\right)\gamma_\mu\left(\not{p}_4 - m_e\right)\gamma_\nu\Big\} \\
&= 4\left(p_1^\mu p_3^\nu - g^{\mu\nu}\left(p_1 p_3\right) + p_1^\nu p_3^\mu - m_e^2 g^{\mu\nu}\right) \times 4i m_e q^\alpha \mathcal{S}^\beta \varepsilon_{\mu\nu\alpha\beta} = 0,
\end{aligned} \tag{5.131}$$

again by antisymmetry of the Levi–Civita tensor.

We now turn to the axial–vector structure, $\Gamma_j = \gamma^\mu\gamma^5$

$$\begin{aligned}
&\mathrm{Tr}\Big\{\big(\not{p}_3 + m_e\big)\,\gamma^\mu\,\big(\not{p}_1 + m_e\big)\,\gamma^\nu\gamma^5\Big\} \times \mathrm{Tr}\Big\{\not{\mathcal{S}}\,\big(\not{p}_2 - m_e\big)\,\gamma_\mu\,\big(\not{p}_4 - m_e\big)\,\gamma_\nu\Big\} \\
&= -4i\varepsilon_{\mu\nu\alpha\beta}p_1^\alpha p_3^\beta \times 4m_e\left[-\left(p_4^\mu + p_2^\mu\right)\mathcal{S}^\nu - q^\nu\mathcal{S}^\mu + g^{\mu\nu}\left(q\mathcal{S}\right)\right] \\
&= -32im_e\varepsilon_{\mu\nu\alpha\beta}P_-^\alpha q^\beta P_+^\mu\mathcal{S}^\nu = 32im_e\left(\mathcal{S}n\right).
\end{aligned} \tag{5.132}$$

The tensor contribution, $\Gamma_j = \sigma^{\mu\nu}$, is quite an involved case. However, we find the first trace is proportional to the momentum transfer q

$$\mathrm{Tr}\Big\{\big(\not{p}_3 + m_e\big)\,\gamma^\mu\,\big(\not{p}_1 + m_e\big)\,\sigma^{\alpha\beta}\Big\} = 4im_e\left(q^\alpha g^{\beta\mu} - q^\beta g^{\alpha\mu}\right). \tag{5.133}$$

Contracting the Lorentz tensor structure $q^\alpha g^{\beta\mu}$ with the second trace yields

$$\frac{i}{2}\,\mathrm{Tr}\Big\{\gamma^5\not{\mathcal{S}}\,\big(\not{p}_2 - m_e\big)\,\gamma^\mu\,\big(\not{p}_4 - m_e\big)\,\big(\not{q}\gamma_\mu - \gamma_\mu\not{q}\big)\Big\}, \tag{5.134}$$

where contraction of γ^μ with γ_μ eliminates two gamma matrices. Using the properties of γ^5 then, the result reduces to

$$-4\varepsilon_{\mu\nu\alpha\beta}p_2^\mu p_4^\nu q^\alpha\mathcal{S}^\beta = 0, \tag{5.135}$$

and the same conclusion follows for the term proportional to $q^\beta g^{\alpha\mu}$.

We now proceed to the axial–vector case, $\Gamma_i = \gamma^\mu\gamma^5$. The diagonal contribution with $\Gamma_j = \gamma_\mu\gamma^5$ vanishes in the same manner as the diagonal vector term considered above, since the two γ^5 matrices can be anticommuted through the trace and combined, reducing the expression to a previously considered structure. We therefore turn to the tensor case, $\Gamma_j = \sigma_{\mu\nu}$.

The first trace evaluates to

$$\mathrm{Tr}\Big\{\big(\not{p}_3 + m_e\big)\,\gamma^\mu\gamma^5\,\big(\not{p}_1 + m_e\big)\,\sigma^{\alpha\beta}\Big\} = -8m_e\varepsilon_{\alpha\beta\mu\nu}P_-^\nu, \tag{5.136}$$

while the second trace reads

$$-\,\mathrm{Tr}\Big\{\not{\mathcal{S}}\,\big(\not{p}_2 + m_e\big)\,\gamma_\mu\,\big(\not{p}_4 - m_e\big)\,\sigma_{\alpha\beta}\Big\}. \tag{5.137}$$

It is useful to note that

$$\mathrm{Tr}\Big\{\not{\mathcal{S}}\gamma_\mu\sigma_{\alpha\beta}\Big\} = 4i\left(\mathcal{S}^\beta g^{\alpha\mu} - \mathcal{S}^\alpha g^{\beta\mu}\right), \tag{5.138}$$

which vanishes upon the contraction with $\varepsilon_{\alpha\beta\mu\nu}$ from the first trace.

The remaining contribution therefore involves traces containing six gamma matrices, which must be evaluated explicitly. Fortunately, all terms proportional to the metric tensors $g^{\alpha\beta}$, $g^{\alpha\mu}$, and $g^{\beta\mu}$, as well as symmetric momentum combinations such as $p_2^\mu p_4^\alpha + p_2^\alpha p_4^\mu$ and $p_2^\mu p_4^\beta + p_2^\beta p_4^\mu$, vanish upon contraction with the antisymmetric Levi–Civita tensor. This significantly reduces the number of surviving terms. One is left with

$$\begin{aligned}
&\mathrm{Tr}\Big\{\big(\not{p}_3 + m_e\big)\,\gamma^\mu\gamma^5\,\big(\not{p}_1 + m_e\big)\,\sigma^{\alpha\beta}\Big\} \\
&\times(-1)\,\mathrm{Tr}\Big\{\not{\mathcal{S}}\,\big(\not{p}_2 + m_e\big)\,\gamma_\mu\,\big(\not{p}_4 - m_e\big)\,\sigma_{\alpha\beta}\Big\} \\
&= -8m_e\varepsilon_{\alpha\beta\mu\nu}P_-^\nu \times 4i\mathcal{S}^\mu\left(p_4^\alpha p_2^\beta - p_2^\alpha p_4^\beta\right) = -64im_e\left(\mathcal{S}n\right).
\end{aligned} \tag{5.139}$$

Finally, the tensor–tensor contribution with $\Gamma_i = \sigma^{\mu\nu}$ and $\Gamma_j = \sigma_{\mu\nu}$ vanishes in the second trace due to the presence of γ^5, since the number of remaining gamma matrices is odd. Comparing the resulting expressions with Eq. (5.21), we confirm the entries listed in Table 5.3.

Appendix 5D: Explicit calculation of t-channel box diagram

In this Appendix we provide the detailed derivation of the imaginary part of the t-channel box correction, shown in Fig. 5.2f and given in Eq. (5.56). We begin by expanding the numerator of the integrand as

$$\begin{aligned}&\bar{u}_3\gamma^\mu \not{k}\gamma^\nu u_1\, \bar{v}_2\gamma_\nu \not{k}\gamma_\mu v_4 + \bar{u}_3\gamma^\mu \not{k}\gamma^\nu u_1\, \bar{v}_2\gamma_\nu \left(-\not{p}_1 - \not{p}_2 + m_e\right)\gamma_\mu v_4 \\ &+ m_e\, \bar{u}_3\gamma^\mu\gamma^\nu u_1\, \bar{v}_2\gamma_\nu \not{k}\gamma_\mu v_4 + m_e\, \bar{u}_3\gamma^\mu\gamma^\nu u_1\, \bar{v}_2\gamma_\nu \left(-\not{p}_1 - \not{p}_2 + m_e\right)\gamma_\mu v_4,\end{aligned} \tag{5.140}$$

and proceed by sequentially evaluating the k-independent, linear, and quadratic terms, after which the projection onto the chosen basis is performed.

Basic angular integrals

We begin by adopting the standard center-of-mass parametrization of the external four-momenta. In terms of the Mandelstam variable s and the velocity parameter β, the momenta read

$$p_1 = \frac{\sqrt{s}}{2}\,(1,\,0,\,0,\,\beta)\,, \qquad p_2 = \frac{\sqrt{s}}{2}\,(1,\,0,\,0,\,-\beta)\,, \tag{5.141}$$

$$p_3 = \frac{\sqrt{s}}{2}\,(1,\,\beta\sin\theta,\,0,\,\beta\cos\theta)\,, \qquad p_4 = \frac{\sqrt{s}}{2}\,(1,\,-\beta\sin\theta,\,0,\,-\beta\cos\theta)\,. \tag{5.142}$$

This choice makes the scattering plane explicit: the incoming momenta are aligned with the z-axis, while the outgoing particles are scattering by the polar angle θ in the $x-z$ plane.

The four-vector n is orthogonal to the scattering plane. With the above conventions and $\varepsilon^{0123} = 1$, we obtain

$$n^\mu = \sqrt{-n^2}\,(0,\,0,\,1,\,0)\,, \tag{5.143}$$

where the normalization factor is given by

$$\sqrt{-n^2} = \frac{s^{3/2}\beta^2}{4}\sin\theta. \tag{5.144}$$

We now parametrize the loop momentum k. In spherical coordinates relative to the center-of-mass frame, it can be written as

$$k = \frac{\sqrt{s}}{2}\,(1,\,\beta\sin\theta_{\mathbf{k}}\cos\phi_{\mathbf{k}},\,\beta\sin\theta_{\mathbf{k}}\sin\phi_{\mathbf{k}},\,\beta\cos\theta_{\mathbf{k}})\,. \tag{5.145}$$

Now, weaponized by this knowledge, we turn to the evaluation of the angular integrals. These are, in fact, quite trivial and can be fully expressed in terms of the Legendre functions of the second kind Q_0 and Q_1.

For later convenience, we introduce the denominators

$$D_i = (p_i - k)^2 - m_\gamma^2. \tag{5.146}$$

The lowest-order angular integrals appearing in the calculation are of the form

$$I_1 \equiv \int \frac{1}{D_i}\frac{d\Omega_{\mathbf{k}}}{4\pi} = \frac{1}{2Y}\ln\left(\frac{X+Y}{X-Y}\right), \tag{5.147}$$

where denoted

$$X = 2m_e^2 - m_\gamma^2 - \frac{s}{2}, \tag{5.148a}$$

$$Y = \frac{\beta^2 s}{2}. \tag{5.148b}$$

The proof is straightforward, as the integrand yields the form $(a + b\cos\theta)^{-1}$, which is, essentially, the definition of Q_0.

Beyond the scalar integral I_1, we will also encounter angular averages in which one of the propagators appears in the numerator, in particular

$$\begin{aligned} I_2(p_1, p_3) &\equiv \int \frac{D_3}{D_1}\frac{d\Omega_{\mathbf{k}}}{4\pi} \\ &= \frac{X}{2Y}\ln\left(\frac{X+Y}{X-Y}\right) + \frac{u-t}{u+t}\left[1 - \frac{X}{2Y}\ln\left(\frac{X+Y}{X-Y}\right)\right]. \end{aligned} \tag{5.149}$$

This case is quite trivial as well, since the numerator differs only by a term proportional to $\cos\theta$, which can be expressed via the Legendre function Q_1.

We next turn to integrals containing two propagators

$$I_t \equiv \int \frac{1}{D_1 D_3}\frac{d\Omega_{\mathbf{k}}}{4\pi} = \sqrt{\frac{t+u}{t}}\frac{1}{2YZ}\ln\left(\frac{Z + Y\sqrt{\frac{t}{t+u}}}{Z - Y\sqrt{\frac{t}{t+u}}}\right), \tag{5.150}$$

where, for compactness, we have introduced the auxiliary quantity

$$Z = \sqrt{m_\gamma^4 + s\beta^2 m_\gamma^2 + \frac{s^2\beta^4}{4}\frac{t}{t+u}}. \tag{5.151}$$

Although the calculation of this integral follows the same logic as in the cases of I_1 and $I_2(p_1, p_3)$, the algebra becomes slightly more involved. It can be undertaken by employing the Feynman parameters; the details of the procedure are outlined in Appendix 5E.

Finally, from these we also derive

$$\int \frac{[k(P_+ - P_-)]}{D_1 D_3}\frac{d\Omega_{\mathbf{k}}}{4\pi} = \left(m_\gamma^2 + Y\right) I_t + I_1, \tag{5.152}$$

which immediately follows from the simple observation that

$$\begin{aligned} [k(P_+ - P_-)] &= [k(p_3 + p_4)] - [k(p_1 + p_3)] \\ &= \frac{s}{2} - \left(2m_e^2 - m_\gamma^2\right) + \frac{D_1 + D_3}{2}, \end{aligned} \tag{5.153}$$

where the scalar products kp_1 and kp_3 were expressed from the respective propagators D_1 and D_3.

Linear angular integrals

We now consider linear integrals, i.e. those containing a single factor of k^μ in the numerator. Although they may appear more involved at first sight, they simplify considerably once the symmetry properties of the angular integration are properly exploited.

First, any term proportional to (kn) vanishes upon the integration over the ϕ angle, since n^μ is orthogonal to the scattering plane. Second, the product of propagators

$$\begin{aligned}&\frac{1}{(p_1-k)^2-m_\gamma^2}\frac{1}{(p_3-k)^2-m_\gamma^2}\\&=\frac{1}{\left(P_-+\frac{q}{2}-k\right)^2-m_\gamma^2}\frac{1}{\left(P_--\frac{q}{2}-k\right)^2-m_\gamma^2},\end{aligned}\tag{5.154}$$

is an even function of the momentum transfer q. Combining this with the basis decomposition

$$\begin{aligned}k^\mu=&\frac{(kq)}{t}q^\mu+\frac{[k\,(P_++P_-)]}{s}\,(P_++P_-)^\mu\\&+\frac{[k\,(P_+-P_-)]}{u}\,(P_+-P_-)^\mu+\frac{(kn)}{n^2}n^\mu,\end{aligned}\tag{5.155}$$

we conclude that the for the terms linear in k we can simply replace

$$k^\mu\to\frac{1}{2}\,(P_-+P_+)^\mu+\frac{[k\,(P_+-P_-)]}{u}\,(P_+-P_-)^\mu\,.\tag{5.156}$$

Therefore, all linear integrals reduce to combinations of the scalar structures already computed in the previous section.

Quadratic angular integrals

The next step is to decompose the integrals quadratic in the integration variable k. Given the symmetries of the integrand, the most general parameterization reads

$$\begin{aligned}\int\frac{k^\alpha k^\beta}{D_1D_3}\frac{d\Omega_{\mathbf{k}}}{4\pi}=&\,c_1\,g^{\alpha\beta}+c_2\,(P_++P_-)^\alpha\,(P_++P_-)^\beta+c_3\,q^\alpha q^\beta\\&+c_4\,(P_+-P_-)^\alpha\,(P_+-P_-)^\beta\\&+c_5\left[(P_+-P_-)^\alpha\,(P_++P_-)^\beta+(P_+-P_-)^\beta\,(P_++P_-)^\alpha\right].\end{aligned}\tag{5.157}$$

The coefficients c_i can be extracted by contracting the above decomposition with each tensor structure appearing in the basis. In this way, the tensor equation is reduced to a set of scalar relations for the unknown coefficients, which can be easily solved.

The left-hand side contractions yield

$$\int \frac{g_{\alpha\beta}k^\alpha k^\beta}{D_1 D_3}\frac{d\Omega_{\mathbf{k}}}{4\pi} = m_e^2 I_t, \tag{5.158a}$$

$$\int \frac{(P_+ + P_-)_\alpha (P_+ + P_-)_\beta k^\alpha k^\beta}{D_1 D_3}\frac{d\Omega_{\mathbf{k}}}{4\pi} = \frac{s^2}{4} I_t, \tag{5.158b}$$

$$\int \frac{q_\alpha q_\beta k^\alpha k^\beta}{D_1 D_3}\frac{d\Omega_{\mathbf{k}}}{4\pi} = \frac{I_2(p_1,p_3)-1}{2}, \tag{5.158c}$$

$$\int \frac{(P_+ - P_-)_\alpha (P_+ - P_-)_\beta k^\alpha k^\beta}{D_1 D_3}\frac{d\Omega_{\mathbf{k}}}{4\pi} = \frac{I_2(p_1,p_3)+1-2X(2I_1 - XI_t)}{2}, \tag{5.158d}$$

$$\int \frac{(P_+ - P_-)_\alpha (P_+ + P_-)_\beta k^\alpha k^\beta}{D_1 D_3}\frac{d\Omega_{\mathbf{k}}}{4\pi} = \frac{s}{2}(I_1 - XI_t), \tag{5.158e}$$

while the right-hand side give

$$g_{\alpha\beta} \times \text{Decomposition} = 4c_1 + sc_2 + tc_3 + uc_4, \tag{5.159a}$$

$$(P_+ + P_-)_\alpha (P_+ + P_-)_\beta \times \text{Decomposition} = sc_1 + s^2 c_2, \tag{5.159b}$$

$$q_\alpha q_\beta \times \text{Decomposition} = tc_1 + t^2 c_3, \tag{5.159c}$$

$$(P_+ - P_-)_\alpha (P_+ - P_-)_\beta \times \text{Decomposition} = uc_1 + u^2 c_4, \tag{5.159d}$$

$$(P_+ - P_-)_\alpha (P_+ + P_-)_\beta \times \text{Decomposition} = suc_5, \tag{5.159e}$$

resulting in

$$c_1 = m_e^2 I_t - \frac{s}{4}I_t - \frac{I_2(p_1,p_3)-1}{2t} - \frac{I_2(p_1,p_3)+1-4XI_1+2X^2 I_t}{2u}, \tag{5.160a}$$

$$c_2 = \left(1 - \frac{2m_e^2}{s}\right)\frac{I_t}{2} + \frac{I_2(p_1,p_3)-1}{2st} + \frac{I_2(p_1,p_3)+1-4XI_1+2X^2 I_t}{2su}, \tag{5.160b}$$

$$c_3 = \frac{I_2(p_1,p_3)-1}{t^2} + \left(\frac{s}{4t} - \frac{m_e^2}{t}\right) I_t + \frac{I_2(p_1,p_3)+1-4XI_1+2X^2 I_t}{2tu}, \tag{5.160c}$$

$$c_4 = \frac{I_2(p_1,p_3)+1-4XI_1+2X^2 I_t}{u^2} + \left(\frac{s}{4u} - \frac{m_e^2}{u}\right) I_t + \frac{I_2(p_1,p_3)-1}{2tu}, \tag{5.160d}$$

$$c_5 = \frac{I_1 - XI_t}{2u}, \tag{5.160e}$$

thus completing the calculation of the angular integrals. The answer is expressed in terms of simple scalar function I_1, I_t and $I_2(p_1,p_3)$. However, we still have to handle the Dirac projection.

Projecting the free term

As we have previously discussed, the numerator splits in three parts

$$\text{Numerator} = \text{Free} + \text{Linear} + \text{Quadratic}, \tag{5.161}$$

in terms of the powers of loop momentum k^μ.

Let's start by projecting the free term onto the basis (5.2). This can be easily done by utilizing the formulas given in Appendix 5B.

$$\begin{aligned}\text{Free} &= m_e\,\bar{u}_3\gamma^\mu\gamma^\nu u_1\,\bar{v}_2\gamma_\nu\left(-\not{p}_1-\not{p}_2+m_e\right)\gamma_\mu v_4\\ &= 2m_e^2\,\bar{u}_3u_1\,\bar{v}_2v_4-2m_e^2\,\bar{u}_3\gamma^5u_1\,\bar{v}_2\gamma^5v_4\\ &+2m_e^2\,\bar{u}_3\gamma^\mu u_1\,\bar{v}_2\gamma_\mu v_4-2m_e^2\,\bar{u}_3\gamma^\mu\gamma^5u_1\,\bar{v}_2\gamma_\mu\gamma^5v_4.\end{aligned}\tag{5.162}$$

Projecting the linear term

Let us now turn to the linear terms, which read

$$\text{Linear} = \bar{u}_3\gamma^\mu\not{k}\gamma^\nu u_1\,\bar{v}_2\gamma_\nu\left(-\not{p}_1-\not{p}_2+m_e\right)\gamma_\mu v_4+m_e\,\bar{u}_3\gamma^\mu\gamma^\nu u_1\,\bar{v}_2\gamma_\nu\not{k}\gamma_\mu v_4.\tag{5.163}$$

To proceed, we substitute the decomposition (5.156) for $\not{k}$. It is convenient to organize the resulting expression according to the two independent Dirac structures that arise, namely the combinations $\not{P}_+ + \not{P}_-$ and $\not{P}_+ - \not{P}_-$. We begin with the contribution proportional to $\not{P}_+ + \not{P}_-$

$$\begin{aligned}&\frac{1}{2}\,\bar{u}_3\gamma^\mu\left(\not{P}_+ + \not{P}_-\right)\gamma^\nu u_1\,\bar{v}_2\gamma_\nu\left(-\not{p}_1-\not{p}_2+m_e\right)\gamma_\mu v_4\\ &+\frac{m_e}{2}\,\bar{u}_3\gamma^\mu\gamma^\nu u_1\,\bar{v}_2\gamma_\nu\left(\not{P}_+ + \not{P}_-\right)\gamma_\mu v_4\\ &= m_e^2\,\bar{u}_3u_1\,\bar{v}_2v_4+m_e^2\,\bar{u}_3\gamma^5u_1\,\bar{v}_2\gamma^5v_4-\left(m_e^2+\frac{3s}{2}\right)\bar{u}_3\gamma^\mu u_1\,\bar{v}_2\gamma_\mu v_4\\ &+\left(m_e^2+\frac{s}{2}\right)\bar{u}_3\gamma^\mu\gamma^5u_1\,\bar{v}_2\gamma_\mu\gamma^5v_4+\frac{m_e^2}{2}\,\bar{u}_3\sigma^{\mu\nu}u_1\,\bar{v}_2\sigma_{\mu\nu}v_4.\end{aligned}\tag{5.164}$$

We next consider the part proportional to $\not{P}_+ - \not{P}_-$. Performing the same Dirac algebra and rearranging the result in the standard S, P, V, A, and T basis, we obtain

$$\begin{aligned}&\bar{u}_3\gamma^\mu\left(\not{P}_+ - \not{P}_-\right)\gamma^\nu u_1\,\bar{v}_2\gamma_\nu\left(-\not{p}_1-\not{p}_2+m_e\right)\gamma_\mu v_4\\ &+m_e\,\bar{u}_3\gamma^\mu\gamma^\nu u_1\,\bar{v}_2\gamma_\nu\left(\not{P}_+ - \not{P}_-\right)\gamma_\mu v_4\\ &=\left(8m_e^2-s-\frac{t}{2}\right)\bar{u}_3u_1\,\bar{v}_2v_4-\left(4m_e^2+s+\frac{t}{2}\right)\bar{u}_3\gamma^5u_1\,\bar{v}_2\gamma^5v_4\\ &+s\,\bar{u}_3\gamma^\mu u_1\,\bar{v}_2\gamma_\mu v_4+\left(s-6m_e^2\right)\bar{u}_3\gamma^\mu\gamma^5u_1\,\bar{v}_2\gamma_\mu\gamma^5v_4\\ &+\left(m_e^2-\frac{t}{4}\right)\bar{u}_3\sigma^{\mu\nu}u_1\,\bar{v}_2\sigma_{\mu\nu}v_4+2m_e\left[\bar{u}_3u_1\,\bar{v}_2\not{P}_-v_4+\bar{u}_3\not{P}_+u_1\,\bar{v}_2v_4\right].\end{aligned}\tag{5.165}$$

In this expression we have suppressed the overall prefactor of $[k\,(P_+ - P_-)]\,/u$, which is understood to multiply the entire result.

Finally, we remark that the last line contains a mixed structure which, although reminiscent of (5.106), cannot be decomposed into the desired basis. This term, however, does not contribute in the final result: it cancels once the linear contributions are combined with the quadratic ones.

Projecting the quadratic term

The quadratic term in its full glory reads

$$\begin{aligned}\text{Quad} = {} & c_1\,\bar{u}_3\gamma^\mu\gamma^\alpha\gamma^\nu u_1\,\bar{v}_2\gamma_\nu\gamma_\alpha\gamma_\mu v_4 \\ & + c_2\,\bar{u}_3\gamma^\mu\left(\not{P}_+ + \not{P}_-\right)\gamma^\nu u_1\,\bar{v}_2\gamma_\nu\left(\not{P}_+ + \not{P}_-\right)\gamma_\mu v_4 \\ & + c_3\,\bar{u}_3\gamma^\mu\not{q}\gamma^\nu u_1\,\bar{v}_2\gamma_\nu\not{q}\gamma_\mu v_4 \\ & + c_4\,\bar{u}_3\gamma^\mu\left(\not{P}_+ - \not{P}_-\right)\gamma^\nu u_1\,\bar{v}_2\gamma_\nu\left(\not{P}_+ - \not{P}_-\right)\gamma_\mu v_4 \\ & + c_5\left[\bar{u}_3\gamma^\mu\left(\not{P}_+ - \not{P}_-\right)\gamma^\nu u_1\,\bar{v}_2\gamma_\nu\left(\not{P}_+ + \not{P}_-\right)\gamma_\mu v_4\right. \\ & \left. + \bar{u}_3\gamma^\mu\left(\not{P}_+ + \not{P}_-\right)\gamma^\nu u_1\,\bar{v}_2\gamma_\nu\left(\not{P}_+ - \not{P}_-\right)\gamma_\mu v_4\right].\end{aligned} \tag{5.166}$$

The first term is purely algebraic and reduces immediately to vector and axial vector structures

$$\bar{u}_3\gamma^\mu\gamma^\alpha\gamma^\nu u_1\,\bar{v}_2\gamma_\nu\gamma_\alpha\gamma_\mu v_4 = 10\,\bar{u}_3\gamma^\mu u_1\,\bar{v}_2\gamma_\mu v_4 - 6\,\bar{u}_3\gamma^\mu\gamma^5 u_1\,\bar{v}_2\gamma_\mu\gamma^5 v_4. \tag{5.167}$$

Next, we consider the term quadratic in $\not{P}_+ + \not{P}_-$. After performing the Dirac algebra and rearranging the result, we obtain

$$\begin{aligned}&\bar{u}_3\gamma^\mu\left(\not{P}_+ + \not{P}_-\right)\gamma^\nu u_1\,\bar{v}_2\gamma_\nu\left(\not{P}_+ + \not{P}_-\right)\gamma_\mu v_4 \\ &= -2m_e^2\,\bar{u}_3 u_1\,\bar{v}_2 v_4 - 2m_e^2\,\bar{u}_3\gamma^5 u_1\,\bar{v}_2\gamma^5 v_4 \\ &+ \left(2m_e^2 + 3s\right)\,\bar{u}_3\gamma^\mu u_1\,\bar{v}_2\gamma_\mu v_4 - \left(2m_e^2 + s\right)\,\bar{u}_3\gamma^\mu\gamma^5 u_1\,\bar{v}_2\gamma_\mu\gamma^5 v_4 \\ &- m_e^2\,\bar{u}_3\sigma^{\mu\nu}u_1\,\bar{v}_2\sigma_{\mu\nu}v_4.\end{aligned} \tag{5.168}$$

The third contribution involves $\not{q}$ on both fermion chains. Its reduction yields only P, V, and A structures

$$\begin{aligned}&\bar{u}_3\gamma^\mu\not{q}\gamma^\nu u_1\,\bar{v}_2\gamma_\nu\not{q}\gamma_\mu v_4 \\ &= -8m_e^2\,\bar{u}_3\gamma^5 u_1\,\bar{v}_2\gamma^5 v_4 + 2t\,\bar{u}_3\gamma^\mu u_1\,\bar{v}_2\gamma_\mu v_4 - 2t\,\bar{u}_3\gamma^\mu\gamma^5 u_1\,\bar{v}_2\gamma_\mu\gamma^5 v_4.\end{aligned} \tag{5.169}$$

We now turn to the quadratic term built from $\not{P}_+ - \not{P}_-$. Proceeding as before, we find

$$\begin{aligned}&\bar{u}_3\gamma^\mu\left(\not{P}_+ - \not{P}_-\right)\gamma^\nu u_1\,\bar{v}_2\gamma_\nu\left(\not{P}_+ - \not{P}_-\right)\gamma_\mu v_4 = \left(2m_e^2 - s + u\right)\,\bar{u}_3 u_1\,\bar{v}_2 v_4 \\ &+ \left(2m_e^2 - s + u\right)\,\bar{u}_3\gamma^5 u_1\,\bar{v}_2\gamma^5 v_4 + \left(2m_e^2 - s + 2u\right)\,\bar{u}_3\gamma^\mu u_1\,\bar{v}_2\gamma_\mu v_4 \\ &+ \left(2m_e^2 - s - 2u\right)\,\bar{u}_3\gamma^\mu\gamma^5 u_1\,\bar{v}_2\gamma_\mu\gamma^5 v_4 + \frac{2m_e^2 - t}{2}\,\bar{u}_3\sigma^{\mu\nu}u_1\,\bar{v}_2\sigma_{\mu\nu}v_4.\end{aligned} \tag{5.170}$$

Finally, we consider the mixed contribution proportional to the most complicated term, proportional to c_5. Its reduction leads to

$$\begin{aligned}
&\bar{u}_3\gamma^\mu\left(\not{P}_+ - \not{P}_-\right)\gamma^\nu u_1\,\bar{v}_2\gamma_\nu\left(\not{P}_+ + \not{P}_-\right)\gamma_\mu v_4 \\
&+\bar{u}_3\gamma^\mu\left(\not{P}_+ + \not{P}_-\right)\gamma^\nu u_1\,\bar{v}_2\gamma_\nu\left(\not{P}_+ - \not{P}_-\right)\gamma_\mu v_4 \\
&=-4m_e\left[\bar{u}_3 u_1\,\bar{v}_2\not{P}_- v_4 + \bar{u}_3\not{P}_+ u_1\,\bar{v}_2 v_4\right].
\end{aligned} \tag{5.171}$$

The crucial feature of the last term is that it cancels exactly against the analogous non-projectable Dirac structure encountered in the evaluation of the linear contribution. This nontrivial cancellation between the linear and quadratic parts of $\mathcal{T}_{t-\mathrm{box}}$ completes the calculation, as the full amplitude can now be expressed in the S, P, V, A, T basis. With this final simplification, we collect the remaining terms and recover the result shown in Eq. (5.57).

Appendix 5E: Angular integration with Feynman parameters

In this Appendix we demonstrate how the integral (5.150) can be reduced to a form mimicking the basic integral (5.147). The key idea is to combine the two propagators using a Feynman parameter and then perform the angular integration in a manner similar to the I_1.

We begin by rewriting the denominators in a form that makes their angular dependence explicit

$$D_1 = (p_1 - k)^2 - m_\gamma^2 = X + Y\,(\hat{\mathbf{n}}_k \hat{\mathbf{n}}_1)\,, \tag{5.172}$$

$$D_3 = (p_3 - k)^2 - m_\gamma^2 = X + Y\,(\hat{\mathbf{n}}_k \hat{\mathbf{n}}_3)\,, \tag{5.173}$$

where we have introduced the unit direction vectors

$$\hat{\mathbf{n}}_1 = (0,\, 0,\, 1)\,, \tag{5.174a}$$

$$\hat{\mathbf{n}}_3 = (\sin\theta,\, 0,\, \cos\theta)\,, \tag{5.174b}$$

$$\hat{\mathbf{n}}_k = (\sin\theta_{\mathbf{k}} \cos\phi_{\mathbf{k}},\, \sin\theta_{\mathbf{k}} \sin\phi_{\mathbf{k}},\, \cos\theta_{\mathbf{k}})\,. \tag{5.174c}$$

To combine the denominators, we introduce a Feynman parameter z as

$$\frac{1}{D_1 D_3} = \int_0^1 \frac{dz}{D^2}, \tag{5.175}$$

where the combined denominator reads

$$\begin{aligned} D &= z\,[X + Y\,(\hat{\mathbf{n}}_k \hat{\mathbf{n}}_3)] + (1-z)\,[X + Y\,(\hat{\mathbf{n}}_k \hat{\mathbf{n}}_1)] \\ &= X + Y\,[\hat{\mathbf{n}}_k\,(z\hat{\mathbf{n}}_3 + (1-z)\,\hat{\mathbf{n}}_1)]\,. \end{aligned} \tag{5.176}$$

Let us define the mixing vector then

$$\mathbf{v} = z\hat{\mathbf{n}}_3 + (1-z)\,\hat{\mathbf{n}}_1, \tag{5.177}$$

so that

$$D^2 = [X + Y\,(\hat{\mathbf{n}}_k \mathbf{v})]^2 \sim (a + b\cos\theta_{\mathbf{k}})^2\,, \tag{5.178}$$

and the integral over angular variables can be easily taken. As a result

$$I_t = \int_0^1 \frac{dz}{X^2 - Y^2 \mathbf{v}^2}. \tag{5.179}$$

The square of the mixing vector follows directly from its definition

$$\mathbf{v}^2 = 1 - 2z\,(1-z)\,(1 - \cos\theta)\,. \tag{5.180}$$

The remaining z-integration is elementary, since the denominator is a quadratic polynomial in z. Carrying it out leads to

$$I_t = \sqrt{\frac{t+u}{t}}\,\frac{1}{2YZ}\,\ln\left(\frac{Z + Y\sqrt{\frac{t}{t+u}}}{Z - Y\sqrt{\frac{t}{t+u}}}\right). \tag{5.181}$$

Appendix 5F: Explicit calculation of s-channel box diagram

We now turn to Eq. (5.62) in order to carry the same procedure as outlined in Appendix 5D. As a first step, we eliminate the triple-γ combinations as

$$\bar{v}_2\gamma_\nu \not{k}\gamma_\mu u_1\, \bar{u}_3\gamma^\mu \not{k}\gamma^\nu v_4 = 2\,\bar{v}_2\not{k}u_1\,\bar{u}_3\not{k}v_4 + 2\,\bar{v}_2\not{k}\gamma^5 u_1\,\bar{u}_3\not{k}\gamma^5 v_4, \tag{5.182a}$$

$$\bar{v}_2\gamma_\nu \not{k}\gamma_\mu u_1\, \bar{u}_3\gamma^\nu \not{k}\gamma^\mu v_4 = 2\,\bar{v}_2\not{k}u_1\,\bar{u}_3\not{k}v_4 - 2\,\bar{v}_2\not{k}\gamma^5 u_1\,\bar{u}_3\not{k}\gamma^5 v_4, \tag{5.182b}$$

and now perform the angular integration and subsequently carry out the projection. Just like before, we begin with the k-independent terms and then consider the linear and quadratic contributions. Many non-projectable terms vanish upon integration over $\phi_{\mathbf{k}}$, while the remaining ones cancel between the linear and quadratic parts.

Basic angular integrals

Terms that do not contain powers of k in the numerator can be reduced to scalar integrals, in complete analogy with the treatment of the t-box contribution. Moreover, the s-box case is technically simpler, since no photon mass is needed to regulate the infrared behavior. We therefore proceed directly to the explicit results.

We begin by introducing the propagator denominators in the form

$$D_i' = (p_i - k)^2 - m_e^2. \tag{5.183}$$

The lowest-order angular integrals are again expressed in terms of the Legendre function Q_0. They reduce to

$$I_1' \equiv \int \frac{1}{D_i'}\frac{d\Omega_{\mathbf{k}}}{4\pi} = -\frac{1}{s\beta}\ln\left(\frac{1+\beta}{1-\beta}\right). \tag{5.184}$$

Integrals with the numerator can be decomposed in terms of Q_1, yielding

$$I_2'(p_1,p_3) \equiv \int \frac{D_3'}{D_1'}\frac{d\Omega_{\mathbf{k}}}{4\pi} = \left(1+\frac{2t}{s\beta^2}\right) - \frac{t}{s\beta^3}\ln\left(\frac{1+\beta}{1-\beta}\right), \tag{5.185a}$$

$$I_2'(p_1,p_4) \equiv \int \frac{D_4'}{D_1'}\frac{d\Omega_{\mathbf{k}}}{4\pi} = \left(1+\frac{2u}{s\beta^2}\right) - \frac{u}{s\beta^3}\ln\left(\frac{1+\beta}{1-\beta}\right). \tag{5.185b}$$

Finally, the integrals involving two propagators in the denominator take the form

$$I_t' \equiv \int \frac{1}{D_1' D_3'}\frac{d\Omega_{\mathbf{k}}}{4\pi} = -\frac{1}{2st}\frac{1}{\beta_t}\ln\left(\frac{\beta_t+1}{\beta_t-1}\right), \tag{5.186a}$$

$$I_u' \equiv \int \frac{1}{D_1' D_4'}\frac{d\Omega_{\mathbf{k}}}{4\pi} = -\frac{1}{2su}\frac{1}{\beta_u}\ln\left(\frac{\beta_u+1}{\beta_u-1}\right), \tag{5.186b}$$

where we denoted

$$\beta_t = \sqrt{1 - \frac{4m_e^2}{t}}, \tag{5.187a}$$

$$\beta_u = \sqrt{1 - \frac{4m_e^2}{u}}. \tag{5.187b}$$

From these expressions, we also immediately derive

$$\int \frac{[k\,(P_- - P_+)]}{D_1' D_3'} \frac{d\Omega_{\mathbf{k}}}{4\pi} = -\frac{sI_t' + 2I_1'}{2}, \tag{5.188a}$$

$$\int \frac{(kq)}{D_1' D_4'} \frac{d\Omega_{\mathbf{k}}}{4\pi} = -\frac{sI_u' + 2I_1'}{2}. \tag{5.188b}$$

Linear angular integrals

Before proceeding, it is useful to analyze the symmetry properties of the remaining integrands. First, we recall that terms linear in (kn) vanish after angular integration, which simplifies the calculation of terms linear in the variable k. Second, we note that the products of propagators can be rewritten as

$$\begin{aligned} &\frac{1}{(p_1 - k)^2 - m_e^2} \frac{1}{(p_3 - k)^2 - m_e^2} \\ &\qquad = \frac{1}{\left(P_- + \frac{q}{2} - k\right)^2 - m_e^2} \frac{1}{\left(P_- - \frac{q}{2} - k\right)^2 - m_e^2}, \end{aligned} \tag{5.189a}$$

$$\begin{aligned} &\frac{1}{(p_1 - k)^2 - m_e^2} \frac{1}{(k - p_4)^2 - m_e^2} \\ &\qquad = \frac{1}{\left(P_- + \frac{q}{2} - k\right)^2 - m_e^2} \frac{1}{\left(k - P_+ - \frac{q}{2}\right)^2 - m_e^2}. \end{aligned} \tag{5.189b}$$

The first expression is even in q, while the second is symmetric under $P_- \leftrightarrow P_+$. These symmetry properties together with the basis decomposition allow us to replace the loop momentum k in terms, which are linear in it, as

$$k^\mu \to \frac{1}{2}(P_- + P_+)^\mu + \frac{[k\,(P_- - P_+)]}{u}(P_- - P_+)^\mu, \tag{5.190a}$$

$$k^\mu \to \frac{(kq)}{t} q^\mu + \frac{1}{2}(P_- + P_+)^\mu. \tag{5.190b}$$

Therefore, terms linear in k reduce to linear combinations of the scalar integrals computed in the previous section (just as in the t-box case).

Quadratic angular integrals

The final piece of this puzzle are the quadratic integrals. Their evaluation follows the same reduction algorithm that was applied previously in Sec. 5.5.

Given the symmetry properties of the integrands, the most general parametrization can be written in the form

$$\begin{aligned}\int \frac{k^\alpha k^\beta}{D_1' D_3'} \frac{d\Omega_{\mathbf{k}}}{4\pi} &= c_{t1}\, g^{\alpha\beta} + c_{t2}\, (P_+ + P_-)^\alpha (P_+ + P_-)^\beta + c_{t3}\, q^\alpha q^\beta \\ &+ c_{t4}\, (P_+ - P_-)^\alpha (P_+ - P_-)^\beta \\ &+ c_{t5} \left[(P_+ - P_-)^\alpha (P_+ + P_-)^\beta + (P_+ - P_-)^\beta (P_+ + P_-)^\alpha\right],\end{aligned} \tag{5.191a}$$

$$\begin{aligned}\int \frac{k^\alpha k^\beta}{D_1' D_4'} \frac{d\Omega_{\mathbf{k}}}{4\pi} &= c_{u1}\, g^{\alpha\beta} + c_{u2}\, (P_+ + P_-)^\alpha (P_+ + P_-)^\beta + c_{u3}\, q^\alpha q^\beta \\ &+ c_{u4}\, (P_+ - P_-)^\alpha (P_+ - P_-)^\beta + c_{u5} \left[(P_+ + P_-)^\alpha q^\beta + (P_+ + P_-)^\beta q^\alpha\right].\end{aligned} \tag{5.191b}$$

To determine the coefficients c_t and c_u, we proceed exactly as in the t-channel case: both sides of the above decompositions are contracted sequentially with each of the Lorentz structures entering the left-hand side, yielding a closed linear system to be solved.

For the direct diagram, they give

$$c_{t1} = \left[-\left(\frac{1}{s}+\frac{1}{u}\right)\frac{s^2}{4} I_t' + \frac{1}{2}\left(\frac{1}{t}-\frac{1}{u}\right) - \frac{s}{u} I_1' - \frac{1}{2}\left(\frac{1}{t}+\frac{1}{u}\right) I_2'(p_1,p_3)\right], \tag{5.192a}$$

$$c_{t2} = \frac{1}{s}\left[\frac{s}{2}\left(1+\frac{s}{2u}\right) I_t' - \frac{1}{2}\left(\frac{1}{t}-\frac{1}{u}\right) + \frac{s}{u} I_1' + \frac{1}{2}\left(\frac{1}{t}+\frac{1}{u}\right) I_2'(p_1,p_3)\right], \tag{5.192b}$$

$$c_{t3} = \frac{1}{t}\left[\left(\frac{1}{s}+\frac{1}{u}\right)\frac{s^2}{4} I_t' - \left(\frac{1}{t}-\frac{1}{2u}\right) + \frac{s}{u} I_1' + \left(\frac{1}{t}+\frac{1}{2u}\right) I_2'(p_1,p_3)\right], \tag{5.192c}$$

$$c_{t4} = \frac{1}{u}\left[\frac{s}{4}\left(1+\frac{2s}{u}\right) I_t' - \left(\frac{1}{2t}-\frac{1}{u}\right) + \frac{2s}{u} I_1' + \left(\frac{1}{2t}+\frac{1}{u}\right) I_2'(p_1,p_3)\right], \tag{5.192d}$$

$$c_{t5} = \frac{sI_t' + 2I_1'}{4u}. \tag{5.192e}$$

Whereas for the crossed diagram, one obtains

$$c_{u1} = \left[-\left(\frac{1}{s}+\frac{1}{t}\right)\frac{s^2}{4} I_u' - \frac{1}{2}\left(\frac{1}{t}-\frac{1}{u}\right) - \frac{s}{t} I_1' - \frac{1}{2}\left(\frac{1}{t}+\frac{1}{u}\right) I_2'(p_1,p_4)\right], \tag{5.193a}$$

$$c_{u2} = \frac{1}{s}\left[\frac{s}{2}\left(1+\frac{s}{2t}\right) I_u' + \frac{1}{2}\left(\frac{1}{t}-\frac{1}{u}\right) + \frac{s}{t} I_1' + \frac{1}{2}\left(\frac{1}{t}+\frac{1}{u}\right) I_2'(p_1,p_4)\right], \tag{5.193b}$$

$$c_{u3} = \frac{1}{t}\left[\frac{s}{4}\left(1+\frac{2s}{t}\right) I_u' + \left(\frac{1}{t}-\frac{1}{2u}\right) + \frac{2s}{t} I_1' + \left(\frac{1}{t}+\frac{1}{2u}\right) I_2'(p_1,p_4)\right], \tag{5.193c}$$

$$c_{u4} = \frac{1}{u}\left[\frac{s^2}{4}\left(\frac{1}{s}+\frac{1}{t}\right) I_u' + \left(\frac{1}{2t}-\frac{1}{u}\right) + \frac{s}{t} I_1' + \left(\frac{1}{2t}+\frac{1}{u}\right) I_2'(p_1,p_4)\right], \tag{5.193d}$$

$$c_{u5} = -\frac{sI_u' + 2I_1'}{4t}. \tag{5.193e}$$

It only remains now to analyze the resulting Dirac structures and project them onto the S, P, V, A, T basis.

Projecting the linear term

Upon the angular integration, the linear terms evaluate to

$$\begin{aligned} &-\int \frac{1}{D_1}\left[\frac{L_1+\frac{2[k(P_--P_+)]}{u}L_3}{D_3}-\frac{L_2+\frac{2(kq)}{t}L_4}{D_4}\right]\frac{d\Omega_{\mathbf{k}}}{4\pi} \\ &=-I_t\,L_1+I_u\,L_2+\left(\frac{s}{2}I_t+I_1\right)\frac{2L_3}{u}-\left(\frac{s}{2}I_u+I_1\right)\frac{2L_4}{t}, \end{aligned} \tag{5.194}$$

where the four Dirac structures L_1, L_2, L_3 and L_4 can be projected onto S, P, V, A, T basis by applying the formulas summarized in Appendix 5B. After performing the projection, the expressions simplify considerably and yield a compact form.

We begin with L_1, which reduces to

$$\begin{aligned} L_1&=\bar v_2\gamma^\nu\left(\not P_-+\not P_+\right)\not p_3 u_1\,\bar u_3\gamma_\nu v_4+\bar v_2\gamma^\nu u_1\,\bar u_3\not p_1\left(\not P_-+\not P_+\right)\gamma_\nu v_4\\ &=-4m_e^2\,\bar v_2\gamma^5 u_1\,\bar u_3\gamma^5 v_4+s\left(\bar v_2\gamma^\mu u_1\,\bar u_3\gamma_\mu v_4-\bar v_2\gamma^\mu\gamma^5 u_1\,\bar u_3\gamma_\mu\gamma^5 v_4\right). \end{aligned} \tag{5.195}$$

The second structure, L_2, exhibits a similar pattern, differing only by sign changes in the pseudoscalar and axial vector terms

$$\begin{aligned} L_2&=\bar v_2\gamma^\nu\left(\not P_-+\not P_+\right)\not p_4 u_1\,\bar u_3\gamma_\nu v_4+\bar v_2\gamma^\nu u_1\,\bar u_3\gamma_\nu\left(\not P_-+\not P_+\right)\not p_1 v_4\\ &=4m_e^2\,\bar v_2\gamma^5 u_1\,\bar u_3\gamma^5 v_4+s\left(\bar v_2\gamma^\mu u_1\,\bar u_3\gamma_\mu v_4+\bar v_2\gamma^\mu\gamma^5 u_1\,\bar u_3\gamma_\mu\gamma^5 v_4\right). \end{aligned} \tag{5.196}$$

The structure L_3 is slightly more cumbersome. In addition, it gives rise to some unprojectable terms

$$\begin{aligned} L_3&=\bar v_2\gamma^\nu\left(\not P_--\not P_+\right)\not p_3 u_1\,\bar u_3\gamma_\nu v_4+\bar v_2\gamma^\nu u_1\,\bar u_3\not p_1\left(\not P_--\not P_+\right)\gamma_\nu v_4\\ &=-\frac{12m_e^2-s-2u}{4}\,\bar v_2 u_1\,\bar u_3 v_4+\frac{12m_e^2+s+2u}{4}\,\bar v_2\gamma^5 u_1\,\bar u_3\gamma^5 v_4\\ &+\left(u-t+m_e^2\right)\bar v_2\gamma^\mu u_1\,\bar u_3\gamma_\mu v_4+s\,\bar v_2\gamma^\mu\gamma^5 u_1\,\bar u_3\gamma_\mu\gamma^5 v_4\\ &-\frac{s}{8}\,\bar v_2\sigma^{\mu\nu}u_1\,\bar u_3\sigma_{\mu\nu}v_4-\frac{2im_e}{s}\left(\bar v_2\gamma^5 u_1\,\bar u_3\not k v_4-\bar v_2\not k u_1\,\bar u_3\gamma^5 v_4\right). \end{aligned} \tag{5.197}$$

Lastly, L_4 is decomposable into

$$\begin{aligned} L_4&=\bar v_2\gamma^\nu\not q\not p_4 u_1\,\bar u_3\gamma_\nu v_4+\bar v_2\gamma^\nu u_1\,\bar u_3\gamma_\nu\not q\not p_1 v_4\\ &=\frac{12m_e^2-s-2t}{4}\,\bar v_2 u_1\,\bar u_3 v_4-\frac{12m_e^2+s+2t}{4}\,\bar v_2\gamma^5 u_1\,\bar u_3\gamma^5 v_4\\ &+\left(t-u+m_e^2\right)\bar v_2\gamma^\mu u_1\,\bar u_3\gamma_\mu v_4-s\,\bar v_2\gamma^\mu\gamma^5 u_1\,\bar u_3\gamma_\mu\gamma^5 v_4\\ &-\frac{s}{8}\,\bar v_2\sigma^{\mu\nu}u_1\,\bar u_3\sigma_{\mu\nu}v_4+\frac{2im_e}{s}\left(\bar v_2\gamma^5 u_1\,\bar u_3\not k v_4+\bar v_2\not k u_1\,\bar u_3\gamma^5 v_4\right). \end{aligned} \tag{5.198}$$

Although the last terms in L_3 and L_4 lie outside the standard projection basis, they do not contribute to the final result. Upon combining the linear contributions with the quadratic terms, these problematic pieces cancel identically. This cancellation mirrors the mechanism already encountered in the analysis of the t-channel box diagram and ensures that the full amplitude can ultimately be expressed within the desired basis.

Projecting the quadratic term

Having determined the tensor decomposition, we now project the quadratic contribution onto the chosen bilinear basis. Since both vector- and axial-type structures are present, $\bar{v}_2 \not{k} u_1 \, \bar{u}_3 \not{k} v_4$ and $\bar{v}_2 \not{k} \gamma^5 u_1 \, \bar{u}_3 \not{k} \gamma^5 v_4$, we will have to do twice as much work.

We begin with the contraction involving the metric tensor $g^{\alpha\beta}$, which immediately gives

$$g^{\alpha\beta} \, \bar{v}_2 \gamma_\alpha u_1 \, \bar{u}_3 \gamma_\beta v_4 = \bar{v}_2 \gamma_\alpha u_1 \, \bar{u}_3 \gamma^\alpha v_4, \tag{5.199a}$$

$$g^{\alpha\beta} \, \bar{v}_2 \gamma_\alpha \gamma^5 u_1 \, \bar{u}_3 \gamma_\beta \gamma^5 v_4 = \bar{v}_2 \gamma_\alpha \gamma^5 u_1 \, \bar{u}_3 \gamma^\alpha \gamma^5 v_4. \tag{5.199b}$$

The next contribution involves the symmetric tensor $(P_+ + P_-)^\alpha \, (P_+ + P_-)^\beta$. For the s-channel graphs, this trivially reduces if we apply the Dirac equation

$$(P_+ + P_-)^\alpha \, (P_+ + P_-)^\beta \; \bar{v}_2 \gamma_\alpha u_1 \, \bar{u}_3 \gamma_\beta v_4 = 0, \tag{5.200a}$$

$$(P_+ + P_-)^\alpha \, (P_+ + P_-)^\beta \; \bar{v}_2 \gamma_\alpha \gamma^5 u_1 \, \bar{u}_3 \gamma_\beta \gamma^5 v_4 = -4m_e^2 \, \bar{v}_2 \gamma^5 u_1 \, \bar{u}_3 \gamma^5 v_4. \tag{5.200b}$$

The third contribution involves the symmetric tensor $q^\alpha q^\beta$. It requires a slightly more extended reduction and yields

$$\begin{aligned} q^\alpha q^\beta \, \bar{v}_2 \gamma_\alpha u_1 \, \bar{u}_3 \gamma_\beta v_4 &= -\frac{s+2t}{4} \left(\bar{v}_2 u_1 \, \bar{u}_3 v_4 + \bar{v}_2 \gamma^5 u_1 \, \bar{u}_3 \gamma^5 v_4 \right) \\ &+ \frac{s+2t}{4} \, \bar{v}_2 \gamma^\mu u_1 \, \bar{u}_3 \gamma_\mu v_4 - \frac{s}{4} \, \bar{v}_2 \gamma^\mu \gamma^5 u_1 \, \bar{u}_3 \gamma_\mu \gamma^5 v_4 - \frac{s}{8} \, \bar{v}_2 \sigma^{\mu\nu} u_1 \, \bar{u}_3 \sigma_{\mu\nu} v_4, \end{aligned} \tag{5.201a}$$

$$\begin{aligned} &q^\alpha q^\beta \, \bar{v}_2 \gamma_\alpha \gamma^5 u_1 \, \bar{u}_3 \gamma_\beta \gamma^5 v_4 = \\ &= \frac{1}{4} \Big[(t-u) \left(\bar{v}_2 u_1 \, \bar{u}_3 v_4 + \bar{v}_2 \gamma^5 u_1 \, \bar{u}_3 \gamma^5 v_4 \right) - \left(s - 4m_e^2 \right) \, \bar{v}_2 \gamma^\mu u_1 \, \bar{u}_3 \gamma_\mu v_4 \\ &+ (t-u) \, \bar{v}_2 \gamma^\mu \gamma^5 u_1 \, \bar{u}_3 \gamma_\mu \gamma^5 v_4 + \frac{s - 4m_e^2}{2} \, \bar{v}_2 \sigma^{\mu\nu} u_1 \, \bar{u}_3 \sigma_{\mu\nu} v_4 \Big]. \end{aligned} \tag{5.201b}$$

The fourth tensor structure, built from $(P_+ - P_-)^\alpha \, (P_+ - P_-)^\beta$, is treated analogously and leads to

$$
\begin{aligned}
&(P_+ - P_-)^\alpha\,(P_+ - P_-)^\beta\;\bar v_2\gamma_\alpha u_1\,\bar u_3\gamma_\beta v_4\\
&=\frac{s+2u}{4}\left(\bar v_2\gamma^5 u_1\,\bar u_3\gamma^5 v_4+\bar v_2 u_1\,\bar u_3 v_4\right)\\
&+\frac{s+2u}{4}\,\bar v_2\gamma^\mu u_1\,\bar u_3\gamma_\mu v_4+\frac{s}{4}\,\bar v_2\gamma^\mu\gamma^5 u_1\,\bar u_3\gamma_\mu\gamma^5 v_4-\frac{s}{8}\,\bar v_2\sigma^{\mu\nu}u_1\,\bar u_3\sigma_{\mu\nu}v_4,
\end{aligned}
\tag{5.202a}
$$

$$
\begin{aligned}
&(P_+ - P_-)^\alpha\,(P_+ - P_-)^\beta\;\bar v_2\gamma_\alpha\gamma^5 u_1\,\bar u_3\gamma_\beta\gamma^5 v_4\\
&=-\frac{1}{4}\Big[(t-u)\left(\bar v_2 u_1\,\bar u_3 v_4+\bar v_2\gamma^5 u_1\,\bar u_3\gamma^5 v_4\right)-\left(s-4m_e^2\right)\,\bar v_2\gamma^\mu u_1\,\bar u_3\gamma_\mu v_4\\
&+(t-u)\;\bar v_2\gamma^\mu\gamma^5 u_1\,\bar u_3\gamma_\mu\gamma^5 v_4+\frac{s-4m_e^2}{2}\,\bar v_2\sigma^{\mu\nu}u_1\,\bar u_3\sigma_{\mu\nu}v_4\Big].
\end{aligned}
\tag{5.202b}
$$

Finally, the fifth structure vanishes when contracted with the vector-like currents. The contraction with the axial-like currents yields (for the direct and crossed diagrams)

$$
\begin{aligned}
&\left[(P_+ - P_-)^\alpha\,(P_+ + P_-)^\beta+(P_+ - P_-)^\beta\,(P_+ + P_-)^\alpha\right]\;\bar v_2\gamma_\alpha\gamma^5 u_1\,\bar u_3\gamma_\beta\gamma^5 v_4\\
&=-\frac{4im_e}{s}\left(\bar v_2\not{p}u_1\,\bar u_3\gamma^5 v_4-\bar v_2\gamma^5 u_1\,\bar u_3\not{p}v_4\right),
\end{aligned}
\tag{5.203a}
$$

$$
\begin{aligned}
&\left[(P_+ - P_-)^\alpha\,q^\beta+(P_+ - P_-)^\beta\,q^\alpha\right]\;\bar v_2\gamma_\alpha\gamma^5 u_1\,\bar u_3\gamma_\beta\gamma^5 v_4\\
&=-\frac{4im_e}{s}\left(\bar v_2\not{p}u_1\,\bar u_3\gamma^5 v_4+\bar v_2\gamma^5 u_1\,\bar u_3\not{p}v_4\right).
\end{aligned}
\tag{5.203b}
$$

It can be easily seen that these unprojectable terms cancel exactly with those arising from the calculation of terms linear in k variable.

The final step consists in inserting the derived expressions into the formula (5.62) and systematically collecting all contributions. The procedure itself is entirely mechanical, as all necessary ingredients have been established above. After carrying out this substitution and performing the required simplifications, we reproduce the result from Eq. (5.63).

Chapter 6

Conclusion

> Rest and enjoyment are sweet
> because of labor.
> *William Ellery Channing*

During the past decades, axions and ALPs have been among the most extensively studied extensions of the Standard Model of particle physics. Motivated by the strong CP problem, dark matter, the muon magnetic moment anomaly, and other open questions, extensive experimental and observational programs have been developed to probe these pseudoscalar states across a broad mass range, from peV to TeV scales. Searches have been conducted in diverse environments, including supernova explosions, helioscopes, precision atomic experiments, and high-energy collider facilities. The resulting constraints exhibit qualitatively different sensitivities in the low- and high-mass regimes. In the low-mass region, astrophysical observations provide strong and relatively model-independent bounds. In contrast, for masses $m_a \gtrsim 10\,\mathrm{MeV}$, existing constraints are significantly weaker and generally more model-dependent.

Several factors contribute to this situation. First, laboratory searches in the MeV–GeV mass range typically require large integrated luminosities to compensate for suppressed production rates and small couplings. Second, and more importantly, the sensitivity in this domain depends critically on the assumed structure of ALP couplings to SM fields. Both production mechanisms and decay signatures vary substantially depending on whether the ALP predominantly couples to photons, gluons, or fermions. As a consequence, exclusion limits may differ by more than an order of magnitude under different coupling assumptions. Moreover, limits derived within different effective field theory frameworks, or under different assumptions about branching ratios and total widths, are frequently presented together without uniform normalization conventions, complicating the comparison and, sometimes, obscuring the real experimental sensitivity.

The goal of this work was to systematically revise the least constrained part of the parameter space, namely the MeV–GeV mass region. Being at the same time too heavy for most astrophysical probes and too light for LHC searches, this region relies primarily on electron–positron collider experiments and high-intensity low-energy electron beam facilities. Our guiding principle was to remain conservative and to make minimal assumptions about the origin of ALP interactions. Whenever additional assumptions were unavoidable, they were explicitly stated and appropriately justified.

The first study within this program concerned ALP searches at the BESIII and Belle II electron–positron colliders. Existing analyses are typically performed under the assumption of a single ALP–photon coupling, while direct couplings to leptons are neglected.

The usual argument is that introducing additional production channels can only enhance the sensitivity. However, this expectation does not generally hold once both production and decay processes are treated consistently. In particular, the signal is strongly affected by the presence of lepton couplings. As a consequence, the currently weak constraints on ALP–lepton interactions can lead to up to an order-of-magnitude weakening of the derived ALP-photon bounds, especially in the lower-mass region of a few hundred MeV, where leptonic decay modes dominate over the diphoton channel.

The second aspect of this work concerned the implications of recent measurements of $(g-2)_\ell$, with particular emphasis on the long-standing muon anomaly. At the time this study was initiated, the discrepancy between experimental measurements and the Standard Model prediction was quoted at the level of approximately 4σ, which could be accommodated by an ALP with a mass of order 1 GeV and couplings satisfying $g_{a\gamma\gamma}g_{a\mu\mu} \sim 10^{-7}$, if lepton and photon coupling are taken into account simultaneously.

Subsequently, significant progress in lattice determinations of the hadronic contributions reduced the tension to below the 1σ level. This development, in turn, placed one of the most stringent constraints on any possible BSM scenarios and motivated an extension of the analysis to include vector and axial vector mediators.

It is also important to emphasize that the current uncertainty is dominated by theoretical inputs, so that further reduction of these will undoubtedly constrain the parameter space even more.

Next, the direct searches for ALPs at electron–positron colliders were shown to be limited below masses of a few hundred MeV. The reason for this limitation lies in the finite angular resolution for highly collimated diphoton pairs, which significantly reduces the reconstruction efficiency in this regime and leaves an open window in parameter space.

The proposed search strategy, based on Bethe–Heitler pair production, had previously been employed by the A1@MAMI Collaboration in searches for dark photons at higher masses. Here, this approach was extended to scalar and pseudoscalar mediators and adapted to the updated MAGIX@MESA setup. As it operates below the hadroproduction threshold, it avoids associated hadronic uncertainties and offers an exceptionally clean, well-controlled environment for BSM searches.

The resulting bounds not only provide one of the few direct probes of ALP–lepton couplings in this mass range, but also improve constraints on the dark photon kinetic mixing parameter ϵ. These sensitivity estimates were obtained under conservative assumptions regarding the MAGIX kinematic cuts, bin resolutions, and beam operation periods, thereby leaving substantial room for further improvement through optimized experimental conditions.

Finally, another experiment probing a complementary region of parameter space is currently being pursued. A JLab program utilizing polarized positron scattering off an unpolarized atomic target will provide access to polarization-sensitive observables, such as the beam-normal single-spin asymmetry, measured with unprecedented precision. The setup allows for efficient background suppression, and preliminary studies suggest a precision at the level of 1 ppm or smaller (for comparison, previously operated polarized electron–nucleon scattering experiments at JLab achieved a precision of 10 ppb).

Although a pseudoscalar particle (such as an ALP), despite being among the most theoretically well-motivated scenarios, does not contribute to the aforementioned asymme-

try, under the conservative assumptions adopted in this work, however, competitive constraints are obtained for a scalar mediator. The reason for this is that the scalar–lepton coupling induces a helicity flip, whereas the dominant QED background—mediated by photon exchange—is helicity conserving. This mismatch enhances sensitivity to certain BSM contributions. Nevertheless, for the dark photon scenario it is still possible to get a visible improvement over the existing results, demonstrating the power of this approach.

At leading order, the observable B_n arises from the interference between tree-level QED amplitudes and the imaginary parts of the corresponding 1-loop corrections. The extraction of these imaginary parts is itself technically demanding, especially in the context of box diagrams, but in addition, the amplitude must be projected onto the complete set of Dirac bilinears S, P, V, A, T, which requires an extensive and algebraically demanding manipulation of gamma matrices and Dirac structures.

A major advantage of this framework is its straightforward generalization to double-spin asymmetries, as these are expressed in terms of the exact same S, P, V, A, T amplitudes. Setting up an experiment with a polarized electron target would, however, be experimentally demanding, as it would lead to substantially reduced event rates and consequently larger statistical uncertainties. Nevertheless, such an extension would be highly valuable and constitutes a well-motivated direction for future investigation. In addition, a dedicated analysis of initial-state radiation effects would be necessary for a comprehensive scan of the relevant parameter space, as varying the beam energy to cover the mediator mass range would be quite inefficient. Incorporating these radiative corrections represents another natural extension of the current study.

To conclude, it should be emphasized once again that assessing the sensitivity of laboratory facilities to BSM effects in the considered mass window is a nontrivial task. Unlike in the low-mass regime—where the ALP–photon coupling can be safely treated as effectively isolated interaction channel—in the intermediate and higher-mass domains one must adopt a more comprehensive and model-aware framework. In particular, reliable projections demand explicit assumptions about the ultraviolet origin of the effective operators, the relative hierarchy of couplings, and the resulting interplay between production and decay mechanisms.

The analysis presented in this thesis demonstrates that substantial progress is within reach. Over the coming years, low-energy, high-precision experiments, such as MESA and JLab, are expected to significantly extend the sensitivity to weakly coupled new states. Their capability to combine high luminosity with excellent control over systematic uncertainties makes them uniquely suited to probe small effective couplings and rare decay signatures.

The JLab experiment also serves as a prime example of a novel approach based on polarization-sensitive observables, which can be extended in several ways and applied in the context of future lepton collider and beam-dump facilities. Although the implications for direct ALP searches remain an open question and will likely require the study of double-spin asymmetries, the framework was shown to be highly promising for scalar and vector mediators. It provides not only a uniquely sensitive probe of these particles, but also a clear pathway to distinguish their underlying spin structures (e.g., between vector and axial vector couplings).

As precision experiments continue to advance, it can be expected that in the near future, this previously underexplored region of parameter space will be systematically

probed, significantly narrowing the viable landscape for light BSM mediators. Ultimately, the combination of advanced experimental techniques with rigorous, model-aware theoretical frameworks—such as the one developed in this thesis—will be essential to definitively constrain, or perhaps uncover, the physics of the dark sector.

Chapter 7

Use of AI Tools

Tool	Purpose	Reason for Use	Scope of Use
Gemini 3.1 Pro	Minor language improvements, grammar correction, and stylistic suggestions	To improve readability and overall linguistic quality of the text	Applied selectively throughout the manuscript
	Front page figure	To assist in expressing the author's visual concept	Front page only

Table 7.1: AI tools used during the preparation of this thesis.

Chapter 8

Special acknowledgments

> Everything we hear is an opinion,
> not a fact. Everything we see is a
> perspective, not the truth.
>
> *Marcus Aurelius*

This is a just small personal section, which I am writing informally and mostly for myself, as a conclusion to the period preceding the defense, toward which I have been striving for the last four and a half years.

It so happens that my sensory experience suggests the following: in the overwhelming majority of cases, I am either very lucky or very unlucky. This impression is supported by a long series of stories where, by pure and otherwise difficult to imagine coincidence, I found myself in various difficult circumstances in which, in general, a person should not find themselves.

At the same time, I am deeply convinced that I have been incredibly lucky in two aspects of my life—the education I received and the people I have met. My PhD supervisor, Marc Vanderhaeghen, as well as my Master's supervisor, Victor Yu. Petrov, are among those from whom I have learned the most in my life. I would also like to thank Andrei G. Shuvaev from the bottom of my heart for his boundless patience and his willingness to answer my countless questions, sometimes late into the night.

And, **most importantly**, the person without whom neither this work would ever have been written, nor I would have be myself, is my wife, Victoria, who is my world.

I would also like to thank several other people who contributed to this—Alexander P. Dmitriev for his insightful comments, as well as Kirill M. Semenov-Tian-Shansky and Maxim V. Polyakov for their guidance and support. I also cannot express in words how sorry I am that both Maxim Polyakov and Victor Petrov, who happened to be not only my supervisor but also Maxim's at the time, passed away too early, with a difference of only a month. Both were not only extraordinary and unparalleled physicists but also widely educated individuals of remarkable character.

I would further like to express my gratitude to Konstantin Yu. Platonov, whose teaching skills are simply immeasurable, and to Victor V. Dubov, for supervising my Bachelor's degree and for his valuable comments. Furthermore, I am proud to have Dmitry A. Varshalovich, Alexandre V. Ivanchik and Denis A. Baiko among my teachers, whose lectures on general relativity, QED and other subjects were truly invaluable.

And, of course, if for some reason someone was not mentioned above, it is solely my fault and a manifestation of impending sclerosis.

My driving force was, and remains, curiosity about how all this works—from the

smallest to the largest things—and I am still curious about it. I would also like to note that I am deeply convinced that if I was able to reach this stage, then **you**, too, can achieve what you have planned, if you want it badly enough. I just see no other way to explain how a person who barely passed the university entrance exams and was admitted to the physics department with the lowest score in physics among all the students that year was nevertheless able to make it[1].

I'll be honest, I wasn't sure I'd succeed, but I knew I had to try. And then, after two years of intense struggle, I, all of a sudden, received a scholarship for academic excellence. It's been surely a long journey for a kid from Norilsk, who at an early age, by chance, came across Hawking's "A Brief History of Time" book, which shaped his perception of the world and explained a lot about this reality, full of wonders. And honestly, I don't know what I would do in my life without knowing how Faddeev–Popov quantization works—because it is so cool, and people who don't know what we're talking about simply don't understand what they're missing.

I am thankful to Saint Petersburg Academic University for the time I spent there, and to PRISMA+ for their trust in me and for the scholarship they provided. I am also grateful to everyone else who supported me along the way—Linda York, without whom I would never have been able to deal with all that countless paperwork; Eleni Kapnisti, for her willingness to explain the difference between Nebensatz and Hauptsatz for the tenth time, as well as other peculiarities of the German language; and the MPA team, including Freya Luberg and Victoria Durant, for their patience with my lack of social communication skills.

And finally, Victor I. Pashin, who is probably sure that I have forgotten about him—thank you too, for an amazingly long friendship over more than 20 years.

[1] Special thanks to the flexibility of the Russian educational system, due to which I was admitted because of a perfect score in the Russian language—quite an uncommon achievement among physics students.

Bibliography

[1] F. Englert and R. Brout, "Broken Symmetry and the Mass of Gauge Vector Mesons", Phys. Rev. Lett. **13**, edited by J. C. Taylor, 321–323 (1964).

[2] P. W. Higgs, "Broken Symmetries and the Masses of Gauge Bosons", Phys. Rev. Lett. **13**, edited by J. C. Taylor, 508–509 (1964).

[3] S. Chatrchyan et al., "Observation of a New Boson at a Mass of 125 GeV with the CMS Experiment at the LHC", Phys. Lett. B **716**, 30–61 (2012), arXiv:1207.7235 [hep-ex].

[4] S. Weinberg, "Phenomenological Lagrangians", Physica A **96**, edited by S. Deser, 327–340 (1979).

[5] W. Buchmuller and D. Wyler, "Effective Lagrangian Analysis of New Interactions and Flavor Conservation", Nucl. Phys. B **268**, 621–653 (1986).

[6] C. P. Burgess, "Introduction to Effective Field Theory", Ann. Rev. Nucl. Part. Sci. **57**, 329–362 (2007), arXiv:hep-th/0701053.

[7] I. Brivio and M. Trott, "The Standard Model as an Effective Field Theory", Phys. Rept. **793**, 1–98 (2019), arXiv:1706.08945 [hep-ph].

[8] V. C. Rubin and W. K. Ford Jr., "Rotation of the Andromeda Nebula from a Spectroscopic Survey of Emission Regions", Astrophys. J. **159**, 379–403 (1970).

[9] V. C. Rubin, N. Thonnard, and W. K. Ford Jr., "Rotational properties of 21 SC galaxies with a large range of luminosities and radii, from NGC 4605 /R = 4kpc/ to UGC 2885 /R = 122 kpc/", Astrophys. J. **238**, 471 (1980).

[10] G. Bertone, D. Hooper, and J. Silk, "Particle dark matter: Evidence, candidates and constraints", Phys. Rept. **405**, 279–390 (2005), arXiv:hep-ph/0404175.

[11] J. L. Feng, "Dark Matter Candidates from Particle Physics and Methods of Detection", Ann. Rev. Astron. Astrophys. **48**, 495–545 (2010), arXiv:1003.0904 [astro-ph.CO].

[12] N. Aghanim et al., "Planck 2018 results. VI. Cosmological parameters", Astron. Astrophys. **641**, [Erratum: Astron.Astrophys. 652, C4 (2021)], A6 (2020), arXiv:1807.06209 [astro-ph.CO].

[13] G. Bertone and T. Tait M. P., "A new era in the search for dark matter", Nature **562**, 51–56 (2018), arXiv:1810.01668 [astro-ph.CO].

[14] R. D. Peccei and H. R. Quinn, "CP Conservation in the Presence of Instantons", Phys. Rev. Lett. **38**, 1440–1443 (1977).

[15] R. D. Peccei and H. R. Quinn, "Constraints Imposed by CP Conservation in the Presence of Instantons", Phys. Rev. D **16**, 1791–1797 (1977).

[16] S. Weinberg, "A New Light Boson?", Phys. Rev. Lett. **40**, 223–226 (1978).

[17] F. Wilczek, "Problem of Strong P and T Invariance in the Presence of Instantons", Phys. Rev. Lett. **40**, 279–282 (1978).

[18] M. A. Shifman, A. I. Vainshtein, and V. I. Zakharov, "Can Confinement Ensure Natural CP Invariance of Strong Interactions?", Nucl. Phys. B **166**, 493–506 (1980).

[19] M. Dine, W. Fischler, and M. Srednicki, "A Simple Solution to the Strong CP Problem with a Harmless Axion", Phys. Lett. B **104**, 199–202 (1981).

[20] J. E. Kim and G. Carosi, "Axions and the Strong CP Problem", Rev. Mod. Phys. **82**, [Erratum: Rev.Mod.Phys. 91, 049902 (2019)], 557–602 (2010), arXiv:0807.3125 [hep-ph].

[21] D. J. E. Marsh, "Axion Cosmology", Phys. Rept. **643**, 1–79 (2016), arXiv:1510.07633 [astro-ph.CO].

[22] L. Di Luzio, M. Giannotti, E. Nardi, and L. Visinelli, "The landscape of QCD axion models", Phys. Rept. **870**, 1–117 (2020), arXiv:2003.01100 [hep-ph].

[23] M. Magg and C. Wetterich, "Neutrino Mass Problem and Gauge Hierarchy", Phys. Lett. B **94**, 61–64 (1980).

[24] S. F. King, "Models of Neutrino Mass, Mixing and CP Violation", J. Phys. G **42**, 123001 (2015), arXiv:1510.02091 [hep-ph].

[25] S. Vagnozzi, E. Giusarma, O. Mena, K. Freese, M. Gerbino, S. Ho, and M. Lattanzi, "Unveiling ν secrets with cosmological data: neutrino masses and mass hierarchy", Phys. Rev. D **96**, 123503 (2017), arXiv:1701.08172 [astro-ph.CO].

[26] E. Bertuzzo, S. Jana, P. A. N. Machado, and R. Zukanovich Funchal, "Neutrino Masses and Mixings Dynamically Generated by a Light Dark Sector", Phys. Lett. B **791**, 210–214 (2019), arXiv:1808.02500 [hep-ph].

[27] M. Lindner, T. Ohlsson, and G. Seidl, "Seesaw mechanisms for Dirac and Majorana neutrino masses", Phys. Rev. D **65**, 053014 (2002), arXiv:hep-ph/0109264.

[28] A. D. Sakharov, "Violation of CP Invariance, C asymmetry, and baryon asymmetry of the universe", Pisma Zh. Eksp. Teor. Fiz. **5**, 32–35 (1967).

[29] A. Pilaftsis, "CP violation and baryogenesis due to heavy Majorana neutrinos", Phys. Rev. D **56**, 5431–5451 (1997), arXiv:hep-ph/9707235.

[30] K. Petraki and R. R. Volkas, "Review of asymmetric dark matter", Int. J. Mod. Phys. A **28**, 1330028 (2013), arXiv:1305.4939 [hep-ph].

[31] A. Hook, "Baryogenesis from Hawking Radiation", Phys. Rev. D **90**, 083535 (2014), arXiv:1404.0113 [hep-ph].

[32] N. Blinov, J. Kozaczuk, D. E. Morrissey, and C. Tamarit, "Electroweak Baryogenesis from Exotic Electroweak Symmetry Breaking", Phys. Rev. D **92**, 035012 (2015), arXiv:1504.05195 [hep-ph].

[33] L. Covi, H.-B. Kim, J. E. Kim, and L. Roszkowski, "Axinos as dark matter", JHEP **05**, 033 (2001), arXiv:hep-ph/0101009.

[34] Y. Nomura and J. Thaler, "Dark Matter through the Axion Portal", Phys. Rev. D **79**, 075008 (2009), arXiv:0810.5397 [hep-ph].

[35] L. D. Duffy and K. van Bibber, "Axions as Dark Matter Particles", New J. Phys. **11**, 105008 (2009), arXiv:0904.3346 [hep-ph].

[36] J. Jaeckel and A. Ringwald, "The Low-Energy Frontier of Particle Physics", Ann. Rev. Nucl. Part. Sci. **60**, 405–437 (2010), arXiv:1002.0329 [hep-ph].

[37] A. Ringwald, "Exploring the Role of Axions and Other WISPs in the Dark Universe", Phys. Dark Univ. **1**, 116–135 (2012), arXiv:1210.5081 [hep-ph].

[38] K. Baker et al., "The quest for axions and other new light particles", Annalen Phys. **525**, A93–A99 (2013), arXiv:1306.2841 [hep-ph].

[39] P. W. Graham, I. G. Irastorza, S. K. Lamoreaux, A. Lindner, and K. A. van Bibber, "Experimental Searches for the Axion and Axion-Like Particles", Ann. Rev. Nucl. Part. Sci. **65**, 485–514 (2015), arXiv:1602.00039 [hep-ex].

[40] K. Choi, S. H. Im, and C. Sub Shin, "Recent Progress in the Physics of Axions and Axion-Like Particles", Ann. Rev. Nucl. Part. Sci. **71**, 225–252 (2021), arXiv:2012.05029 [hep-ph].

[41] P. Svrcek and E. Witten, "Axions In String Theory", JHEP **06**, 051 (2006), arXiv:hep-th/0605206.

[42] A. Arvanitaki, S. Dimopoulos, S. Dubovsky, N. Kaloper, and J. March-Russell, "String Axiverse", Phys. Rev. D **81**, 123530 (2010), arXiv:0905.4720 [hep-th].

[43] C. Abel et al., "Measurement of the Permanent Electric Dipole Moment of the Neutron", Phys. Rev. Lett. **124**, 081803 (2020), arXiv:2001.11966 [hep-ex].

[44] S. Navas et al., "Review of particle physics", Phys. Rev. D **110**, 030001 (2024).

[45] R. Kitano and Y. Nomura, "Supersymmetry, naturalness, and signatures at the LHC", Phys. Rev. D **73**, 095004 (2006), arXiv:hep-ph/0602096.

[46] G. F. Giudice, "Naturally Speaking: The Naturalness Criterion and Physics at the LHC", edited by G. Kane and A. Pierce, 155–178 (2008), arXiv:0801.2562 [hep-ph].

[47] E. Halkiadakis, G. Redlinger, and D. Shih, "Status and Implications of Beyond-the-Standard-Model Searches at the LHC", Ann. Rev. Nucl. Part. Sci. **64**, 319–342 (2014), arXiv:1411.1427 [hep-ex].

[48] S. Rappoccio, "The experimental status of direct searches for exotic physics beyond the standard model at the Large Hadron Collider", Rev. Phys. **4**, 100027 (2019), arXiv:1810.10579 [hep-ex].

[49] J. L. Hewett et al., "Fundamental Physics at the Intensity Frontier", in (May 2012), arXiv:1205.2671 [hep-ex].

[50] J. Alexander et al., "Dark Sectors 2016 Workshop: Community Report", in (Aug. 2016), arXiv:1608.08632 [hep-ph].

[51] M. Battaglieri et al., "US Cosmic Visions: New Ideas in Dark Matter 2017: Community Report", in U.S. Cosmic Visions: New Ideas in Dark Matter (July 2017), arXiv:1707.04591 [hep-ph].

[52] J. Beacham et al., "Physics Beyond Colliders at CERN: Beyond the Standard Model Working Group Report", J. Phys. G **47**, 010501 (2020), arXiv:1901.09966 [hep-ex].

[53] G. Heinrich, "Collider Physics at the Precision Frontier", Phys. Rept. **922**, 1–69 (2021), arXiv:2009.00516 [hep-ph].

[54] L. Gan, B. Kubis, E. Passemar, and S. Tulin, "Precision tests of fundamental physics with η and η' mesons", Phys. Rept. **945**, 1–105 (2022), arXiv:2007.00664 [hep-ph].

[55] P. Agrawal et al., "Feebly-interacting particles: FIPs 2020 workshop report", Eur. Phys. J. C **81**, 1015 (2021), arXiv:2102.12143 [hep-ph].

[56] C. Antel et al., "Feebly Interacting Particles: FIPs 2022 workshop report", Eur. Phys. J. C **83**, 1122 (2023), arXiv:2305.01715 [hep-ph].

[57] M. Pospelov and A. Ritz, "Electric dipole moments as probes of new physics", Annals Phys. **318**, 119–169 (2005), arXiv:hep-ph/0504231.

[58] M. Pospelov, "Secluded U(1) below the weak scale", Phys. Rev. D **80**, 095002 (2009), arXiv:0811.1030 [hep-ph].

[59] G. F. Giudice, P. Paradisi, and M. Passera, "Testing new physics with the electron g-2", JHEP **11**, 113 (2012), arXiv:1208.6583 [hep-ph].

[60] C.-Y. Chen, H. Davoudiasl, W. J. Marciano, and C. Zhang, "Implications of a light "dark Higgs" solution to the g_μ-2 discrepancy", Phys. Rev. D **93**, 035006 (2016), arXiv:1511.04715 [hep-ph].

[61] W. J. Marciano, A. Masiero, P. Paradisi, and M. Passera, "Contributions of axionlike particles to lepton dipole moments", Phys. Rev. D **94**, 115033 (2016), arXiv:1607.01022 [hep-ph].

[62] M. Lindner, M. Platscher, and F. S. Queiroz, "A Call for New Physics : The Muon Anomalous Magnetic Moment and Lepton Flavor Violation", Phys. Rept. **731**, 1–82 (2018), arXiv:1610.06587 [hep-ph].

[63] A. Keshavarzi, K. S. Khaw, and T. Yoshioka, "Muon $g-2$: A review", Nucl. Phys. B **975**, 115675 (2022), arXiv:2106.06723 [hep-ex].

[64] P. Athron, K. Möhling, D. Stöckinger, and H. Stöckinger-Kim, "The muon magnetic moment and physics beyond the standard model", Prog. Part. Nucl. Phys. **148**, 104225 (2026), arXiv:2507.09289 [hep-ph].

[65] M. Pospelov and A. Ritz, "Electric Dipole Moments and New Physics", (2025), arXiv:2509.23531 [hep-ph].

[66] T. Aoyama et al., "The anomalous magnetic moment of the muon in the Standard Model", Phys. Rept. **887**, 1–166 (2020), arXiv:2006.04822 [hep-ph].

[67] G. W. Bennett et al., "Final Report of the Muon E821 Anomalous Magnetic Moment Measurement at BNL", Phys. Rev. D **73**, 072003 (2006), arXiv:hep-ex/0602035.

[68] R. Aliberti et al., "The anomalous magnetic moment of the muon in the Standard Model: an update", Phys. Rept. **1143**, 1–158 (2025), arXiv:2505.21476 [hep-ph].

[69] C. O'Hare, *Cajohare/axionlimits: axionlimits*, https://cajohare.github.io/AxionLimits/, version v1.0, July 2020.

[70] D. P. Aguillard et al., "Measurement of the Positive Muon Anomalous Magnetic Moment to 127 ppb", Phys. Rev. Lett. **135**, 101802 (2025), arXiv:2506.03069 [hep-ex].

[71] A. Pustyntsev and M. Vanderhaeghen, "Improved constraints for axion-like particles from 3-photon events at e^+e^- colliders", Eur. Phys. J. C **84**, 546 (2024), arXiv:2309.15106 [hep-ph].

[72] A. Pustyntsev and M. Vanderhaeghen, "Constraints for scalars and pseudoscalars from (g-2)l and existing e+e- colliders", Phys. Rev. D **110**, 075027 (2024), arXiv:2407.20202 [hep-ph].

[73] A. Hook, "TASI Lectures on the Strong CP Problem and Axions", PoS **TASI2018**, 004 (2019), arXiv:1812.02669 [hep-ph].

[74] M. Meyer, D. Horns, and M. Raue, "First lower limits on the photon-axion-like particle coupling from very high energy gamma-ray observations", Phys. Rev. D **87**, 035027 (2013), arXiv:1302.1208 [astro-ph.HE].

[75] G. Galanti and M. Roncadelli, "Axion-like Particles Implications for High-Energy Astrophysics", Universe **8**, 253 (2022), arXiv:2205.00940 [hep-ph].

[76] M. Giannotti, I. Irastorza, J. Redondo, and A. Ringwald, "Cool WISPs for stellar cooling excesses", JCAP **05**, 057 (2016), arXiv:1512.08108 [astro-ph.HE].

[77] K. Saikawa and T. T. Yanagida, "Stellar cooling anomalies and variant axion models", JCAP **03**, 007 (2020), arXiv:1907.07662 [hep-ph].

[78] M. J. Dolan, T. Ferber, C. Hearty, F. Kahlhoefer, and K. Schmidt-Hoberg, "Revised constraints and Belle II sensitivity for visible and invisible axion-like particles", JHEP **12**, [Erratum: JHEP 03, 190 (2021)], 094 (2017), arXiv:1709.00009 [hep-ph].

[79] M. Acciarri et al., "Search for anomalous Z –> gamma gamma gamma events at LEP", Phys. Lett. B **345**, 609–616 (1995).

[80] M. Acciarri et al., "Tests of QED at LEP energies using e+ e- –> gamma gamma (gamma) and e+ e- –> lepton+ lepton- gamma gamma", Phys. Lett. B **353**, 136–144 (1995).

[81] E. Izaguirre, T. Lin, and B. Shuve, "Searching for Axionlike Particles in Flavor-Changing Neutral Current Processes", Phys. Rev. Lett. **118**, 111802 (2017), arXiv:1611.09355 [hep-ph].

[82] J. P. Lees et al., "Search for an Axionlike Particle in B Meson Decays", Phys. Rev. Lett. **128**, 131802 (2022), arXiv:2111.01800 [hep-ex].

[83] M. J. Dolan, F. Kahlhoefer, C. McCabe, and K. Schmidt-Hoberg, "A taste of dark matter: Flavour constraints on pseudoscalar mediators", JHEP **03**, [Erratum: JHEP 07, 103 (2015)], 171 (2015), arXiv:1412.5174 [hep-ph].

[84] J. P. Lees et al., "Search for hadronic decays of a light Higgs boson in the radiative decay $\Upsilon \to \gamma A^0$", Phys. Rev. Lett. **107**, 221803 (2011), arXiv:1108.3549 [hep-ex].

[85] J. Liu, X. Ma, L.-T. Wang, and X.-P. Wang, "ALP explanation to the muon (g-2) and its test at future Tera-Z and Higgs factories", Phys. Rev. D **107**, 095016 (2023), arXiv:2210.09335 [hep-ph].

[86] J. Liu, Y. Luo, and M. Song, "Investigation of the concurrent effects of ALP-photon and ALP-electron couplings in Collider and Beam Dump Searches", JHEP **09**, 104 (2023), arXiv:2304.05435 [hep-ph].

[87] M. Ablikim et al., "Search for an axion-like particle in radiative J/ψ decays", Phys. Lett. B **838**, 137698 (2023), arXiv:2211.12699 [hep-ex].

[88] M. Ablikim et al., "Search for di-photon decays of an axion-like particle in radiative J/ψ decays", (2024), arXiv:2404.04640 [hep-ex].

[89] R. Z. Ferreira, M. C. D. Marsh, and E. Müller, "Strong supernovae bounds on ALPs from quantum loops", JCAP **11**, 057 (2022), arXiv:2205.07896 [hep-ph].

[90] S. I. Eidelman and E. A. Kuraev, "e+ e- Annihilation Into Two and Three Photons at High-Energy", Nucl. Phys. B **143**, 353–364 (1978).

[91] R. Gastmans and T. T. Wu, *The Ubiquitous photon: Helicity method for QED and QCD*, Vol. 80 (1990).

[92] J. Fujimoto and M. Igarashi, "Distributions for $e^+e^- \to 3\gamma$ at High-energy", Prog. Theor. Phys. **74**, 791 (1985).

[93] W. Altmannshofer et al., "The Belle II Physics Book", PTEP **2019**, edited by E. Kou and P. Urquijo, [Erratum: PTEP 2020, 029201 (2020)], 123C01 (2019), arXiv:1808.10567 [hep-ex].

[94] F. Abudinén et al., "Search for Axion-Like Particles produced in e^+e^- collisions at Belle II", Phys. Rev. Lett. **125**, 161806 (2020), arXiv:2007.13071 [hep-ex].

[95] A. M. Sirunyan et al., "Evidence for light-by-light scattering and searches for axion-like particles in ultraperipheral PbPb collisions at $\sqrt{s_{\mathrm{NN}}} = 5.02$ TeV", Phys. Lett. B **797**, 134826 (2019), arXiv:1810.04602 [hep-ex].

[96] G. Aad et al., "Measurement of light-by-light scattering and search for axion-like particles with 2.2 nb^{-1} of Pb+Pb data with the ATLAS detector", JHEP **03**, [Erratum: JHEP 11, 050 (2021)], 243 (2021), arXiv:2008.05355 [hep-ex].

[97] B. Batell, N. Lange, D. McKeen, M. Pospelov, and A. Ritz, "Muon anomalous magnetic moment through the leptonic Higgs portal", Phys. Rev. D **95**, 075003 (2017), arXiv:1606.04943 [hep-ph].

[98] M. W. Winkler, "Decay and detection of a light scalar boson mixing with the Higgs boson", Phys. Rev. D **99**, 015018 (2019), arXiv:1809.01876 [hep-ph].

[99] W. Abdallah, R. Gandhi, and S. Roy, "Understanding the MiniBooNE and the muon and electron $g-2$ anomalies with a light Z' and a second Higgs doublet", JHEP **12**, 188 (2020), arXiv:2006.01948 [hep-ph].

[100] A. Berlin, N. Blinov, G. Krnjaic, P. Schuster, and N. Toro, "Dark Matter, Millicharges, Axion and Scalar Particles, Gauge Bosons, and Other New Physics with LDMX", Phys. Rev. D **99**, 075001 (2019), arXiv:1807.01730 [hep-ph].

[101] G. Arcadi, A. Djouadi, and M. Raidal, "Dark Matter through the Higgs portal", Phys. Rept. **842**, 1–180 (2020), arXiv:1903.03616 [hep-ph].

[102] P. Athron, C. Balázs, D. H. J. Jacob, W. Kotlarski, D. Stöckinger, and H. Stöckinger-Kim, "New physics explanations of a_μ in light of the FNAL muon g − 2 measurement", JHEP **09**, 080 (2021), arXiv:2104.03691 [hep-ph].

[103] H. Davoudiasl, H.-S. Lee, and W. J. Marciano, "'Dark' Z implications for Parity Violation, Rare Meson Decays, and Higgs Physics", Phys. Rev. D **85**, 115019 (2012), arXiv:1203.2947 [hep-ph].

[104] P. Athron et al., "Status of the scalar singlet dark matter model", Eur. Phys. J. C **77**, 568 (2017), arXiv:1705.07931 [hep-ph].

[105] C. Mondino, M. Pospelov, J. T. Ruderman, and O. Slone, "Dark Higgs Dark Matter", Phys. Rev. D **103**, 035027 (2021), arXiv:2005.02397 [hep-ph].

[106] M. Fabbrichesi, E. Gabrielli, and G. Lanfranchi, "The Dark Photon", 10.1007/978-3-030-62519-1 (2020), arXiv:2005.01515 [hep-ph].

[107] M. D. Schwartz, *Quantum Field Theory and the Standard Model* (Cambridge University Press, Mar. 2014).

[108] G. 't Hooft and M. J. G. Veltman, "Scalar One Loop Integrals", Nucl. Phys. B **153**, 365–401 (1979).

[109] J. S. Schwinger, "On Quantum electrodynamics and the magnetic moment of the electron", Phys. Rev. **73**, 416–417 (1948).

[110] T. Aoyama, M. Hayakawa, T. Kinoshita, and M. Nio, "Tenth-Order Electron Anomalous Magnetic Moment — Contribution of Diagrams without Closed Lepton Loops", Phys. Rev. D **91**, [Erratum: Phys.Rev.D 96, 019901 (2017)], 033006 (2015), arXiv:1412.8284 [hep-ph].

[111] A. Pustyntsev and M. Vanderhaeghen, "Implications of recent (g-2)μ measurements for MeV-GeV dark sector searches", Phys. Rev. D **112**, 095001 (2025), arXiv:2506.17750 [hep-ph].

[112] V. B. Berestetskii, E. M. Lifshitz, and L. P. Pitaevskii, *QUANTUM ELECTRODYNAMICS*, Vol. 4, Course of Theoretical Physics (Pergamon Press, Oxford, 1982).

[113] S. Abrahamyan et al., "Search for a New Gauge Boson in Electron-Nucleus Fixed-Target Scattering by the APEX Experiment", Phys. Rev. Lett. **107**, 191804 (2011), arXiv:1108.2750 [hep-ex].

[114] H. Merkel et al., "Search at the Mainz Microtron for Light Massive Gauge Bosons Relevant for the Muon g-2 Anomaly", Phys. Rev. Lett. **112**, 221802 (2014), arXiv:1404.5502 [hep-ex].

[115] J. P. Lees et al., "Search for a Dark Photon in e^+e^- Collisions at BaBar", Phys. Rev. Lett. **113**, 201801 (2014), arXiv:1406.2980 [hep-ex].

[116] J. R. Batley et al., Phys. Lett. B **746**, 178–185 (2015).

[117] A. Anastasi et al., "Limit on the production of a low-mass vector boson in $e^+e^- \to U\gamma$, $U \to e^+e^-$ with the KLOE experiment", Phys. Lett. B **750**, 633–637 (2015), arXiv:1509.00740 [hep-ex].

[118] A. Anastasi et al., "Limit on the production of a new vector boson in $e^+e^- \to U\gamma$, $U \to \pi^+\pi^-$ with the KLOE experiment", Phys. Lett. B **757**, 356–361 (2016), arXiv:1603.06086 [hep-ex].

[119] M. Ablikim et al., "Dark Photon Search in the Mass Range Between 1.5 and 3.4 GeV/c^2", Phys. Lett. B **774**, 252–257 (2017), arXiv:1705.04265 [hep-ex].

[120] D. Banerjee et al., "Search for a Hypothetical 16.7 MeV Gauge Boson and Dark Photons in the NA64 Experiment at CERN", Phys. Rev. Lett. **120**, 231802 (2018), arXiv:1803.07748 [hep-ex].

[121] R. Aaij et al., "Search for $A' \to \mu^+\mu^-$ Decays", Phys. Rev. Lett. **124**, 041801 (2020), arXiv:1910.06926 [hep-ex].

[122] M. Bauer, M. Neubert, and A. Thamm, "LHC as an Axion Factory: Probing an Axion Explanation for $(g-2)_\mu$ with Exotic Higgs Decays", Phys. Rev. Lett. **119**, 031802 (2017), arXiv:1704.08207 [hep-ph].

[123] M. Bauer, M. Neubert, S. Renner, M. Schnubel, and A. Thamm, "Axionlike Particles, Lepton-Flavor Violation, and a New Explanation of a_μ and a_e", Phys. Rev. Lett. **124**, 211803 (2020), arXiv:1908.00008 [hep-ph].

[124] M. A. Buen-Abad, J. Fan, M. Reece, and C. Sun, "Challenges for an axion explanation of the muon $g-2$ measurement", JHEP **09**, 101 (2021), arXiv:2104.03267 [hep-ph].

[125] X. Fan, T. G. Myers, B. A. D. Sukra, and G. Gabrielse, "Measurement of the Electron Magnetic Moment", Phys. Rev. Lett. **130**, 071801 (2023), arXiv:2209.13084 [physics.atom-ph].

[126] M. Bauer, M. Neubert, and A. Thamm, "Collider Probes of Axion-Like Particles", JHEP **12**, 044 (2017), arXiv:1708.00443 [hep-ph].

[127] D. V. Kirpichnikov, V. E. Lyubovitskij, and A. S. Zhevlakov, "Constraints on CP-odd ALP couplings from EDM limits of fermions", Particles **3**, 719–728 (2020), arXiv:2004.13656 [hep-ph].

[128] C. E. Carlson and B. C. Rislow, "New Physics and the Proton Radius Problem", Phys. Rev. D **86**, 035013 (2012), arXiv:1206.3587 [hep-ph].

[129] J. P. Lees et al., "Search for Invisible Decays of a Dark Photon Produced in e^+e^- Collisions at BaBar", Phys. Rev. Lett. **119**, 131804 (2017), arXiv:1702.03327 [hep-ex].

[130] M. Ablikim et al., "Search for invisible decays of a dark photon using e+e− annihilation data at BESIII", Phys. Lett. B **839**, 137785 (2023), arXiv:2209.13893 [hep-ex].

[131] N. Berger, A. Denig, F. Maas, and C. Sfienti, "The MESA Experimental Program: A Laboratory for Precision Physics with Electron Scattering at Low Energy", Nuclear Physics News **31**, 5–10 (2021), eprint: https://doi.org/10.1080/10619127.2021.1954434.

[132] S. Schlimme et al., "The MESA physics program", EPJ Web Conf. **303**, 06002 (2024), arXiv:2402.01027 [nucl-ex].

[133] B. S. Schlimme et al., "Operation and characterization of a windowless gas jet target in high-intensity electron beams", Nucl. Instrum. Meth. A **1013**, 165668 (2021), arXiv:2104.13503 [physics.ins-det].

[134] D. Banerjee et al., Phys. Rev. D **101**, 071101 (2020).

[135] L. Di Luzio, P. Paradisi, and N. Selimovic, "Hunting for a 17 MeV particle coupled to electrons", Nucl. Phys. B **1021**, 117177 (2025), arXiv:2504.14014 [hep-ph].

[136] S. Egli et al., "Measurement of the Decay $\pi^+ \to e^+\nu_e e^+ e^-$ and Search for a Light Higgs Boson", Phys. Lett. B **222**, 533–537 (1989).

[137] Y. M. Andreev et al., Phys. Rev. Lett. **131**, 161801 (2023).

[138] G. Moortgat-Pick et al., "The Role of polarized positrons and electrons in revealing fundamental interactions at the linear collider", Phys. Rept. **460**, 131–243 (2008), arXiv:hep-ph/0507011.

[139] E. Voutier, "Physics potential of polarized positrons at the Jefferson Laboratory", Nucl. Theor. **33**, edited by A. Georgieva and N. Minkov, 142–151 (2014), arXiv:1412.1249 [nucl-ex].

[140] A. Accardi et al., "An experimental program with high duty-cycle polarized and unpolarized positron beams at Jefferson Lab", Eur. Phys. J. A **57**, 261 (2021), arXiv:2007.15081 [nucl-ex].

[141] M. K. Jones et al., "G_{Ep}/G_{Mp} ratio by polarization transfer in $\vec{e}p \to e\vec{p}$", Phys. Rev. Lett. **84**, 1398–1402 (2000), arXiv:nucl-ex/9910005.

[142] V. Punjabi, C. F. Perdrisat, M. K. Jones, E. J. Brash, and C. E. Carlson, "The Structure of the Nucleon: Elastic Electromagnetic Form Factors", Eur. Phys. J. A **51**, 79 (2015), arXiv:1503.01452 [nucl-ex].

[143] D. Müller, D. Robaschik, B. Geyer, F. M. Dittes, and J. Hořejši, "Wave functions, evolution equations and evolution kernels from light ray operators of QCD", Fortsch. Phys. **42**, 101–141 (1994), arXiv:hep-ph/9812448.

[144] X.-D. Ji, "Gauge-Invariant Decomposition of Nucleon Spin", Phys. Rev. Lett. **78**, 610–613 (1997), arXiv:hep-ph/9603249.

[145] X.-D. Ji, "Deeply virtual Compton scattering", Phys. Rev. D **55**, 7114–7125 (1997), arXiv:hep-ph/9609381.

[146] S. Stepanyan et al., "Observation of exclusive deeply virtual Compton scattering in polarized electron beam asymmetry measurements", Phys. Rev. Lett. **87**, 182002 (2001), arXiv:hep-ex/0107043.

[147] M. Guidal, M. V. Polyakov, A. V. Radyushkin, and M. Vanderhaeghen, "Nucleon form-factors from generalized parton distributions", Phys. Rev. D **72**, 054013 (2005), arXiv:hep-ph/0410251.

[148] A. V. Belitsky and A. V. Radyushkin, "Unraveling hadron structure with generalized parton distributions", Phys. Rept. **418**, 1–387 (2005), arXiv:hep-ph/0504030.

[149] D. Androić et al., "Precision measurement of the weak charge of the proton", Nature **557**, 207–211 (2018), arXiv:1905.08283 [nucl-ex].

[150] A. Pustyntsev, M. S. Ramasamy, and M. Vanderhaeghen, "New Physics Searches via Beam Normal Spin Asymmetry in Bhabha Scattering", (2025), arXiv:2511.22568 [hep-ph].

[151] M. Goldberger, Y Nambu, and R Oehme, Annals of Physics **2**, 226–282 (1957).

[152] C. Fronsdal, Phys. Rev. **121**, 916–919 (1961).

[153] D. Mack, *Searches for BSM interference terms in unpolarized and polarized Bhabha scattering*, "Hadron Physics 2030" workshop, https://indico.ijclab.in2p3.fr/event/10641/, 2024.

[154] V. Kozhuharov and M. Naydenov, Nucl. Phys. B **986**, 116044 (2023).

[155] The Belle II Collaboration, *Input to the European Strategy for Particle Physics - 2026 update*, https://indico.cern.ch//event/1439855/contributions/6461621/, 2026.

ALEKSANDR **PUSTYNTSEV**

Mainz | apustynt@uni-mainz.de | 10.07.1997

SUMMARY

Strongly self-motivated stress-resistant doctoral student focused on theoretical research work with advanced skills in mathematics, quantum field theory and more. Purposefulness and enthusiasm are my strong sides.

For me physics is not a craft, but an art. My main research interests are physics beyond the Standard Model, quantum anomalies, symmetry breaking and quantum gravity.

EDUCATION & EXPERIENCE

2021-Present

PhD: Physics
Johannes Gutenberg University of Mainz

Funded by PRISMA+ Cluster of Excellence and Research Unit 5327 "Photon-photon interactions in the Standard Model and beyond" (German Funding Agency DFG)

I am currently finishing my PhD program at the Nuclear Physics institute (funded by PRISMA+ Cluster of Excellence). My primal research is focused on the search for New Physics signals, such as potential effects from axion-like particles, extended Higgs or dark photons, at electron-positron colliders, beam dump experiments and $(g-2)_l$.

During my studies, I had a chance to attend multiple conferences, schools and workshops, as well as gain experience in teaching fundamental courses in English and conference organizing.

2019-2021

Master of Science: Physics (with honors, GPA 1.0)*
Saint Petersburg Academic University

My 2 year-long program was especially focused on field theory, quantum electrodynamics, quantum field theory, group theory, path integral techniques etc. I graduated with Honors (red diploma in Russian).

Thesis: The baryon charge nonconservation and hadron multiproduction at high energies

My research was related to baryon number violation at high energies and the production of large number of particles, sphaleron transitions, asymptotic of perturbation series, singular classical solutions, etc. This topic is complex, but becomes rather hot again due to the hope to observe corresponding effects at LHC energies.

2015-2019

Bachelor of Science: Physics (with honors, GPA 1.2)
Saint Petersburg State Polytechnical University

I finished 4 year-long bachelor program at faculty of astrophysics. During this period, I successfully passed general courses such as theoretical physics (classical mechanics, electrodynamics, thermodynamics, quantum mechanics and quantum electrodynamics), complex analysis and linear algebra, C/C++/Fortran/Matlab/Maple programming, numerical modeling, chemistry and others. I also attended such special courses as supernova physics, general relativity, nuclear astrophysics and more.

Thesis: Resonance kinematics of the Breit-Wheeler process in a laser field

The study of resonant QED processes in an external field has had high priority in the last 30 years due to active development of the powerful laser sources. During my undergraduate studies I performed a research on resonant Breit-Wheeler effect in

an external electromagnetic field, analyzed resonant kinematics in details and obtained an estimate for the cross section.

PRIMARY SKILLS

Advanced Quantum Field Theory
Path Integrals Techniques
Condensed Matter Physics
Semiclassical Methods
Gauge Theories
General Relativity
Effective Field Theories
Non-perturbative Methods
Group Theory
Analytical calculations

TALKS & POSTERS

Low Energy Electron Positron Physics Workshop at Jefferson Lab (2026) – "BSM signals from spin asymmetries in Bhabha scattering" (scheduled)

16th European Research Conference on Electromagnetic Interactions with Nucleons and Nuclei EINN (2025) – "New Physics searches in low-energy precision experiments" (talk at parallel session)

Axions in Stockholm (2025) – "Combined constraints for axion-like particles from $(g-2)_l$ and e^+e^- colliders" (talk)

Workshop of Research Unit FOR5327 (2025) – "Axion-like particles searches at collider and beam dump experiments: theory overview" (talk)

15th European Research Conference on Electromagnetic Interactions with Nucleons and Nuclei EINN (2023) – "Improved constraints for axion-like particles from 3-photon events at e^+e^- colliders" (poster session)

15th EINN preconference "Frontiers and Careers in Photonuclear Physics" (2023) – "Improved constraints for axion-like particles from 3-photon events at e^+e^- colliders" (talk)

International Conference on Meson-Nucleon Physics and the Structure of the Nucleon MENU (2023) – "Study of axion-like particles constraints from 3-photon events at e^+e^- colliders" (poster session)

Mainz Physics Academy (MPA) Retreat (2022) – "Dark sector searches at MESA accelerator and e^+e^- colliders" (talk)

Peter the Great St.Petersburg Polytechnic University (SPbPU) Week of Science (2019) – "Kinematics and cross section of resonant Breit-Wheeler process in the field of a plane monochromatic electromagnetic wave" (talk)

10th Alexander Friedmann International Seminar on Gravitation and Cosmology and 4th Symposium on the Casimir Effect (2019) – "Resonant Breit-Wheeler process in an external electromagnetic field" (talk)

SCHOOLS & WORKSHOPS

CRC (Collaborative Research Center) 1660: Annual Graduate School (2025)

Mainz Physics Academy (MPA) Summer School (2025)

Tutoring the tutors. Design your perfect class: beauty of teaching and beyond (2024)

The Fundamentals: Summer School in high-energy and gravitational physics (2024)

Mainz Physics Academy (MPA) Retreat (2024)

Mainz Physics Academy (MPA) Summer School (2023)

EPT (Engaging Physics Tutoring) Summer Camp for physics teachers (2023)

Presentation Skills Workshop by the Institute of Molecular Biology Mainz (2023)

PSI (Paul Scherrer Institute) Particle Physics Summer School – Vision and Precision (2022)

EPT (Engaging Physics Tutoring) Summer Camp for physics teaching assistants (2022)

ORGANIZING ACTIVITIES

16th European Research Conference on Electromagnetic Interactions with Nucleons and Nuclei EINN (2025) – organizing committee

16th EINN preconference "Frontiers and Careers in Photonuclear Physics" (2025) – main organizer and chair (35 participants)

Mainz Physics Academy (MPA) Summer School (2025) – organizing committee

Mainz Physics Academy (MPA) retreat (2024) – organizing committee

Mainz Physics Academy (MPA) Summer School (2023) – organizing committee

PUBLICATIONS

Sensitivity of MESA to BSM effects via Bethe-Heitler pair production – in preparation, 1Q 2026

New Physics Searches via Beam Normal Spin Asymmetry in Bhabha Scattering – under review

Implications of recent $(g-2)_\mu$ measurements for MeV-GeV dark sector searches – Phys. Rev. D 112, 095001 (2025)

Constraints for scalars and pseudoscalars from $(g-2)_l$ and existing e^+e^- colliders – Phys. Rev. D 110, 075027 (2024)

Study of axion-like particles constraints from 3-photon events at e^+e^- colliders – EPJ Web of Conferences 303, 05007 (2024)

Improved constraints for axion-like particles from 3-photon events at e^+e^- colliders – Eur. Phys. J. C 84, 546 (2024)

Resonant Breit-Wheeler process in an external electromagnetic field – Mod.Phys.Lett.A 35 (2020) 03, 2040027

TEACHING & PEDAGOGICS

Master student supervision (Muthubharathi Subbulakshmi) – "Searches for BSM effects in polarized Bhabha scattering", summer & winter semester 2025

Quantum field theory II (6b) – main assistant, summer semester 2024 (student evaluation – 1.7)†

Quantum field theory II (6b) – main assistant, winter semester 2022/2023 (student evaluation – 1.2)

Quantum field theory (6a) – main assistant, summer semester 2022 (student evaluation – 1.9)

---

* Grade Point Average in German grading system, ranging from 1.0 (top) to 5.0 (bottom)
† In German classification and grading system